Site BT1: fluid and mass exchange on a subduction zone plate boundary[1]

Kelemen, P.B., Matter, J.M., Teagle, D.A.H., Coggon, J.A., and the Oman Drilling Project Science Team[2]

Keywords: Oman Drilling Project, OmanDP, Site BT1, Hole BT1B, fluid transport, Samail ophiolite, metamorphic sole, mantle wedge, subduction zone deformation, listvenite, serpentinized peridotite, mass transport, Wadi Mansah

Chapter contents

Site BT1

To investigate the topics outlined in Science Theme 2 and particularly the mechanisms of carbon, oxygen, and hydrogen mass transfer via transport of subduction zone fluids into the mantle wedge, we chose to drill at Site BT1. This site is adjacent to a massive outcrop of listvenite underlain by other bands of serpentinite and listvenite. In turn, these bands overlie the basal thrust of the ophiolite, east of the village of Fanjah. In this area, prior work has identified a wide region of listvenite outcrop (Falk and Kelemen, 2015; Nasir et al., 2007; Stanger, 1985; Wilde et al., 2002). In this region, our recent work shows that the basal thrust, the underlying metamorphic sole, and the overlying, partially serpentinized and carbonated mantle peridotites are broadly folded and regionally subhorizontal (de Obeso and Kelemen, unpubl. data; Falk and Kelemen, 2015).

Hole BT1A penetrated 1.90 m of gravels of Wadi Mansah, just south of listvenite outcrops flanking the Wadi. After we became concerned that a steep hole there might intersect several tens of meters of gravel before reaching bedrock, we moved the drill. Hole BT1B is 3–4 m closer to the listvenite outcrop (Figs. F1, F2).

Noteworthy results from studies of drill core from Hole BT1B include documentation of nearly constant Mg/Si/Fe ratios in carbonated peridotites (listvenites) indicating large-scale addition of CO_2, Ca, and a few soluble trace elements (K, Rb, Cs, and Sr) to peridotite in the hanging wall of a subduction zone with little or no dissolution and removal of peridotite components. This requires >50% solid volume expansion relative to the partially serpentinized peridotite protolith (Kelemen et al., 2019; Kelemen and Manning, 2017). The protolith was probably similar to the "banded horizon" elsewhere in the ophiolite, which is enriched in incompatible trace elements relative to average residual mantle harzburgite in most of the Samail ophiolite mantle section (Godard et al., 2017; Lafay et al., 2019).

Pseudomorphs of opal and chalcedony confirm that replacement of peridotite by carbonate + quartz took place at ~100°C (Falk and Kelemen, 2015; Kelemen et al., 2019; Kelemen and Manning, 2017). Intergrown graphite and hematite attest to oxidizing conditions in a CO_2-rich fluid below 200°C. Intergrown antigorite + quartz requires an H_2O-rich fluid cooler than 120°C. These results suggest that a CO_2-rich aqueous fluid produced by devolatilization of subducting sediment and/or crust at depth unmixed during ascent, producing two immiscible fluids that both delivered CO_2 to the mantle wedge overlying the subduction zone at the site of Hole BT1B (de Obeso and Kelemen, 2018b; de Obeso et al., 2017;

[1]Kelemen, P.B., Matter, J.M., Teagle, D.A.H., Coggon, J.A., and the Oman Drilling Project Science Team, 2020. Site BT1: fluid and mass exchange on a subduction zone plate boundary. *In* Kelemen, P.B., Matter, J.M., Teagle, D.A.H., Coggon, J.A., and the Oman Drilling Project Science Team, *Proceedings of the Oman Drilling Project*: College Station, TX (International Ocean Discovery Program.
https://doi.org/10.14379/OmanDP.proc.113.2020
[2]OmanDP Science Team affiliations.

MS OmanDP-113
Published 23 July 2020

Kelemen et al., 2019; Kelemen and Manning, 2017; Manning et al., 2017, 2018; Urai et al., 2019).

Age-corrected Sr isotope ratios in carbonated peridotites, serpentinites, and metamorphic sole indicate that the CO_2-rich fluid(s) that modified the mantle overlying the basal thrust of the ophiolite had relatively high $^{87}Sr/^{86}Sr$ ratios compared to fresh residual mantle peridotites. The fluids were not derived from relatively unradiogenic lithologies such as those observed in the metamorphic sole but could have come from pelagic clastic units similar to those in the Hawasina formation, which underlies the ophiolite and the sole (de Obeso et al., 2018a). If so, this must have been accompanied by selective dehydration of clastic sediments with minimal decarbonation of the relatively unradiogenic carbonates that are also found in the Hawasina formation.

Remarkably, fine-grained quartz, serpentine, and carbonate show well-developed lattice-preferred orientation in some samples, formed by ductile deformation at low temperature in a subduction zone. Ductile fabrics are cut by veins, cataclastic shear zones, faults, and pseudotachylites. Study of these features will yield insights into subduction zone deformation at low temperature (Kelemen et al., 2019; Kelemen and Manning, 2017; Urai et al., 2019). The depth of carbonation and serpentinization of the Hole BT1B hanging wall peridotites remains unknown, as 100°C is a possible subduction zone temperature at ~6–60 km depth. High fluid pressures and micrometer-scale grain sizes might facilitate low-temperature ductile deformation.

Continued analysis of drill core from the hanging wall and footwall of the basal thrust, spanning the contact between metasediments and the overlying mantle (Figs. F1, F2), will allow direct study of chemical and physical processes of mass transfer and deformation in a subduction zone. Because the thrust beneath the Samail ophiolite was initially very young and hot, observations there will be interpreted in the context provided by investigations of other settings, especially along active subduction zones in different stages of evolution. In the context of research to be addressed via drilling in Oman, ideas and observations outlined above can be quantified through detailed 1-D geochemical and structural transects in drill core(s) combined with detailed mapping of the surrounding 3-D geology. Of particular interest will be identifying the footwall source(s) of carbon-rich fluids, the mechanical processes of fluid migration, the diffuse or localized nature of hanging wall alteration, the overall balance of low-temperature mass transfer, the pressure and temperature range over which mass transfer was active, the nature of low-temperature deformation in and above a subduction zone, and the extent to which Oman observations can be extrapolated to subduction zones worldwide.

Operations

All times are reported as local time in Oman (UTC + 4 h). An overview of all holes drilled is given in Table T3 in the **Methods** chapter. Drilling operations and core curation information are reported in Table T1.

Hole BT1A summary

- Spud-in: 06/03/2017, 11:16 h
- First core on deck: 06/03/2017, 12:20 h
- Surface casing (HW) installed: not applicable
- Surface casing (HW) extended: not applicable
- NW casing installed: not applicable
- Final core on deck: 06/03/2017, 12:45 h
- Total depth of borehole: 1.9 m

Technical issues

Hole BT1A was drilled to 1.9 m, sampling wadi sediments, but the string was repeatedly stuck in the hole. P. Kelemen made the decision to abort Hole BT1A and resite the rig 4 m closer to the outcrop to start drilling Hole BT1B to reduce the distance to be drilled through alluvium from an estimated 22 m to an estimated 14 m.

Hole BT1B summary

- Spud-in: 07/03/2017, 07:30 h
- First core on deck: 07/03/2017, 08:22 h
- Surface casing (HW) installed: 07/03/2017, 6.0 m
- Surface casing (HW) extended: not applicable
- NW casing installed: 16/03/2017, 167.10 m
- Final core on deck: 22/03/2017, 10:56 h
- Total depth of borehole: 300.05 m

Geology summary

- Veined listvenite with core-scale variability and strongly heterogeneous textures including weathered massive listvenite, some prominent gneissic fabric in long intervals, and fuchsite in numerous sections.
- Sampled a contact between listvenite and serpentinite at ~80 m and a spectacular transition from serpentinite back to listvenite at ~100 m.
- A second significant interval of serpentinite was sampled at ~180–185 m.
- Drilled across the basal thrust of the ophiolite at ~197 m, recovering fault gouge and strongly fragmented chlorite- and epidote-bearing, fine-grained rocks below.
- Folded and foliated greenschist facies metasediments and metabasalts make up the lowermost ~100 m of the hole.

Technical issues

Loss of 100% of circulating fluid during HQ drilling combined with sometimes insufficient deliveries of water by Lalbuksh tankers resulted in delays to drilling on occasion. The other major issue with this well was the extreme hardness of the listvenite, which caused rapid wear of even the hardest drill bits and resulted in slow advance downhole throughout this formation.

Drilling summary

- 07 Mar 2017: spud-in at 07:30 h. Drilled first 2 cores then incrementally reamed with HW casing to 6 m into bedrock. Reaming with shoe bit slow in weathered listvenite so decided to continue drilling HQ and leave casing set to 6 m.
- 08 Mar 2017: changed to new HQ bit first thing in the morning.
- 09 Mar 2017: lost 100% of drilling fluid circulation, making it difficult to clear cuttings. 15:15 h: bit check-up revealed that it has been smoothed by the formation. Drillers used a chisel and hammer to expose the second layer of the bit, sharpening it. Run in hole (RIH) and resumed drilling at 16:00 h.
- 10 Mar 2017: routine coring until 12:00 h when drillers stopped for day (Friday).
- 11 Mar 2017: pulled out of hole (POOH) first thing in morning to change bit. 12:30 h: after 3.05 m advance, POOH again to sharpen the “teeth” of new bit, which is getting polished by the hard, quartz-rich rocks. At previous sites (altered gabbros and diorites) a no. 7 bit was used; for this site a no. 10 bit (hardest in scale) is being used for quartzite and similar. Green water tanker broke down late morning so at 14:30 h a blue tanker arrived to fill drillers’ water tanks (continuing to lose 100% circulation into the formation). POOH again at end of day to inspect bit once more.
- 12 Mar 2017: RIH and continued drilling. Sampled a contact between listvenite and serpentinite at ~80 m.
- 13 Mar 2017: routine coring for most of day. POOH at 15:45 h to inspect bit as advance has slowed. Continued drilling at 16:52 h.
- 14 Mar 2017: routine coring in morning. 13:00 h: problem with the lock at the top of the core barrel failing to engage so had to trip pipe to retrieve the core barrel. 13:34 h: bit on deck. 14:10 h: started RIH after bit was resharpened.
- 15 Mar 2017: routine coring in morning but still loosing 100% circulation and lack of water tanker deliveries is causing delays—drilling paused 14:32–15:55 h. Temperatures have been increasing over the past couple of weeks to >40°C and the rig has been getting very hot over the last few days; drilling team intermittently throwing water onto the engine using a bowl.
- 16 Mar 2017: POOH at 13:45 h to check the bit—condition is fine, not worn, yet torque is high, so Wali recommended changing down to NQ; J. Coggon and C. Manning agreed. NW casing installed to 132 m.
- 17 Mar 2017: NW casing installed to bottom of hole (167.10 m). Started drilling NQ core. NW casing has restored circulation; lots of tan-colored mud is being cleared from the bottom of the hole.
- 18 Mar 2017: return circulation is much clearer today, milky rather than red. Drilled through an interval of serpentinite at ~180–185 m. At ~197 m drilled across the basal thrust of the ophiolite, sampling fault gouge and the strongly fragmented chlorite- and epidote-bearing, fine-grained rocks below.
- 19 Mar 2017: routine coring of greenschist facies metasediments and metabasalts.
- 20 Mar 2017: engine maintenance under way upon arrival on site. 08:00 h: routine coring resumed. Heavy rain forecast for tomorrow so P. Kelemen and J. Coggon arranged for removal of most core boxes and DMT core scanner today.
- 21 Mar 2017: 07:10 h: crew fixing a hydraulic leak that apparently started last night during final run. Coring resumed at 08:10 h. Prepared site in case of heavy rain overnight.
- 22 Mar 2017: despite heavy rain last night, no issues apparent on site. Coring as normal. Final core on deck at 10:56 h—the last core recovered in OmanDP Phase 1. Drillers POOH while science team completed core curation and description.
- 23 Mar 2017: demobilization for end of Phase 1.

Host rock

Major rock types

Hole BT1B intercepts alluvium, listvenite, ophicarbonate, serpentinite, and the metamorphic sole that is separated from listvenite by the basal thrust of the Oman ophiolite. Listvenite is the most abundant lithology (57%), followed by the metamorphic sole (35%), serpentinite (6%), and ophicarbonate (2%) (Fig. F3). We use the term listvenite to refer to rocks composed mainly of quartz and carbonate but also containing relict chromian spinel and/or chromian mica (fuchsite) as a minor phase; ferromagnesian silicate minerals may be absent or present as minor relict inclusions. All units, their depths, and whole-rock characteristics are summarized in Table T2. Their distribution with depth is shown in Figure F4. Listvenite is dominantly composed of carbonate and quartz with additional minor fuchsite, Fe oxide and hydroxide phases, and relict spinel and serpentine. The ophicarbonate assemblage represents a transitional rock type between serpentinite and listvenite composed of serpentine minerals together with carbonate, spinel, and magnetite. Closer to the contact with listvenite the ophicarbonate may contain carbonate in the matrix. Near the contact with serpentinite, carbonate is present only in veins. The serpentinite is dominantly composed of mesh-textured serpentine (not further characterized) with additional spinel, magnetite, and pseudomorphs of olivine and orthopyroxene as minor phases. The underlying metamorphic sole can be described as foliated greenstone composed of interlayered metasedimentary and metavolcanic sequences. It is mainly composed of micro- to cryptocrystalline clinozoisite, albite, and blue-green amphibole together with minor titanite, chlorite, pumpellyite, quartz, carbonate, and accessory sulfide.

Contacts between major rock types

Contacts between listvenite and ophicarbonate and between listvenite and serpentinite are gradational and caused by reaction with one or more CO_2-bearing alteration fluids. Listvenite results from interaction of ultramafic rock with a fluid that is relatively high in dissolved CO_2, whereas the ophicarbonate assemblage is the result of relatively lower fluid CO_2 concentrations. The contact between the listvenite and the metamorphic sole is tectonic and resulted in the formation of a ~0.6 m thick layer of fault gouge.

Listvenite

Lithologic units—general approach

Listvenite lithologic units were defined based on difference in host rock color, abundance of thick (>1 mm diameter) and thin (<1 mm diameter) veins, rock texture (massive, foliated), breccia clast proportion, proportion of vugs, shear zone proportion, and mineral modal abundance. A detailed definition of these descriptors is provided in **Metamorphic rock description, Site BT1**, in the **Methods** chapter. Generally, the grain size of the listvenite is too small to allow for unambiguous characterization of mineral abundance in hand specimen. However, frequently occurring quartz-fuchsite intergrowths that typically form larger (<1 cm) blebs with a distinct green color have been used to differentiate between fuchsite-bearing and fuchsite-absent listvenite (Fig. **F5**). Host rock texture describes rock foliation or banding by approximately evenly spaced mineral segregations. Observations of structures and vein abundance as well as paragenesis were also made by the structure group and vein group, respectively. The observations made by these two groups were in greater detail and are therefore used in the VCD plots.

Lithologic units and unit contacts

A total of 83 lithologic units were defined in the Hole BTB1 listvenite. Most listvenite internal unit boundaries were defined by the change in host rock color (44%), followed by breccia clast mode (20%), vein abundance (12%), and mineral abundance (8%; fuchsite-bearing) (Fig. **F6**). The relatively large number of units defined by breccia clast mode reflects the volume of brittlely deformed listvenite. Unit boundaries defined as structural describe a change in foliation intensity and may indicate either a change in foliation intensity or a change from massive to foliated listvenite. Unit boundaries defined as modal/mineral contrast are generally related to the presence or absence of fuchsite.

Five bands of serpentinite are intercalated within the listvenite at the following depths:

- 80.54–80.73 m
- 81.47–83.63 m
- 86.82–88.07 m
- 89.24–100.23 m
- 181.26–185.47 m

The listvenite/serpentinite contacts appear gradual and are interpreted to represent fluid-driven replacement fronts rather than tectonic juxtaposition. Shallower than 100.23 m, additional ophicarbonate (serpentine + carbonate) forms a transitional unit between listvenite and serpentinite. Additional ophicarbonate units have been defined within the serpentinite bands shallower than 89.24 m depth.

Color variation

Hole BT1B listvenites occur in a wide range of colors from pale yellow to dark reddish brown, and color distribution changes appear nonsystematic, varying on the millimeter to meter scale, often within the same core section (Fig. **F5**). The dominant colors are dark red (47%), light red (19%), and orange (14%), particularly in the upper part of the listvenite. Pale (2%) and green (16%) listvenite occur more frequently deeper than the large serpentinite band at 89–100 m depth. During onboard core logging, color description was based on the Munsell chart (see **Metamorphic rock description, Site BT1**, in the **Methods** chapter) in order to obtain a consistent classification scheme. A total of 27 different colors describe the different listvenite host rock colors. Distinct color changes were often used to define unit boundaries (Fig. **F6**), even if rock texture, grain size, and macroscopically identifiable relative mineral proportions remained constant. The Munsell-type color classification yielded consistent and reproducible results for different hues of red and reddish brown, whereas the choice of green often remained a subjective decision, as the olive-green hues of the Munsell chart do not resemble the intense green of fuchsite. Furthermore, the presence of relatively large (~2 mm to 1 cm) patches of fuchsite-quartz intergrowths in a distinctly colored matrix (e.g. red-brownish, beige, or gray) made choosing a representative host rock color challenging. For such samples color classification was based on the dominant color on the macroscopic scale. Subsequent to detailed core logging, the Munsell-type colors were integrated into five groups that are highlighted in the visual core description (VCD) charts: dark red, light red, orange, green, and pale (Fig. F7). These colors are meant to provide a first impression of the rock on a macroscopic scale only. Further investigation at higher magnification (hand lens, microscope) reveals that the macroscopic color is primarily related to the abundance and spacing of submillimeter-wide veins and their mineralogy. Thin section observations show that dark gray patches, which are nonsystematically distributed throughout the listvenite, often contain serpentine relics. Intense hematite/goethite veining of relict serpentine zones results in an overall dark reddish hue, often retaining the precursor serpentinite mesh texture. Light red and orange colored listvenite may be the result of hematite/goethite veining in zones containing abundant carbonate (mainly magnesite, minor dolomite) and quartz. Listvenite core sections without hematite/goethite veins are often light gray or pale, which may be more representative of the "true" listvenite color prior to formation of iron oxide veins. These often display different hues of green as a function of the distribution and grain size of fuchsite. Preservation of spinel and/or magnetite from the precursor serpentinite/peridotite and their distribution and grain size is an additional variable influencing the final listvenite host rock color.

Sample analysis/element mapping by XRF-CL

A total of 27 intervals were selected for nondestructive X-ray chemical analysis of the flat surface of the archive half in the mapping mode of X-ray fluorescence core logger (XRF-CL) (Table T3). Complete analyses and compositional maps are provided in the **Supplementary material** > **F2A_Core scanning XRF (BT1B)**. Ideally, we chose cores with as flat a surface as possible and without significant saw marks or surface unevenness. This proved difficult, as the cores were not always smoothly cut and often contained beveled surfaces or ripples (Fig. F8). We learned that chemical data from nonhorizontal surfaces are inaccurate and must be manually removed from the data set if greater accuracy is desired. Saw residue from cutting also affects the data, and effort should be made to clean the surfaces by light grinding prior to analysis whenever possible.

Data correction can be done to improve the raw output from the XRF-CL scanner. We analyzed both powders and core intervals corresponding to samples analyzed previously in shore-based laboratories, including Hole BT1B samples that were analyzed at the Southampton XRF facility. Postprocessing correction procedures were found to be necessary, as averaged values from the XRF-CL scanner differed systematically from Southampton XRF analyses for the same core intervals. We combined analyses of gabbros from Leg 1 with analyses of listvenites from Leg 2 to produce correction procedures that bring the scanning results into approximate agreement with the Southampton XRF data for gabbros and listvenites. Results obtained from a combination of the corrected XRF-CL scanner, Southampton XRF analyses, shipboard XRF analyses, and prior work (Falk and Kelemen, 2015) are described in **Mass exchange at the Basal Thrust: Site BT1** in the **Summary** chapter.

In addition, we had success in utilizing element contour plots generated by the XRF-CL instrument. Elemental concentrations were contoured from grid analyses at 5 mm point spacing (see **Metamorphic rock description, Site BT1** in the **Methods** chapter). The color contour maps display approximate oxide concentrations along the core. These maps are useful for distinguishing relative element abundances and were used to identify mineralogical and lithological variability, compositional transitions, and unit boundaries when visual identification was uncertain. Additional core scans were made with X-ray computed tomography (X-ray CT) and infrared (IR) images from the imaging spectrometer systems on board *Chikyu*. XRF-CL, X-ray CT, and IR imaging plots used together provide detailed information on rock compositions, textures, and mineralogy that assist naked eye visual observations.

In this section we present several examples of color contour maps generated by XRF-CL for core sections with compositional contrasts at several intervals in Hole BT1B. These contrasts are primarily linked to lithologic changes and mineral occurrence and will be displayed with core photos and false-color IR scanned images. Detailed measurement conditions were described in the **Methods** chapter, but basic conditions were as follows:

- High voltage = 30 kV
- Beam current = 0.04 mA
- Counting time = 60 s
- Spot size = 7 mm
- Spacing between spots = 5 mm

It should be noted that our strategy for choosing intervals for scanning was not aimed at providing a representative suite of analyses of the listvenite in Hole BT1. Instead, we sought lithological and mineralogical diversity to improve our calibration of the procedure for future users, to guide visual core description, and to develop cross-correlations with X-ray CT and IR spectroscopy observations that can be integrated onshore to estimate the bulk composition and compositional variability in the entire core.

This is reflected in relatively dense sampling of 15 listvenite intervals from Cores 28Z to 53Z (~60–125 m depth) comprising ~20 m of listvenite above the thick serpentinite band at ~80–100 m and 25 m of listvenite below the serpentinite, for an average of 1 scan per 3 m of listvenite core. In contrast, the other ~135 m of listvenite in Hole BT1B was analyzed in 10 scans, for an average of 1 scan per 13.5 m.

Analytical results

All raw analyses and instrument-generated composition maps are reported in the **Supplementary material** > **F2A_Core scanning XRF (BT1B)**. The following sections are examples of co-registered maps of XRF-CL scans and mineral indicator map showing three mineral components derived from measurements by the shortwave infrared sensor (SWIR) of the imaging spectrometer. These examples were selected to describe intervals of the cores that exhibit compositional features amenable to XRF-CL mapping capabilities and other imaging methods.

Core 32Z-3A,15–30 cm, and 57–65 cm. Sample 32Z-3, 15–30 cm, is a red and tan foliated listvenite in lithologic Unit 36. The scanned interval is shown in the upper part of the Figure **F9** core photograph, which shows an upper mottled tan and red zone and a lower red zone with a subhorizontal contact at ~23 cm. The XRF-CL maps of MgO, SiO_2, and CaO show an upper mixed zone with relatively high concentrations of SiO_2 and lower but variable CaO and MgO levels relative to the lower part of the interval, suggesting greater proportions of quartz in the upper half and a higher proportion of dolomite in the lower half. The IR and XRF-CL scans of this interval pick up a strong signal in the center of the image with low CaO and high SiO_2 and MgO, suggestive of a centimeter-scale quartz-magnesite inclusion that is weakly visible in the scanned core photo.

Sample 32Z-3, 57–65 cm, is also part of Unit 36. The scanned interval is shown in the lower portion of Figure **F9**. The core photo and IR image both show subdued signals, but the XRF-CL images of MgO, SiO_2, and CaO show that the upper portion of the interval contains a relatively greater proportion of dolomite than the lower portion of the interval. Centimeter-scale regions of silica-poor dolomite can be discerned in mottling the lower half of the interval.

Core 49Z-1A, 20–55 cm. Sample 49Z-1, 20-55 cm, contains an inclined contact between massive listvenite in Unit 60 and brecciated, veined listvenite in Unit 61 (Fig. **F10**). The core photograph shows this contact as a left-dipping feature at 40–50 cm, with lighter pink-yellow-orange listvenite above and red listvenite below the contact. XRF-CL scans indicate a complex transition from Unit 60 to Unit 61 with high concentrations of CaO and low SiO_2 at and above the contact, suggesting a dolomite-rich zone. The scans also show a zone of high MgO and low CaO toward the bottom of the scan, suggesting a patch of magnesite in that region. Two prominent centimeter-scale features with very high CaO are seen in the central portion of the interval and were confirmed to be calcite pockets. Also seen at about 32 cm in the section is a very high MgO feature, which shows as darker pink in the core photo. This is likely a patch of magnesite. A zone of Fe enrichment seen above the contact feature may represent localized concentration of an Fe oxyhydroxide phase.

Core 52Z-3A, 39–46 cm. Sample 52Z-3A, 39–46 cm, contains a contact between veined fuchsite-bearing listvenite (Unit 66) and massive fuchsite-bearing listvenite (Unit 67) (Fig. **F11**). The IR map from the imaging spectrometer shows distinct patches of fuchsite (color-coded red in the image) throughout both units. Variable enrichments in Cr and Si, also seen in the XRF-CL map in both units, may indicate local fuchsite-enriched zones. A distinct dolomite vein is clearly imaged in the lower right corner of the IR map and the XRF-CL CaO map. A centimeter-scale magnesite-quartz zone is seen in the MgO and SiO_2 XRF-CL maps but is not clear in the photo or the IR image. The Unit 66/67 contact can be discerned from a reduction in SiO_2 from Unit 66 to 67, as well as a distinct depletion in Cr along the contact.

Summary

Element maps produced by the XRF-CL scanner show variations in element concentrations on a centimeter scale. The accuracy of the analyses performed on a grid pattern on the flat surface of the half core is sufficient to distinguish mineral phases and concentration variations associated with unit boundaries, mineralization zones, layering, brecciation, and so on. XRF-CL scan data complement and enhance visual core descriptions, conventional geochemical methods, and other core scanning procedures including but not limited to imaging spectrometry and X-ray CT.

Downhole characterization based on XRD

Systematic X-ray diffraction (XRD) analysis performed on powder from bulk rock samples obtained by the geochemical group (40 samples for listvenite + serpentinite) allows estimating the main constituent minerals from listvenite and serpentinite samples throughout Hole BT1B (Table **T4**).

Carbonate content estimations inferred from XRD characterizations are in good agreement with LOI (loss on ignition) data acquired by the geochemistry team by weight difference after sample combustion (Fig. **F12**). About two-thirds of all samples (24 samples) have total carbonate minerals at 52%–70%, and 8 samples contain >75% carbonate (referred as carbonate rich). Three samples contain >60% quartz and have LOI < 25 wt% (referred as quartz rich). The other samples with LOI < 25 wt% mostly contain serpentine and belong to the ophicarbonate and serpentinite rock units.

From this dataset we assume that semiquantitative estimation for the primary rock-forming minerals of listvenite (dolomite, magnesite, and quartz) can be taken into consideration for all other XRD analyses. However, the amount of minor phases (including oxyhydroxide) and hydrosilicate (i.e., serpentine, talc, micas) remains difficult to estimate from XRD results. Thus, the minor mineral results from XRD were only used for mineral identification and estimation of relative abundance rather than for quantification. In most cases, accessory phases have been removed for semiquantitative estimations of mineral proportions.

Semiquantitative relative proportions of magnesite and dolomite throughout Hole BT1B are shown in Figure **F13**, including estimates of mineral proportions from both onboard XRF and XRD analyses. Magnesite is the dominant carbonate mineral throughout most of the core. The amount of dolomite estimated for bulk-rock samples from the geochemical group rarely exceeds 15%. Two very dolomite rich excursions are observed in interval 23Z-1, 37–42 cm (~49 m depth) and in Section 40Z-1 within serpentinite/ophicarbonates. Additionally, 4 samples at 50–60 m depth have >15% dolomite. This is reflected in the fact that many of the XRF-CL core scans in this depth interval also yield dolomite-rich average compositions. We also note an increase of dolomite content with respect to the entire dataset in the deepest part of the listvenite unit near the contact with the metamorphic sole (Sections 74Z-3, 77Z-3, and 77Z-4).

The quartz vs. carbonate ratio throughout the listvenite ranges from 0.13 (carbonate-rich listvenite) to 1.93 (quartz-rich listvenite), with most values between 0.3 and 0.5.

These data combined with microscopic observations from nearby thin section and hand-lens logging provide a first impression of the rock mineralogy and can be merged with data obtained from more specific domains.

Characterization of typical listvenite

Previous sections highlight the heterogeneity of listvenite rocks in terms of both color and rock-forming mineral abundance. Most of the listvenites display a red hue, and a majority of listvenites contain ~2/3 carbonate minerals (mostly magnesite), and ~1/3 quartz (Fig. **F14**). This assemblage constitutes “typical listvenite” and has the same molar Mg/Si ratio as the Oman peridotites that we infer the listvenites replaced. Moreover, listvenite contains minor amounts of Fe (oxy)hydroxides (<10 vol%), and relics of chromite are present in almost all samples (Fig. **F15**). Relict mesh texture outlined by oxides, sometimes containing serpentine relics, and the presence of isolated, partially altered chromite imply that serpentinite and/or partially serpentinized dunite and harzburgite were the source rocks that were replaced by listvenite (Fig. **F15**).

Characterization of fuchsite-bearing listvenite

In contrast to the major minerals in listvenite such as carbonates, quartz, and serpentine, fuchsite can easily be recognized in the core by the presence of green spots or blebs (Figs. **F5**; **F16A**). In all thin sections from samples in which fuchsite was identified macroscopically, it was also evident under the microscope (Table **T5**). In thin section, fuchsite rarely forms discrete crystals larger than 10 µm, as was inferred from macroscopic observations. Instead, it is generally a trace component with modal amounts <1 vol% forming lepidoblastic aggregates in clusters mainly composed of calcite and quartz in a polygonal granoblastic pattern (Fig. **F16B**, **F16C**). XRD semiquantitative estimation yields values of 17–20 vol% (Table **T4**), which we think probably overestimates he proportion of fuchsite. Apparently, a relatively small amount of fuchsite within these clusters is responsible for the obvious light green color spots in the corresponding rock samples.

Relics of serpentinite mesh texture in listvenite

In the core from Hole BT1B, at many places we made macroscopic observations of greenish to blackish patches resembling relict serpentinite mesh texture (e.g., Fig. **F17A**). Detailed thin section work confirmed the presence of relict serpentinite mesh texture (polygonal cells surrounded by diffuse oxide trails) in many listvenites (Table **T5**). This is illustrated in Figures **F17**, **F18**, **F19**, and **F20**. In a few of these structures serpentine minerals are still present (Table **T4**). In some listvenite samples, preserved bastite (pseudomorphs of serpentine after orthopyroxene) of the precursor harzburgite could be observed, replaced by magnesite (Fig. **F18**). In one thin section (Section 38Z-3) that contains two lithologic domains (domain 1: carbonated serpentinite; domain 2: listvenite), relics of a former mesh texture can still be observed in the listvenite domain, although it is fully carbonated (Fig. **F19**).

Thin sections of many listvenite samples show carbonate grains with micrometer-sized inclusions of iron oxides. Detailed thin section work on the corresponding microstructures revealed that many of these oxide inclusions are related to relics of serpentinite mesh textures, implying a mode of formation in which tiny iron oxide phases that formed diffuse trails in the former mesh texture could be regarded as nuclei for additional oxide crystallization during the formation of listvenite (Fig. **F20**).

Talc-rich domains

Talc is present in the transition zone between serpentinite and listvenite at ~98–100 m depth, displaying olive-gray color (Sections 44Z-2, 44Z-3, and 44Z-4), as observed during macroscopic core description and through XRD analyses on two specific samples (Fig. F21). Semiquantitative characterization indicates a comparable amount of 27%–28% talc and 24%–31% serpentine in two samples (Table T4). Quartz was not detected in these samples, and the remainder of rocks is mostly composed of Mg carbonate. Therefore, these rocks are assigned to the ophicarbonate group. Talc seems to be more abundant in pale green, massive domains (millimeter to centimeter size), but it is not restricted to this area. The occurrence of talc is not specific to this horizon. Other serpentinite sections from Hole BT1B contain minor amounts of talc, especially at listvenite–serpentinite transitions, as previously observed from mapping and sampling by Falk and Kelemen (2015).

Ophicarbonate

Lithologic units

Ophicarbonate represents a transitional rock type at serpentinite/listvenite contacts. The occurrence of ophicarbonate in the upper part of Hole BT1B is accompanied by a distinct color change relative to both serpentinite and listvenite, whereas the listvenite/serpentinite transitions at contacts at 100.2 m, 181.3 m, and 185.5 m appear sharp at hand specimen scale. However, thin section and XRD analyses confirmed the coexistence of abundant carbonate together with serpentine also at the deeper listvenite–serpentinite transitions (e.g. Core 44Z). The vertical extent of the ophicarbonate assemblage at these transitions could not be constrained because of the lack of host rock discoloration.

Four ophicarbonate bands are present in Hole BT1B at depth intervals 80.3–80.5 m (Unit 41), 80.7–81.5 m (Unit 43), 83.6–86.8 m (Units 45–47), and 88.1–89.2 (Unit 49). Three of the four ophicarbonate bands are classified as individual units, and the ophicarbonate band between 83.63 and 86.82 m is further divided into three units based on color change and foliation. Unit 45 is described as veined and moderately foliated olive-yellow ophicarbonate, Unit 46 is intensely foliated reddish brown ophicarbonate, and Unit 47 is veined but otherwise massive pale yellow ophicarbonate. Transitions from both listvenite and serpentinite to ophicarbonate are gradational (Fig. F22). The serpentinite mesh texture is preserved in most of the investigated ophicarbonate units, whereas the host rock color is distinct. The gradational nature of the ophicarbonate is also evident at thin section scale. Ophicarbonate near the contact with serpentinite is characterized by a serpentine-dominated matrix transected by carbonate veins (Fig. F23). Ophicarbonate near the contact with listvenite has a larger proportion of carbonate in the rock matrix. As described above, ophicarbonate can contain talc. Quartz is typically absent in ophicarbonate samples, and minor phases comprise spinel and magnetite. Additional bastite intergrowths after primary orthopyroxene occur together with serpentine.

Serpentinite

Lithologic units

Serpentinite lithologic units were defined based on difference in host rock color, abundance of thick (>1 mm diameter) and thin (<1 mm diameter) veins, rock texture (massive, foliated), breccia clast proportion, proportion of vugs, shear zone proportion, and mineral modal abundance (Fig. F24). Detailed definitions of these descriptors are provided in **Metamorphic rock description, Site BT1** in the **Methods** chapter. In addition, serpentinites are sometimes classified into either dunite or harzburgite precursors for several units in hand specimen by the presence of bastite textures (pseudomorphs after orthopyroxene). The presence of bastite texture was also confirmed from several thin sections by optical microscopy. Typical examples of these rocks are described below.

A total of 14 serpentinite units were defined in Hole BTB1 (Fig. F25). Serpentinites are present at two specific depth intervals: 7 units (42, 44, 48, 50, 51, 52, and 53) are from Cores 38Z–44Z (80.54–100.225 m depth: 19.685 m long), and 7 other consecutive units (99–105) are in Cores 73Z–75Z (181.26–185.47 m depth: 4.21 m long). The ophicarbonate bands generally alternate with serpentinite bands in the shallow serpentinite interval, Cores 38Z–44Z (80.54–100.225 m depth).

Contacts

The boundary contact between the serpentinite group and listvenite/ophicarbonate groups varies between planar and gradual/irregular (Fig. F26).

Serpentinite internal unit boundaries were mainly defined by vein abundance, structure (brecciated/foliation intensity), and change in color (Fig. F24). Vein (i.e., carbonate-silica vein) abundances in serpentinite increase toward the listvenite. This observation, coupled with close association with the ophicarbonate in the shallower serpentinite interval, suggests a gradually increasing degree of carbonation from massive serpentinite through ophicarbonate to listvenite.

Relics of primary peridotite

Serpentinite is mainly composed of serpentine with minor amounts of chromite, talc, and magnetite. Some samples of serpentinite contain abundant thin carbonate veins (<1 mm thick). Some serpentinite units might be, therefore, categorized as ophicarbonate by further investigation.

Although chromite is the dominant relict primary phase from the peridotite precursor, bastite pseudomorphs of pyroxene porphyroclasts are well preserved in some samples (Fig. F27). Because the mantle section of the Oman ophiolite is mainly composed of harzburgite with small amounts of dunite, bastites in the serpentinite are interpreted as orthopyroxene pseudomorphs. Bastite-bearing and bastite-free samples in the studied core were identified as harzburgite and dunite, respectively (harz-serpentinite and dun-serpentinite, hereafter). Harz- and dun-serpentinites are confirmed for 6 thin sections and 3 thin sections, respectively, from the serpentinite-ophicarbonate intervals (Table T6).

Bastite in the harz-serpentinite is generally rounded in shape and is as large as 0.5 cm. Estimated primary orthopyroxene mode ranges <10%–30%. Serpentine in bastite is partly replaced by talc, particularly in carbonate-rich samples (Fig. F28). Chromite in the harz-serpentinite is mostly anhedral, and some grains show holly-leaf texture, whereas subhedral grains are abundant in the dun-serpentinite (Fig. F27). The modal abundance of chromite is 1%–3% in the serpentinites and may be higher in the dun-serpentinite than in the harz-serpentinite. Chromite also shows shape-preferred orientation parallel to serpentine foliation in foliated samples (Fig. F28). Magnetite occurs as replacement rims surrounding chromite and as tiny grains aligned with serpentine mesh texture.

Carbonate minerals in serpentinite

Carbonate minerals mainly occur as thin veins (usually <1 mm thick) in the serpentinite. Extremely tiny (<10 µm) grains are also disseminated in several samples (Fig. F29). These tiny grains are occasionally aggregated and cut the earlier carbonate veins. Small amounts of silicate mineral are observed in the late carbonate aggregates (Fig. F29).

Metamorphic sole

Lithologic units

A total of 102.53 m of core was sampled from the metamorphic sole in Hole BT1B. Based on macroscopic appearance, the metamorphic sole is divided into 9 units (Units 113–121; Fig. F30). In general, the metamorphic sole is relatively uniform, greenish, microcrystalline, and finely laminated. Folds and breccia zones are abundant in the upper part below the basal thrust and decrease in abundance with depth (e.g. Fig. F30B). Unit boundaries are defined based on color change and brecciation. The change in rock color reflects the presence or absence of pistachio green intergrowths of albite, epidote, and minor amphibole and titanite as large as 5 cm diameter (e.g., Fig. F31C, F31F, F31A, F31B). These intergrowths may be pseudomorphs of phenocrysts, suggesting that the macroscopically darker matrix can be identified as metabasalt. The matrix of the metabasalts is dominated by blue-green amphibole and albite plus minor amounts of epidote, titanite, and chlorite + quartz. One sample contains tiny needles of pumpellyite intergrown with albite in a lens surrounded mainly by chlorite (Fig. F31C, F31D). Metasedimentary sequences in the metamorphic sole are in general laminated, more heterogeneous, and more greenish than the metabasalt sequences because of the large proportions of chlorite and epidote. The typical assemblage comprises epidote, chlorite, albite, quartz, titanite, and carbonate. In some of the metapelite sequences the assemblage quartz, muscovite, chlorite, titanite, albite, and minor epidote was observed (e.g., thin section Sample 82Z-1, 65–69 cm).

Veins

All lithologies in Hole BT1B are densely veined. The generation and filling of fractures to form veins is an important part of the mechanical and chemical evolution of rocks throughout the core. In the hanging wall of the basal thrust, veining events likely predate, accompany, and postdate formation of listvenite and therefore provide a record of fluid delivery, fluid-rock interaction, and attendant deformation. Below the basal thrust, veining spans folding, foliation development, and transition from ductile to brittle behavior with time. All recovered lithologies in Hole BT1B are metamorphic rocks. Veins were described separately from their host rocks; however, it is important to recognize that veining may be integral to the metamorphic processes that generated the host rocks themselves.

During macroscopic core description, the vein petrology team characterized the densities of veins and other structural features as well as the textural and mineralogical features of specific veins and vein sets (see supplemental Table ST1). High density, wide textural variation, diverse mineral associations, and multiple, complex crosscutting relations were observed throughout the core. As core logging and thin section petrography proceeded, broad systems of vein generations and types became evident in the major listvenite, serpentinite, and footwall metamorphic rock lithologies. A preliminary simplified classification scheme was therefore prepared for each of the three major lithologies with the purpose of placing the veins in an evolutionary framework and informing models of metamorphism, metasomatism, and deformation (see supplemental Table ST2). As described in the Methods chapter, the tools used to identify, compare, and contrast the vein types included macroscopic core description, thin section petrography, and XRD. XCT and IR imaging were used on selected cores to further elucidate vein characteristics. Thin section descriptions can be found in **Supplementary material > B_Thin section descriptions**. XRD results are tabulated in supplemental Table ST2 and keyed to core images in supplemental Table ST3.

It should be noted that these schemes are imprecise. Textures and mineral identifications on which they are based were particularly challenging. For example, a core describer can in principle easily distinguish the carbonate minerals common to listvenites (calcite, dolomite, and magnesite) because she can scratch the vein and test for acid reaction; however, testing every occurrence is impractical when a large volume of core must be described in a short time. In addition, many of the key relations are evident only in thin sections, which are by necessity prepared only for a small subset of nominally representative samples. In any case, this preliminary attempt can serve as a starting point for refining subsequent work on vein petrology.

Vein types in the classification scheme are described separately for each of three general rock types: hanging wall listvenites, hanging wall serpentinites, and footwall metamorphic sole rocks. The order of presentation is relative age. Relative ages were first identified based on crosscutting relations observed during core description. Final determinations were made using thin section petrography. Some vein sets involve multiple generations, and crosscutting relations are occasionally inconsistent. We report the relative timing as predominantly observed.

Overall density of veins, fractures, and deformation features

Veins, fractures, shear zones, and breccia zones are abundant in Hole BT1B. The intensity of veining precluded logging individual veins. Instead, density bins were developed for two classes of vein widths: <1 mm and ≥1 mm. During macroscopic core description, the vein petrology team identified veins <1 mm and ≥1 mm and characterized their densities (see supplemental Table ST1). Logging identified the presence of at least 60,500 veins <1 mm wide and 6,800 veins ≥1 mm wide. Thus, there are more than 67,200 macroscopically visible veins in Hole BT1B. (The actual number is probably much greater than this figure.) In addition, the vein petrology team identified and logged 986 fractures, 1,130 faults, and 681 cataclasites.

The downhole variation in the density of structural features in Hole BT1B is illustrated in Figure F32 and summarized in Table T7. Above the basal thrust, the downhole density of veins <1 mm is >200/m in every section examined; that is, there at least 48,800 such veins in the 190.5 m of listvenite and serpentinite in Hole BT1B, though this may be due in part to the relative ease of identifying light-colored veins in dark serpentinites. The number of veins ≥1 mm is generally 50–100/m in both listvenite and serpentinite. Density data indicate the presence of at least 5200 such veins in these two lithologies. The density of ≥1 mm veins is higher in serpentinite than in listvenite: densities generally vary from 10–50/m to 100–200/m in listvenite and from 50–100/m to >200/m in serpentinite. The density of faults, cataclasites, and shear zones increases with depth approaching the basal thrust. Fault density is generally higher in listvenite (1/m) relative to serpentinite (0.79/m), whereas fracture density tends to be higher in serpentinite (2.34/m) than listvenite (0.78/m). The number of cataclasites and shear zones in serpentinite is lower relative to listvenite. A large spike in cataclasites within 10 m of the basal thrust was observed in listvenite.

The density of <1 mm veins decreases below the basal thrust. The logging data indicate at least 11,700 of these veins in the 108.5 m of footwall metamorphic rocks in Hole BT1B. The number of veins ≥1 mm generally decreases in the metamorphic rocks below the basal thrust, particularly in the uppermost 30 m. The density of ≥1 mm veins below the thrust ranges from 10–50/m to 100–200/m. Overall, the density data indicate at least 6800 such veins in the footwall metamorphic rocks. The average number of fractures increases markedly below the thrust zone (5.35/m) relative to the listvenite above (0.78/m). It should be noted the differentiation of drilling-induced breaks from natural joints was hindered in sections with a very high density of fractures and/or rubble. The average number of faults and shear/cataclasites zones in the metamorphic rocks was 9.18/m and 3.15/m, respectively. Faulting below the thrust zone tended to occur as inconspicuous submillimeter faults in high-density bands of up 40 faults/m, often associated with broken and boudinaged vein fragments and an increased number of local fractures (joints). Broad-scale shearing was observed in the footwall lithologies, and an increase in the average number of cataclasites and shear zones (3.15/m) was observed relative to the listvenite (2.71/m).

Vein petrology: listvenites and serpentinites

The vein petrology team identified and logged 486 vein sets in listvenite and serpentinite lithologies in Hole BT1B (see supplemental Table ST1). The vein sets were placed in a provisional classification scheme with five broad vein classes in each lithology (supplemental Table ST2) based on macroscopic and microscopic crosscutting relations, mineral fill, and textures, as described below.

Listvenites

The preliminary vein classification scheme for listvenites is given in Table T8. Figure F33 illustrates the overall downhole distribution of vein types in the listvenites.

Carbonate oxide veins

Carbonate oxide (carb-ox) veins are consistently the earliest veins observed in listvenites. The only exception is in banded listvenite from Sections 31Z-4 to 32Z-4, where an earlier set was logged in recognition of the possibility of an earlier fabric-parallel coarse vein set; however, subsequent thin section petrography indicated that the banding did not possess textural features associated with veins. Carb-ox veins are usually significantly less than 1 mm wide and are responsible for the elevated density of <1 mm veins described above. These veins form box-like to anastomosing sets that are irregular and discontinuous. The textures were usually evident during visual core description (Fig. F34) but typically require the highest magnification available. High-resolution XCT imaging may aid in identification of this vein type.

The microscopic texture of carb-ox veins is distinctive (Fig. F35). The veins typically display a medial line rich in opaque inclusions, which in reflected light can be identified as hematite. The hematite is locally altered to goethite; magnetite may also be present in some cases. Modal variations in hematite and the extent of alteration to goethite are partly responsible for the color of red listvenite. Magnesite typically displays antitaxial growth habit in which optically continuous crystals grow outward in opposite directions from the centerline. Magnesite may be blocky to fibrous; subhedral terminations against vein margins are common. Attempts to confirm optical identification of the vein minerals by XRD were inconclusive because of the difficulty of separating host rock from vein minerals and the low modal abundance of oxides. Petrographic examination reveals that where listvenite is deformed these veins may be rotated into broadly subparallel arrays that contribute to fabric definition (Fig. F35).

Carbonate and carbonate-quartz veins

The vein petrology team identified multiple types of carbonate veins that crosscut carbonate oxide veins. Relative ages based on macroscopic crosscutting relations were not always consistent. Crosscutting relations were generally more consistent in individual thin sections, but ambiguities persisted.

Most generally, the carbonate oxide veins are followed by longer irregular carbonate veins. These veins display a wide range of colors and textures. They may be gray, white, pink, or red. Widths range from <1 mm to >5 mm. Carbonate veins may be wispy, branched, or splayed (Figs. F34, F36).

Thin section petrography confirms macroscopically identified crosscutting relations (Fig. F37). Grain size is typically similar to or greater than vein width, as crystals commonly elongate along the vein axis. These veins frequently have a dusty appearance, due in part to submicrometer-sized unidentifiable inclusions. Associated minerals include minor Fe oxides and quartz. XRD data indicate that the carbonate phase is predominantly magnesite but also routinely indicate the presence of dolomite (see supplemental Table ST3).

Veins with a higher modal abundance of quartz are termed “carbonate-quartz veins.” They crosscut carbonate oxide veins (Fig. F37) and, usually, at least some macroscopic carbonate veins with less quartz. Diagnostic macroscopic features of these veins are greater width and length than earlier veins. Carbonate-quartz veins are locally vuggy. They are a common vein type cutting many listvenite sections but are typically less densely distributed than earlier veins.

Thin section petrography reveals abundant coexisting carbonate and silica phases. Quartz often has seriate texture (Fig. F38): it commonly forms microcrystalline radiating or fibrous crystals along margins that grade into progressively coarser and elongate crystals toward vein centers. Banding is frequently observed. The textures are interpreted to indicate that amorphous silica or chalcedony initially crystallized on vein margins, giving way to coarser quartz crystals with time. Associated carbonate crystals are typically limpid and may reach several millimeters in length. XRD data indicate that the carbonate phase is predominantly magnesite (see supplemental Table ST3).

Quartz abundance is highly variable. There are numerous examples of later veins that appear identical to carbonate-quartz veins but contain little to no quartz. Thus, veins identified as either carbonate or carbonate-quartz type are best treated, at least for the purposes of preliminary core description, as a single petrologic group with multiple generations.

Late carbonate veins

Late carbonate veins are often several centimeters in width. These veins may be complexly zoned and contain multiple carbonate phases based on color variations. Residual open space is common, forming millimeter- to centimeter-scale vugs lined with gemmy subhedral crystal terminations. The most common carbonate mineral is dolomite based on acid testing and XRD determination (supplemental Table ST3). Detailed study of Section 32Z-4 shows key features of these veins. The presence of dolomite is revealed by XRD and inferred from elevated CT number along the visually identified late carbonate vein (Fig. F39). IR spectra also highlight the presence of dolomite-rich veining in the core center. Both data sets also highlight additional late carbonate veins that are difficult to trace during visual core description. In addition, XRF scanning indicates high CaO concentrations along the trace of the vein (Fig. F40). Notably, IR data suggest that the SiO_2-rich white patch on the upper left of the core is amorphous.

Also common are yellowish carbonate veins that appear to be Fe-rich magnesite. An example of this vein type is in Section 50Z-1 (Fig. F41). XRD results indicate that the 5 mm wide, curving yellow vein at 7–14 cm is magnesite. SWIR imaging shows an absorption feature centered near ~1.0–1.2 mm, likely related to the presence of Fe^{2+}. This is consistent with XCT data showing higher X-ray absorption than for normal Mg-rich magnesite (Fig. F41), and in turn this may be due to the dramatic variation in density from magnesite (3 tons/m^3) to siderite (3.9 tons/m^3). Unfortunately, from the perspective of this phase of the project, Fe substitution in magnesite may cause the XCT peak to overlap with dolomite-ankerite solid solutions.

Other veins in listvenite

Hematite-rich veins with textures similar to the earliest carbonate veins were identified in ~20 sections in Hole BT1B and locally confirmed by XRD (e.g., page 25 in supplemental Table ST3). These veins may be more abundant than indicated by logging, as they are easy to miss in otherwise oxidized rocks. For example, one hematite vein was identified in Section 34Z-2. Inspection of the XCT scan indicated that the vein had high intensity (Fig. F39), which led to identification of additional texturally similar veins in this section.

Other veins in this category are usually late veins distinguished from the other vein types based on textural variation and/or mineralogy. The main mineral associations include Fe oxide, Fe oxide bearing, quartz bearing, and graphite. Discrete bands of microcrystalline hematite ± goethite narrower than 5 mm and usually limited extension were observed throughout the core; these are readily recognizable in XCT scans (Fig. F39). The Fe oxides also appear together with carbonate or quartz, often as anastomosing or splaying brecciated veins including wall-rock fragments or outlining wider brecciated sections; open spaces with crystal terminations were commonly observed. Composite quartz-bearing veins consist of microgranular, 5 mm wide pink carbonate margins and a core of green-turquoise-colored material interpreted to be microcrystalline quartz similar to chrysoprase (Fig. F42). The presence of quartz was validated by XRD (see page 38 in supplemental Table ST3). Similar features were observed in the 152.9–165.1 m depth interval (Sections 64Z-2 to 68Z-1). The veins have irregularly developed selvages several millimeters wide with black minerals that are also observed elsewhere in other quartz-carbonate veins where the distinctive bluish green central quartz is lacking (e.g., Fig. F36). Quartz veins were observed sporadically as very late crack-seal fillings.

Submillimetric anastomosing or branching vein nets coated by a black, soft mineral that can stain the fingers of core loggers were provisionally identified as "graphite" or "polymineralic" in core descriptions. Prominent examples occur in Sections 78Z-1 and 78Z-2. To confirm graphite, powders were prepared from material scraped from three black veins in these sections (Fig. F43). Care was taken to remove as little material as possible. This is problematic because the positions of graphite diffraction peaks are sensitive to the amount of material irradiated by X-rays, which makes working with small sample masses challenging. Using the most readily available standard (a graphite crucible), the vein team empirically calibrated the graphite [002] peak position as a function of sample mass identified found shifts of –0.40°, –0.35°, and –0.29°2θ for 1, 4, and 12 mg samples, respectively, relative to the RRUFF reference value. These calibrated shifts were applied to shipboard diffractograms. Figure F43 shows mass-corrected diffractograms indicating that the shipboard samples contain graphite along with hematite and dolomite. A caveat is that peaks at 20.6°2θ suggest that some quartz was intermixed in two of the samples. It was not possible to resolve differences between quartz [001] and graphite [002] with the amount of material available. In any case, the 20.6°2θ peak appears to be absent in the vein sample from Sample 78Z-2, 16–24 cm, lending confidence to the identification of graphite in these veins.

Serpentinites

The preliminary vein classification scheme for serpentinites is given in Table T9. Figure F33 compares the downhole distribution of vein types in the serpentinites with that in other lithologies.

Serpentine mesh veins

The earliest vein type observed in serpentinites is mesh-textured serpentine (Fig. F44). These veins are termed serpentine mesh (serp mesh) and are typically black to dark green and <0.5 mm wide. The veins are anastomosing, irregular, and discontinuous. Thin section petrography indicates that the serpentine is commonly accompanied by fine-grained magnetite (Fig. F45). Magnetite abundance is lower where these veins cut relict orthopyroxene.

Serpentine veins

Coarser serpentine (serp) veins crosscut the mesh texture (Fig. F44). These veins are gray, green, and/or white. Widths range widely from <1 mm to >5 mm and have irregular branching textures. Multiple generations are commonly present in the same sample.

The vein petrology team typically logged these veins as carbonate + serpentine veins.

Thin section petrography confirmed interpreted crosscutting relations (Fig. F45). Serpentine is the dominant vein mineral with minor carbonate. Magnetite may be locally abundant. XRD data were collected on several serpentine veins. The best match to observed diffraction peaks is lizardite, but chrysotile is also possible; antigorite was not observed (see pages 29–30 in supplemental Table ST3).

Carbonate oxide veins

The serpentinite 3.5 m above the serpentinite/listvenite contact at 100.23 m depth is crosscut by a macroscopic set of regularly oriented, inclined thin veins ≤0.1 mm wide (Fig. F46). Their abundance increases downhole from the first noted macroscopic occurrence in Section 43Z-4.

Petrographic characterization reveals these veins to be carbonate oxide veins similar in texture and mineralogy to the carb-ox veins observed in listvenites (Fig. F45). They commonly possess oxide (hematite?) inclusions along medial lines. The carbonate, interpreted to be magnesite based on acid testing, frequently displays antitaxial growth textures. Locally, these veins are associated with fracturing of the host rock and growth of new serpentine along vein margins (Fig. F45). This set may occur alone or as densely spaced swarms cutting serpentine (Fig. F46). When first noted as a distinct set during core logging, the soft mineral fill led the vein petrology team to describe these as serpentine veins (see the Vein petrology sheet in supplemental Table ST2). Petrographic study revealed that this vein set is widely distributed throughout the upper serpentine body (Supplementary material > **B_Thin section descriptions**). Textures may be box-like to anastomosing and irregular.

Carbonate veins

As in the listvenites, the carbonate oxide veins are cut by a later set of wider, more coarsely crystalline carbonate veins. These veins are as wide as several millimeters, discontinuous, and irregular. The vein-filling mineral is chiefly magnesite. Associated minerals may include quartz and Fe oxides. Figure F47 illustrates crosscutting relations in which the carbonate veins in serpentinites cut the carbonate oxide veins at high angle.

Other veins

Highly irregular veins filled with quartz were observed as branching and splaying nets, locally showing vuggy morphology. Their color ranges from light green to translucent gray, and they are as wide as 10 mm. Near the top contact with listvenite at ~181 m depth (Section 73Z-3), carbonate–Fe oxide veins related to late alteration stages show brecciation features and may reach 170 mm in width.

Footwall metamorphic rocks

The preliminary vein classification scheme for footwall metamorphic rocks is given in Table T10. Figure F33 compares the downhole distribution of vein types in this lithology with that in the serpentinites and listvenites.

Quartz veins, feldspar veins, and epidote veins

Quartz veins, feldspar veins, and epidote veins occur as disrupted, folded, and sheared features in footwall metamorphic rocks (Fig. F48). No crosscutting relations were observed between these vein types. All predate or are synchronous with foliation development and folding in the metamorphic rocks. The veins may be >1 cm in the longest dimension. Crystals as large as 5 mm were observed. Associated minerals were identified in thin section and by XRD (see pages 42–43 in supplemental Table ST3). Quartz veins are found throughout the footwall metamorphic rocks. Textures range from irregular patches and segregations to recognizably deformed veins. Quartz is usually associated with chlorite, calcite, and epidote. Some quartz patches contain chlorite and calcite inclusions and are locally associated with albite and microcline.

Feldspar veins have similar textures but are distinguishable based on white and pinkish centers (see Section 83Z-1 in Fig. F48). They occur as >1 cm folded and irregular veins and segregations. XRD results indicate the presence of both albite and microcline. Associated quartz, chlorite, and epidote were identified as associated minerals in thin section and during core logging.

Epidote veins are texturally similar to quartz and feldspar veins. They may be foliated and folded and are usually subparallel to foliation. Commonly associated minerals include quartz, chlorite, and calcite.

Characterization of the distribution of these three vein types is aided by X-ray CT images. Relative to the host rock, quartz and feldspar veins characteristically have average CT number, whereas epidote is high (Fig. F48).

Chlorite veins

Chlorite veins represent a pervasive set of thin (1–2 mm wide) structures that cut the earlier veins and the foliation (Fig. F49). Chlorite veins are dark green to black. They typically occur with a range of textures, ranging from planar sets to anastomosing, irregular networks. They are widespread throughout the footwall metamorphic rocks and were observed in nearly every section. Associated minerals identified by XRD (see page 44 in supplemental Table ST3) are likely host-rock impurities. Very late veins of this type are altered to (or originally filled with) illite/smectite (see page 46 supplemental Table ST3).

Other veins

An irregular segregation that is probably similar in age to quartz veins contains mica and black tourmaline (see page 45 in supplemental Table ST3). Late fractures and patches infilled with calcite were consistently observed throughout the core. They are as wide as 12 mm with irregular to splaying morphology. Late calcite veins also contain either chlorite or hematite. Quartz-carbonate veins were rarer (only 4 documented examples). A band of anastomosing hematite veinlets commonly outline the borders of brecciated zones, sometimes branching into the breccia. Where hematite is associated with the later vein types, disseminated sulfide (pyrite, sometimes chalcopyrite) is commonly observed.

Structural geology

Hole BT1B was drilled through listvenites and serpentinites, the basal thrust, and metasediments and metabasalts of the metamorphic sole of the Samail ophiolite in Oman. In macroscopic core description, structures in Hole BT1B were identified as "host rock," including the oldest visible deformation in a chosen interval, and "localized structures," which postdate and crosscut the host rock structure. Structures in host rock include massive, breccia, foliation, shear zone, and cataclasite, whereas areas completely obscured by subsequent vein intrusion were described as fragmented by veins. In localized structures, individual veins, sets of veins, cataclasites, shear zones, and faults were identified. Furthermore, we also characterized the crosscutting relationships of observed structures and measured the orientations of host rock structure and localized structures where possible. In addition, we present detailed microstructural and petrographic observations from Hole BT1B to supplement macroscopic core description. Our results for each category are summarized below and in Table T11.

Structural measurements

Structural data measured and presented here are always oriented toward the core reference frame (CRF), which changes arbitrarily across 54 discontinuous core section boundaries and is not rotated back to a geographic reference frame at the time of report completion. This fact makes it impossible to directly interpret spatial data in a geographic or tectonic context. Several intervals of contiguous section, where core sections have not been rotated relative to each other, were identified. We provide stereoplots for structures within these intervals for comparison of the relative orientations of features. We also provide a set of dip angle vs. depth plots allowing first-order comparison of dips downhole (host rock and localized structures). However, Hole BT1B was inclined at ~75°. Rotation of core sections of an inclined hole results in a large variability of possible dip angles (Fig. F50). The presented downhole dip plots therefore have to be read with care. In subsequent sections we will discuss spatial data for six zones with continuous CRF. We caution the reader when using these data to not overinterpret apparent trends and/or structural orientations.

Host rock structures

Downhole frequency

We documented massive, brecciated, foliated, sheared, and cataclastic host rock structures as well as host rock structure fragmented by veins in Hole BT1B. Breccia is the dominant host rock type developed in the upper part of Hole BT1B, as shown in the downhole plot of host rock structures (Fig. F51), but it becomes more sparse below 150 m depth. Penetrative foliations are locally developed throughout the core. Foliation is particularly distinct between ~100 and 300 m depth. We also observed sparse massive, shear zone, and cataclasite structures throughout the core (Fig. F51). Host rock structures qualified as "fragmented by veins" appear intermittently through the whole core.

Massive host rock structure

Massive host rock was defined by the lack of any visible host rock structural features (Fig. F52). We did not observe any massive intervals in the listvenite at the macroscopic scale, but small intervals of the serpentinite, metabasalts, and metasediments are massive (Fig. F51). The presence of massive intervals suggests that some rocks in Hole BT1B are largely unaffected by the multiple stages of cataclasis, brecciation, shearing, veining, and faulting that is observed throughout the core. Static alteration and metamorphism therefore may occur locally.

Breccia

Breccias in host rock structure are the dominant feature in the upper part of Hole BT1B, composing the majority of the listvenite and generally decreasing in abundance downhole (Fig. F51). Breccias are differentiated from cataclasites based on a lack of clast rotation, more angular and subangular fragments, and typically larger clasts (Fig. F53). Breccias also typically formed longer intervals in the core and had more completely cemented matrix than the cataclasites, although these characteristics are not used as defining factors. We also distinguished localized breccias from host rock breccias by whether we could measure a true width perpendicular to the structure, features whose widths exceeded that of the core and spanned several centimeters or more of downhole depth were considered host rock breccias.

In the listvenite, breccias are marked by clasts of the host rock in an iron oxyhydroxide–stained matrix (Fig. F53A, F53B, F53C). The oxide material around the clasts appears to be a product of both the surrounding host rock and later iron oxyhydroxide veining around the clasts. Many of the listvenite breccia clasts show internal foliation that is not parallel to the foliation in the host rock surrounding the breccias; we therefore infer that the breccia clasts have been rotated and that some of the breccias formed after initial foliation development.

Breccias in the serpentinite have serpentine and/or carbonate matrices. Serpentinite breccias sometimes have a "shattered" texture in which the clasts show little rotation or movement relative to the surrounding host rock (Fig. F53C, F53D). The observed breccias range from clast to matrix supported. We used the term "fragmented by veins" when the matrix was derived from veins and contained host rock and/or vein fragments (see description below).

In the metamorphic sole, brecciation is almost exclusively associated with faults (Fig. F53F). It is generally matrix supported with subangular clast sizes of 8–10 mm. The material between clasts is typically either a fine matrix composed of the host rock or more commonly, anastomosing chlorite or epidote veins.

Cataclasite

There are several different generations of cataclasite in Hole BT1B. We distinguished generations of cataclasis by the composition and internal structure of clasts within the feature in different lithologic sections of the core. Host rock cataclasites are distinguished from localized cataclasites largely by feature width. If the cataclasite spanned more than several centimeters downhole and the entire width of the core, it was considered a host rock cataclasite. Localized cataclasites are single features or sets of consistently oriented features that can be differentiated from other structural features. Host rock cataclasites are generally more common in the upper part of the listvenite suite with very few in the serpentinites, metasediments, and metabasalts (Fig. F51).

Host rock cataclasites in the listvenites contain lithic clasts and oxidized massive listvenite clasts with some randomly oriented vein fragments. Cataclasites in the listvenite are typically bands >2 cm wide marked by a finer oxide-rich matrix with 1–2 mm subrounded clasts of host rock (Fig. F54). Further downhole, host rock cataclasites are sometimes defined by sets of localized cataclasites that are clustered in intervals, share a similar orientation, and together form up to 55 cm thick sections of host rock (e.g. Fig. F54). Carbonates rather than oxide-rich material form the matrix in the rare serpentinite cataclasites.

Structural measurements of host rock cataclasites are shown in Figure F55. Stereoplots are shown for contiguous intervals of Hole BT1B core such that data in a single stereoplot are taken from cores that have not been rotated with respect to one another downhole within the defined interval. Of the 17 total cataclasite measurements recorded for Hole BT1B, 6 measurements fall within two contiguous intervals. Orientations of host rock cataclasites in one case show high variability and in the second cluster around a flat-lying orientation. Trends are difficult to determine based on the limited data. Downhole plots of cataclasite dip angle vs. depth are shown in Figure F56 and suggest a majority of host rock cataclasites are moderately dipping with some shallow exceptions. This is supported by dip histograms that show cataclasites with a dominant 55° dip (Fig. F57). However, we caution the reader to not overinterpret these data, as they are not subdivided by contiguous section, and these data have not been corrected for Hole BT1B drilling at ~75° inclination.

Foliation

All major rock types downhole have intermittent to continuous foliation. These penetrative fabrics are defined by high density and alignment of veins, alignment and/or elongation of minerals, and/or shear deformation. Deeper than ~130 m, the Hole BT1B core is dominated by pervasive foliation development (Fig. F51). A histogram of the foliation dip angles in host rock structures is shown in Figure F57. Above the basal thrust there is no dominant dip angle in foliated listvenites; however, below the basal thrust there is a high density of foliation dip angles of 10°–20° (Fig. F57).

Most of the listvenite foliation is defined by a high density of Fe oxyhydroxide and carbonate veins. These veins are typically discrete and sometimes anastomosing, and each vein is generally <2 mm thick (Figs. F52, F58). Within each contiguous core interval of listvenite, Fe oxide veins are parallel to subparallel to the host rock foliation and have generally shallow (but variable) dips (Fig. F55), whereas carbonate veins are present at higher angles and are sometimes orthogonal to the dominant host rock foliation (Fig. F55), but over the entire core they show no consistent orientation (Figs. F55, F57). Thin section observations indicate that some of the listvenite foliation consists of multiple narrow bands of parallel cataclasites. Therefore, the host rock has itself undergone significant deformation prior to multiple generations of crosscutting veining and faulting.

In areas where the listvenite is almost entirely composed of fuchsite, carbonate, and quartz, foliation is defined by parallel carbonate veins and/or shape-preferred orientation (SPO) of carbonate and quartz layers (Fig. F52). Carbonate veins are inferred to be the oldest vein generation based on crosscutting relationships. Because they dominate large sections of core, they are grouped as a host rock feature. In deeper sections, elliptical-to-blocky fuchsite crystals (pseudomorphs after pyroxene) were sufficiently oblate to form foliation (Fig. F58).

The serpentinite has similar foliation to listvenite when foliation is present. Serpentinite foliation is commonly delineated by a high density of closely spaced, parallel to anastomosing carbonate veins. These carbonate veins form parallel to iron oxide veins in the listvenite and in places can be seen directly merging with them across the listvenite/serpentinite boundaries (Fig. F58).

Many of the metasediments and metabasalts in the metamorphic sole have foliation defined by segregated epidote, green and blue amphibole, and chlorite-rich layers (Fig. F59) alternating with quartz, feldspar, chlorite, and carbonate-rich layers. Alignment of the long axes of these minerals produces strong SPO. Some evidence of foliation development by dynamic recrystallization is present, indicated by a consistent fine grain size and some subgrain formation and undulose extinction.

In the upper portions of the metamorphic sole, the foliation contains tight to isoclinal folds (Fig. F59). Folds often have small parasitic folds developed along fold limbs. Under hand lens and in thin section, metasediments and metabasalts also have "eye structures" suggesting sheath folds might be present within the foliation (Fig. F60). These fold types suggest the metamorphic sole was subject to high shear strain.

In the metamorphic sole for the uppermost tens of meters beneath the basal thrust, the foliation wraps around fragmented epidote-quartz veins that are stretched parallel to the foliation. We also documented veins that had been completely transposed and tightly to isoclinally folded within the foliation (Fig. F59). The foliation orientations beneath the basal thrust are generally near horizontal (Fig. F55). Fe oxide, chlorite, and epidote veins are typically nearly parallel or slightly oblique to the orientation of the dominant foliation. Occasionally, larger folds with wavelengths on the order of ~30 cm are developed within the foliation (Fig. F60).

Fragmented by veins

Where the host rock has no visible structure and is crosscut by one or more generations of veins in random orientations, the structure is termed "fragmented by veins." This feature is typically where the structure of host rock is completely obscured by late crosscutting veins (Fig. F61). We also use this term where the core samples were too crumbled to be able to piece together host rock structures.

Localized structures

The downhole frequency of localized features and several vein types in Hole BT1B is shown in Figure F62. Histograms of localized structure dip angles are shown in Figure F63. Dip histograms for localized brittle structures and different vein types in listvenites and serpentinites above the basal thrust are shown in Figure F64. Downhole plots of dip angles for specific vein types are shown in Figure F65. These figures illustrate the spatial distributions and dip angles of faults, cataclasites, shear zones, and different generations of veins that are discussed below.

Veins and vein sets

We documented the main generations of veining and focused on crosscutting relationships in the Hole BT1B core. For a more detailed synthesis of vein generations and mineralogy, see **Vein petrology: listvenites and serpentinites**.

We identified abundant individual veins and vein sets in all rock types present in Hole BT1B. Vein sets are defined as two or more veins of similar geometry, orientation, and mineralogy within a core interval. We characterize vein chemistry by one or two dominant phases. Vein geometry was characterized as planar, irregular, splaying, or anastomosing. Each rock type has a consistent sequence of veining discussed below; however, there are exceptions to each crosscutting relationship and it is possible that generations of veining occur continuously and overprint one another through time.

Multiple generations of veining are preserved in listvenite cores. The earliest generation of veins are fine grained, millimeter- to submillimeter-scale, anastomosing and/or irregular Fe oxyhydroxide veins (Fig. F66). In some listvenites these veins delineate mesh texture around relics of orthopyroxene and serpentine from harzburgite and/or serpentinite protoliths. These veins sometimes define foliation in oxidized listvenites and are locally crenulated (see Fig. F66). Stereoplots of vein orientations reveal that these veins are often parallel to the dominant foliation (Fig. F55). Therefore, these veins are pre- to synkinematic with respect to penetrative fabric formation during and/or after listvenitization. These early veins are crosscut by two main vein types: (1) planar and splaying, millimeter- to centimeter-scale, fine-grained silica-rich carbonate veins (Fig. F66) and (2) planar and splaying, millimeter-scale, fine-grained veins with oxyhydroxide center lines and antitaxial growth of magnesite on the rims. The youngest generation of veins is irregular and splaying, millimeter- to centimeter-scale, fine- to coarse-grained magnesite veins (Fig. F66) that crosscut the foliation at moderate to steep angles (Fig. F55). Magnesite veins sometimes are only partially mineralized and have been identified as open cracks or open veins. In unoxidized listvenites (white host rocks) fuchsite-quartz veins crosscut the earliest foliation, which is defined by aligned parallel to anastomosing carbonate + quartz veins.

A rare feature we observed in the listvenites is veins that are filled with both vein material and cataclastic material. They form as open fractures that are partially filled with cataclastic debris and then subsequently mineralized to completely healed veins (Fig. F67). The paleohorizon is preserved, as the inclination of the contact surface. The contact between the vein fill and cataclastic fill is often planar and sharp.

Vein sets in undeformed serpentinites are characterized by Fe oxyhydroxide and carbonate mesh textures that sometimes surround relics of serpentinite with a harzburgite protolith (Fig. F66). Where serpentinites are deformed, these earliest carbonate veins define strong foliation and shear zones distributed throughout otherwise massive serpentinite. Veins are planar to anastomosing, millimeter-scale, and fine grained. Fe oxyhydroxide veining is more common in the more heavily altered serpentinite. Serpentine veins are found parallel to sheared carbonate veins or shallowly crosscutting carbonate veins. The latest stages of veins in serpentinites are also carbonate and serpentine rich with variable amounts of iron oxide. Veins are millimeter- to centimeter-scale, fine grained, and planar to splaying and often define shear zones, zones of cataclasis, and brittle discontinuities.

The earliest generation of veins in metamorphic sole rocks are fine- to medium-grained epidote and quartz veins that are variably sheared and fragmented throughout the matrix (Fig. F66). Fine-grained planar to splaying sets of quartz, epidote, ± carbonate veins shallowly crosscut the foliation at low to moderate angles and often serve as planes of localized faulting, millimeter-scale ductile shear zones, and/or seams of cataclasis. The latest stages of veining are often submillimeter scale, very fine grained, irregular to splaying black chlorite veins (Fig. F66). We documented tension gashes filled with chlorite crosscutting massive to foliated epidosite pods distributed throughout the foliated greenschist matrix. Earlier Fe oxide, chlorite, and epidote veins have orientations that are roughly parallel to moderately oblique with respect to the host rock foliation (Fig. F55), suggesting these veins have experienced varying degrees of transposition due to postinjection shearing.

A plot of dip angle vs. depth for different vein types in shown in Figure F65. These data show highly variable dips downhole but have not been corrected for the ~75° drilling inclination or for core section discontinuities.

Fragmented veins

Fragmented veins are defined as sets of veins distributed throughout a core interval that have very irregular geometries, lack a consistent orientation and/or sense of shear, and are variably crosscut by other later localized structures such as faults, cataclasites, and other veins (Fig. F68). Fragmented veins are common in all rock types and vary in chemistry from quartz, carbonate, and oxides in listvenites; serpentine and carbonate in serpentinites; and epidote, quartz, and feldspar in the metamorphic sole.

Faults

In listvenite and serpentinite, small-scale faults with offsets in the centimeter range form as sharp discrete features often with splaying fault strands or fault lenses (Fig. F69). Thin sections reveal that faults are often associated with cataclasis and veining (Fig. F69). Fault kinematics are in most cases not clear because of the inclination of the drilled core and the small sample size. Where we could define a shear sense it suggests normal to slightly oblique displacement (not quantitative).

Faults crosscut all vein generations but rarely interact with cataclasites and macroscale shear zones. This implies that faults are typically younger than veins and potentially are similar in age to other brittle features like cataclasites and some semibrittle shear zones. We counted a total of 33 small faults above the basal thrust with an increase in density deeper than 100 m downhole and a slight decrease close above the basal thrust. Small-scale structures near the basal thrust are possibly overprinted by larger scale deformation. Stereographic projections of the orientation data of fault planes for contiguous section intervals show variable fault orientations above the basal thrust compared to highly consistent and shallowly to moderately dipping features below the basal thrust (Fig. F55). Again, we caution the reader not to interpret these stereo-plots in any geographic or tectonic context without further analysis.

Small-scale faults in the metamorphic sole are abundant and often planar or splaying (Fig. F69) and sometimes cohesionless. Their slip planes are polished and mineralized with chlorite, epidote, or oxides. On a microscale we see that cataclasites on the millimeter to centimeter scale contain abundant oxides and evidence of porphyroclast rounding and grain size reduction (Fig. F69). Faults in the metamorphic sole show orientations at steep angles to roughly perpendicular to the dominant host rock foliation (Fig. F55).

Slickensides were identified on a few fault surfaces throughout Hole BT1B. We measured the trends and plunges of these lineations.

Cataclasites

We identified 105 localized cataclasites with thicknesses in the centimeter range. Cataclasites are far more abundant in the listvenite and serpentinite than discrete faults. Their matrix is fine grained to microcrystalline with larger, rounded fragments as large as 1 mm (Fig. F70). Their color reflects the color of the host rock, stained red by oxides in Fe oxyhydroxide–enriched listvenites, whitish in carbonate-rich listvenites, and greenish white in serpentinites (Fig. F70). Whereas most cataclasites have irregular but well-defined boundaries, they occasionally splay and cataclastic material seems to fill nearby preexisting open fractures. It is difficult to discern a shear sense or kinematics because of the limited size of the samples.

Cataclasites are crosscut by carbonate, Fe oxyhydroxide, and magnesite veins, late mineralized cracks, and some shear zones. Cataclasites also crosscut carbonate veins, magnesite veins, and shear zones, implying that cataclasite formation took place continuously or in several stages during the formation of above-mentioned veins. Orientation data (Fig. F55) show that cataclasites are oriented at moderate to steep angles with respect to the dominant foliation in listvenites.

In the metamorphic, sole cataclasites are far less abundant. Where they are present, they are commonly in seams as thick as a few millimeters (Fig. F70). On a microscale, thin black bands rich in oxides define cataclasites (Fig. F70). The orientation of these bands is mostly shallow with respect to the pervasive foliation and dip in various directions (Fig. F64).

Shear zones

Ductile and semibrittle shear zones are abundant throughout Hole BT1B above the basal thrust (Fig. F62). We counted 105 shear zones between 0 and 197 m downhole. There is no clear relationship between ductile vs. semibrittle shearing and depth or lithology in the core. Both ductile and cataclastic shear zones were observed in listvenite and serpentinite, in fuchsite-rich lithologies, and in oxide-rich listvenites. Macroscopically, ductile shear zones often occur where there is a high density of millimeter-scale anastomosing Fe oxyhydroxide veins (Fig. F71). Cataclastic shear zones range from planar to splaying to anastomosing and show varying degrees of comminution and grain size reduction.

The abundance of shear zones increases deeper than 80 m downhole and then remains rather constant across the basal thrust (Fig. F62). At ~225 m in the metamorphic sole, the general deformation regime becomes more brittle and shear zones are replaced by a higher density of faults (Fig. F62).

Orientation data of shear zones in listvenite (Fig. F55) reveal that shear zones are roughly parallel to host rock foliation. For some contiguous intervals they also have similar orientations to cataclasites, although this correlation is difficult to identify because of the limited number of observations.

In the metamorphic sole, shear zones form as planar to splaying assemblages of anastomosing microveins, generally containing quartz, epidote, and oxides (Fig. F71). Such shear zones are only a few millimeters wide. Shear zones in the metamorphic sole are less abundant than in the listvenite. Shear zones are also broadly parallel to host rock foliations, and where data are available, appear to be parallel to cataclasites (Fig. F55).

Folds

Folds in listvenite and serpentinite (Fig. F72) are macroscopically rare. We documented three with wavelengths that do not exceed 35–40 cm. Their presence is not related to depth or lithology, as we found two in listvenite at 39 and 48 m and one in serpentinite at 185 m downhole. Folding within the foliation appears to occur more often in listvenite than serpentinite (Fig. F72). Fracturing and vein fragmentation at fold hinges suggest that folding occurs under semibrittle conditions.

The upper tens of meters of the upper greenschist facies metamorphic sole contain pervasive ductile shear folds with axial planes slightly inclined to parallel to the dominant foliation (Fig. F72). Earlier veins are passively folded within the host rock material (Fig. F73). Parasitic folds on the limbs of folds are common and suggest larger scale folds may be present. The folds indicate passive shearing, and the transport direction is consistently toward 270° in the CRF. The reader is reminded that the CRF represents a two-dimensional slice through the core, and without further analysis a more accurate transport direction cannot be determined. Further downhole, the deformation regime becomes more brittle and only a few small semibrittle folds formed, often associated with faults or shear bands defining the fold axials planes (Fig. F73).

Cracks

Veins including vugs lined with euhedral carbonate crystals occur as a late brittle feature in listvenite and serpentinite (Fig. F74). Thinner cracks are also partially healed by vein material. These mineralized cracks cut through all other vein generations and faults, shear zones, and cataclasites, indicating relatively late formation. We did not document any locations where these veins cut brecciated host rock or where breccias cut mineralized cracks. The limited occurrence of both features does not allow a statement about their age relationship.

Cracks in the metamorphic sole tend to have a smaller aperture with less mineralization. Red iron oxides stain the crack surfaces, and sometimes chlorite and/or quartz can be found. Their appearance is similar to cohesionless mineralized faults in the metamorphic sole, but they show no or very little offset. Again, cracks are late structures, cutting most other veins and shear zones.

Relative age of structural features

Observations of host rock structure indicate that the oldest structures in Hole BT1B are macroscopically ductile foliations found in listvenites, serpentinites, and the metamorphic sole. In listvenites, foliations are defined by alignment of Fe oxyhydroxide veins and/or shape-preferred orientations of magnesite + quartz layers. Fe oxyhydroxide veins are pre- to synkinematic with respect to penetrative fabric formation in listvenites. In serpentinites, foliations are defined by alignment and shearing of anastomosing carbonate + serpentine (± oxide) veins. In the metamorphic sole, ductile foliations are defined by alignment (and potentially recrystallization) of elongate minerals like epidote and amphiboles.

In listvenites and serpentinites, early foliations are crosscut by millimeter-scale red anastomosing Fe oxyhydroxide veins followed by several generations of transparent to whitish carbonate veins that contain mostly dolomite, magnesite, and some silica (Fig. F75). Particularly, some magnesite-rich yellowish veins are relatively late, cutting all previous structures (Fig. F75). The age relationship between magnesite veins, shear zones, and cataclasites is not clear, as crosscuts occur in numerous configurations, implying that these processes were active at the same time or in several stages. Brittle faults, mineralized cracks, and brecciation on the centimeter to tens of centimeter scale are the youngest structures in the core and almost always crosscut all other structures (Fig. F75).

In the metamorphic sole, the earliest ductile foliations contain stretched epidote-quartz veins, and then this structure is crosscut by additional epidote-quartz veins. This suggests that veining began early and continued during fabric formation such that transposition of epidote-quartz veins into the foliation varies from weak to complete. Veins are fragmented, sheared, and folded together with the host rock, forming foliations and shear folding. The age relationship of later features is less clear. Cataclasites and shear zones coexist and rarely crosscut each other. Brittle faults with some chlorite mineralization formed late and crosscut most other structures. Faults are occasionally crosscut by chlorite veins that also form in tension gashes.

In an attempt to quantify the crosscutting relationships and relative ages of structural features downhole, we present histograms summarizing the occurrences of different features divided by their relative age expressed as deformation generation D1, D2, or D3 (Fig. F76). D1 is the oldest feature, subsequently crosscut by D2 and D3. As generation D3 is not always present, the total number of D3s is small. Faults form dominantly as D2 and D3, whereas cataclasites and shear zones are occasionally crosscut by other features. Fe oxide veins form as early D1 features but also occasionally cut other structures in listvenites and serpentinites. Carbonate veins (including carbonate quartz and carbonate oxide) follow the same general trend. Magnesite veins tend to form later as D2 and D3; however, as they are often only cut by brittle structures they also show a significant number of D1s. In the metamorphic sole, epidote and serpentine veins form early as D1 generations, followed by later chlorite veins. As these histograms do not provide information on which feature is crosscut by which other features, please refer to the more detailed descriptions of crosscutting relationships summarized above and in the detailed core descriptions for case-by-case relationships.

Whereas these relative ages are in general well established, we found exceptions for every single one. The reader is advised to check carefully for individual scientific questions to avoid confusion or mistakes.

Conclusions

We characterized host rock and localized structures in listvenites, serpentinites, and the metamorphic sole of materials from Hole BT1B drilled through the Samail ophiolite in Oman. A combination of visual core descriptions and microstructural analysis indicate that all rock types preserve early (macroscopically ductile) foliation development overprinted by multiple stages of brittle to semibrittle deformation.

In listvenites and serpentinites, host rock structures have early foliations that are crosscut by later brecciation and cataclasites. Brecciation is more common in the uppermost part of Hole BT1B. Documentation of localized features reveals many generations of crosscutting veins that in general evolve from Fe oxyhydroxide–rich millimeter-scale seams to centimeter-scale magnesite-rich irregular veins. Stereographic projections of structural data from contiguous core intervals (where cores have not been rotated with respect to one another) show cataclasites and faults cutting at oblique angles to nearly perpendicular to host rock foliations. The observation that localized cataclasites and faults have similar structural orientations suggests these late-stage brittle features may be related to the same tectonic event. With increasing depth downhole, ductile foliations dominate the host rock structure in listvenites and in the metamorphic sole.

In the metamorphic sole, there is pervasive ductile shearing and isoclinal folding in the uppermost part of Hole BT1B. With increasing depth, these features become strongly affected by brittle veins and faults. Fe oxide, chlorite, and epidote veins are present at varying orientations relative to the foliation and may reflect varying degrees of vein transposition during shearing. Chlorite veining and tension gashes crosscut ductile fabrics entirely and appear unaffected by later pervasive shearing. Shear zones are oriented parallel to moderately oblique relative to host rock foliations, whereas brittle faults cut the foliation at moderate to high angles (Fig. **F55**).

There are numerous potential avenues for future structural research with core samples from Hole BT1B. Several of the key outstanding questions include but are not limited to the following:

- The relative timing and tectonic event(s) responsible for shearing in listvenites, serpentinites, and the metamorphic sole;
- The timing and cause of transition to brittle style of deformation;
- The pressure-temperature-time evolution during alteration, metamorphism, and deformation throughout Hole BT1B;
- The significance of listvenitization on bulk core rheology; and
- Active mechanisms of deformation and strain localization operating in different lithologies and across lithologic boundaries through time, including volume changes due to serpentinization and listvenitization.

Geochemistry

Whole-rock chemical analyses were performed on 73 samples collected from Hole BT1B: 44 listvenites, ophicarbonates, and serpentinites from Sections 7Z-4 through 77Z-4 and 13 schists and greenstones from Sections 82Z-1 through 124Z-1 selected by the shipboard science party as representative of the different lithologies recovered. When possible, samples were taken next to a thin section (see **Supplementary material** > **B_Thin section descriptions**). On site, 15 samples were collected every 20 m during operations; they were powdered and analyzed at the Universities of Southampton and St. Andrews (see **Geochemistry** in the **Methods** chapter). A thin section was taken for each on-site sample. XRD analysis was also performed on each geochemistry sample for detailed mineral characterization (see **Host rock**).

The sample powders were ignited and analyzed for major and trace element concentrations by XRF. Additional gas chromatographic separation was undertaken on nonignited powders to determine their volatile element content (H_2O, CO_2, and inorganic carbon). The analytical procedures, precision, and accuracy of the methods are described in detail in **Geochemistry** in the **Methods** chapter.

The major, trace, and volatile element compositions are reported in Table **T12**. Note that V is not reported for schists and greenstones because of an analytical problem identified but not corrected (see **Geochemistry** in the **Methods** chapter). The trace element compositions obtained by inductively coupled plasma–mass spectrometry (ICP-MS) are reported in Table **T12**.

LOI, CO_2, and H_2O contents

Hole BT1B samples display a broad range of values for LOI, 1.29–42.6 wt% (Fig. **F77**). These variations relate to the lithologies of the recovered samples. LOIs in the upper listvenites, ophicarbonates, and serpentinites range 15.23–42.6 wt%, whereas LOIs in the schists and greenstones composing the ophiolite metamorphic sole range 1.29–3.76 wt%.

Concentrations of CO_2 and H_2O measured in Hole BT1B samples correlate with the measured LOI values (Fig. **F77**), although their total appears systematically high compared to LOI values, in particular in samples in which no CO_2 was measured. We hypothesize that H_2O concentrations were overestimated in these samples. The listvenite samples have the highest CO_2 (19.5–43.20 wt%) and the lowest H_2O (<1.10 wt%) concentrations. The high CO_2 values are consistent with their high carbonate contents, mainly magnesite and dolomite (see Host rock descriptions and Thin section descriptions and mineralogy estimates from XRD in **Supplementary material** > **B_Thin section descriptions**). Serpentinites and ophicalcites have CO_2 compositions (5.6–33.05 wt%) overlapping that of listvenites and the highest H_2O concentrations (6.4–24.3 wt%) among Hole BT1B samples. These high and variable compositions reflect their modal contents, with carbonates concentrating CO_2, H_2O-rich serpentines, and anhydrous quartz (see Host rock descriptions and Thin section descriptions and mineralogy estimates from XRD in **Supplementary material** > **B_Thin section descriptions**). Samples from the metamorphic sole have the lowest CO_2 (0.04–0.97 wt%) concentrations of Hole BT1B samples. H_2O concentrations are highly variable (4.0–7.7 wt%) and reflect the occurrence of secondary hydrous minerals in these samples (e.g., chlorite and amphibole) but could not be used to quantify the extent of alteration of these samples because of the overestimate of H_2O concentrations outlined above.

Inorganic carbon recalculated as CO_2 displays the same range of compositions as the CO_2 concentrations measured using the elemental analyzer (0.01–

43.2 wt%; Fig. F77); however, inorganic and total carbon concentrations do not correlate for most samples. The difference between measured elemental inorganic and total carbon values ranges 2.07–9.29 wt%. This difference is generally interpreted as representing the total organic carbon content, but there is no optical evidence of abundant organic carbon in Hole BT1B listvenites. Inorganic carbon is analyzed using a technique involving acidification of samples to dissolve carbonates. Hole BT1B listvenites and serpentine contain magnesite, a mineral characterized by slow dissolution kinetics (Al-Aasm et al., 1990; Pokrovski et al., 2005). We hypothesize that the difference between measured inorganic and total carbon values results from the magnesite not being dissolved during acidification of listvenite, serpentinite, and ophicalcite samples. To test this hypothesis, we calculated the mass of magnesite and dolomite assuming that all inorganic carbon was concentrated in dolomite, and the difference between inorganic and total carbon values was the carbon constitutive of magnesite. Our results suggest that listvenite samples compose up to 65% of magnesite and non-negligible amounts of dolomite (up to 52%, even when dolomite was not described). We compared these results to XRD measurements undertaken on the same powders (Fig. F78). The calculated masses of magnesite and dolomite correlate well with XRD estimates, although there is an offset between XRD and chemistry estimates: the amount of XRD-measured magnesite is systematically higher compared to calculated magnesite contents and, in contrast, the amount of XRD-measured dolomite is systematically lower compared to calculated dolomite contents, in particular for low dolomite contents. This offset might result from partial dissolution of magnesite during inorganic carbon measurements.

Major and trace elements

Downhole plots

Hole BT1B samples are characterized by a broad range of compositions. As illustrated on Figures F79 and F80, the measured changes in compositions correlate with the recovered lithologies as well as with depth. The major lithologic limit encountered in Hole BT1B is the transition from the ophiolitic mantle to the metamorphic sole. This transition is characterized by a sharp gradient in measured compositions except for CaO. Samples recovered down to listvenite interval 77Z-4, 43.0–48.0 cm (194.55 m depth) have high Mg# (100 × cationic Mg/[Mg + Fe]) of 81–93, low Al_2O_3 (<2.5 wt%), and, except for a few carbonate-dominated veins, high Cr and Ni concentrations (416–5304 and 709–5371 ppm, respectively). Less than 5 m deeper (199.38 m), schist interval 80Z-1, 38.0–43.0 cm, has a composition typical of the samples recovered in the metamorphic sole, with Mg# < 53, high Al_2O_3 (15–19 wt%), and low Cr and Ni concentrations (<327 and <101 ppm, respectively). The ophiolite–metamorphic sole transition appears more diffuse for CaO concentrations (Fig. F79). Once excluding carbonate vein–dominated samples (SiO_2 < 37 wt%; CaO + MgO = 55–75 wt%), CaO concentrations increase steadily downhole between 140 m depth in the ophiolitic domain (CaO = 0–3 wt%) to ~250 m depth into the metamorphic sole (CaO ~ 12 wt%), with a peak (CaO ~ 17 wt%) in the deepest 15 m of the ophiolitic section. The main chemical characteristics of these two main lithologic units are detailed below.

Listvenites, ophicalcites, and serpentinites

Listvenites, serpentinites, and ophicalcites represent the main lithologies recovered in the ophiolitic domain in Hole BT1B. The composition of Hole BT1B listvenites reflects primarily their mineralogy, which is dominantly magnesite and/or dolomite and quartz (see Host rock). They overlap in composition with the previously analyzed Oman listvenites, with highly variable SiO_2 and MgO contents (15–69 wt% and 18–56 wt%, respectively) (Falk and Kelemen, 2015; Fig. F81). Most of Hole BT1B ophiolitic samples plot along a trend consistent with a formation by addition of various amount of SiO_2 to the Oman peridotite protolith. Several samples also display evidence of CaO addition (up to 38 wt%), leading to the formation of dolomite identified in veins and in the listvenite matrix (see Host rock). As illustrated on Figure F81, the composition of the serpentinites and ophicalcites recovered from Hole BT1B is significantly less variable compared to that of listvenites and comparable to that of Oman peridotites (e.g., MgO = 35–54 wt%). Nevertheless, their composition was also significantly modified during alteration, as evidenced by their high CaO (up to 33 wt% in ophicalcites) and variable SiO_2 (21.75–49.3 wt%) concentrations.

The listvenites, ophicalcites, and serpentines recovered from Hole BT1B were classified into three groups on the basis of their downhole changes in composition: (1) the serpentine and ophicalcite group, (2) the upper listvenites sampled at 8–81 m depth, and (3) the lower listvenites sampled at 107–195 m depth below the thick serpentine to ophicalcite–dominated interval at 81–100 m.

Serpentinites and ophicalcites sampled between 81 and 107 m depth have on average the most depleted compositions, with Al_2O_3 (0.07–0.49 wt%), TiO_2 (≤0.05 wt%), K_2O (≤0.01 wt%), and Cr (2374–3961 ppm) concentrations generally close to or lower than that of the average Oman mantle (Figs. F82, F83). They have more variable compositions for trace elements, mainly in relation with the occurrence of ophicalcites, which are associated with enrichments in Sr (159–340 ppm) and Ni (up 5371 ppm) relative to the composition of neighboring serpentinites. Sr enrichment is classically associated with precipitation of carbonates, whereas the increase in Ni suggests a high mobility of metals in the CO_2-rich fluids that formed these carbonates. The serpentinite sampled at 183 m overlaps in composition with the upper serpentinites except for its slightly enriched composition in Al_2O_3 (1.84 wt%) and Ni (3986 ppm).

The composition of the upper listvenites overlaps that of the serpentinites but is overall more variable, with Al_2O_3 of 0.02–0.77 wt%, TiO_2 of 0.00–0.05 wt%, and Cr of 1752–5304 ppm. They also have variable Ni and Sr compositions; the lack of correlation between Ni and Sr composition suggests changes in the metal mobility in fluids precipitating carbonates similar to that observed in serpentinite–ophicalcite samples.

The lower listvenites are characterized by highly variable compositions (e.g., Mg# = 80.7–92.6) and selective enrichments in Al_2O_3 (up to 2.42 wt%), TiO_2 (up to 0.10 wt%), and K_2O (up to 0.44 wt%). These strong variations are probably related to formation of fuchsite, a Cr-bearing muscovite, $KAl_2[(Al,Cr)Si_3O_{10}](OH,F)_2$, commonly observed in the lower part of the ophiolitic domain in Hole BT1B. The lower listvenites are depleted or overlap in Cr and Ni compositions with the overlying serpentinites, ophicalcites, and listvenites (Cr = 416–5280 ppm; Ni = 709–4597 ppm). Cr and Ni are on average depleted relative to the composition of the average Oman mantle peridotites, suggesting that the formation of fuchsite-bearing listvenite is not associated with overall enrichment in Cr or Ni. Sr is depleted relative to neighboring ophiolitic units (11–142 ppm) except between the deepest serpentinite sliver (at 183 m), and the metamorphic sole, where it reaches the highest values measured in mantle-derived rocks in Hole BT1B (Sr up 383 ppm). The same zone is also particularly rich in CaO (6.6–32.7 wt%), suggesting contamination by Ca-Sr–bearing fluids originating from the metamorphic sole.

All samples recovered in the ophiolitic domain in Hole BT1B are enriched in fluid mobile and incompatible elements compared to the mean composition of the Oman mantle (Fig. **F84**). These enrichments are as high as ~10^3 times the Oman mantle for Rb and Ba. The precision of shipboard XRF analyses does not allow investigating if the different groups outlined above display variable trace element signatures.

Metamorphic sole

Sediment-derived schists and basalt-derived greenstones were identified in the metamorphic sole based on texture and petrography. The two groups could not be distinguished chemically, as they overlap in composition for the elements measured on board *Chikyu*. Downhole variations are, however, observed from the ophiolite/sole interface to the bottom of Hole BT1B: Mg#, CaO, and Sr increase downhole (20–53, 5 to 12–14 wt%, and ~210 to ~600 ppm, respectively), whereas K_2O and Y show the opposite trend (~4 to ~0.4 wt% and ~60 to ~22 ppm, respectively). Most of the changes in concentrations occur in the upper 50 m below the ophiolite/metamorphic sole interface (to schist interval 101Z-4, 51.0–59.0 cm; 249.395 m). This zone is also characterized by slightly higher TiO_2 (2.5–3.7 wt%) concentrations compared to the samples from greater depths (1.6–2.6 wt%). These variations may result from fluid circulation and chemical exchanges along the ophiolite/metamorphic sole interface or from the metamorphic sole to the overlying ophiolite. It is worth noting that the metamorphic sole samples recovered from Hole BT1B are enriched in fluid mobile and incompatible elements compared to the mean composition of the Oman mantle and to the samples recovered in the ophiolitic domain. The listvenites, ophicalcites, and serpentinites recovered from Hole BT1B are preferentially enriched in the same elements relative to the mean composition of the Oman ophiolite mantle and mimic the pattern of the samples from the metamorphic sole. This suggests that the composition of the listvenites in these elements is controlled by that of the contaminating fluids that may have originated in the same lithologies as those drilled in Hole BT1B.

Summary

The Oman listvenites series were formed after extensive interactions between CO_2-rich fluids, probably originating in subducting sediments, and the overlying serpentinized peridotites (e.g., Falk and Kelemen, 2015). The composition of listvenites, ophicalcites, and serpentinites recovered from Hole BT1B record these reactions involving addition of SiO_2 and formation of carbonates at the expense of the serpentinized peridotite protolith. They also show notable downhole chemical variations with listvenites showing marked variations in Al_2O_3 and TiO_2. The occurrence of lherzolites and clinopyroxene-harburgites at the base of the Oman mantle section has been observed by several authors (Lippard et al., 1986; Godard et al., 2000; Takazawa et al., 2003). The observed variations in the listvenites (Al_2O_3 and TiO_2) could be related to the composition of their protolith, the deepest having more fertile compositions. Alternatively, the observed downhole changes in the composition of listvenites may relate to the progressive equilibration of the reacting listvenites with the fluids originating in the subducting metamorphic sole; these variations could be related to reaction kinetics (control of temperature, reactive surface, etc.) and/or to transport (local variations in permeability).

Paleomagnetism

Remanent magnetizations

Measurements of magnetic remanence were made exclusively on discrete 2 cm wide cube samples cut from the working half cores from Hole BT1B due to malfunction of the on-board long-core cryogenic rock magnetometer. A total of 122 discrete samples were measured for magnetic remanence with 65 samples from listvenites, 8 from the two thin bands of serpentinites, and 49 from metamorphosed sedimentary and volcanic rocks below the basal thrust. Of the total of 122 samples, 11 were subjected to stepwise alternating field (AF) demagnetization that proved ineffective at removing remanence in most cases. Because of this additional challenge, we focused on thermal methods to acquire useful data. In total, 43 samples were thermally demagnetized in the shipboard paleomagnetism laboratory to isolate characteristic remanent magnetization (ChRM) directions. Of these, 6 were initially subjected to AF demagnetization prior to thermal treatment. The limited total number of samples subjected to thermal demagnetization on the ship was due to the limited capacity of thermal equipment, which could only hold 8 cubic samples per batch in the oven. An additional 34 samples were thermally demagnetized in the shore-based paleomagnetism laboratory at Scripps Institution of Oceanography (USA), so in total 82 samples were demagnetized. The remaining samples will be demagnetized in another shore-based laboratory facility at Plymouth University in the near future.

Discrete sample remanence results

Natural remanent magnetization (NRM) intensity values range between 1.48×10^{-4} and 13.64 A/m (geometric mean of all discrete samples = 1.49×10^{-2} A/m) (Table **T13**, Fig. **F85**). The smallest and largest NRM values occur in samples taken from the metamorphic sole rocks below the basal thrust at a depth of 200 m (intervals 125Z-2, 40–42 cm [296.56 m], and 86Z-1, 75–77 cm [207.51 m], respectively). A wide range of NRM values (2.38×10^{-4} to 3.79×10^{-1} A/m) also occurs in the listvenite samples. The few serpentinite samples have a relatively narrow range of higher magnetizations, from 9.30×10^{-3} to 1.20 A/m. The downhole profile of NRM intensity exhibits wide variability with the strongest general correlation with changes in lithology. The two thin bands of serpentinite and a few isolated samples in the metamorphic sole rocks (Fig. **F85**) form distinct anomalies. The most consistently low magnetizations are found in the deepest metamorphic sole rocks between 250–300 m depth.

AF demagnetization was ineffective at removing any significant amount of remanence in samples of listvenite, though demagnetization appeared to be sufficient for the few samples of serpentinite (Fig. **F86**). The few attempts to demagnetize listvenite samples using AF methods revealed a relatively strong remanent magnetization that was extremely stable and could not be significantly demagnetized by the 180 mT maximum AF field. Because of the presence of one or more high-coercivity phases in the listvenite samples, a few samples were thermally demagnetized after AF treatments to 180 mT, and these samples generally show one, two, or more components of magnetization (Fig. **F87**). In the few serpentinite samples subjected to AF methods, one or two components were identified. The low-coercivity component (0–10 mT) shows a shallow to moderate positive inclination and reveals the moderate-coercivity component (either 10–50 mT or 10–100 mT) with a subhorizontal or shallow to moderate positive inclination (in core coordinates). The stability of magnetization against AF demagnetization assessed from the median destructive field of the vector difference sum (MDF′) yields a range of high values for listvenite samples between 60 and 178 mT, whereas the range for serpentinite samples is much lower, between 10 and 25 mT. The highest MDF′ value of 178 mT was found in a listvenite sample from a shallow depth (7Z-4, 21–23 cm; ~8.6 m) in the drill core. No samples from the metamorphic sole rocks below the basal thrust were subjected to AF demagnetization because they are also suspected to contain high-coercivity minerals based on a previous study of metabasites in Oman (Feinberg et al., 1999). Instead, we prioritized thermal demagnetization methods.

The majority of discrete samples were subjected to thermal demagnetization and yield a wide range of behavior that make it challenging to identify general trends within or between lithologies or groups based on similar types of behavior. In general, many samples exhibit two or more components with discrete laboratory unblocking temperatures from low (100°–200°C) to intermediate (300°–400° or 300°–500°C) to high (500°–580°C and/or 600°–690°C) or distributed unblocking between these temperature ranges. Approximately 70% of the samples exhibit a low laboratory unblocking temperature component that is removed by ~200°C. In most cases, the low-temperature component is oriented with a moderate to steep positive inclination (in core coordinates), although few samples show shallow or negative inclinations. In a few samples, an intermediate component is resolved at 300°–400°C or 300°–500°C. In most samples, a stable component that trends to the origin is retained to high laboratory unblocking temperatures (500°–580°C and/or 600°–680°C). In some samples, the highest stability component is almost entirely removed by 580°C, and in other samples the component remains stable until ~680°C (Fig. **F88**). In a few samples, the component at ~500°–580°C appears distinct (~10° directional difference or greater) from the highest temperature component from 600°–680°C. In other cases the two components are subparallel and trend to the origin. The relative importance of these different ranges of high laboratory unblocking temperatures varies from sample to sample, with some exhibiting sharp decreases in remanence intensity at 500°–580°C and again at 590°–680°C, and in some samples more discretely at 650°–690°C. A stable ChRM component that trends to the origin at the highest temperature (or field) steps was identified in most samples. In a few samples, only a low (100°–200°C) and/or intermediate laboratory unblocking temperature component is observed at ~300°–400°C. Although these low-temperature components are generally observed within deeper metamorphic sole rocks (~280–300 m depth), they are also found in a few listvenite samples within ~20 m of the upper contact with the second serpentinite band (i.e., ~157–177 m depth). The highest unblocking-temperature component was interpreted as the most important component of remanence, acquired when the rock formed, known as the ChRM.

Stability of samples is assessed by median destructive temperature of the vector difference sum (MDT′) (Gee et al., 1993) and monitoring changes in magnetic susceptibility after each temperature step during thermal demagnetization. The MDT′ values for listvenite samples range 113°–685°C, whereas the range for serpentinite samples is 287°–479°C and for metamorphic sole rocks is 314°–680°C. Although low MDT′ values are present in each lithology, the overall distribution of MDT′ values is skewed to higher temperatures, with 46 samples (~60%) with MDT′ > 475°C and 18 of these samples (23%) have values >590°C, about half of which are listvenites and half metamorphic sole rocks. Changes in magnetic susceptibility observed after different temperature steps during demagnetization indicate thermal alteration of the magnetic minerals occurred over the course of these temperature steps (Fig. F88C). In general, the magnetic susceptibility changes in listvenite and metamorphic sole rock samples show pronounced increases above 600°C, whereas the few serpentinite samples show a slight increase at low temperature (<200°C), followed by a decrease in susceptibility beginning at 300°C and continuing until the highest temperature treatment. In most samples, these changes in magnetic susceptibility are not associated with any major changes in the remanence vector directions or intensities. However, a few samples of listvenite and metamorphic sole rocks do exhibit abrupt (random) changes in the remanence vector directions and/or increases in intensity at higher temperatures (>580°C). However, these samples are also almost entirely demagnetized at or below 580°C.

Although many samples show clear demagnetization behavior with discrete unblocking revealing one or more components that could be distinguished from thermal demagnetization data, some listvenite and metamorphic sole rock samples do not exhibit clear demagnetization behavior. In the most challenging cases, scattered or weak directional data preclude defining a ChRM. This could be partially due to relatively weak magnetizations of a few samples but may also be related to differences in magnetic mineralogy present in these samples. In few samples, the magnetization decreased rather abruptly at 0°–350°C with a change in remanence direction above 200°C. In some metamorphic sole rock samples deeper in the core (285–300 m), magnetization decreased abruptly at 300°–350°C. Several samples show a steep positive inclination component that may be drilling related that is commonly removed by relatively low temperature steps (<200°C). However, some metamorphic sole rock samples retain a very steep, positive inclination component up to 500°–540°C. One serpentinite sample also showed a similar steep positive inclination almost entirely to the origin, and this sample also exhibits distributed unblocking at 50°–580°C (Fig. F89).

Initial interpretation of remanence results

The ChRM components interpreted from the highest laboratory unblocking temperatures (and coercivities) in discrete samples show shallow to moderate inclinations that are both positive and negative in core coordinates (Fig. F90). Because of the variability of both positive and negative inclinations of ChRM components, it is less likely that remanence from all samples is consistent with a modern-field overprint, although it cannot be ruled out for some individual samples with moderate positive inclinations. A few lower-temperature components with moderate to steep positive inclinations may be drilling-induced remanences, but these are commonly removed by ~200°C, though in some cases they are retained up to 500°–540°C and persist up to 580°C in one serpentinite sample.

The higher temperature, stable ChRM vectors generally have shallow to moderate positive and negative inclinations, although the distribution shows a majority with shallow negative inclinations in core coordinates (Fig. F90B). The large scatter in positive and negative inclinations likely results in part from the nonvertical drilling direction (core drilling plunge of 75°) and variable rotation of individual core section pieces around the inclined core drilling direction. Mean inclination calculations for the highest unblocking component will not be meaningful until reorientation of core sections into a geographical reference frame is complete. In general, the low inclinations are broadly similar to the values reported from outcrop investigations of gabbros (Feinberg et al., 1999; Luyendyk and Day, 1982; Weiler, 2000; Morris et al., 2016) and sheeted dikes (Luyendyk et al., 1982) in the adjacent Wadi Tayin massif of the Samail ophiolite, ~40 km east of the Hole BT1B drill site. Further analyses, core reorientation, and assessment of potential tilt correction(s) are required before magnetic polarity may be determined to allow a more definitive comparison with other paleomagnetic data from the ophiolite and metamorphic sole.

Magnetic susceptibility

Bulk magnetic susceptibility

Bulk magnetic susceptibility values range between 242×10^{-6} and $47,941 \times 10^{-6}$ SI (Fig. F85; Table T14) with a geometric mean of $1,394 \times 10^{-6}$ SI. The downhole profile of bulk magnetic susceptibility is similar to that of NRM intensity, indicating that the variation is controlled by the concentration of magnetic minerals rather than major differences in magnetic grain size and mineralogy. In general, the highest values of bulk magnetic susceptibility coincide with serpentinite bands, plus a few specific bands in the metamorphic sole rocks.

The Königsberger ratios, Q, from Site BT1 range 0.008–57 (geometric mean = 0.25). A majority of samples have $Q < 1$, with most 0.1–1, though some samples do have higher values (Fig. F85; Table T13). Q values <1 indicate that remanent magnetization may be less important than induced magnetization in the samples. In general, there is a downward trend of lower Q values in the lower 50 m of Hole BT1B (Fig. F85), which suggests some change in either magnetic grain size or mineralogy in metamorphic sole rocks beneath the basal thrust. The range of Q is relatively constant throughout the upper 250 m of the hole, with just a few values of 1–100.

Anisotropy of magnetic susceptibility

Anisotropy of magnetic susceptibility (AMS) determinations were performed on all discrete samples prior to stepwise demagnetization to characterize the shape-preferred orientations of magnetic minerals in the core samples. Magnetic fabric shapes vary throughout the hole, ranging from strongly oblate (T = 0.91) to strongly prolate (T = –0.97). No clear trends in magnetic fabric shapes appear downhole (Fig. F91A), and nearly all magnetic fabrics are triaxial in character (Table T14; Fig. F91C). The largest single anisotropy degree (P') value of 2.49 was found in a finely laminated sample of possible metasediment ~40 m below the basal thrust (99Z-3, 44–46 cm; 242.46 m). Excluding this value, the largest anisotropy degree (P') values of 1.10–1.53 were observed in samples within ~40 m below the basal thrust or at 200–240 m depths.

K_{min} inclinations are generally scattered downhole, whereas K_{max} inclinations are relatively shallow (in core coordinates). The K_{max} inclinations are typically <40°, as seen in 94 of 122 samples, and this appears more clearly in samples below the basal thrust. K_{min} orientations do not exhibit any regular variation (Fig. F91A). A very weak correlation exists between the degree of anisotropy, P_j, and the bulk susceptibility (Fig. F91B), and no preference is observed for a specific magnetic anisotropy shape parameter (Fig. F91C).

Magnetic mineralogy

Thermal demagnetization of Hole BT1B samples reveals several magnetic laboratory unblocking temperatures, with a group at 50°–200°C, a large group at 500°–580°C, and some at 580°–690°C. These ranges in laboratory unblocking temperatures are consistent with several possible minerals carrying remanence: goethite at low temperature, titanomagnetite to pure magnetite at moderate temperature, and maghemite and hematite at high temperature. In some samples, particularly from the metamorphic sole rocks deeper than 285 m, unblocking at 300°–350°C is evident, suggesting the presence of another magnetic phase, possibly titanomagnetite or pyrrhotite. The amount of remanence remaining after the 590°C temperature step varies between samples, though ~25% of samples retain more than half their magnetization. In the few samples of listvenites that were AF demagnetized, some retained approximately half their remanence after AF demagnetization at 180 mT. This indicates significant quantities of one or more high-coercivity phases such as hematite or goethite.

Thermomagnetic analysis

Thermomagnetic properties were determined from 47 rock powders of both on-site samples and shipboard chemistry samples, 25 from listvenite, 16 from the metamorphic sole, and 6 from the serpentinite. Each powder weighed several hundred milligrams. Samples were analyzed in argon. Curie temperature estimates were determined using Cureval8 software. For the purposes of characterization based on thermomagnetic properties, each of the three main lithologies, listvenite, serpentinite, and metamorphic sole rocks, are described separately.

Listvenite

Thermomagnetic behavior of susceptibility for the listvenite powder samples is variable, with susceptibility magnitudes approximately one order of magnitude lower than serpentinites. Listvenite samples have distinctively irreversible heating and cooling curves, with a significant increase in susceptibility during cooling (Fig. F92). Despite some differences, similar trends in the heating curves of listvenites include a relatively constant susceptibility until ~500°C, followed by a slight increase to a small broad (Hopkinson) peak centered at ~545°–565°C, followed by a decrease up to ~600°C, after which susceptibility remains relatively constant or slightly decreases. Upon cooling from 700°C, all listvenite samples show a pronounced and abrupt increase in susceptibility below 600°C. In several samples during cooling an additional large magnitude and abrupt increase or broad peak occurs at 500°–450°C, and in other cases a small to moderate increase just below 600°C is followed by one or more increases and peaks at 500°–450°C. In all listvenite samples, the first heating and cooling run shows irreversible heating and cooling curves. Upon repeating the experiments, all listvenite samples show nearly reversible behavior during both heating and cooling and follow almost exactly the cooling curve from the first run or a very similar cooling curve shape with slightly increased susceptibility values (Fig. F92).

Serpentinite

Thermomagnetic behavior of susceptibility for serpentinite powder samples displays ferromagnetic characteristics with Curie temperature estimates of ~570°–585°C, indicative of almost pure magnetite. Similar trends in the heating curves of serpentinites include a relatively constant or slight increase in susceptibility until ~555°C, followed by an abrupt decrease until ~580°–585°C. Some of the heating and cooling curves are nearly reversible, showing an abrupt and large magnitude increase in susceptibility upon cooling just below 600°C. A few samples show irreversible behavior with cooling paths including both the larger magnitude increase in susceptibility below 600°C and either a small or broad increase in susceptibility centered on ~350°C (Fig. F92).

Metamorphic sole

Thermomagnetic behavior of susceptibility for metamorphic sole powders exhibit varied ferromagnetic properties or almost entirely paramagnetic characteristics in some of the deepest samples. In the ferromagnetic cases, Curie temperature estimates are ~560°–585°C, indicative of nearly pure magnetite or possibly low-titanium titanomagnetite. The heating and cooling curves are irreversible, with cooling path shapes generally similar to the heating paths, but always higher susceptibility upon cooling (Fig. F92). Deeper metamorphic sole rock samples show more varied behavior. In several cases, similar to the ferromagnetic behavior described for listvenites, samples show a small or moderate peak in susceptibility centered ~550°–560°C and an irreversible cooling curve with a sharp increase in susceptibility below 600°C and a gradual decline in susceptibility back to room temperature. Some of deepest metamorphic sole samples display either a very gentle decrease in susceptibility throughout the entire heating path or a gentle decrease with a very small break to steeper slope either at 475°–500°C or 550°–600°C. Cooling curves are always higher susceptibility than heating, and they display varied gradual or abrupt increases in susceptibility below 600°C followed by either gradual increase to room temperature or include a broad convex upward curve or peak centered at ~350°–400°C (Fig. F92).

Physical properties

Physical properties of rocks from Hole BT1B were characterized through a series of measurements on whole-round sections, section halves, section-half pieces, and discrete samples (see **Physical properties** in the **Methods** chapter). All whole-round sections were run through the XCT scanner and then were measured for *P*-wave velocity (V_P), gamma ray attenuation (GRA) bulk density, magnetic susceptibility (MS), noncontact electrical resistivity (NCR), and natural gamma radiation (NGR) data with the Whole-Round Multisensor Core Logger (MSCL-W). We also measured point magnetic susceptibility (MSP) and reflectance spectroscopy and colorimetry (RSC) with the Split-Half Multisensor Core Logger (MSCL-C), and line scan color images with calculated RGB value with the Imaging Multisensor Core Logger (MSCL-I) on the cut surface of archive halves. Thermal conductivity was measured on section-half pieces. Compressional wave (*P*-wave) velocity was measured on minicube samples (2 cm × 2 cm × 2 cm), and density and porosity were measured on minicubes and some irregular shape discrete samples. The rock names reported in data tables correspond to the primary lithologies assigned by the igneous petrology team (Table T2).

Whole-round and section half measurements

A total of 401 whole-round and archive-half sections from Hole BT1B were measured. Data are summarized in supplemental Tables ST4, ST5, and ST6).

X-ray computed tomography

XCT was continuously run on all 401 whole-round core sections recovered from Hole BT1B (see **Supplementary material** > **G_XCT data**). An XCT image with XCT number represented on a color scale was generated for every section. The average XCT value for every scan slice (0.625 mm thick) was also computed, and the downhole trend can be found in Figure F93. The XCT value of a material depends on several factors such as the material's density and porosity. As a consequence, the downhole XCT trend follows closely that of GRA density. Figure F94A shows that both XCT and density are positively correlated but with different trends for the metamorphic sole lithologies (greenschist and greenstone) and the lithologies that make up the upper two-thirds of the hole (listvenite, serpentinite, and ophicarbonate). The rocks from the metamorphic sole have elevated CT numbers compared to the overlying rocks for a given density. Overall, variability in the downhole trend reflects the lithologici variation observed in Hole BT1B.

Serpentinite intervals, marked by elevated MS, low *P*-wave velocity, and low resistivity, exhibit the lowest CT numbers (~2500 to ~2800) among all lithologies observed in Hole BT1B. This reflects the porous nature of the serpentinite intervals (see **Density and porosity**) as well as the relatively low density of serpentine minerals. Ophicarbonates exhibit even lower CT numbers and densities that are likely attributable to high fracture densities. On the other hand, the greenschist and greenstone units that make up the metamorphic sole portion of Hole BT1B yield the highest CT numbers (~3600 to ~4000). Elevated CT numbers within this interval are due to the presence of high molecular weight and high-density minerals such as epidote and chlorite and/or possibly due to the different degree of metamorphism. The origin for this density gap is unclear and needs further investigation. Overall, the XCT data, in accordance with other physical property tools, distinguished two different intervals within the metamorphic sole. The second interval, starting at ~230 m, is marked by a distinct increase in CT number (~3700 to ~4000) that corresponds to a steep drop in NGR, an increase in GRA density, and a reduced number of intervals with elevated MS. This interval is marked by large amounts of epidote and amphibole, both of which are dense and may cause the high CT number.

The CT number in the listvenite intervals ranges from ~2900 to ~3500. Specimens of minerals that commonly make up listvenites (quartz [CT number = ~2800]), magnesite [~2950], dolomite [~3350], and calcite [~3650]) were acquired and scanned on board for references on CT number (Fig. **F95**). Variability in the CT number observed from listvenite intervals suggests variations in the abundance of these minerals with no systematic differences between the differently colored listvenites (see Fig. **F94B**). Figure **F96** provides an example to illustrate these variations at the section scale. In Section 68Z-2, the thick white vein has a low CT number, which probably indicates quartz + magnesite composition. The host rock, on the other hand, shows higher and more variable CT numbers from ~2800 to ~3200, which suggests that it is made up of a quartz + magnesite + dolomite assemblage. There is no distinct change in the CT number as the listvenite transitions from green to red, suggesting that the mineral modal abundance likely remains the same across this color transition. Another view of the overall XCT and density trends in the listvenite units can be seen in Figure **F94B**, which also plots CT number determined from the individual mineral specimens. A pure magnesite vein from Section 50Z-1 identified through XRD is also plotted for comparison. The majority of the listvenites plot between the values determined from the quartz and magnesite specimens, suggesting compositions dominated by these two minerals. Close to the basal thrust (~30 m above the thrust), listvenite and serpentinite intervals have CT numbers higher than their counterparts from the shallower portion of the hole. Some of the elevated CT values might be due to the presence of significant dolomite, as some samples plot close to the dolomite specimen. This zone also corresponds to intervals with low thermal conductivity (see **Thermal conductivity**) that might also be attributable to dolomite. Dolomite also has an irregular but perhaps generally increasing abundance in these sections as determined through XRD (see **Host rock**).

However, 7 samples within 15 m of the basal thrust have CT numbers higher than the dolomite analyzed on board. Based on the observed and theoretical correlations between density, mean atomic weight, and CT number, we hypothesis that these high CT values are associated with some degree of Fe substitution in carbonate minerals (ankerite: Fe substitution in dolomite, end-member density = ~3.05 tons/m^3 and/or siderite, Fe-substitution in magnesite, end-member density = 3.96 tons/m^3). Further investigation of compositional effects (e.g., solid solutions, hematite inclusions) on the CT values would be needed for an accurate assessment of the mineralogy as well as the mineral modal abundance of different listvenite intervals.

Colorimetry

Color data acquired from reflectance spectroscopy and high-resolution images can provide insights into the variability of different lithologic units recovered from Hole BT1B. RSC data were obtained from all archive half-sections using the MSCL-C. Lightness (L*) and chromaticity (a* and b*) variables were generated from the reflected light collected through the spectrophotometer at 2 cm intervals. High L* value indicates lighter colors: 0 represents black and 100 white. Directions toward more +a* denote a shift toward red from green, whereas +b* depicts a shift toward yellow from blue.

High-resolution (100 pixels/cm) half-section images produced by the MSCL-I provide an alternative source of color data. RGB values, corrected from a reference gray color, were extracted from every section image. Average RGB pixel intensities were generated from the inner 3 cm of the section at 1 mm interval. Color parameters (redness, greenness, blueness) were generated from the contribution of red, green, and blue values to the total intensity. Both the color spectrophotometer and line scan imager provide complementary color information. Low total RGB intensity depicts dark materials analogous to low L* from the color spectrophotometer, and higher values represent lighter materials. Like the RGB values, the chromaticity variables a* and b* are another color space representation. The line scan imager provides a fast method of generating color data at millimeter-scale resolution. On the other hand, the color spectrophotometer was set to scan at 2 cm intervals given the time constraints. Unlike the imager, however, the spectrophotometer takes specular reflection into account and provides a more accurate representation of the visual appearance of the material.

Figure F96 provides an example of how these color parameters trend at a section scale. The white veins in Section 68Z-2 are characterized by a peak in RGB intensity and the L* parameter. a* and redness increase, whereas greenness, total intensity, and L* decrease as the section transitions from green to dark red listvenite. A downhole plot of color parameters for Hole BT1B can be seen in Figure F93. XY plots of color parameters together with lithologic information can be seen in Figure F97. The upper two-thirds of Hole BT1B is dominated by listvenite units, and the variability in the color observed from these lithologic units is reflected in the variations in their color parameters. The upper 90 m is dominated by dark red listvenites, whereas the 100–190 m interval is marked by alternating green and red listvenite of various shades. This interval is also marked by high RGB intensities, corresponding to the presence of white veins and the occurrence of bright green listvenites. Serpentinite, greenschist, and greenstone units exhibit similar high greenness, low redness, and low total intensities. Dark red and orange listvenite overlap in redness, greenness, and blueness values, but the latter is slightly more intense. Overall, chromaticity parameters correspond closely with macroscopic descriptions. Accordingly, L*a*b* or RGB data extracted from images presents an opportunity to quantify macroscopic observations. Ultimately, if appropriate images are available, these types of data could be used to compare different listvenite units from different localities and establish preliminary lithologic units prior to detailed observation.

Compressional wave velocity

P-wave velocity measured by MSCL-W is correlated with GRA density as expected, although the MSCL-W velocities are slightly lower than the values of discrete samples (see **Discrete sample measurements**) in the whole-round section, perhaps due to the dry condition of the core during scanning. The main serpentinite zones (Sections 38Z-3 and 44Z-4) have lower velocity than other intervals. The MSCL-W data are summarized in the downhole plot in Figure F98, together with the discrete sample measurements. Those data are well correlated with each other as well as with the lithology and/or the weathering state of the Hole BT1B cores.

Gamma ray attenuation density

GRA density is estimated assuming a grain density of 2.7 g/cm^3 and a pore water density of 1.024 g/cm^3. The GRA densities of the main serpentinite zones are generally lower than other intervals in Hole BT1B, in line with the discrete sample measurements.

Electrical resistivity

NCR data generally indicate that the cores from Hole BT1B are very resistive. Most are greater than or equal to the highest measurable value (700 Ω·m). Several intervals are less resistive (e.g., the main serpentinite zone [Sections 38Z-3 to 44Z-4] and highly weathered zones [Section 21Z-1]). These less resistive intervals are probably due to the relatively high abundance of conductive phases, such as hematite.

Natural gamma radiation

NGR is generally low (<1 counts/s [cps] on average) in the uppermost 196 m of Hole BT1B, above the basal thrust, except in a few sections where narrow intervals or veins display significantly higher counts (up to ~8 cps) (Fig. F98), and increases to 38 cps at and below the basal thrust. Remarkably, NGR gradually decreases with depth over ~40 m from the basal thrust to values <5 cps.

Magnetic susceptibility

Magnetic susceptibility was measured on both the MSCL-W with a 80 mm loop sensor (MS), and the MSCL-C with a contact sensor probe (MSP).

Both linear and logarithmic scales of MS and MSP values are shown in the downhole plots (Fig. F98). Base MS is generally low, <100 × 10^{-5} SI, both in MS and MSP (see supplemental Tables ST4, ST5) and high in the main serpentinite zones between Sections 38Z-3 and 44Z-4, and between 73Z-3 and 75Z-1.

The intervals 19Z-1, 65 cm (38.60 m [Chikyu adjusted depth [CAD]), to 19Z-4, 51 cm (39.12 m CAD); 20Z-4, 0 cm (42.25 m CAD), to 21Z-2, 94 cm (44.04 m CAD); and around 61Z-1 (145 m CAD) also show higher and variable MS. These are probably caused by the presence of highly weathered fragmented vein/breccia with abundant hematite and goethite. The interval below the basal thrust also shows high and variable MS.

Discrete sample measurements

Density and porosity

Bulk density, grain density, and porosity were calculated from measurements on 118 cubic (2 cm × 2 cm × 2 cm) and 3 irregular shape samples taken from the working half sections from Hole BT1B (Tables **T15**, **T16**; Figs. **F98**, **F99**). Average bulk and grain densities of cube samples from listvenite are 2.86 and 2.92 g/cm^3, respectively. The porosity of cube samples generally ranges 0.32%–6.8% (mean = 2.9%). In Hole BT1B, the cube samples were taken from relatively homogeneous intervals with no cracks or veins. Noncubic irregular shape samples were also measured for density and porosity. Highly weathered intervals were also measured for density and porosity (Table **T16**; e.g., 19Z-3, 21–23 cm, and 21Z-1, 4–6 cm; Fig. **F98**). The highly weathered samples (e.g., 21Z-1, 4–6 cm; Fig. **F100**) show high porosity (as high as 21.3%) and lower bulk density (as low as 2.56 g/cm^3) and grain density (2.72 g/cm^3). Serpentinite and ophicarbonate samples have low bulk and grain density (maximum = 2.57 g/cm^3, minimum = 2.31 g/cm^3, average = 2.5 g/cm^3) and grain density (maximum = 2.78 g/cm^3, minimum = 2.65 g/cm^3, average = 2.7 g/cm^3).

Bulk density of Hole BT1B listvenite samples roughly correlates with porosity; lower densities correspond to higher porosities (Fig. **F98A**). Those values are comparable to the gabbroic samples from Holes GT1A and GT2A (see the Physical properties sections in the **Site GT1** and **Site GT2** chapters) (Fig. **F98**) and hence are also similar to gabbroic rocks from Hess Deep (IODP Expedition 345; Gillis et al., 2014). This suggests that it may be difficult to distinguish between gabbroic rocks and highly carbonated peridotite using density and/or porosity. Serpentinite and ophicarbonate show low density and higher porosity compared to listvenites (Fig. **F98**). The observed densities are comparable to the serpentinite cores from other ocean drilling expeditions (e.g., ODP Leg 209) and slightly lower than the reference serpentinite value of 2.56 g/cm^3 (Christensen, 1996).

Density and porosity do not have a clear correlation with the color differences of listvenite (Fig. **F98**).

P-wave velocity

P-wave velocity was measured on 104 cube samples along the three principal directions *x*, *y*, and *z* in the CRF. Results are listed in Table **T16** and plotted in Figures **F97**, **F98**, and **F99**. *P*-wave velocity ranges 3.46–7.28 km/s (average = 6.17 km/s). Higher velocities are observed in the listvenite samples, where the maximum velocity = 7.28 km/s and minimum = 5.44 km/s (average = 6.43 km/s). In contrast, serpentinite and ophicarbonate samples (Sections 38Z-4 through 44Z-4) show significantly lower velocity (as low as 3.46 km/s). Greenschists below the basal thrust have relatively high velocity, 4.94–6.58 km/s (average = 5.97 km/s). The apparent anisotropy varies 0%–31%; it is generally low (mean = 5.7%). As detailed in the **Methods** chapter, the precision of our V_P measurements is on the order of 1.8%. Hence, the lowest measured apparent anisotropies should be treated with caution.

Results for Hole BT1B samples are plotted in Figure **F99**, together with V_P and density measurements from Holes GT1A and GT2A and the data for serpentinites from the Mid-Atlantic Ridge 15°20′N Fracture Zone (Ocean Drilling Program [ODP] Leg 209; Kelemen et al., 2004). V_P values of listvenite from Hole BT1B are similar to those of the gabbros from Holes GT1A and GT2A and show a weak correlation between density and velocity. Measured velocities at room pressure also show a weak inverse correlation with porosity (Fig. **F98A**). There is no obvious correlation between sample V_P and the color of the listvenite samples (Figs. **F98**, **F99**).

There are two different relationships between *P*-wave velocity and porosity in the Hole BT1B cube samples. Listvenite and some greenschist samples show similar trends to the gabbros from Holes GT1A and GT2A. However, some greenschist and greenstone samples show an inverse relationship similar to that of the serpentinite from the Mid-Atlantic Ridge 15°20′N Fracture Zone (Fig. **F99**; Hole 1274A, ODP Leg 209).

Thermal conductivity

A total of 77 measurements were taken on 75 core pieces from the working halves from Hole BT1B (Table **T17**; Figs. **F101**, **F102**). Thermal conductivity ranges 3.89–6.38 W/m·K (average = 5.16 W/m·K) for listvenite samples, 2.59–2.69 W/m·K (average = 2.64 W/m·K) for serpentinite samples, and 2.49–2.43 W/m·K (average = 2.83 W/m·K) for greenschist and greenstone samples. Mean value for all samples = 4.15 W/m·K. The standard deviation of the average 6–10 measurements for each piece ranges 0.00–0.68 W/m·K. Thermal conductivity of the listvenite samples is significantly higher than that of all other lithologies from Hole B1B and all gabbroic rock samples from Holes GT1A and GT2A cores (average = 2.58 and 2.39 W/m·K, respectively) and similar or slightly higher than that of a typical peridotite (4.7 W/m·K; Horoman lherzolite). These high values are due to the high thermal conductivity of the constituent minerals in listvenite (e.g., quartz = 6–10, magnesite ~7.6; magnetite ~4.6, and hematite ~12.4 W/m·K; Clauser and Huenges, 1995). On the other hand, thermal conductivity of the samples of serpentinite, greenschist, and greenstone from Hole BT1B have values similar to those of gabbroic samples from Holes GT1A and GT2A. There is a systematic gradient in thermal conductivity in listvenite at the top of the hole, from ~6 W/m·K near the surface to ~5 W/m·K at 40 m CAD. The listvenite samples taken from near the basal thrust at 190–196 m depth show slightly lower thermal conductivity (3.90–4.38 W/m·K) than shallower samples. This could indicate high Ca contents in the listvenite near the basal thrust because calcite (~3.2 W/m·K) and dolomite (~4.8 W/m·K) have lower thermal conductivities than magnesite and quartz (Clauser and Huenges, 1995). Thermal conductivity of serpentinite from Hole BT1B is similar to that of abyssal serpentinite cores from Hole 1274A, ODP Leg 209, Mid-Atlantic Ridge 1520′N Fracture Zone (Kelemen et al., 2004).

Imaging spectroscopy

All archive sections of core recovered from Hole BT1B were imaged during the first week of Leg 2 at 250–260 µm/pixel. This effort yielded 414 sets of images (visible-near infrared + shortwave infrared) and 2.545 TB of data. This imaging occurred over 6 days. Thus far, a quick look at only a few images yields a variety of mineral identifications, including dolomite, magnesite, calcite, serpentine, Si-OH-bearing phases (quartz and an amorphous hydrated silica), illite (fuchsite), kaolinite, epidote, and iron oxides. Quartz, while common in this core, is transparent at the wavelengths measured by this instrument. An absorption feature due to Si-OH is often present in spectra of pure quartz because of minor H_2O within quartz (Aines and Rossman, 1986), but that feature is generally not observable when quartz is mixed with other minerals with stronger absorption features, such as magnesite and dolomite, as is often the case here. More minerals will almost certainly be identified through a complete analysis of all images that will occur over the next year. Imaging of the metamorphic rocks below the listvenite reveals significant compositional variation and structural features. Future work will include systematic mapping of minerals identified through imaging spectroscopy within all sections of Core BT1B. Results of preliminary single image analyses are shown within other sections of this chapter as part of the descriptions of various aspects of this core, allowing for comparison between these and other measurements. While more analysis is required, imaging spectroscopy rapidly provides insight into mineral distinctions not observable by eye.

Downhole measurements

Downhole logging and hydrogeological testing operations and acquisition parameters for each borehole are available in Table T56 and T57 in the **Methods** chapter. Raw and processed data from all downhole logs are available in **Supplementary material** > **L_Wireline Logging** and in the ICDP Oman Drilling Project online data repository.

References

Aines, R.D., and Rossman, G.R., 1984. Water in minerals? A peak in the infrared. Journal of Geophysical Research: Solid Earth, 89(B6), 4059-4071.

Aines, R.D., and Rossman, G.R., 1986. Relationships between radiation damage and trace water in zircon, quartz, and topaz. American Mineraologist, 71(9-10):1186-1193.

Al-Aasm, I.S., Taylor, B.E., and South, B., 1990. Stable isotope analysis of multiple carbonate samples using selective acid extraction. Chem. Geol., 80:119-125.

Burns, R.G., 1993. Mineralogical Applications of Crystal Field Theory, second ed. Cambridge University Press, Cambridge.

Christensen, N.I., 1996. Poisson's ratio and crustal seismology. Journal of Geophysical Research, 101:3139-3156. https://doi.org/10.1029/95JB03446

Clauser, C., and Huenges, E., 1995. Thermal conductivity of rocks and minerals. Rock physics and phase relations: a handbook of physical constants, 105-126.

de Obeso, J., Cai, Y., Kelemen, P., and the Oman Drilling Project Phase 1 Science Party, 2018. Strontium isotope profile of Oman Drilling Project Hole BT1B. AGU Fall Meeting Abstracts: V11B-08.

de Obeso, J.C., and Kelemen, P.B., 2018. Fluid rock interactions in residual mantle peridotites overlain by shallow oceanic limestones: Insights from Wadi Fins, Sultanate of Oman. Chem. Geol., 498:139-149.

de Obeso, J.C., Kelemen, P.B., Manning, C.E., Michibayashi, K., Harris, M., and the Party ODPPS, 2017. Listvenite formation from peridotite: Insights from Oman Drilling Project Hole BT1B and preliminary reaction path model approach. AGU Fall Meeting Abstracts: 328802.

Falk, E.S., and Kelemen, P.B., 2015. Geochemistry and petrology of listvenite in the Oman Ophiolite: Complete carbonation of peridotite during ophiolite emplacement. Geochim. Cosmochim. Acta, 160:70-90.

Feinberg, H., Horen, H., Michard, A., and Saddiqi, O., 1999. Obduction related remagnetization at the base of an ophiolite: Paleomagnetism of the Samail nappe lower sequence and of its continental substratum, southeast Oman Mountains. Journal of Geophysical Research: Solid Earth, 104(B8):17703-17714.

Gee, J., Staudigel, H., Tauxe, L., Pick, T., and Gallet, Y., 1993. Magnetization of the La Palma seamount series: Implications for seamount paleopoles. Journal of Geophysical Research: Solid Earth, 98:11743–11767.

Gillis, K.M., Snow, J.E., Klaus, A., and the Expedition 345 Scientists, 2014. Proceedings of the Integrated Ocean Drilling Program, 345: College Station, TX (Integrated Ocean Drilling Program). https://doi.org/10.2204/iodp.proc.345.2014

Godard, M., Bennett, E., Carter, E., Kourim, F., Lafay, R., Noël, J., Kelemen, P.B., Michibayashi, K., Harris, M., and the Party ODPPS, 2017. Geochemical and Mineralogical Profiles Across the Listvenite-Metamorphic Transition in the Basal Megathrust of the Oman Ophiolite: First Results from Drilling at Oman Drilling Project Hole BT1B. 328591.

Godard, M., Jousselin, D., Bodinier, J.-L., 2000. Relationships between geochemistry and structure beneath a palaeo-spreading centre: a study of the mantle section in the Oman ophiolite. Earth Planet. Sci. Lett., 180:133-148.

Hanghoj, K., Kelemen, P., Hassler, D., Godard, M., 2010. Composition and genesis of depleted mantle peridotites from the Wadi Tayin massif, Oman ophiolite. Major and trace element geochemistry, and Os isotope and PGE systematics. J. Petrol., 51(1-2):201-227. https://doi.org/10.1093/petrology/egp077

Kelemen, P., de Obeso, J.C., Manning, C., Godard, M., Bach, W., Cai, M., Choe, S., Coggon, J., Ellison, E., Eslami, A., Evans, K., Harris, M., Kahl, W.-A., Matter, J., Michibayashi, K., Okazaki, K., Pezard, P., Teagle, D., Templeton, A., and Team OS, 2019. Peridotite alteration in OmanDP cores. Geophysical Research Abstracts, 21:EGU2019-17259.

Kelemen, P.B., Kikawa, E., and Miller, D.J., et al., 2004. Proc. ODP, Init. Repts., 209: College Station, TX (Ocean Drilling Program). https://doi.org/10.2973/odp.proc.ir.209.2004

Kelemen, P.B., Manning, C.E., 2015. Reevaluating carbon fluxes in subduction zones, what goes down, mostly comes up. Proc. Nat. Acad. Sci., 112:E3997-E4006. https://doi.org/10.1073/pnas.1507889112

Kelemen, P.B., and Manning, C.E., 2017. Carbonation and decarbonation of oceanic plates and the mantle wedge: Implications for the subduction zone carbon cycle. Deep Carbon Observatory Meeting, St. Andrews, Scotland, March 2017.

Lafay, R., Godard, M., Beinlich, A., Harris, M., Kelemen, P., Michibayashi, K., and the Party ODPPS, 2019. Mantle rock carbonation atop the Samail ophiolite metamorphic sole (Oman DP Hole BT1B): The importance of inherited petrography during large scale metasomatism. Geophysical Research Abstracts, 21:EGU2019-13716.

Lippard, S.J., Shelton, A.W., and Gass, I.G., 1986. The ophiolite of northern Oman. Geological Society of London Memoir, 11:178.

Luyendyk, B.P., and Day, R., 1982. Paleomagnetism of the Samail ophiolite, Oman: 2. The Wadi Kadir gabbro section. Journal of Geophysical Research: Solid Earth, 87(B13):10903-10917.

Luyendyk, B.P., Laws, B.R., Day, R., and Collinson, T.B., 1982. Paleomagnetism of the Samail ophiolite, Oman: 1. The sheeted dike complex at Ibra. Journal of Geophysical Research: Solid Earth, 87(B13):10883-10902.

Manning, C., Lu, S., Kelemen, P., and the Oman Drilling Project Phase 1 Science Party, 2018. Origin of Serpentinite and Listvenite Near the Basal Thrust of the Samail Ophiolite Recorded in Oman Drilling Project Hole BT1B. AGU Fall Meeting Abstracts: V11B-07.

Manning, C.E., Kelemen, P.B., Michibayashi, K., Harris, M., Urai, J.L., de Obeso, J.C., Jesus, A.P.M., Zeko, D., and the Party ODPPS, 2017. Transformation of serpentinite to listvenite as recorded in the vein history of rocks From Oman Drilling Project Hole BT1B. AGU Fall Meeting Abstracts: 328604.

Morris, A., Meyer, M., Anderson, M.W., and MacLeod, C.J., 2016. Clockwise rotation of the entire Oman ophiolite occurred in a suprasubduction zone setting. Geology, 44(12):1055-1058.

Nasir, S., Al Sayigh, A., Al Harthy, A., Al-Khirbash, S., Al-Jaaidi, O., Musllam, A., Al-Mishwat, A., and Al-Bu'saidi, S., 2007. Mineralogical and geochemical characterization of listwaenite from the Semail Ophiolite, Oman. Chemie der Erde, 67:213-228.

Pokrovsky, O.S., Golubev, S.V., Schott, J., 2005. Dissolution kinetics of calcite, dolomite and magnesite at 25 8C and 0 to 50 atm pCO_2. Chem. Geol., 217:239–255.

Stanger, G., 1985. Silicified serpentinite in the Semail nappe of Oman. Lithos, 18:13-22.

Takazawa, E., Okayasu, T., Satoh, K., 2003. Geochemistry and origin of the basal lherzolites from the northern Oman ophiolite (northern Fizh block). Geochemistry, Geophysics, Geosystems, 4(2). https://doi.org/10.1029/2001GC000232

Urai, J.L., Manning, C.E., Kelemen, P.B., Kettermann, M., Jesus, A.P.M., and the Party ODPPS, 2019. Multiscale structure evolution during peridotite carbonation and hydration in an oceanic subduction zone: a case study of listvenite in the Oman Ophiolite. Geophysical Research Abstracts, 21:EGU2019-10446.

Weiler, P.D., 2000. Differential rotations in the Oman ophiolite: paleomagnetic evidence from the southern massifs. Marine Geophysical Researches, 21(3-4):195-210.

Wilde, A., Simpson, L., and Hanna, S., 2002. Preliminary study of Tertiary hydrothermal alteration and platinum deposition in the Oman ophiolite. J. Virtual Explorer, 6:7-13.

Figure F1. Geological map of the MOD Mountain region showing the location of Hole BT1B.

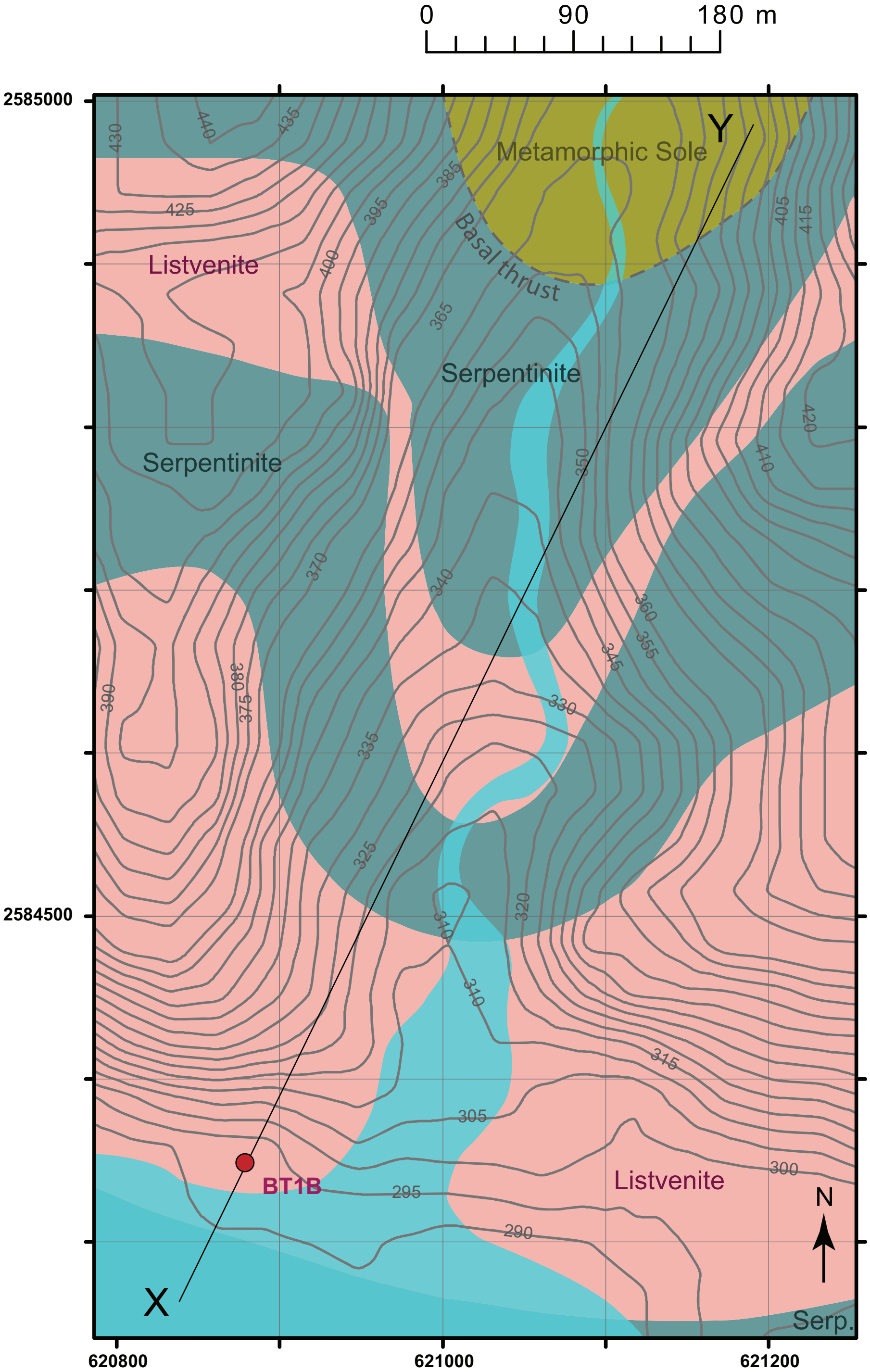

Figure F2. Cross-section through the BT1 drill site showing the depth to the basal thrust and the major lithologic subdivisions of Hole BT1B.

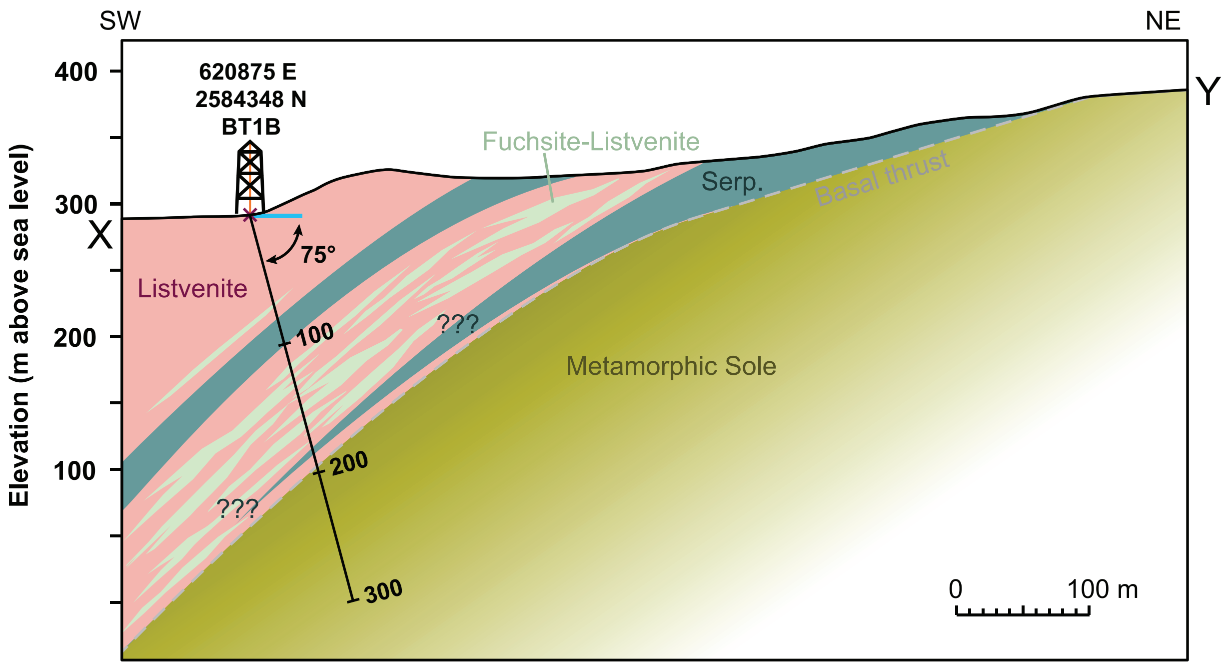

Figure F3. Proportions of major lithologic units in Hole BT1B.

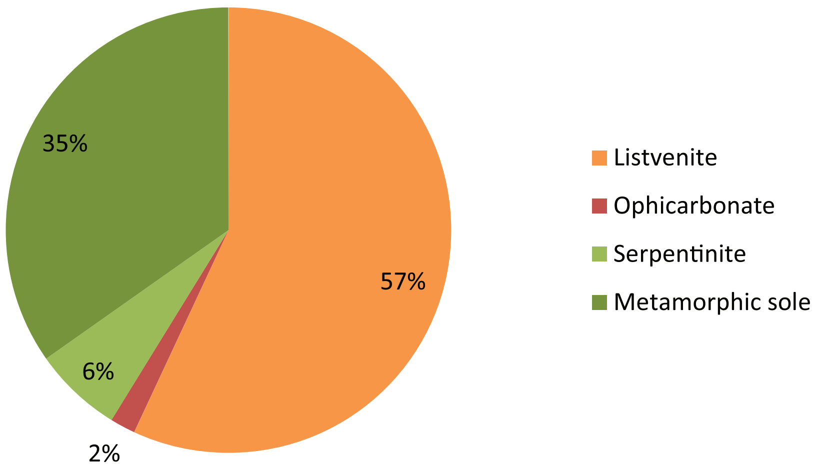

Figure F4. Principal rock types recovered, Hole BT1B.

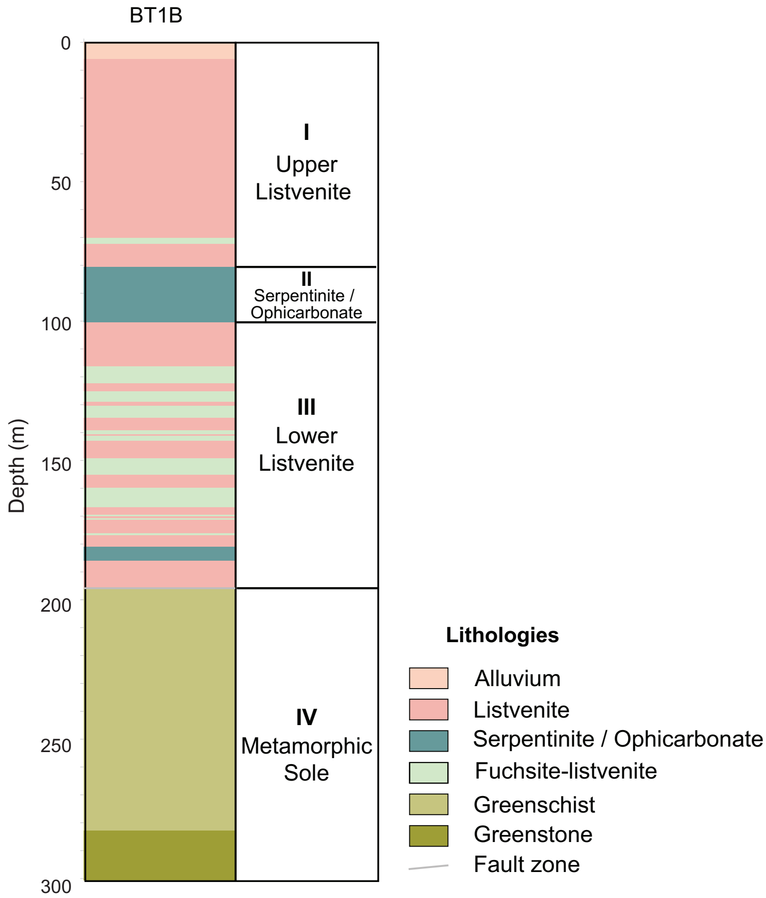

Figure F5. Characteristic listvenite host rock colors, color transitions, and rock textures. **A, C.** Sharp transitions are common between green/gray and red listvenite. **E, F, G.** Domains containing relict serpentine and/or the precursor harzburgitic mesh texture frequently occur in red (dark red, light red, orange) listvenite units. **D, H.** Dark red listvenite is representative of the majority of the listvenite units in Hole BT1B. Note the presence of (**B**, **C**) relatively large fuchsite-quartz intergrowths and (B) the potential occurrence of graphite.

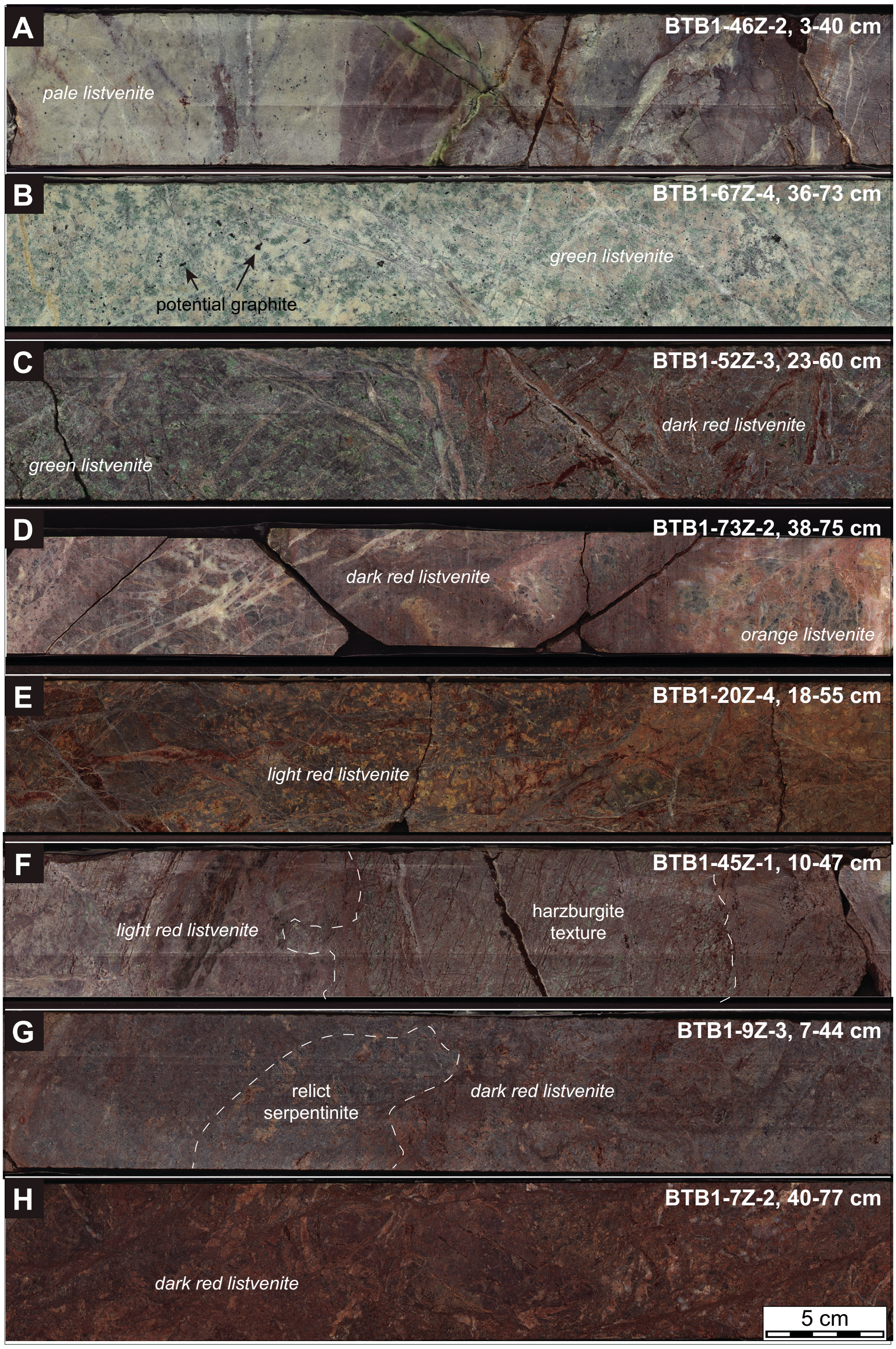

Figure F6. Nature and proportion of listvenite internal unit contact types. Most of the unit boundaries are defined by a change in host rock color, followed by contacts related to texture changes: breccia-clast proportion, structural, and vein abundance.

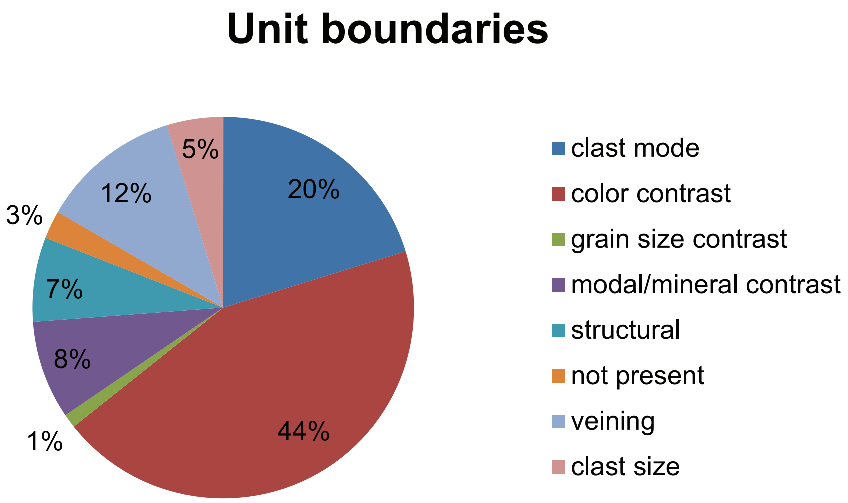

Figure F7. Relative abundances of different listvenite host rock colors. Red hues (dark red, light red, orange) dominate; green listvenites usually contain large (<1 cm) fuchsite-quartz intergrowths in a pale and sometimes dark gray matrix.

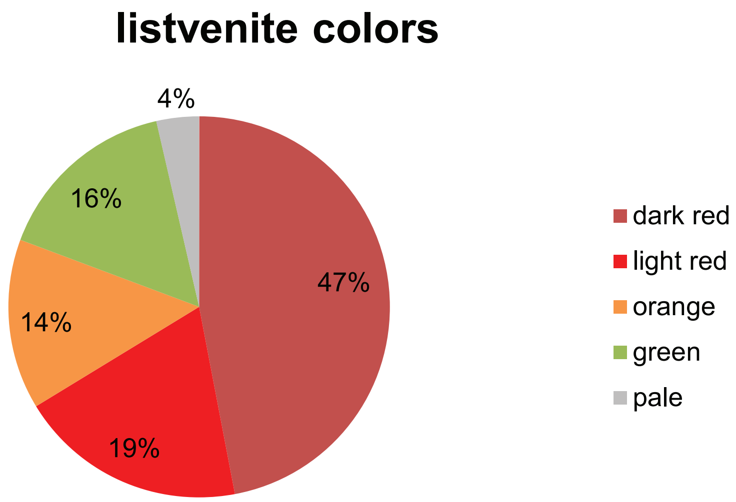

Figure F8. Smoothly cut horizontal surface of the half core (right side of image) and beveled cut surface (left area enclosed by polygon). XRF-CL scan data from this area are not accurate and were removed from the calculation of the average composition of affected intervals.

Figure F9. Core photos, short-wave infrared (SWIR) sensor map, and XRF-CL element maps. The IR mineral indicator map shows three mineral components derived from SWIR. Red = absorption feature due to Si-OH (dominantly in quartz). Carbonate minerals are also shown: blue = Mg carbonate (magnesite), green = Ca-Mg carbonate (i.e., dolomite). Note that quartz is transparent in the SWIR and can only be identified when pure. Minor H_2O producing an Si-OH absorption feature is often present in quartz, but this is difficult to discern when mixed with other minerals at the 250 µ-pixel resolution of the spectrometer (Aines and Rossman, 1984).

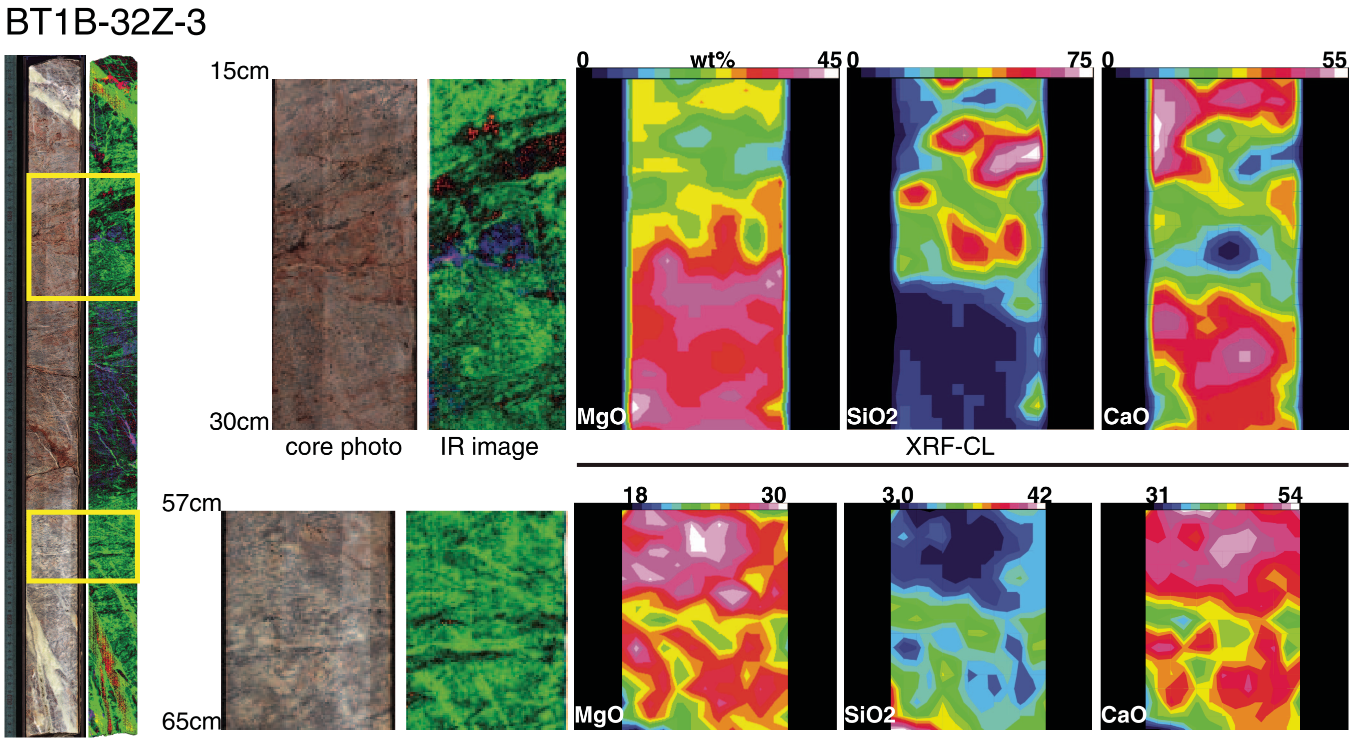

Figure F10. Core photo and XRF-CL element maps.

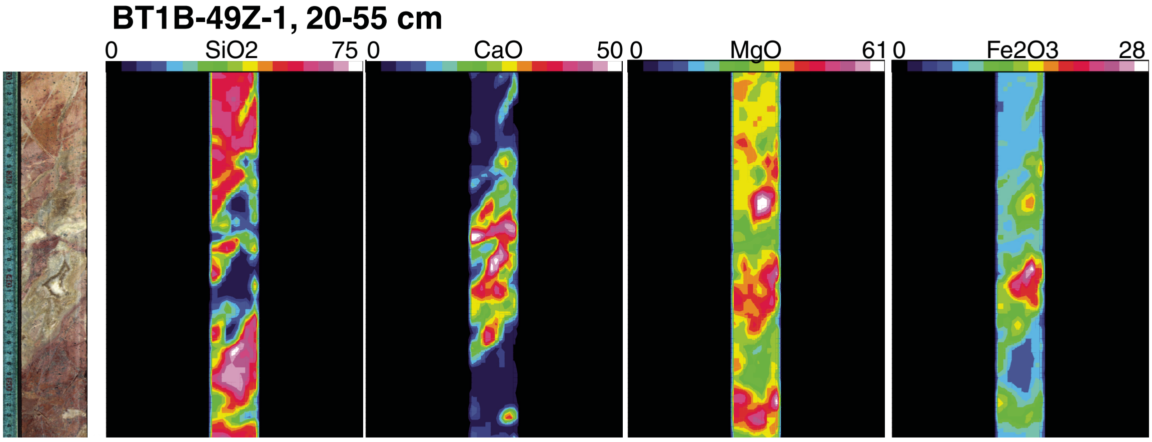

Figure F11. (**A**) Core photo, (**B**) SWIR sensor map, and (**C–F**) XRF-CL element maps. The IR map shows three mineral components at 250 µ-pixel resolution. Red = absorption features at ~2.2 and 2.35 µm, consistent with the presence of a muscovite-related mineral such as fuchsite. This parameter may also pick up some areas with an Si-OH absorption feature in a mineral such as quartz (with minor water). Carbonate minerals are also shown in green and blue: blue = Mg carbonate (magnesite), green = Ca-Mg carbonate (i.e., dolomite).

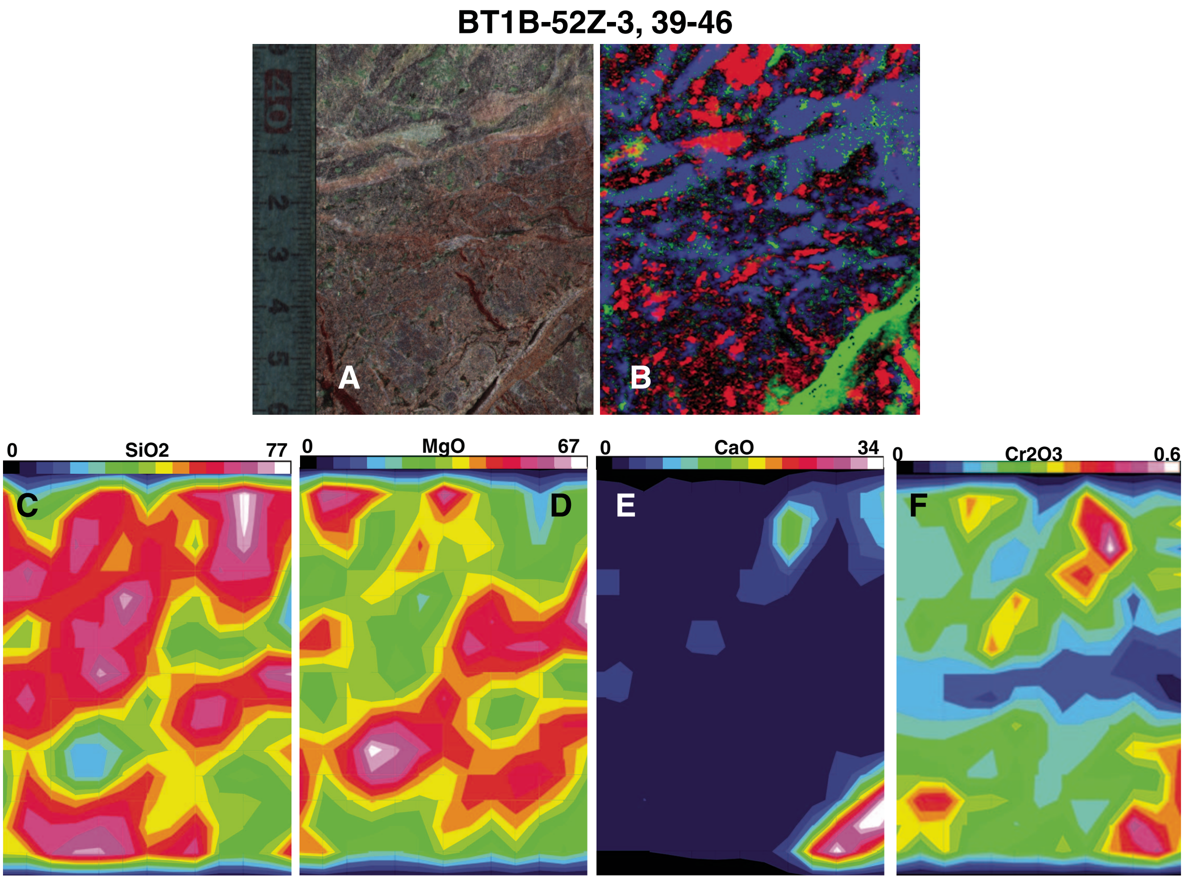

Figure F12. Carbonate (magnesite + dolomite) vs. LOI for listvenites, ophicarbonates, and serpentinites in Hole BT1B. Carbonate content is inferred from XRD characterization and semiquantitative estimation, and LOI was obtained by weight difference after sample combustion by the chemistry group.

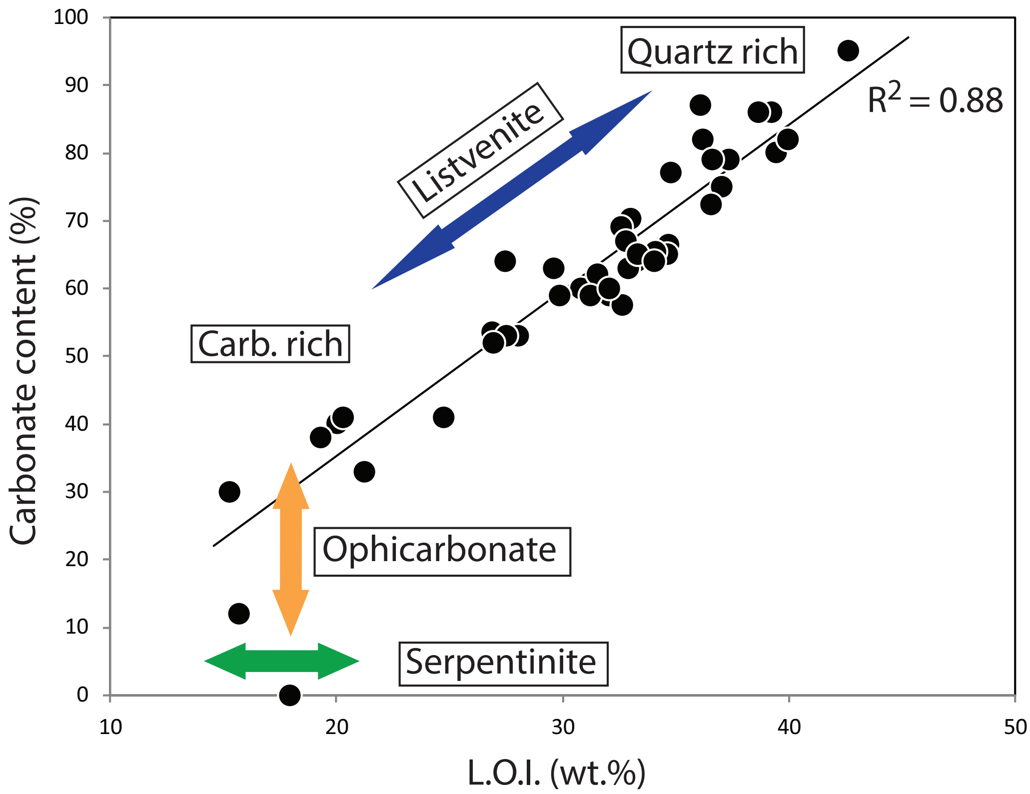

Figure F13. Relative dolomite, magnesite, and quartz in metamorphic sole rocks in Hole BT1B inferred from XRD data (red) and XRF (black) analyses of fused beads analyzed on board *Chikyu*.

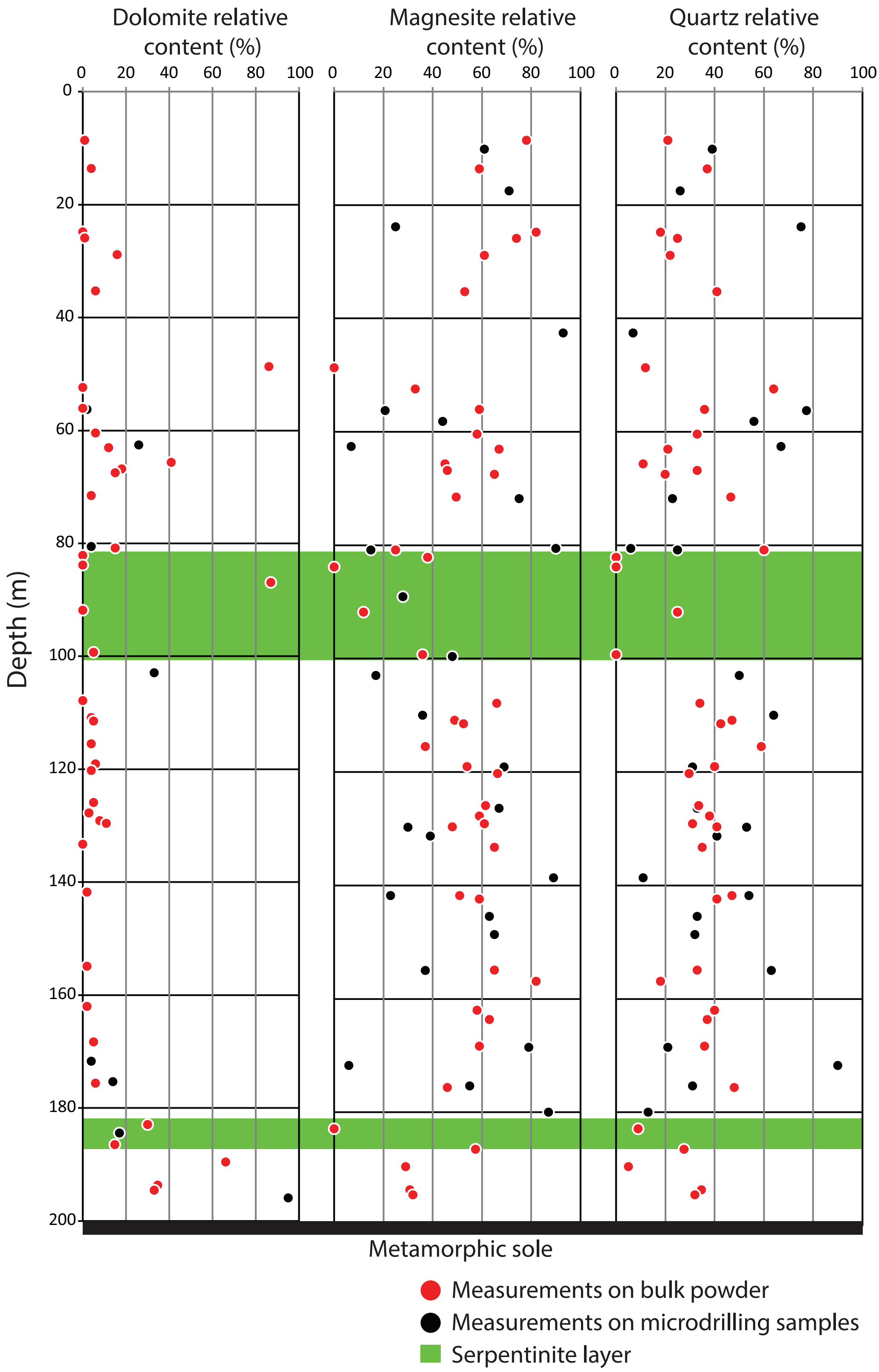

Figure F14. Core photos and XRD diffractograms for "typical" listvenites. **A, C.** Sample 11Z-2, 31–34 cm (17.35 m depth). **B, D.** Sample 61Z-4, 30–31 cm (145.50 m). These listvenite samples are ~2/3 magnesite and ~1/3 quartz + variable amounts of Fe (oxy)hydroxides. Dotted circles = XRD sample areas.

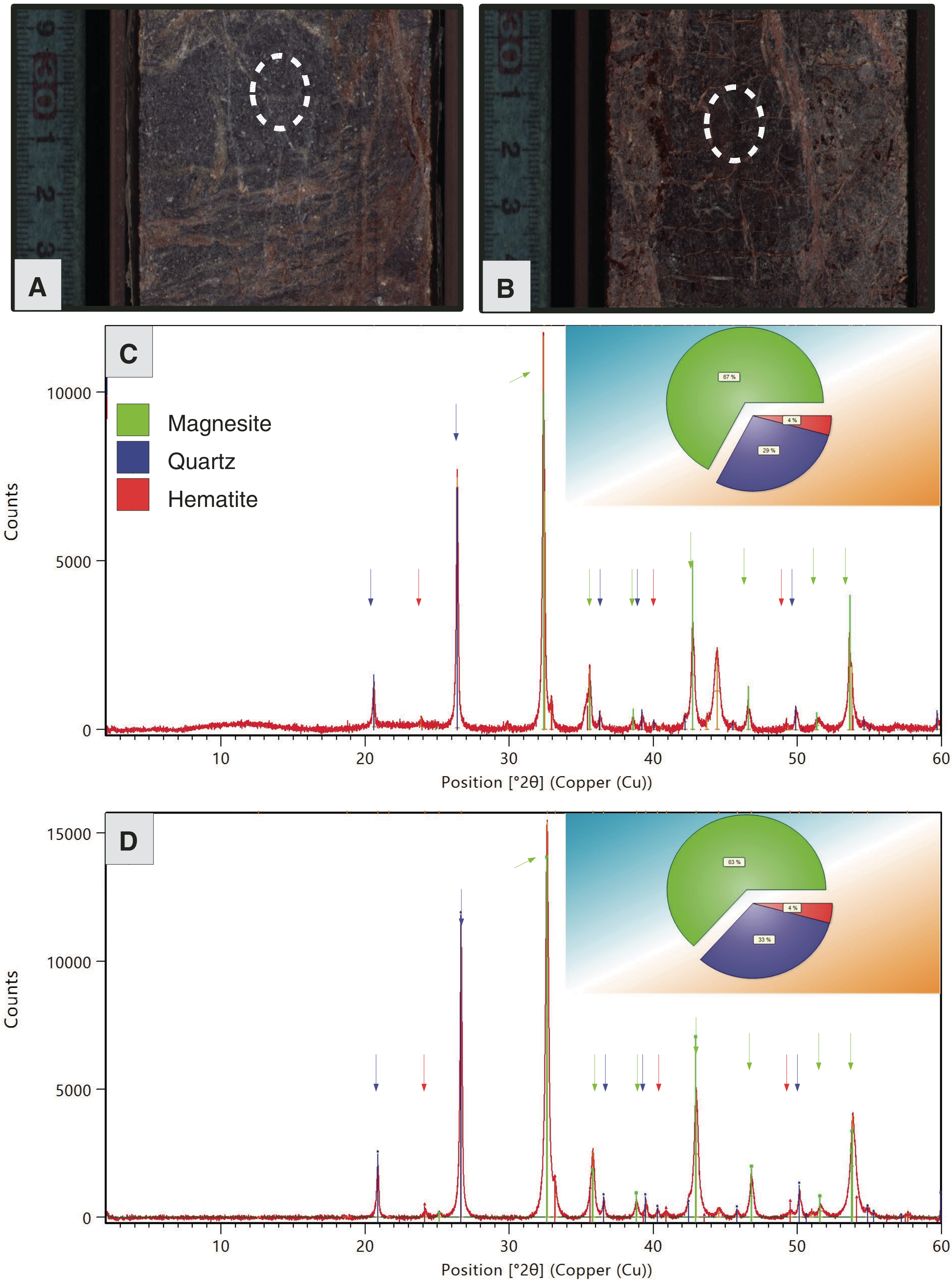

Figure F15. A, B. Sample 26Z-3, 8–12 cm. (A) Typical relics of mesh texture outlined by oxide minerals (maybe magnetite, Mag) recognizable in the carbonate (Carb) + quartz matrix. (B) Relict chromite (Chr) crystal in carbonate + quartz (Qtz) matrix. **C, D.** Backscatter electron microscope images for chromite cut by chlorite (Chl) veins (Section 73Z-2) and (D) variably replaced by magnetite (Section 26Z-3).

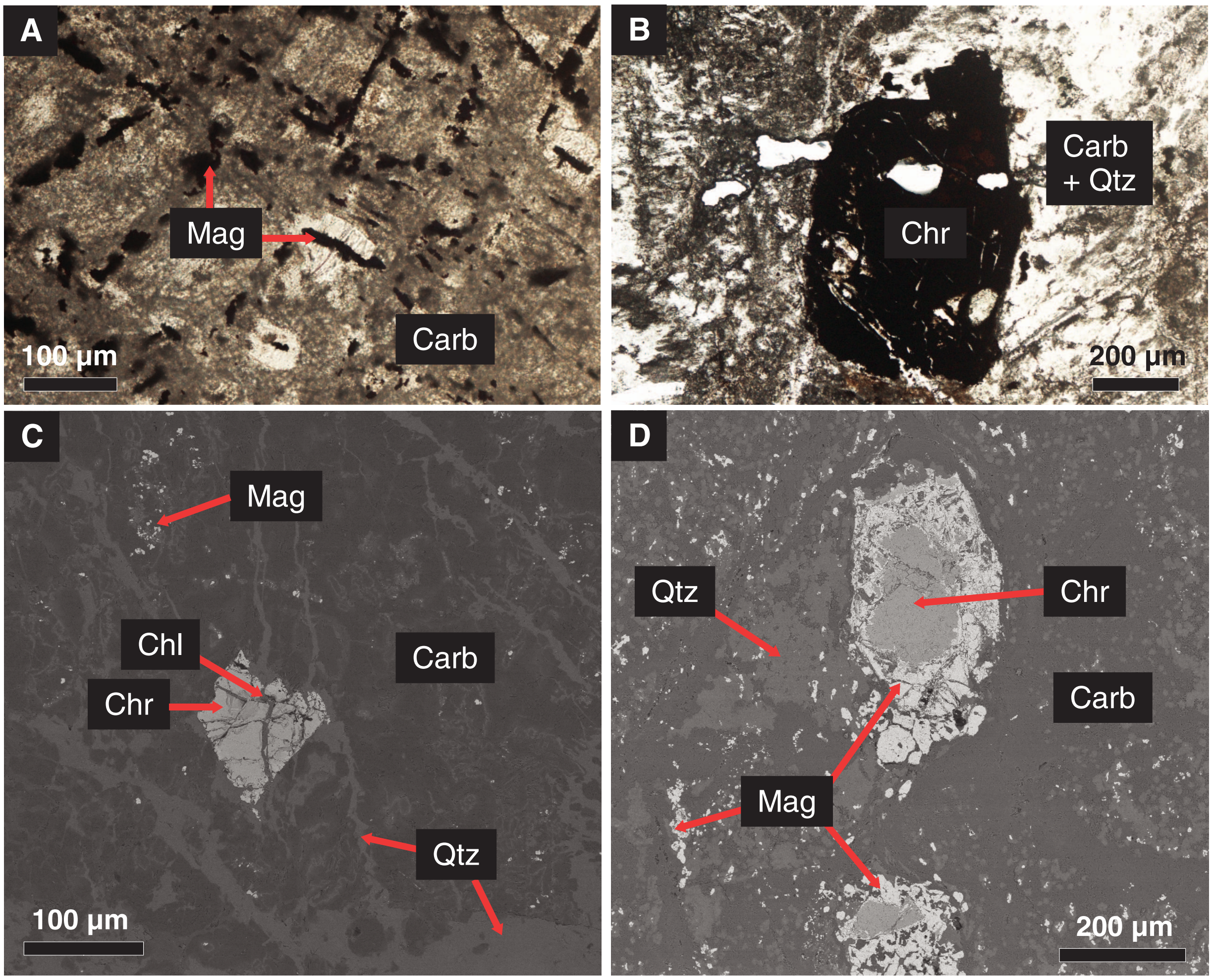

Figure F16. Typical petrographic features in fuchsite-bearing listvenite. **A.** Characteristic listvenite-bearing rock showing green spots of fuchsite in a typical dark red listvenite matrix. **B.** In thin section, fuchsite does not form discrete crystals larger than 10 µm as was initially inferred from macroscopic observation. Instead, it is a minor component in aggregates mainly composed of calcite and quartz (plane-polarized light [PPL]). The aggregates are arranged in polygonal granoblastic clusters. Red box indicates the position of inset. **C.** Detail at the rim of a quartz/carbonate assemblage with green fuchsite at the rim forming lepidoblastic aggregates.

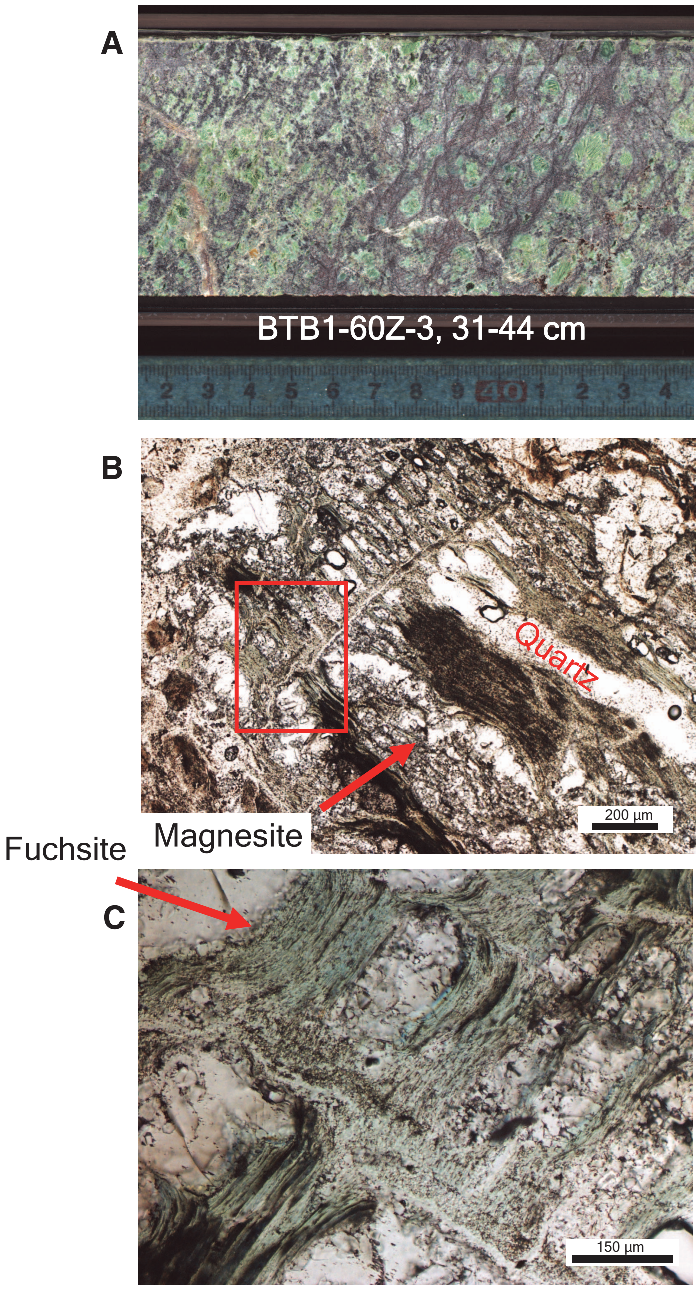

Figure F17. Relict serpentinite mesh textures observed in listvenites. **A.** Cut core surface showing listvenite with greenish patches characteristic of relics of serpentine mesh texture. **B.** Intact mesh texture visible in thin section of typical serpentinite intercalated within the listvenite horizon (PPL). **C.** Relic of a serpentinite mesh texture with serpentinite minerals still present in cataclastic listvenite (PPL).

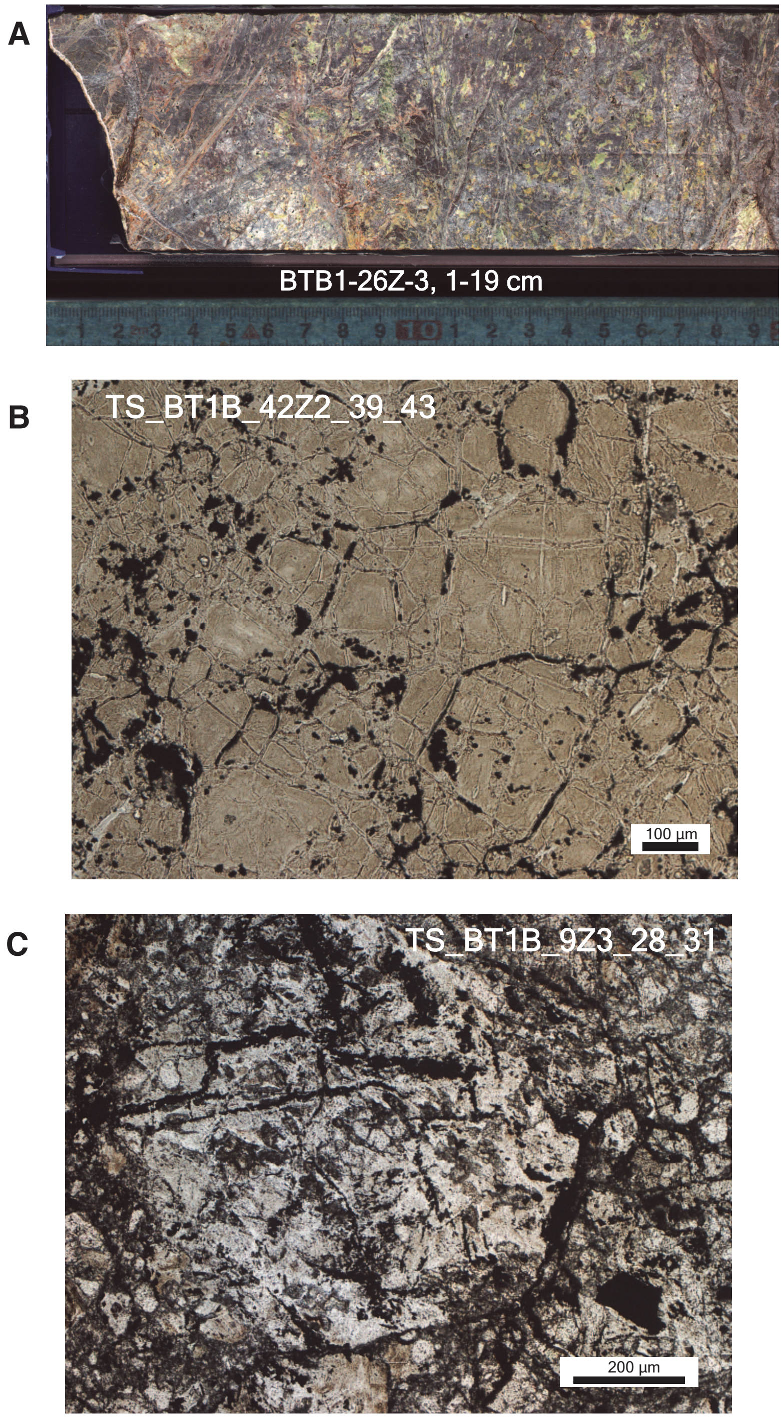

Figure F18. Relict serpentinite mesh textures with bastite, a serpentine pseudomorph after orthopyroxene, observed in listvenite. **A.** Bastite at left and relict mesh texture at right (PPL). Red box indicates the position of closeup. **B.** Bastite is associated with serpentinite mesh texture. The bastite-bearing serpentinite patch is replaced by carbonate (red arrows) from the margin as well as internally (XPL).

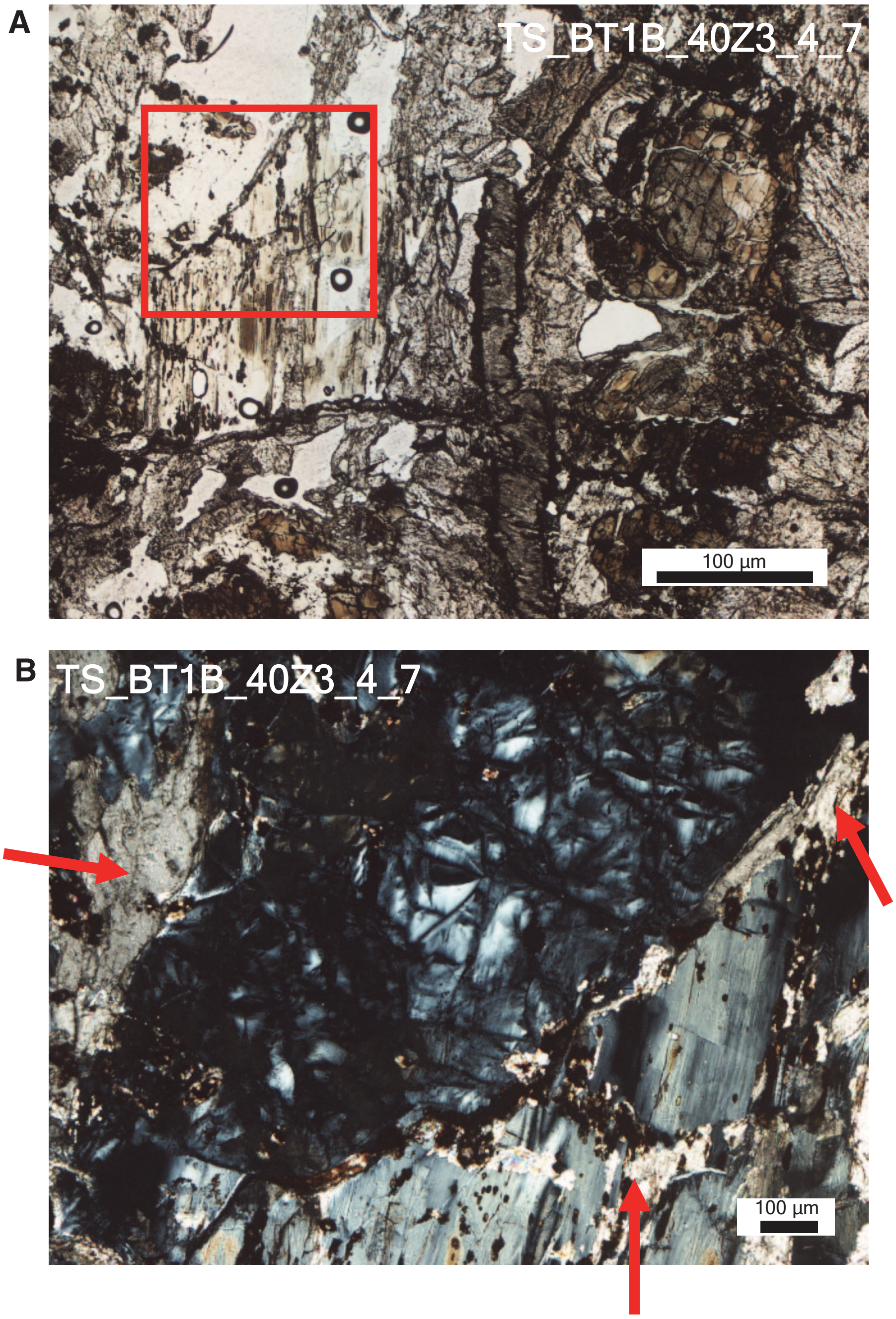

Figure F19. Relict serpentinite mesh textures observed in a listvenite showing two lithologic domains; Domain 1: partially carbonated serpentinite; Domain 2: listvenite. **A.** Whole thin section scan. **B.** Domain 1. Relict serpentinite mesh texture showing typical cells separated by trails of iron oxide. The large grain in the lower left is chromite (PPL). **C.** Domain 2. Although this sample is fully carbonated, relics of the mesh texture are still visible. Note that this domain shows foliation with aligned oxide trails and lattice-preferred orientation of carbonate crystals. The large grain in the lower left is relict chromite (PPL).

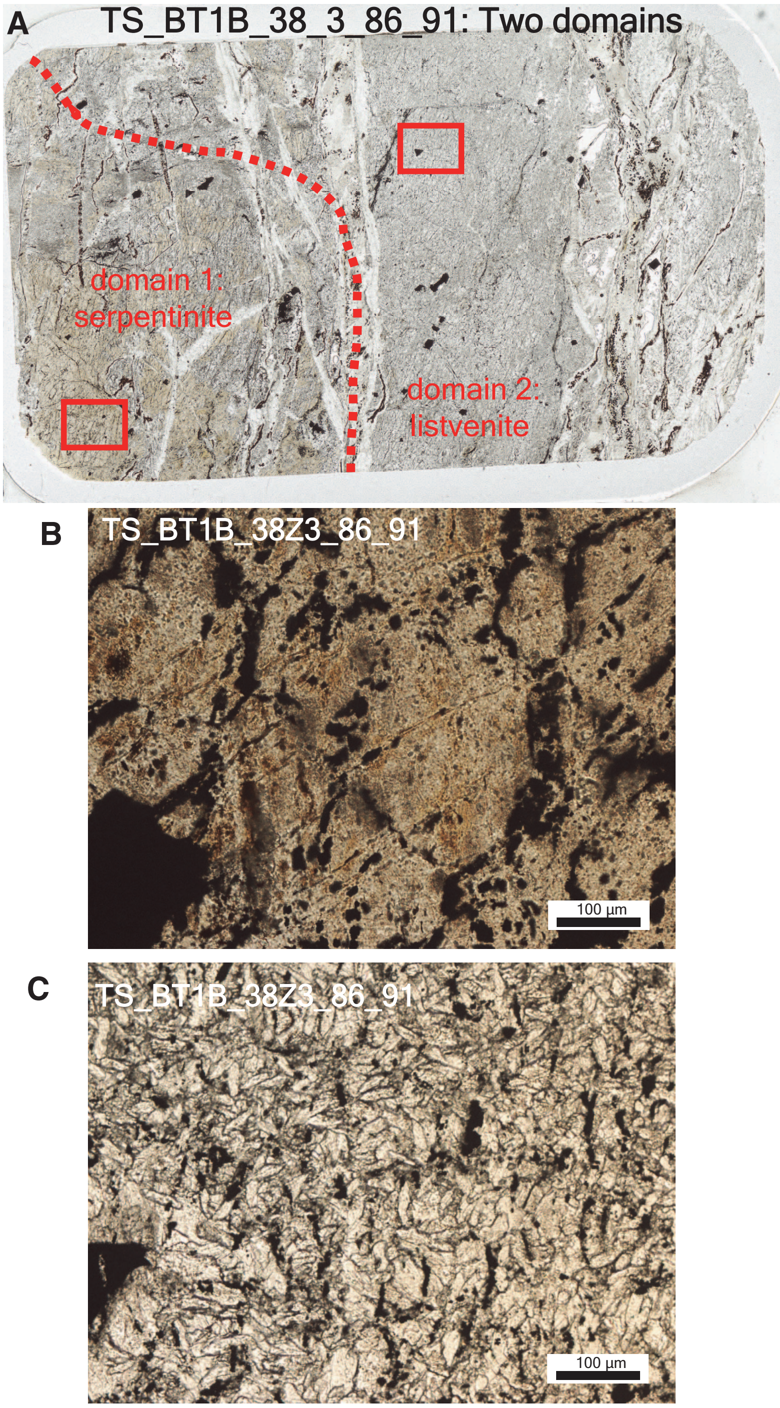

Figure F20. Oxide inclusions in magnesite grains in listvenites, illustrating the observations supporting a hypothesis that tiny iron oxides that formed diffuse trails in the original serpentinite mesh texture were nuclei for additional oxide crystallization during the formation of listvenite. **A, B.** Early stages (PPL). **C.** Elongated magnesite grains in a strongly foliated listvenite show characteristic inclusion of iron oxides (or iron hydroxide). Note that each magnesite aggregate has radiating crystals grown from an oxide nucleus (PPL).

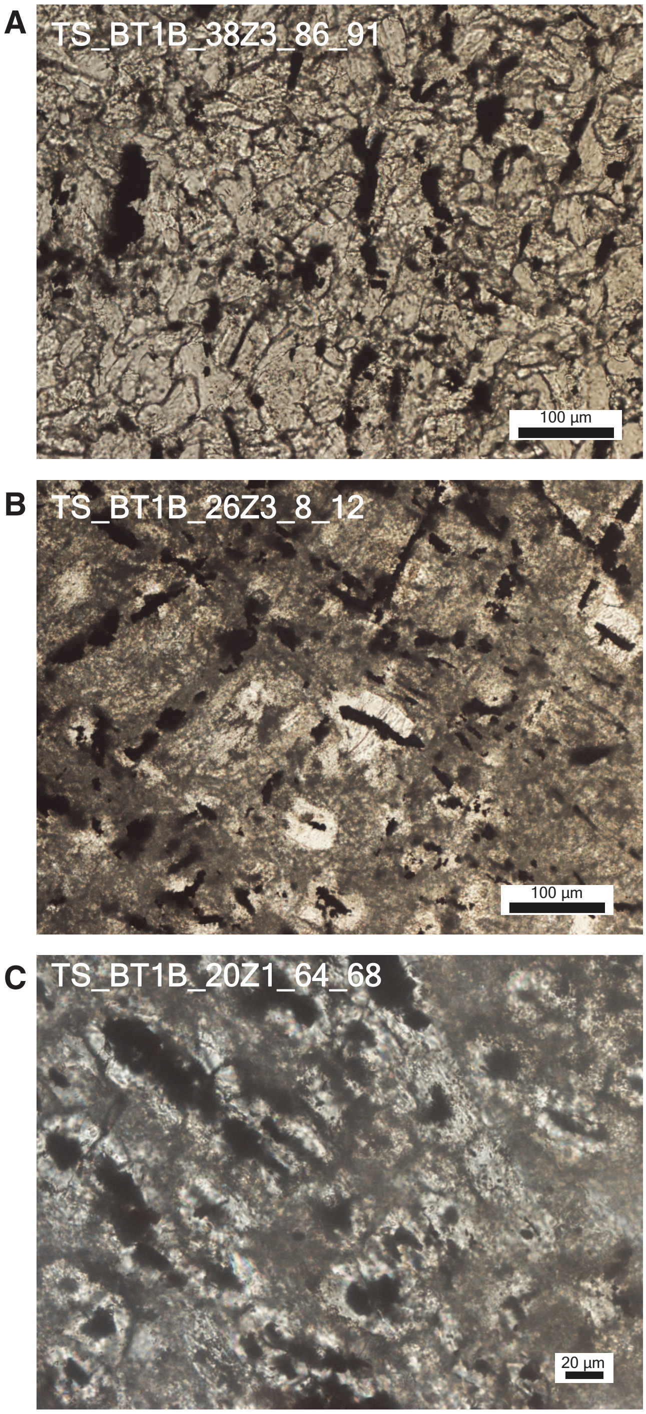

Figure F21. A–C. Talc-bearing serpentinite/ophicarbonate dominantly composed of serpentinite displaying two shades of green, resembling serpentinite after harzburgite. XRD characterization (C) revealed the presence of talc in the pale green matrix.

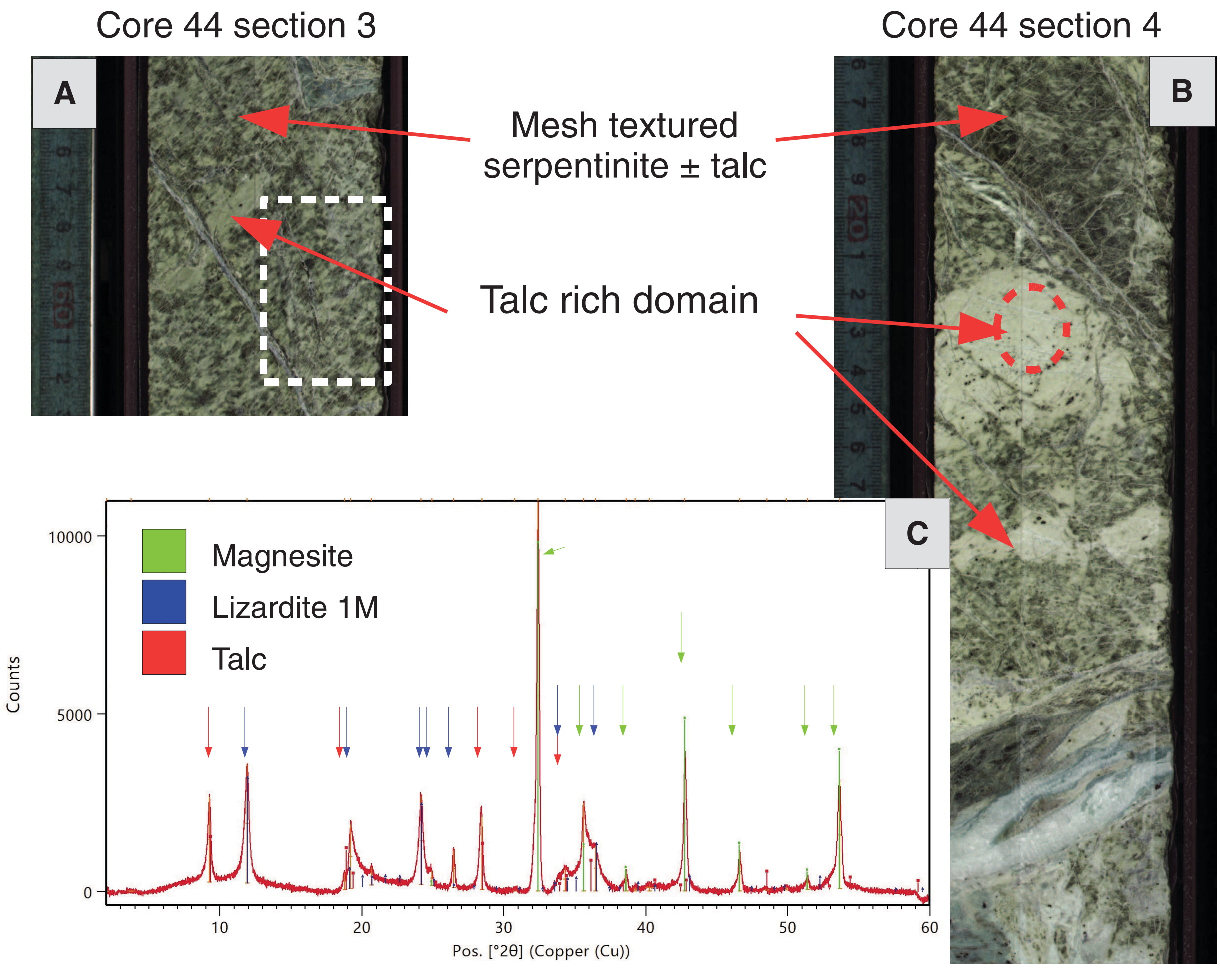

Figure F22. Typical appearance of ophicarbonate in drill core. Transitions from serpentinite can be (**A**) gradual or (**B**) relatively sharp. The serpentinite mesh texture is typically preserved in the ophicarbonate.

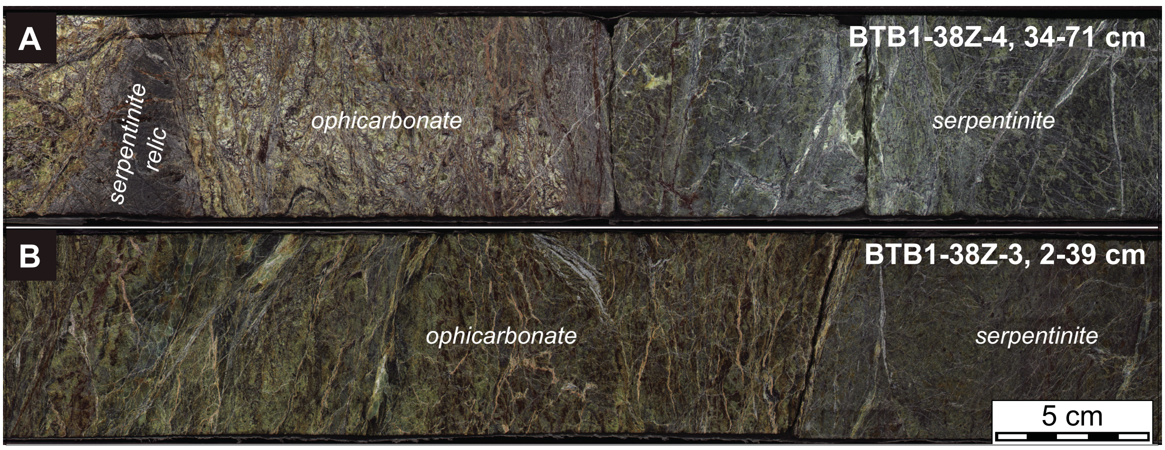

Figure F23. Appearance of ophicarbonate in thin section under (**A**) PPL and (**B**) XPL. The matrix is dominated by serpentine and is transected by frequent carbonate veins.

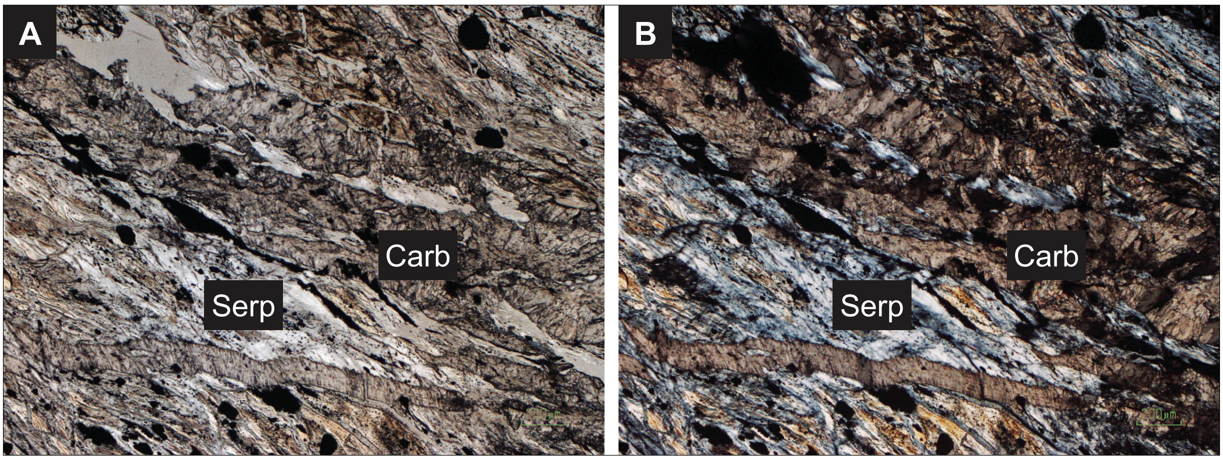

Figure F24. Major serpentinite lithologic units. **A.** Massive serpentinite after dunite and harzburgite. **B.** Massive serpentinite after harzburgite. **C.** Massive and brecciated, veined serpentinite. **D.** Veined serpentinite. **E.** Foliated, veined serpentinite.

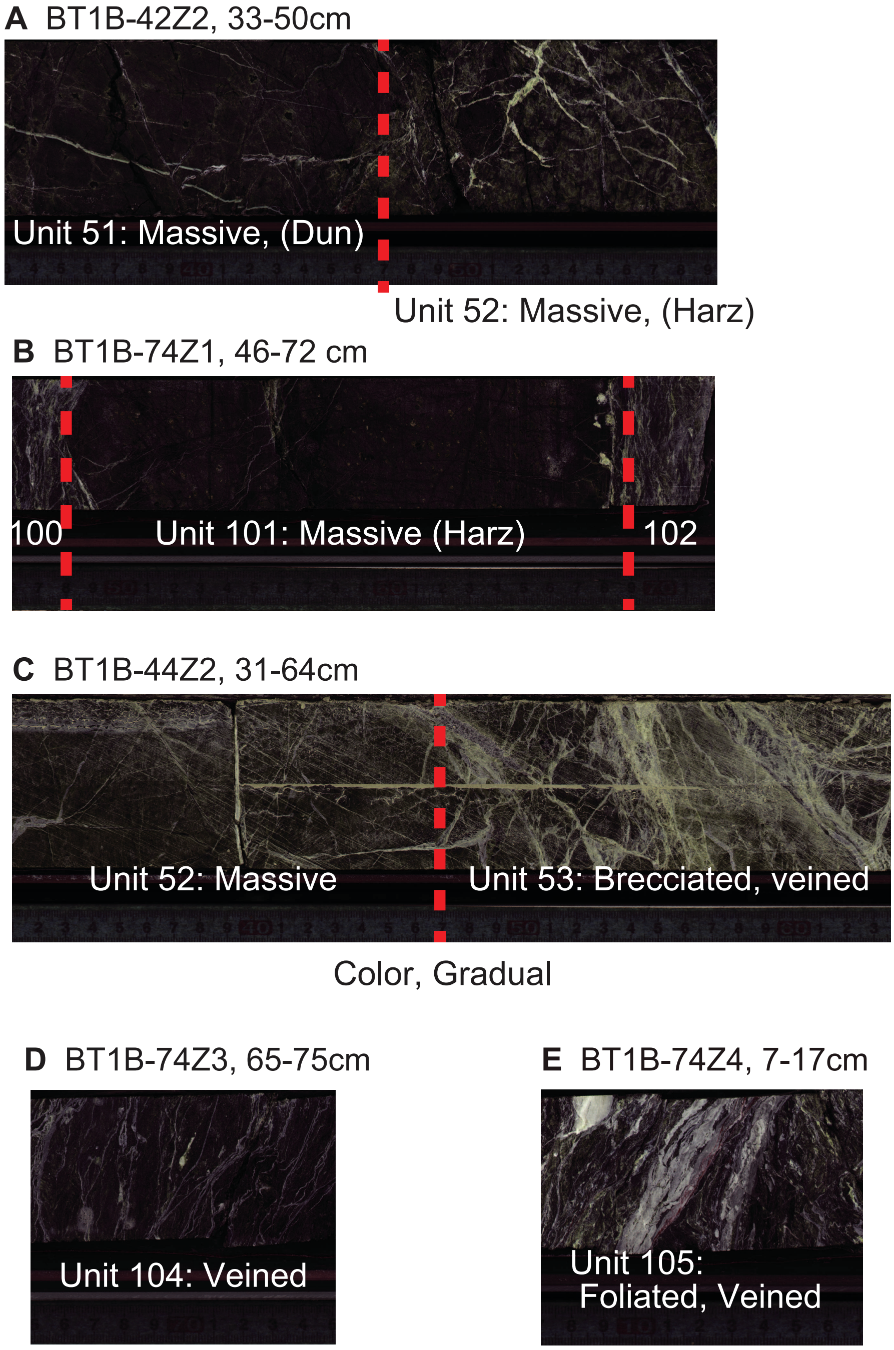

Figure F25. Detailed cross section for the serpentinite (+ ophicarbonate) group intervals with lithologic unit and thin section locations.

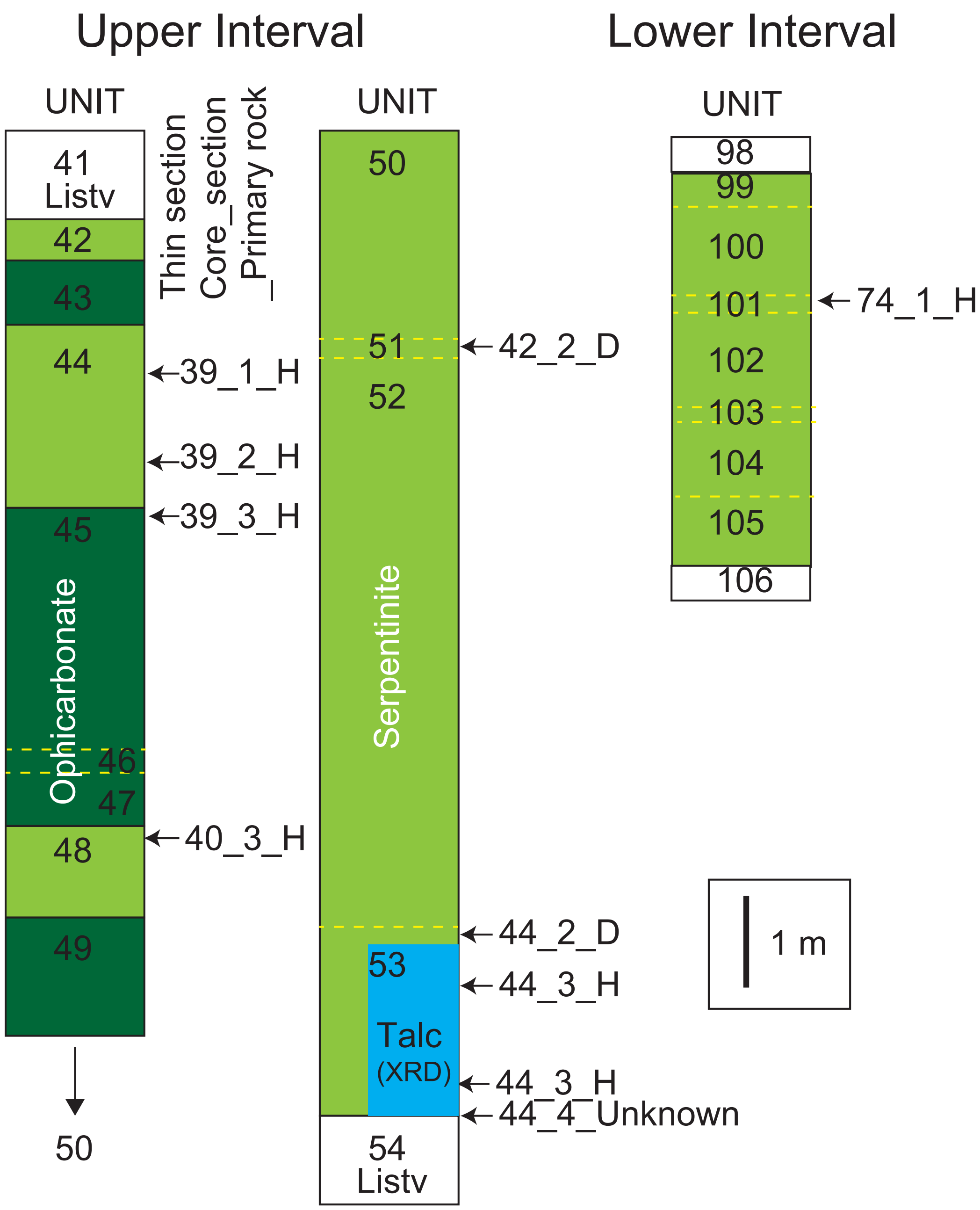

Figure F26. Lithologic boundary between the serpentinite group and other groups. **A.** Sharp color contrast between Unit 41 ophicarbonate and Unit 42 serpentinite. **B.** Irregular color contrast between Unit 98 listvenite and Unit 99 serpentinite. **C.** Gradual color contrast between Unit 49 ophicarbonate and Unit 50 serpentinite.

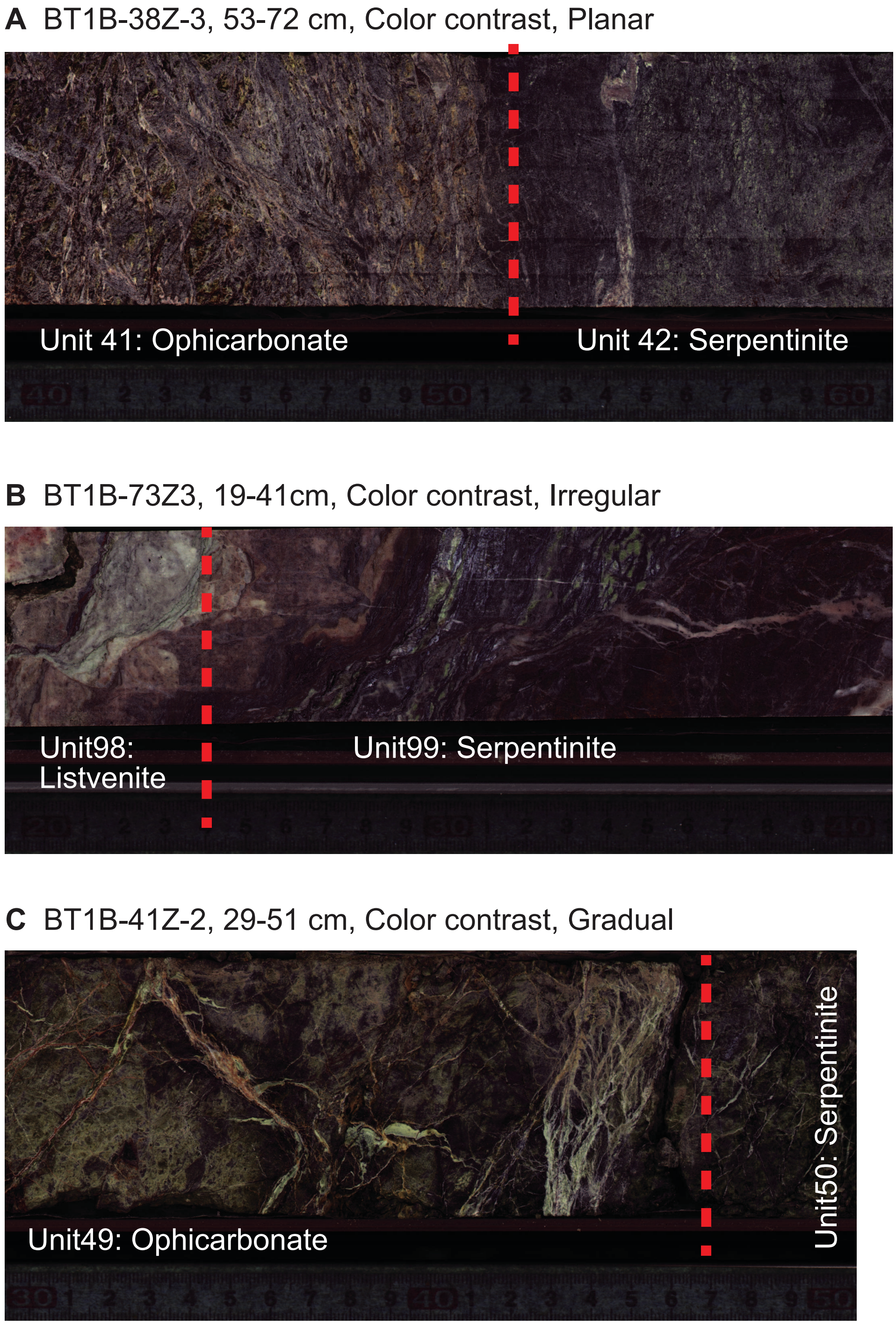

Figure F27. Typical harzburgite-serpentinite in (**A**) PPL and (**B**) XPL. **C.** Dunite-serpentinite (PPL). Spl = spinel.

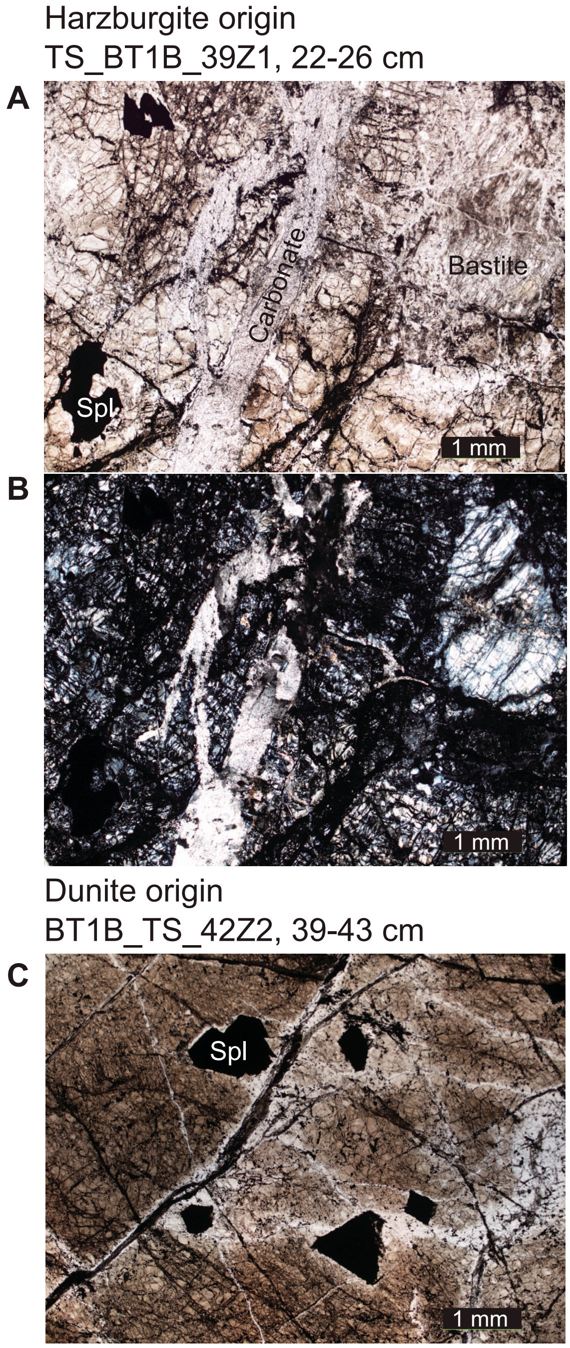

Figure F28. A. Harzburgite-serpentinite (whole thin section). **B, C.** Bastite (Ba) elongates parallel to serpentine foliation in carbonate-poor weakly foliated domain (B: PPL, C: XPL). **C, D.** Bastite is partly replaced by talc in carbonate-rich domain (D: PPL, E: XPL).

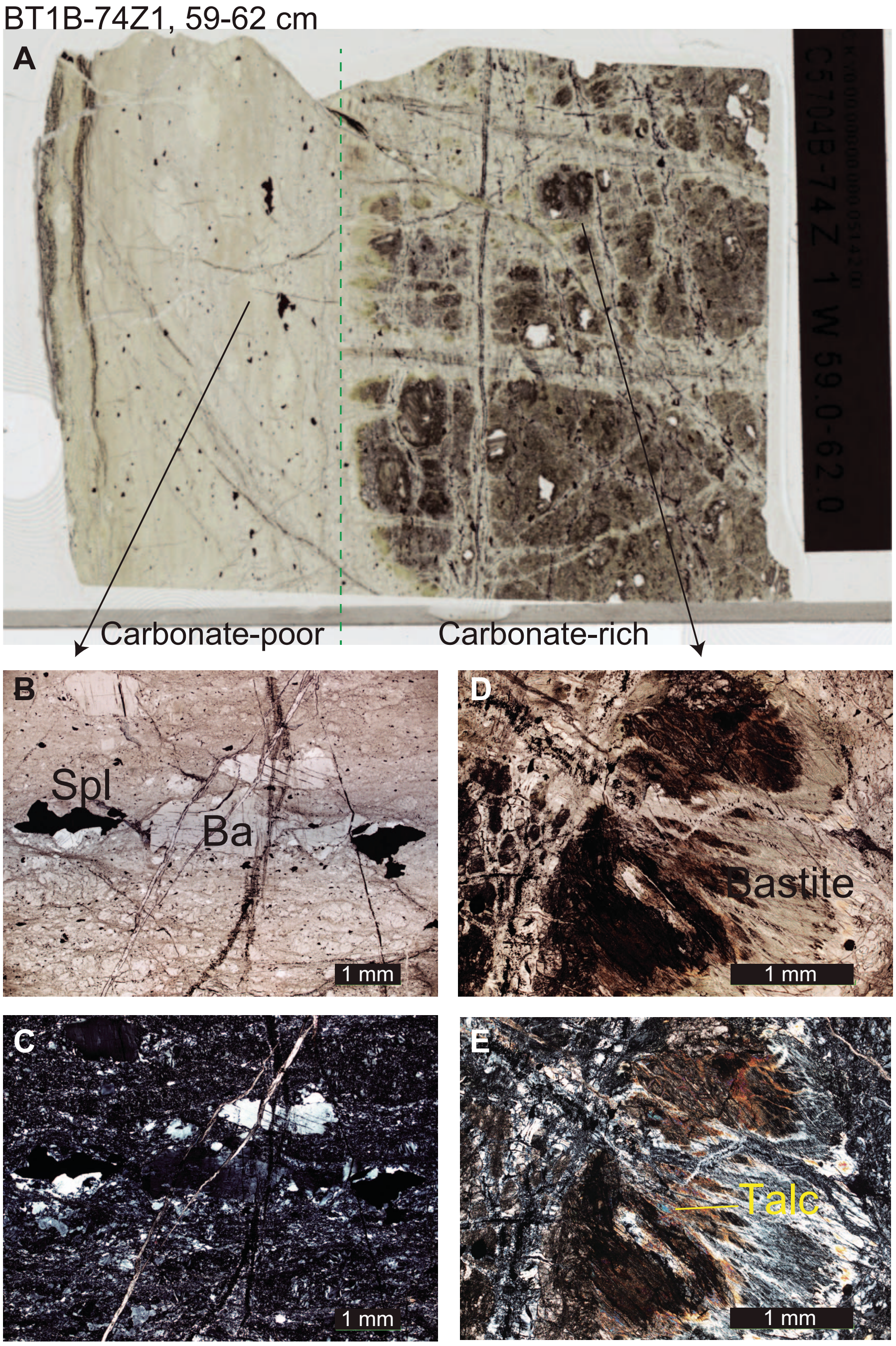

Figure F29. Carbonate minerals in serpentinite. **A, B.** Extremely fine grained carbonate grains in serpentine matrix (A: PPL, B: XPL). **C, D.** Late carbonate-silicate aggregate cuts early carbonate veins. Note that silica is associated with the late carbonate aggregate (C: PPL, D: XPL).

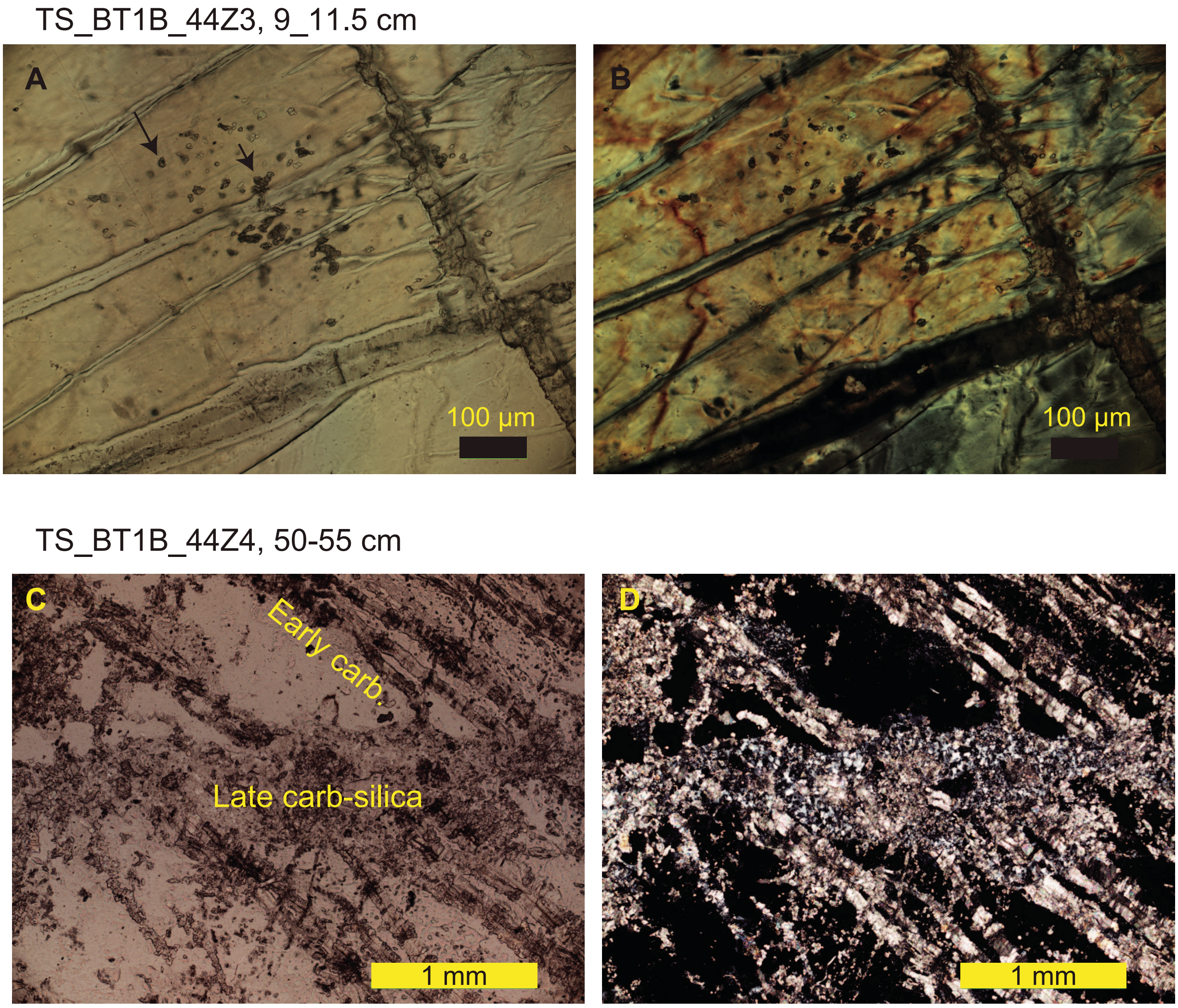

Figure F30. A–G. Representative core from the metamorphic sole. Unit 115 is similar to Unit 113 (shown on the right-hand side of B). Note the relatively sharp contact between (E) Units 117/118 and 118/119, (F) Units 119/120, and (G) Units 120/121.

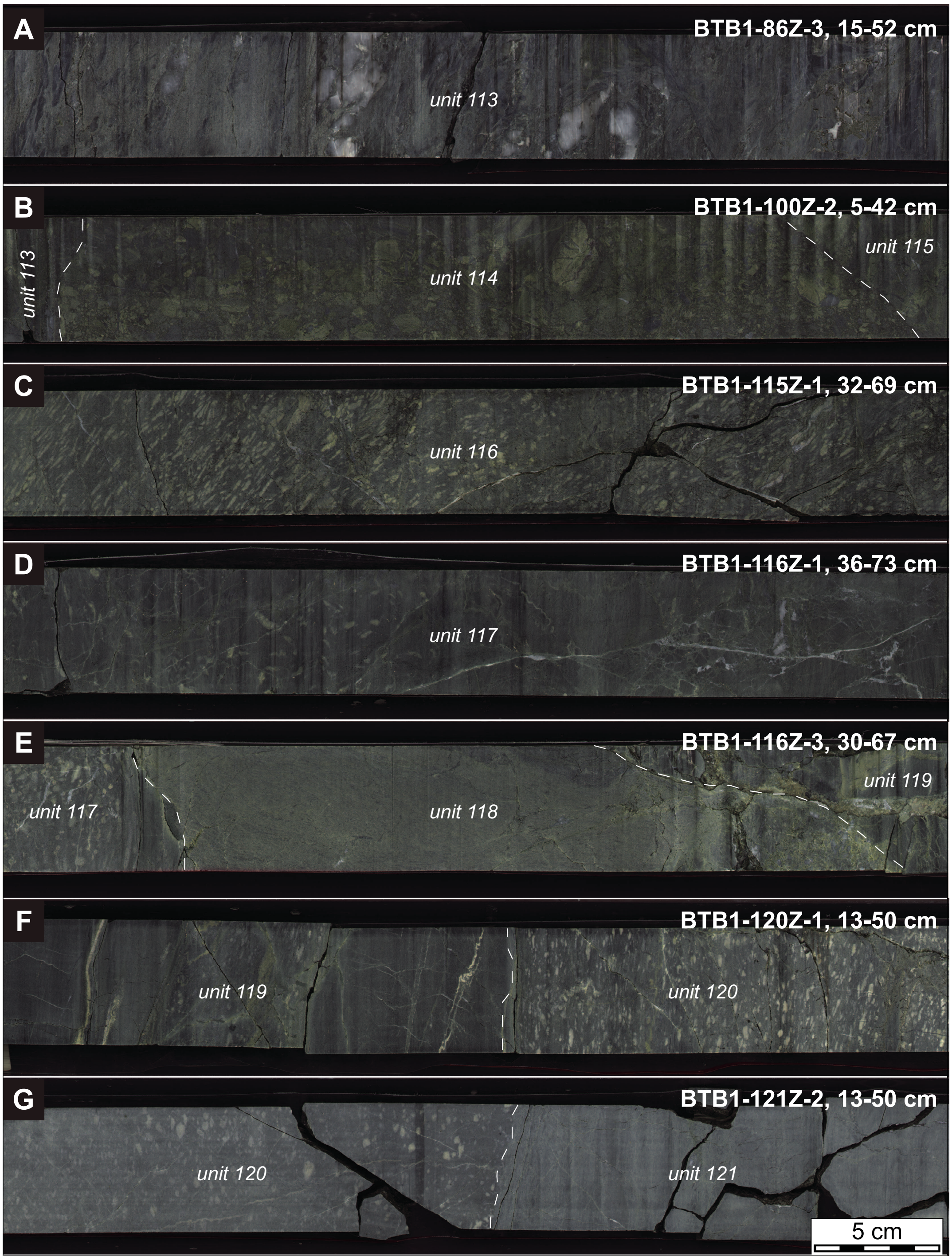

Figure F31. A, B. Representative greenschist metamorphosed phenocrysts in metablastic sequences of the metamorphic sole (A: PPL, B: XPL). **C, D.** Rarely occurring pumpellyite inclusions in albite (C: PPL, D: XPL). Amph = amphibole; Ab = albite; Czo = clinozoisite; Ttn = titanite; Pmp = pumpellyite.

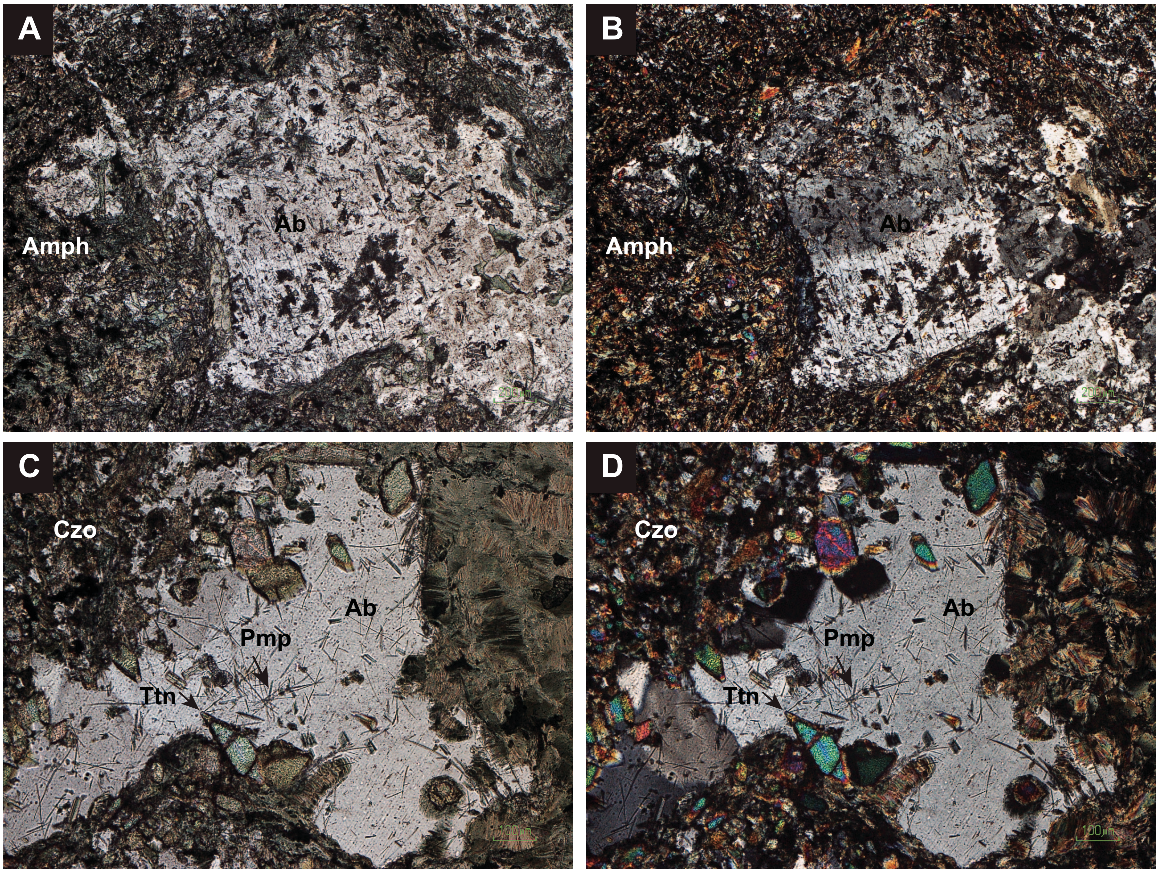

Figure F32. Variation in density of structural features in Hole BT1B as recorded in the structure log. A = alluvium, Lv = listvenite, Sp = serpentinite, M = footwall metamorphic rocks, BT = basal thrust.

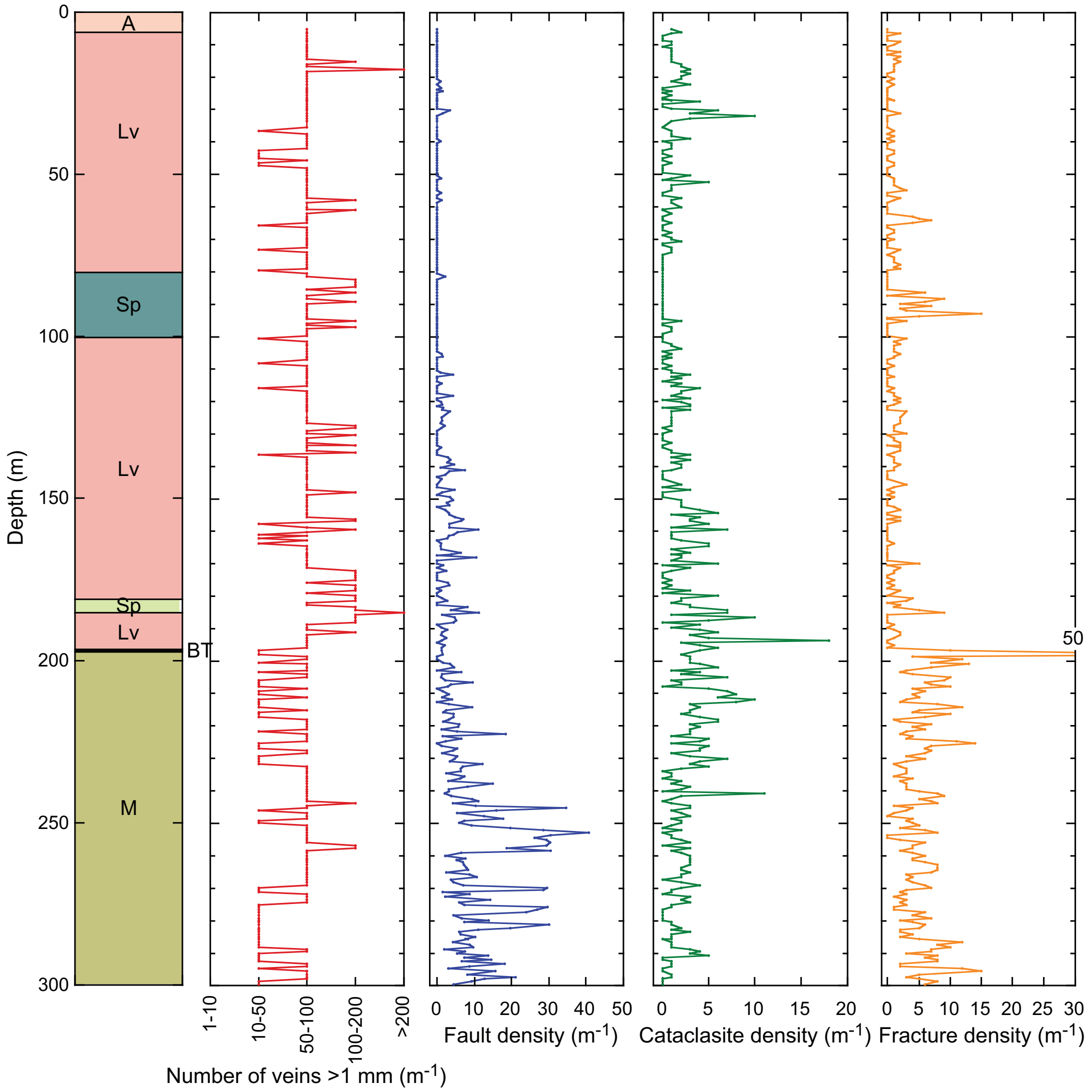

Figure F33. Occurrences of identified vein types in Hole BT1B.

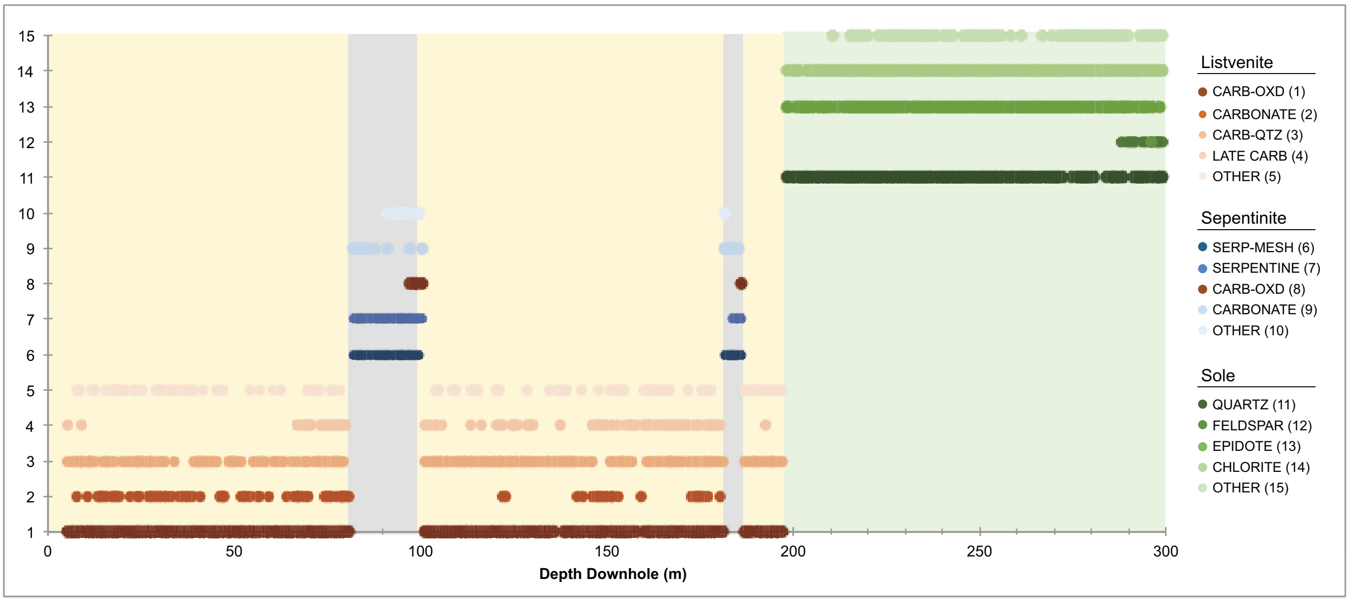

Figure F34. Carbonate-oxide net veins in listvenite and high-resolution XCT imaging. Blue rectangle = thin section location. carb = carbonate, qtz = quartz, hem = hematite.

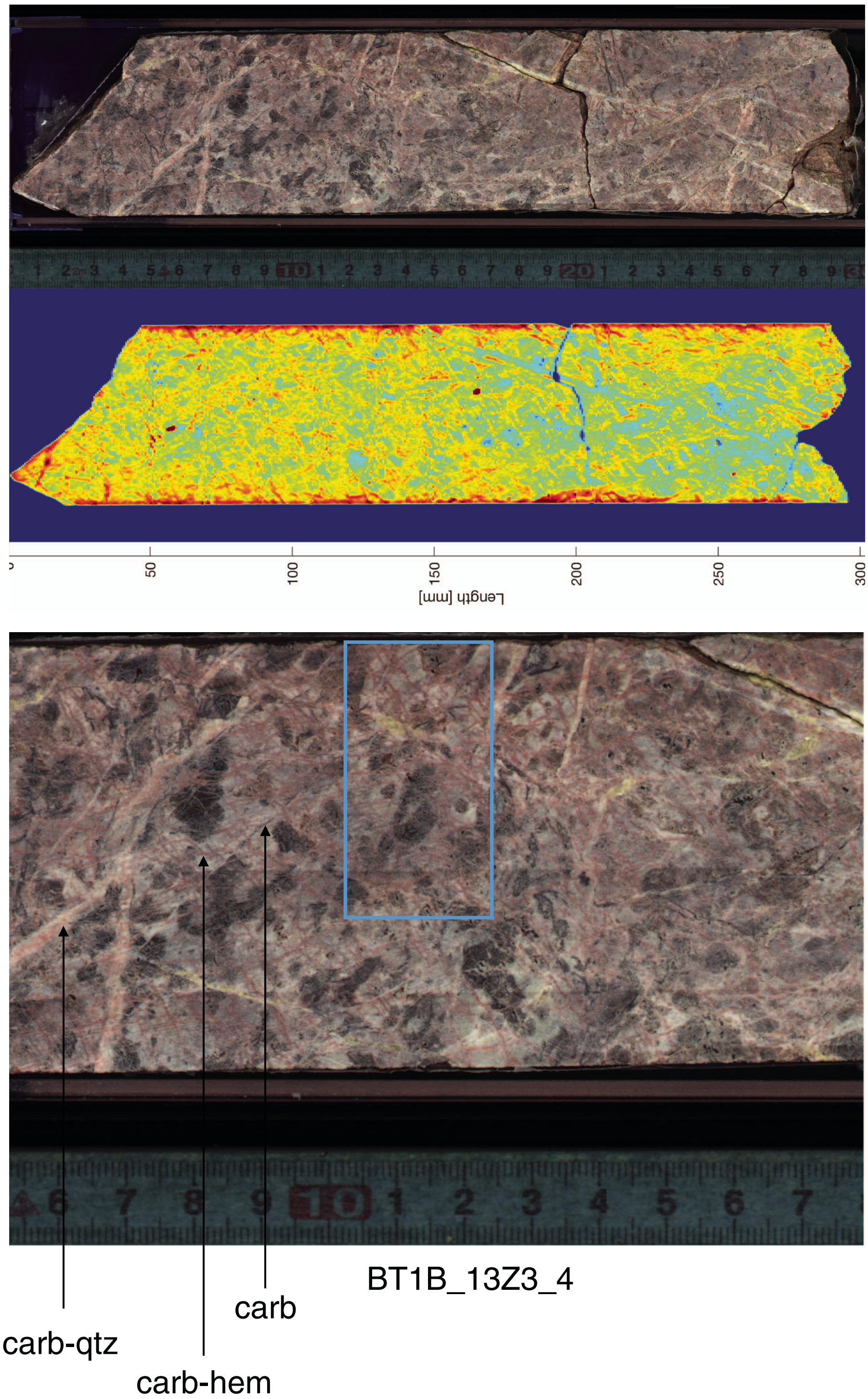

Figure F35. Textural aspects of veins in listvenite. **A**, **B**. Carbonate-oxide vein showing oxides in medial line and antitaxial growth of magnesite fibers: (7Z-4, 20–22 cm; A: PPL, B: reflected light-cross-polarized light [RL-XPL]). **C**, **D**. Carbonate-oxide vein showing oxides on medial line and antitaxial growth of magnesite. Host-rock matrix is fine-grained quartz and coarser grained magnesite: (C) 47Z-3, 15–19 cm (XPL-λ); (D) 16Z-3, 12–16 cm (XPL-λ). **E**, **F**. Dense networks of fabric-defining carbonate-oxide veins: (E) 30Z-3, 65.5–68.5 cm (RL-XPL); (F) 8Z-3, 20–22 cm (RL-XPL).

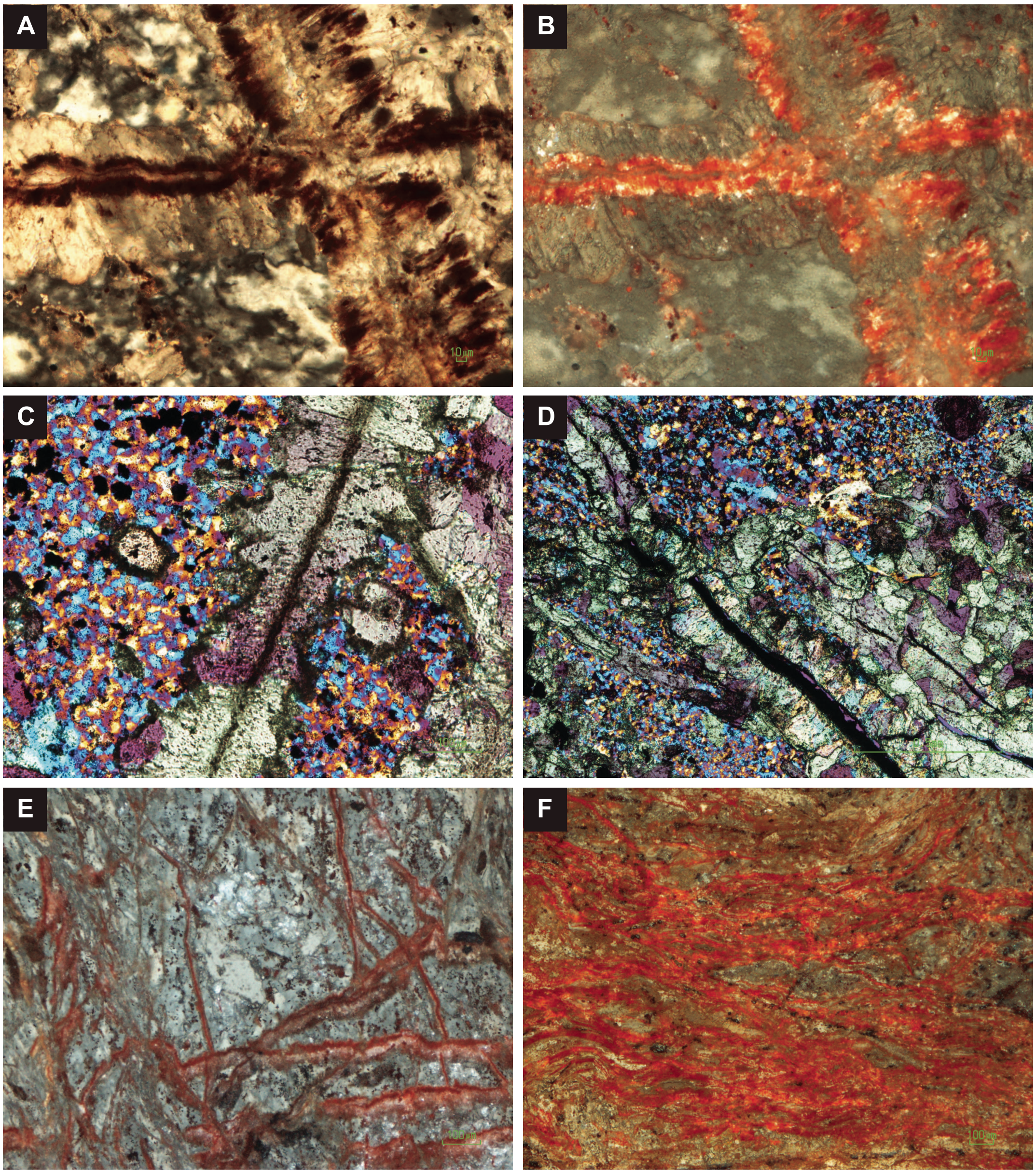

Figure F36. Late carbonate-quartz (carb-qtz) veins crosscutting earlier gray carbonate (carb) veins. Carb-qtz veins show a pink rim and a core of fine anastomosing pink veins set in a clearer groundmass with local green spots. Some show millimeter-scale black halos or selvages.

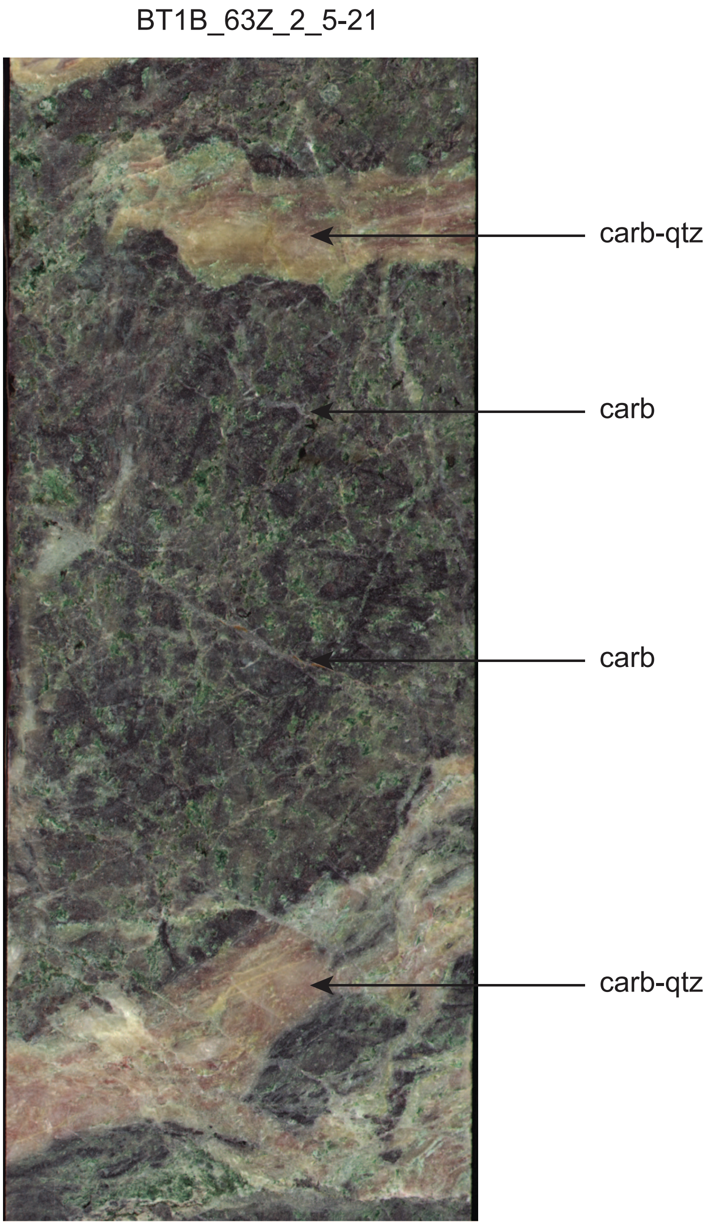

Figure F37. Vein crosscutting relationships. An early carbonate-oxide vein (carb-ox) is cut by a carbonate (carb) vein, which is cut in turn by a carbonate-quartz (carb-qtz) vein (XPL- λ).

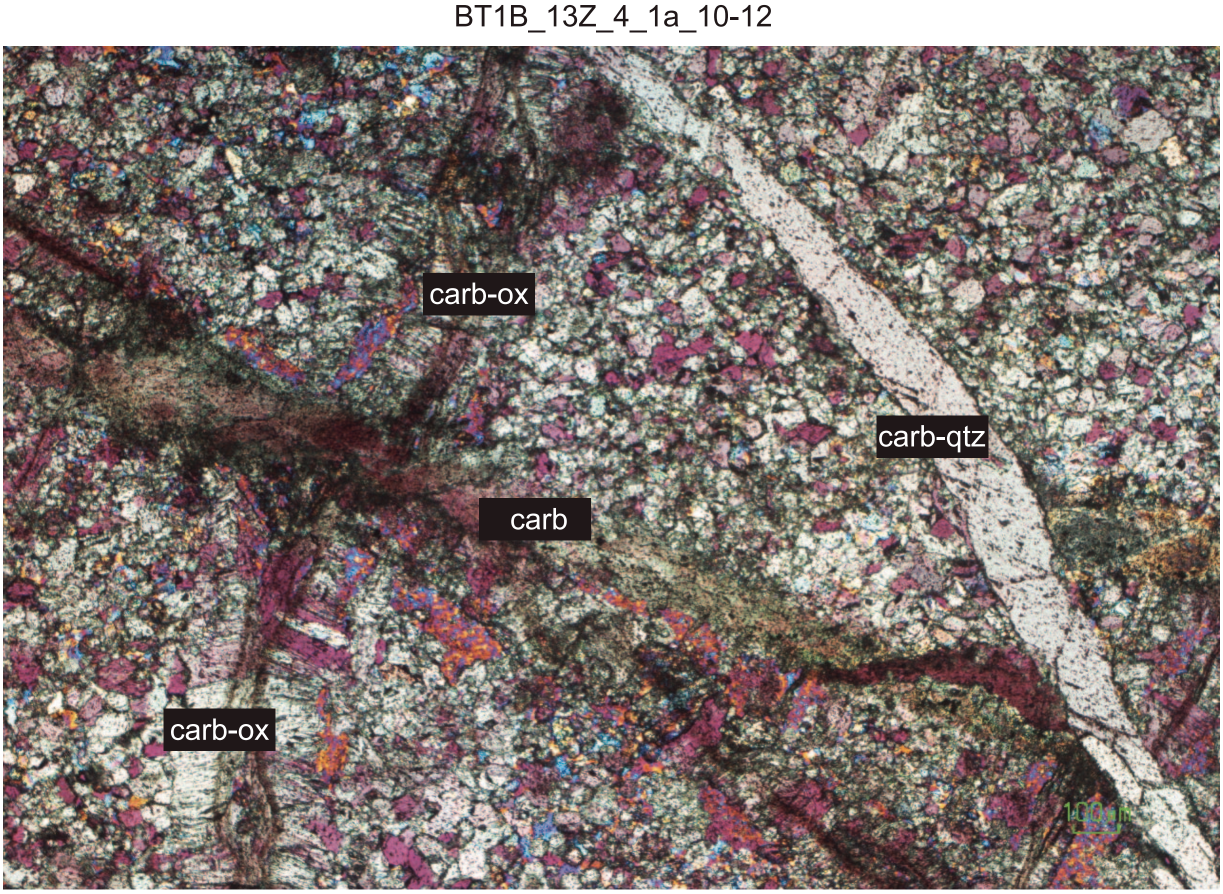

Figure F38. Growth textures of silica phases in carbonate-quartz vein. Fine-grained, radiating quartz (chalcedony) at vein margin (bottom) grades into coarse quartz toward vein center (top) (3Z-1, 32–35.5 cm, XPL-λ).

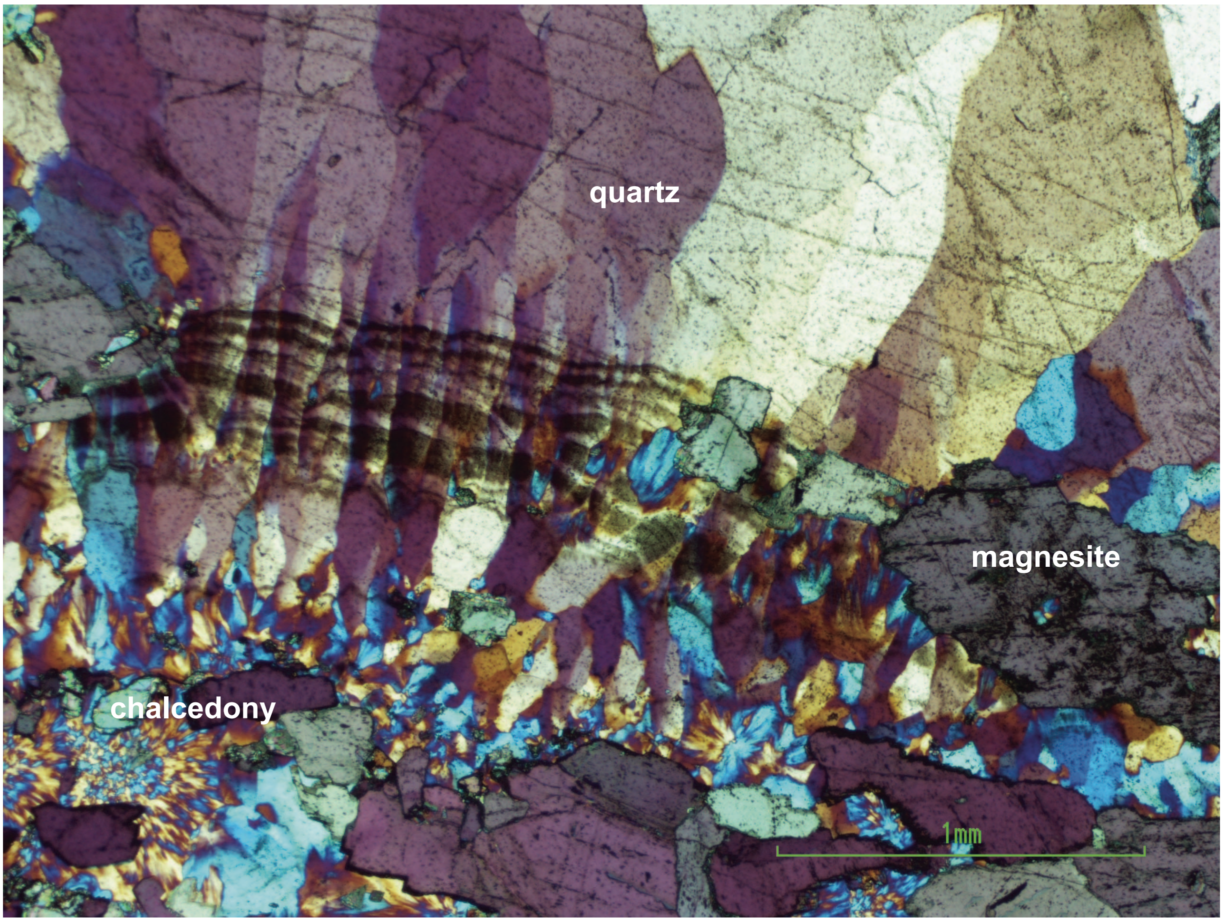

Figure F39. (**A**) Photo, (**B**) SWIR, and (**C**) XCT. Dolomite is indicated by elevated X-ray intensity in XCT scans along the visually identified late carbonate vein. IR spectra also highlight the presence of dolomite-rich veining in the core center. IR data further suggest that the SiO_2-rich white patch on the upper left of the core is amorphous.

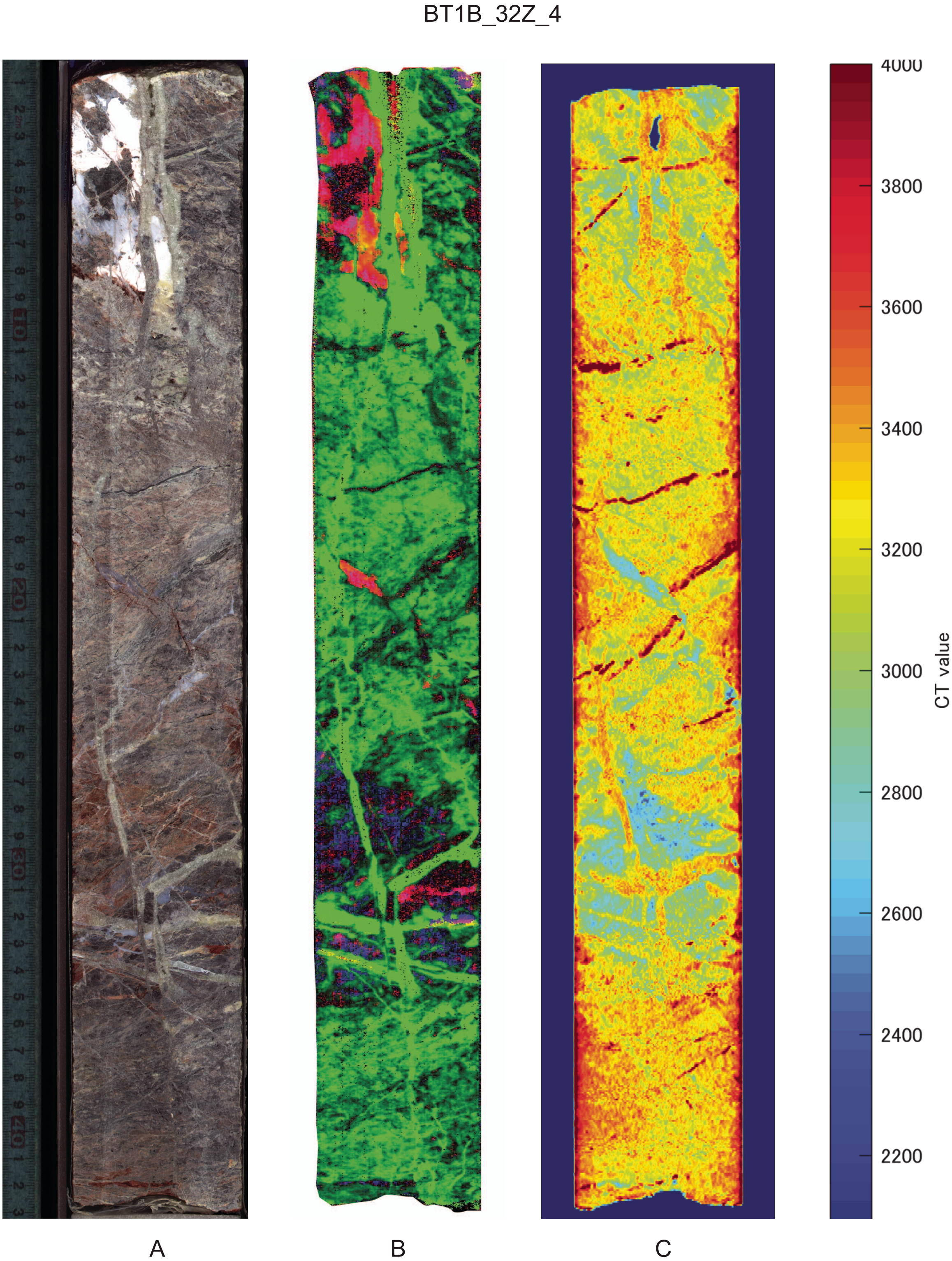

Figure F40. (**A**) Core photo and (**B–D**) XRF-CL results. The portion interpreted to be dolomite rich, principally the vein and the wall rock on the right side of the core, are relatively rich in MgO and CaO and depleted in SiO_2, consistent with the presence of dolomite. The white patch to the left and top of the interval shows the opposite relative concentrations, consistent with the presence of a silica-rich phase.

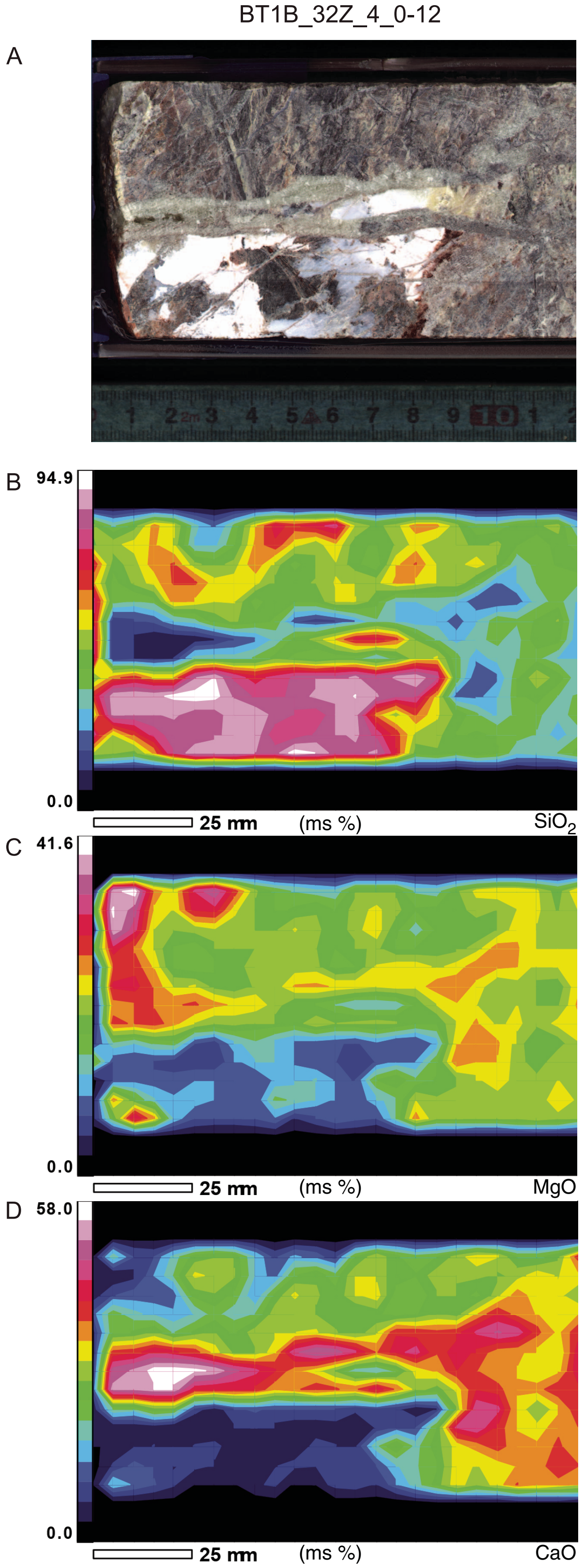

Figure F41. Late carbonate veins filled with well-developed yellow magnesite with bladed crystals growing perpendicular to the vein. **A.** Core photo. **B.** False-color IR composite from imaging spectrometer (red = 2.31 µm, green = 1.58 µm, blue = 1.08 µm). **C.** SWIR spectral parameter map showing the strength of an absorption feature centered near ~1.0–1.2 µm. Although further work is needed to constrain the phase responsible for this spectral feature, it is likely related to Fe^{2+} (e.g., Burns, 1993). **D.** XCT image.

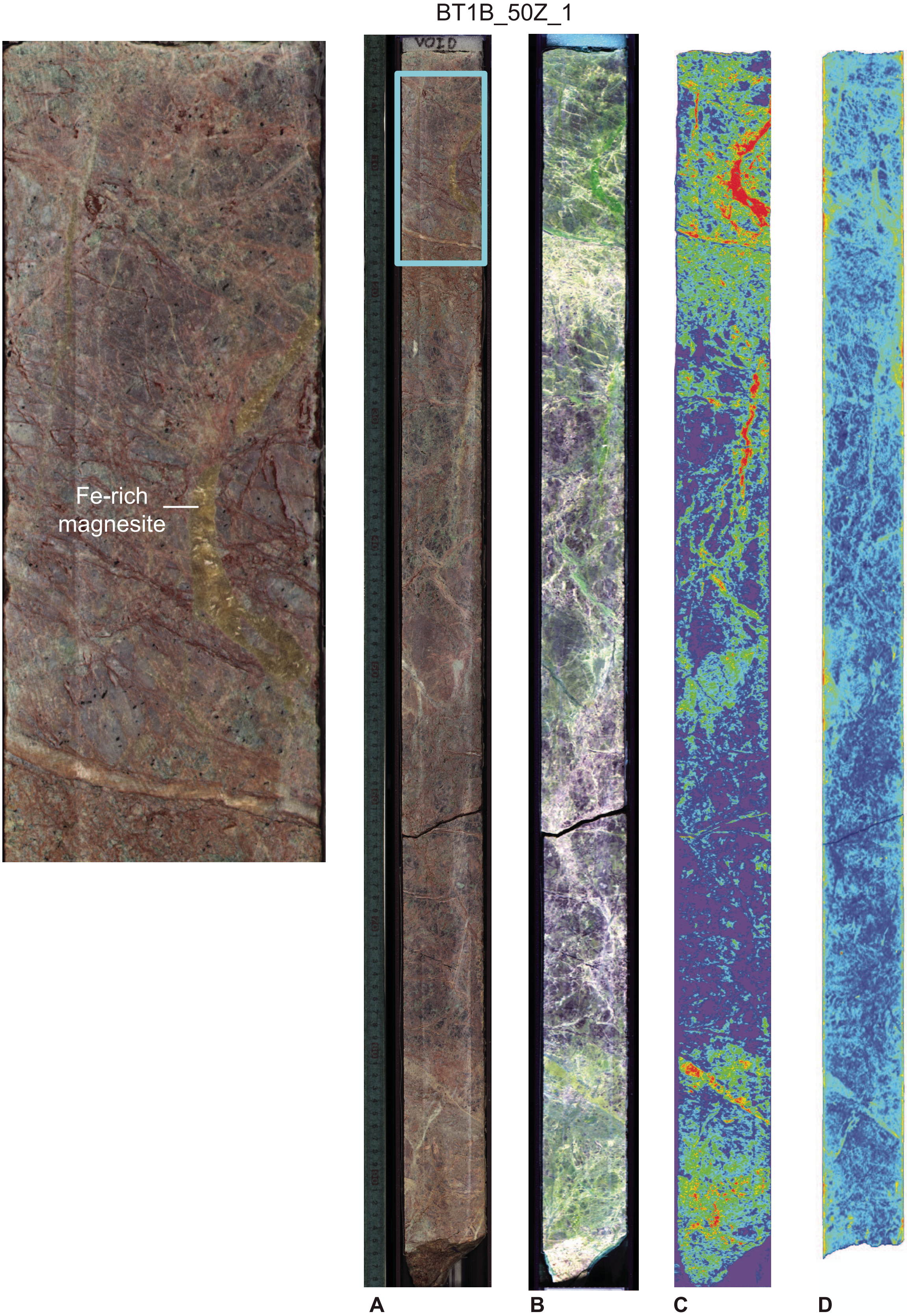

Figure F42. Detail of fuchsite listvenite showing late veins filled with green microcrystalline silica resembling chrysoprase.

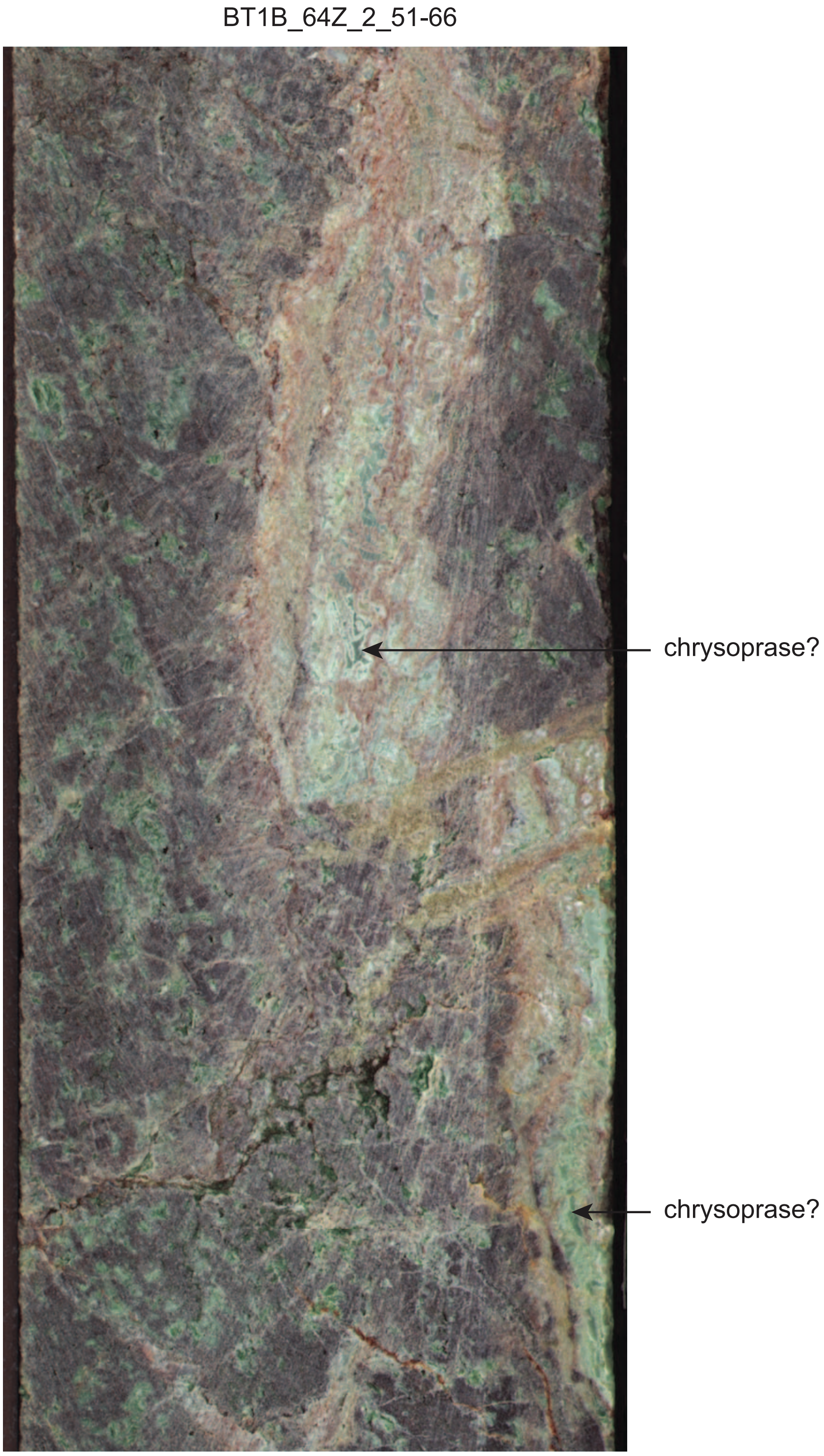

Figure F43. X-ray diffractograms of material scraped from three veins. Small sample sizes available for shipboard XRD necessitated investigation of the effects of powder mass on peak position. It was determined that the graphite [002] peak position in a graphite standard (a surplus crucible from the geochemistry lab) was shifted by –0.40°, –0.35°, and –0.29°2θ for 1, 4, and 12 mg samples, respectively, compared to the RRUFF reference pattern (R050503-1). Black = 4 mg sample, similar to the vein scrapings studied. Maroon = hematite (R050300-1), gold = dolomite (R040030-1) reference patterns from RRUFF shifted –0.35°2θ to give the same overall peak shifts for this sample size. Comparison of the observed diffractograms indicates peaks consistent with the presence of graphite, hematite, and dolomite. The peak at 20.6°2θ suggests that some quartz is present in two of the veins. This peak is apparently absent in the vein from interval 78-2, 16–24 cm. It is impossible to resolve differences between quartz [001] and graphite [002] with the amount of material available. All diffractograms are normalized to the highest peak recorded in the diffractogram.

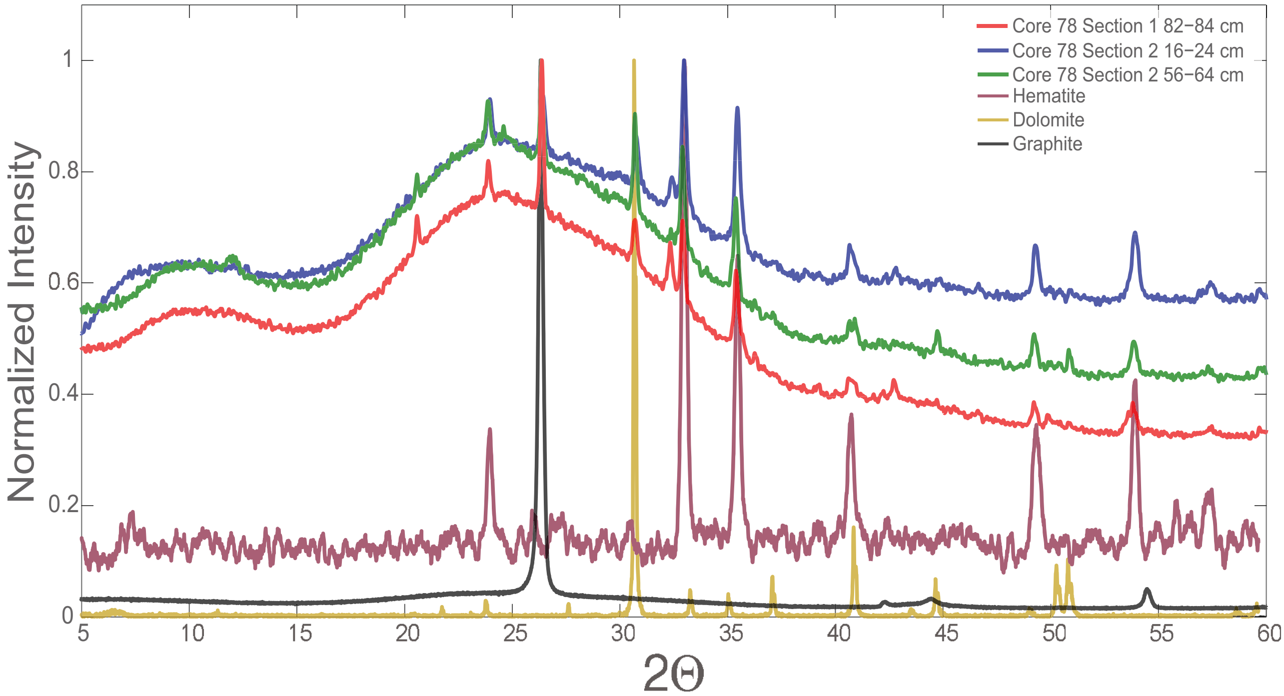

Figure F44. Mesh-textured serpentine (serp) veins are cut by later, through-going, and wider serpentine veins.

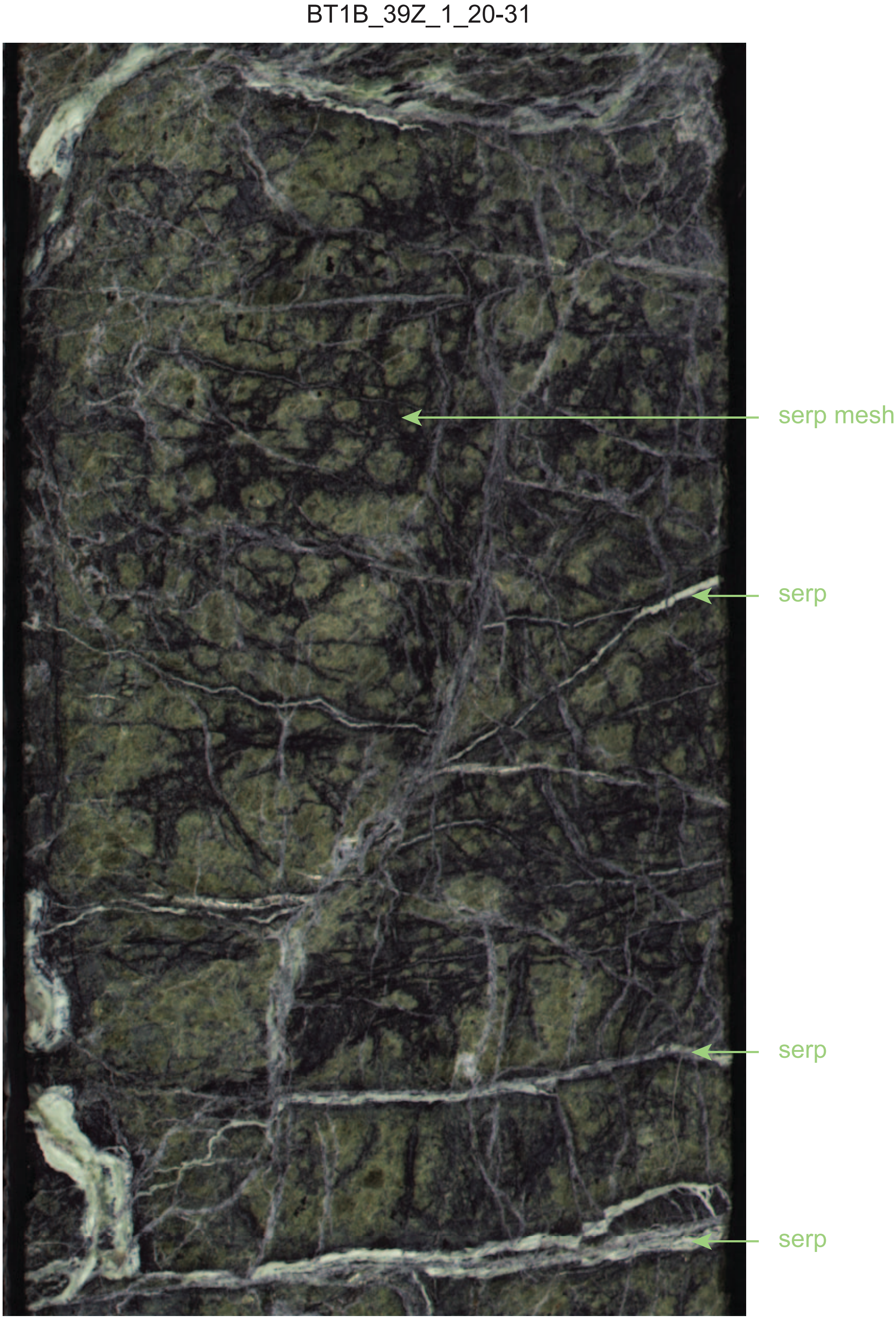

Figure F45. Thin section and interpretation of crosscutting relationships of veins in serpentinite (XPL). An early, irregular serpentine vein is cut by a dense anastomosing set of carbonate-oxide (carb-ox) veins, which are in turn cut by a carbonate vein. All are cut by a late quartz vein.

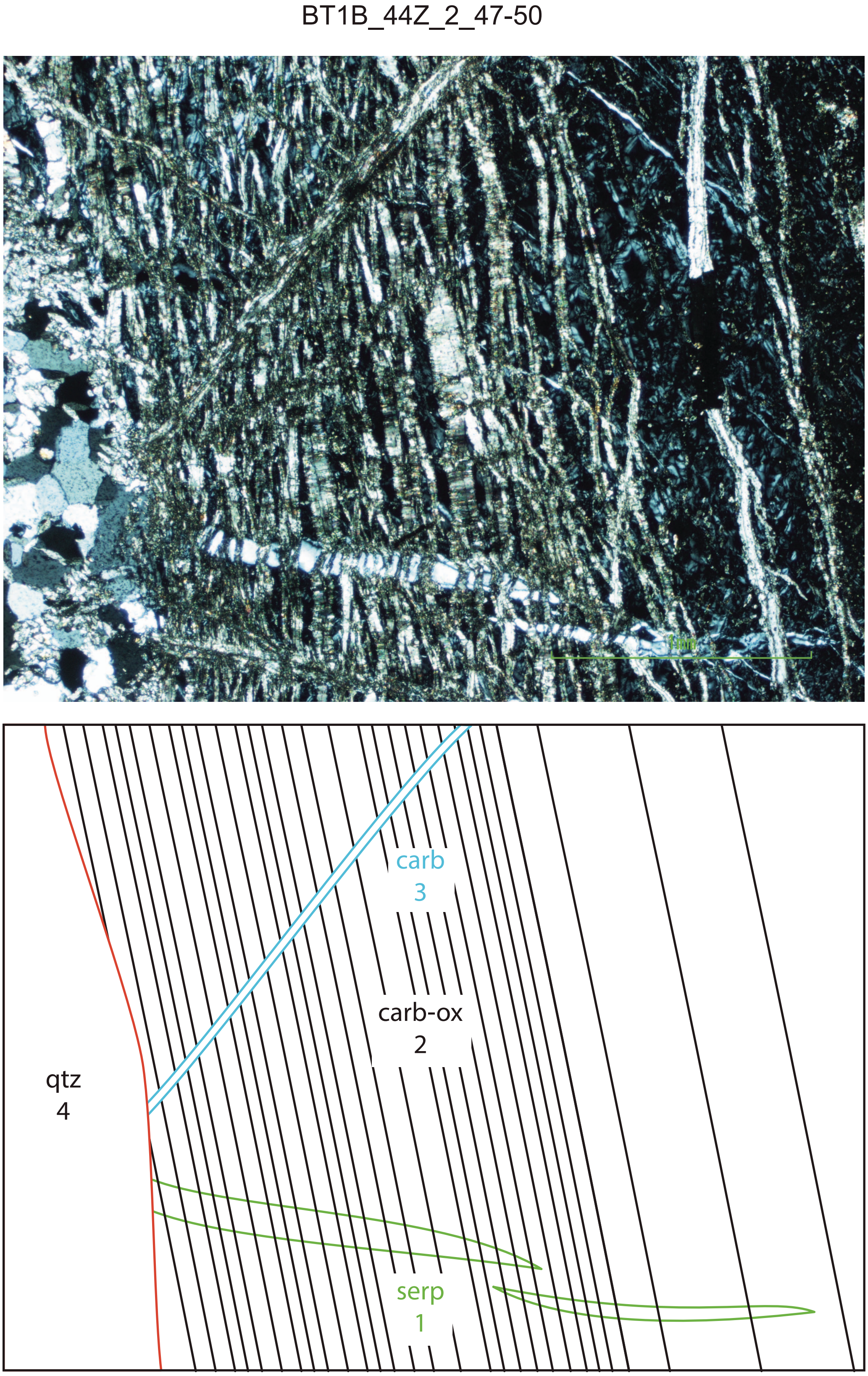

Figure F46. Carbonate-oxide (carb-ox) veins in serpentinite 3.5 m above the serpentinite (serp)/listvenite contact at 100.23 m. The veins are ≤0.1 mm wide and form a dense, regularly oriented, inclined set. Microtextural study reveals these veins commonly contain oxide (hematite?) inclusions along medial lines and magnesite with antitaxial growth textures.

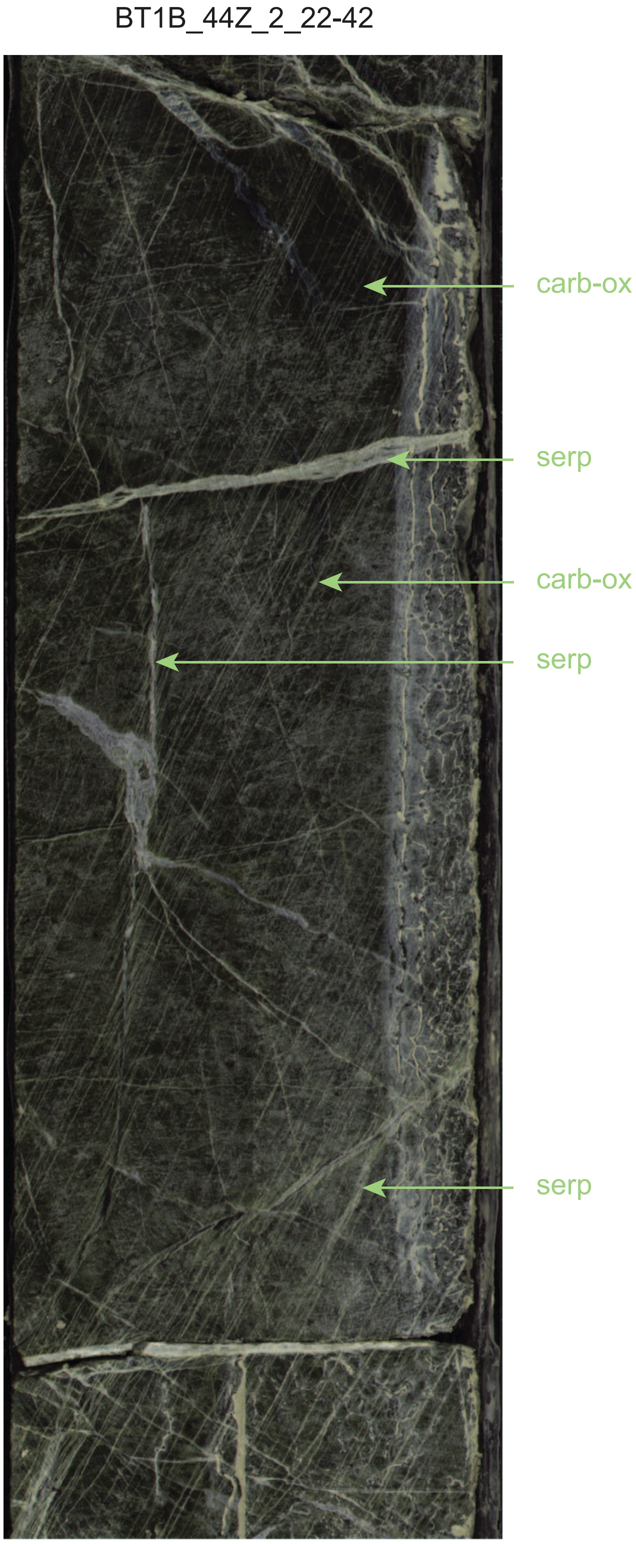

Figure F47. Carbonate-oxide veins in serpentinites. **A**. Serpentinite cut by anastomosing carb-ox vein network (39Z-3, 9–13 cm; PPL). **B**. Mesh-textured serpentinite cut by carb-ox vein (39Z-3; PPL). **C**, **D**. Carb-ox vein cutting mesh-textured serpentinite, showing oxides on centerline with antitaxial magnesite growth textures. Vein margin shows late, optically distinct serpentine after earlier mesh-textured serpentine. The newly grown serpentine also fills orthogonal fractures emanating from the carb-ox vein (Section 44Z-3, 9–11.5 cm; C: PPL; D: XPL-λ). **E, F.** Interval 44Z-3, 47–50 cm; (E) carb-ox veins cutting and offsetting serpentine vein in serpentinite (PPL); (F) dense network of carb-ox veins cutting serpentine vein in serpentinite (XPL).

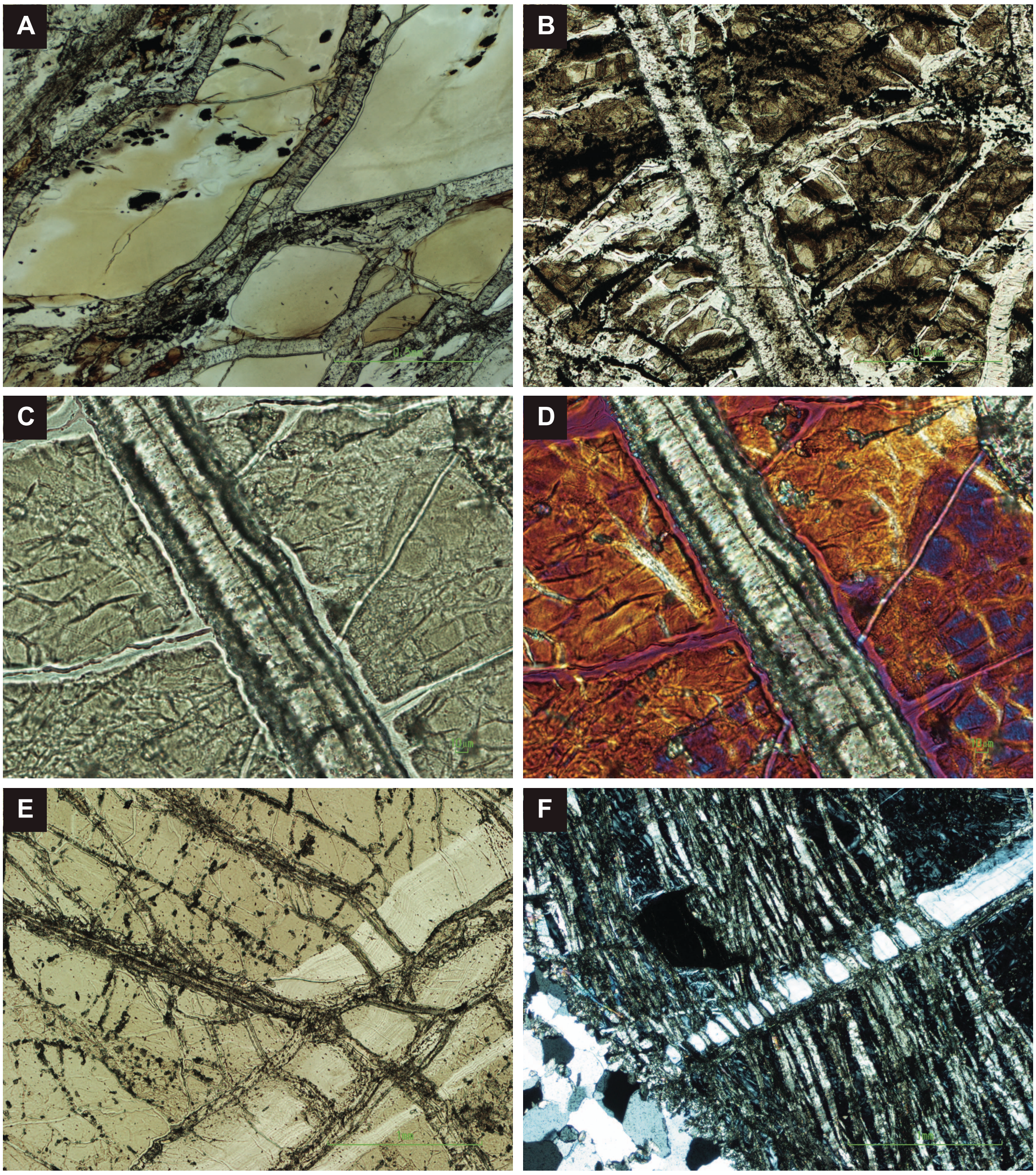

Figure F48. Early quartz, epidote, and feldspar veins in metamorphic sole rocks with corresponding XCT scans. XCT image shows distinctively lower intensity for quartz and feldspar relative to background. Values for epidote-rich bands are higher. All veins are pre- to synfoliation development.

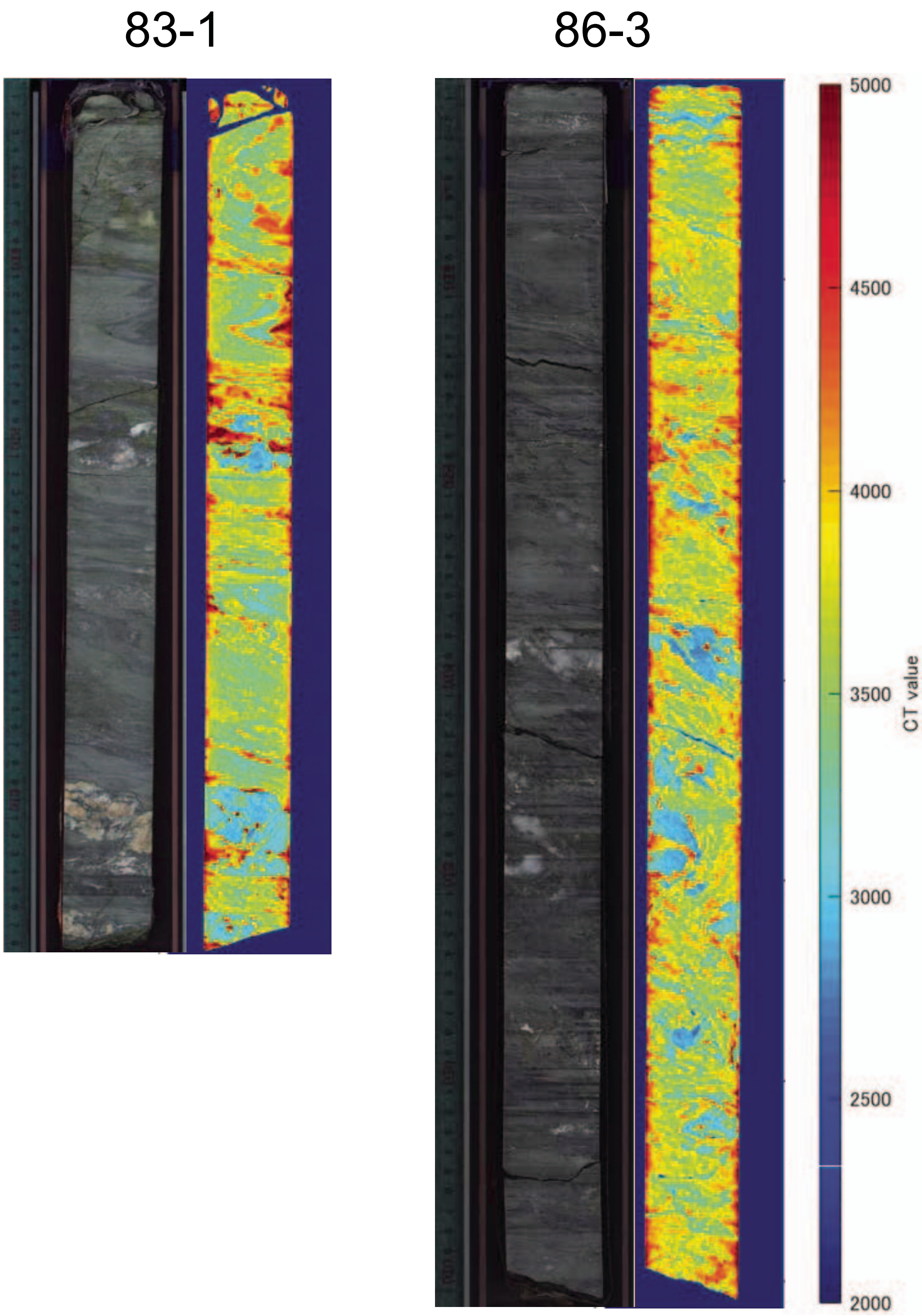

Figure F49. Late chlorite veins crosscutting early quartz veins and foliation in metamorphic sole rocks (249.5–250.38 m).

BT1B_102Z_1_16-23

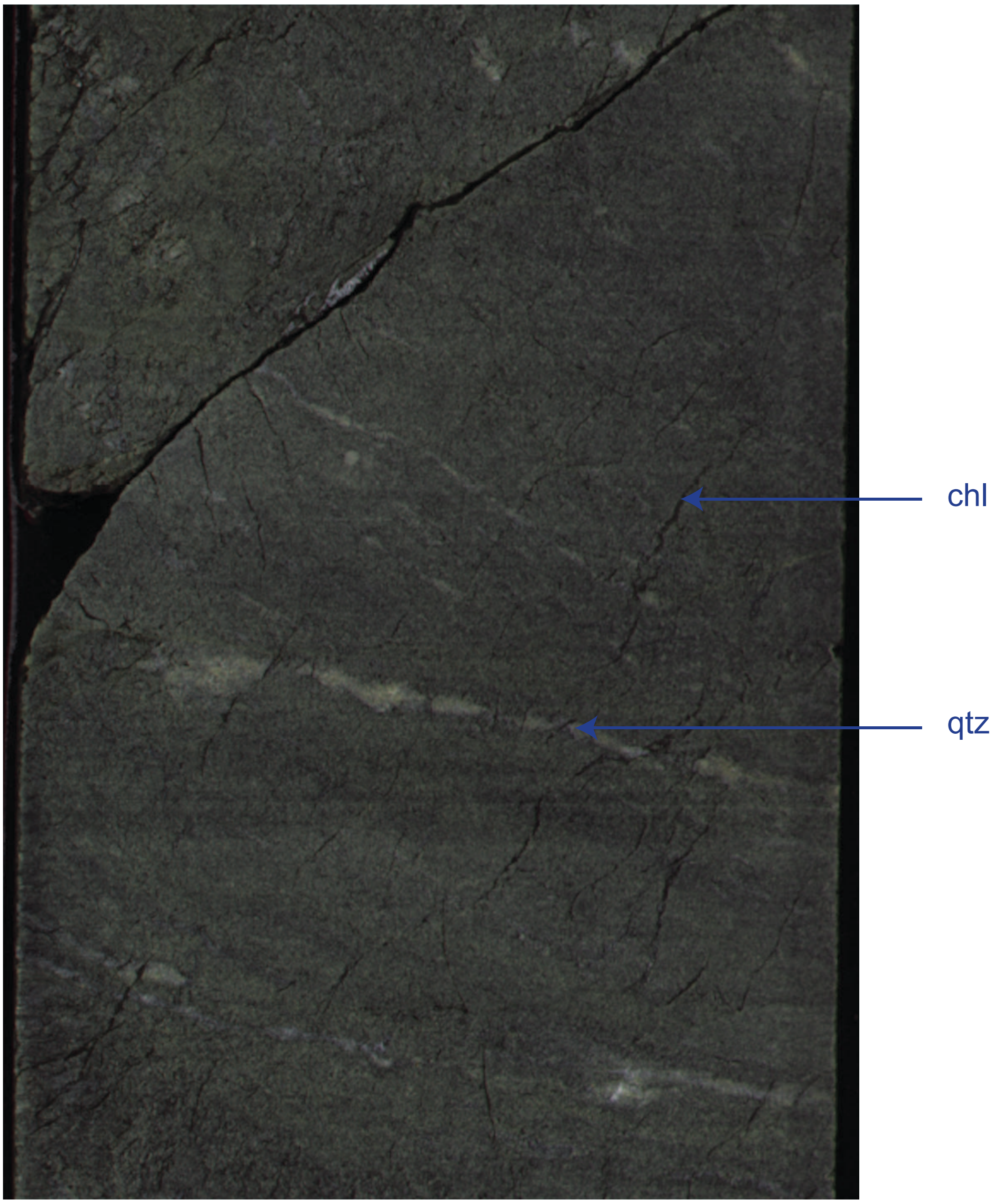

Figure F50. Schematic diagram showing the influence of an inclined borehole on the apparent dip of a planar feature. Note the same plane can have a broad range of apparent dips depending on the angle between it and the borehole inclination. Diagram not to scale.

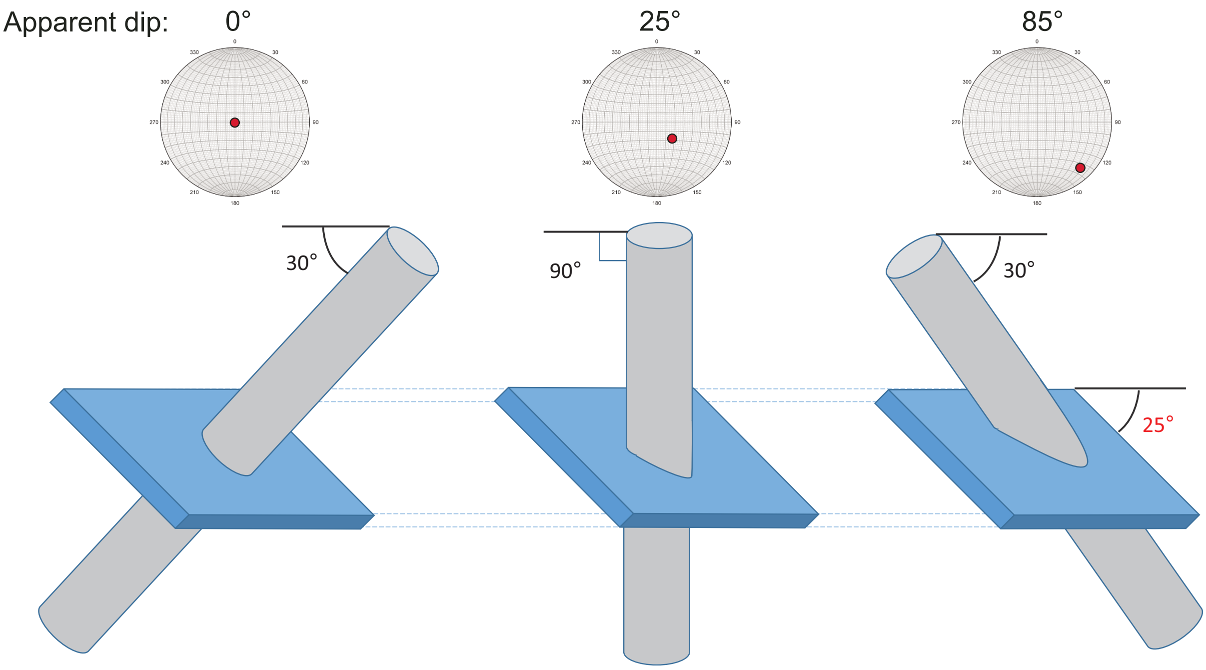

Figure F51. Percentage of host rock composed of specific structural features downhole. 0 = no proportion of the rock is composed of a feature (i.e., a foliation, cataclasite, breccia, etc.), 1 = entire section consists of the structural feature. Black broken line = basal thrust, green areas above the basal thrust = serpentinite. Blue solid line below the basal thrust = the boundary between metasediments and metabasalts as derived from physical property data.

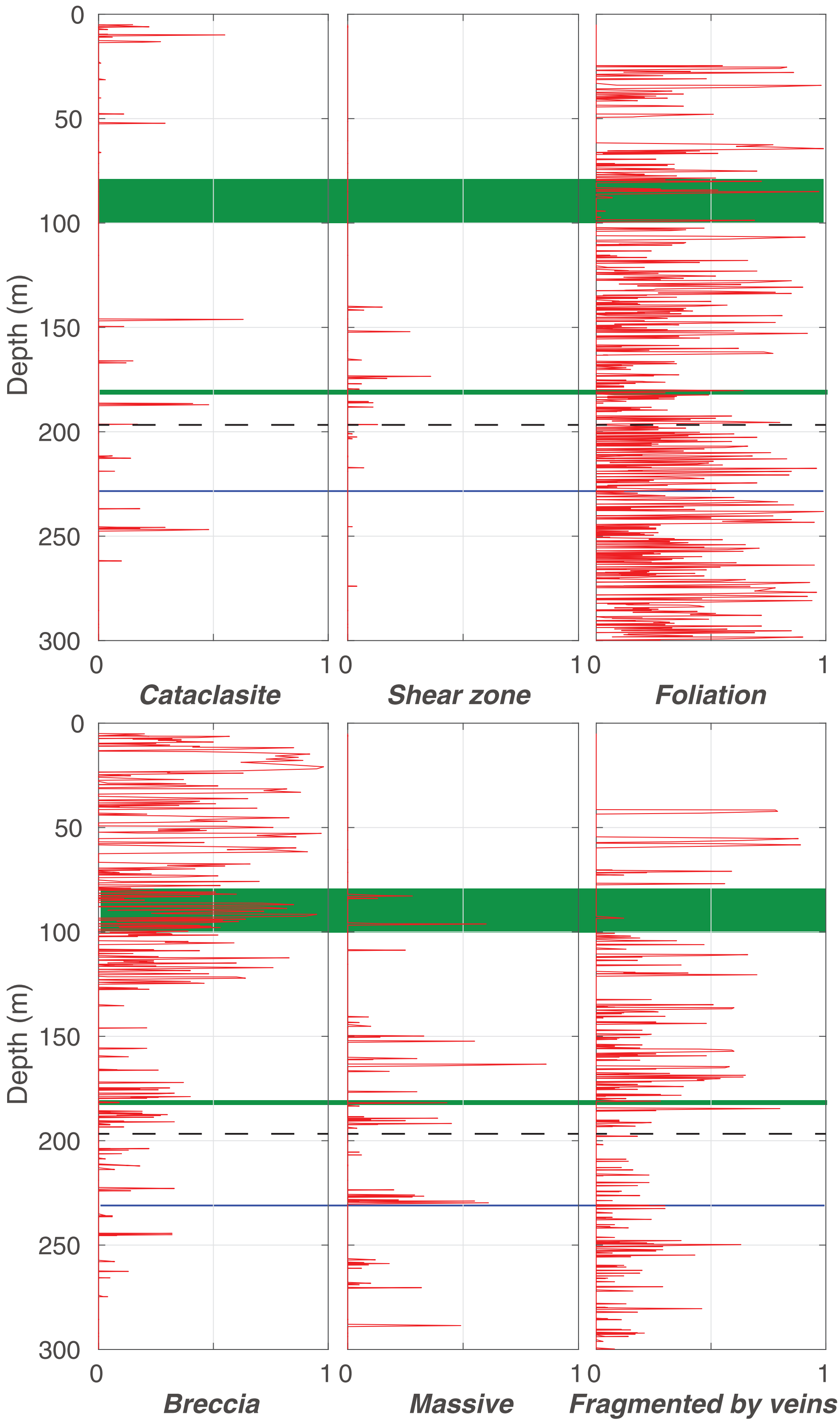

Figure F52. Representative host rock structures (XPL). **A.** Unfoliated massive listvenite with magnesite and quartz (57Z-3, 19–22 cm). **B.** Mesh texture in listvenite defined by Fe oxyhydroxide veins crosscut by carbonate vein (55Z-2, 67–70 cm; thin section [TS]250). **C.** Foliated, oxidized “red” listvenite (15Z-1, 32–35.5 cm; TS215). **D.** Unoxidized “white” listvenite with strong SPO in magnesite and quartz crosscut by carbonate vein (14Z-3, 77–80 cm; TS205). **E.** Sheared serpentinite crosscut by carbonate vein (39Z-2, 34–35.5 cm; TS235). **F.** Foliation in listvenite defined by SPO of carbonate and quartz near the basal thrust (78Z-2, 34–38 cm; TS263).

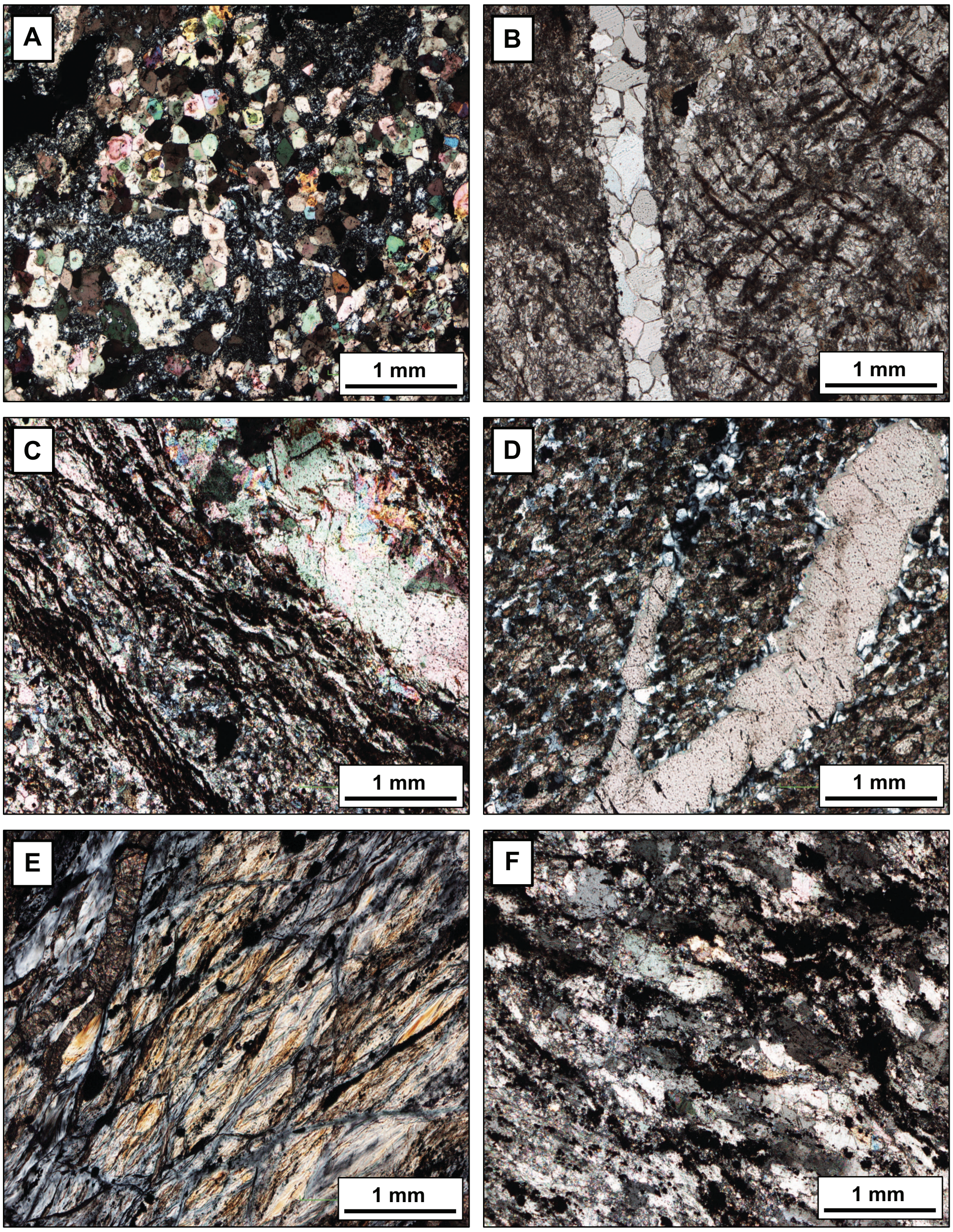

Figure F53. Representative host rock breccias in different lithologies. **A**, **B**. Breccias in listvenite. **C**. Breccia carbonate. **D**. Fuchsite-bearing listvenite. **E**. Serpentinite breccia. **F**. Metasediment breccia in the metamorphic sole.

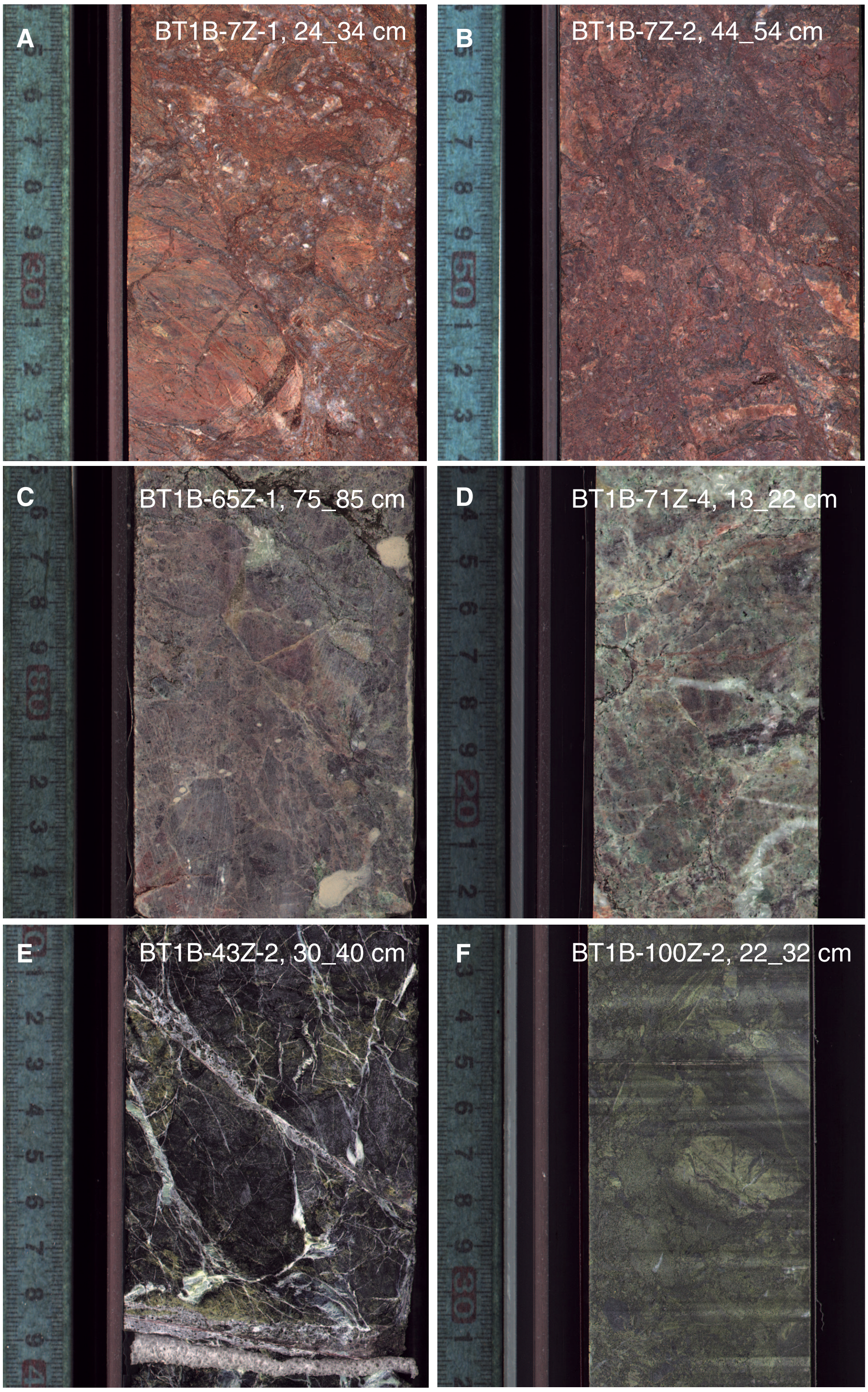

Figure F54. Representative cataclasites in host rocks. **A**, **B**. Listvenite cataclasites. **C**. Serpentinite cataclasite. **D**. Cataclasite with clasts of foliated fuchsite-bearing listvenite and veins. **E**. Cataclasite with clasts of metasediment in the metamorphic sole.

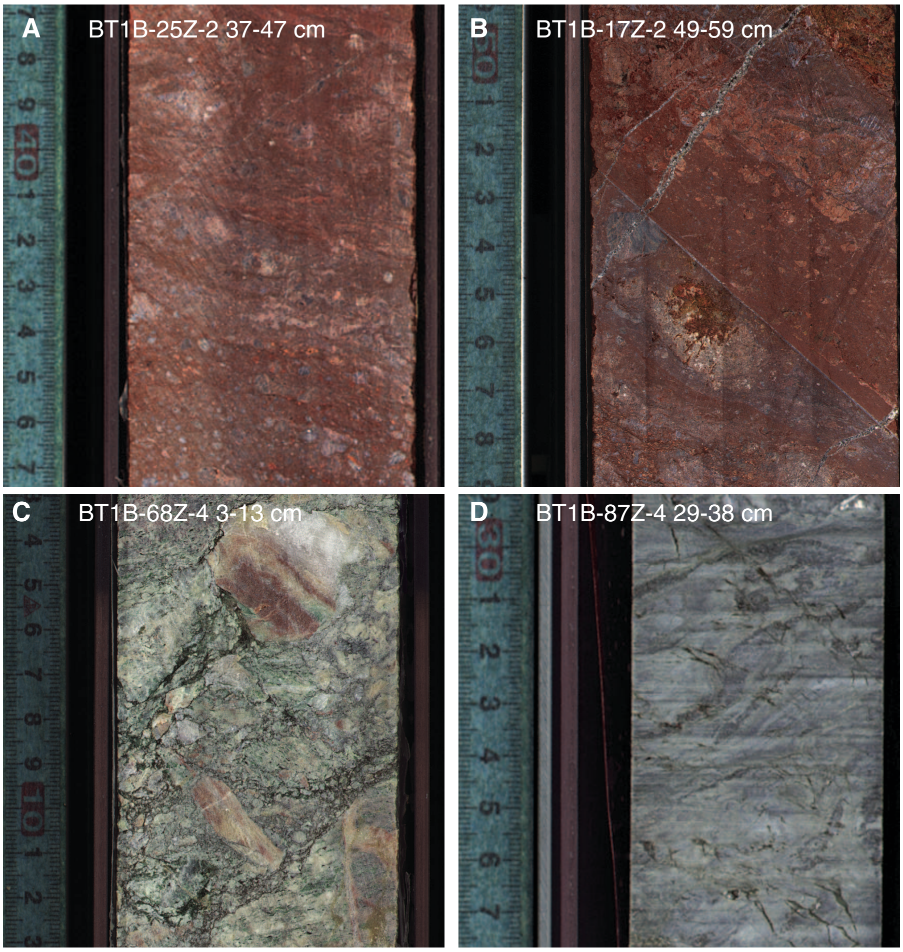

Figure F55. Orientation of localized structures and different vein types plotted as poles to planes for several continuous core sections. The column on the left indicates the depth of discontinuities in the CRF.

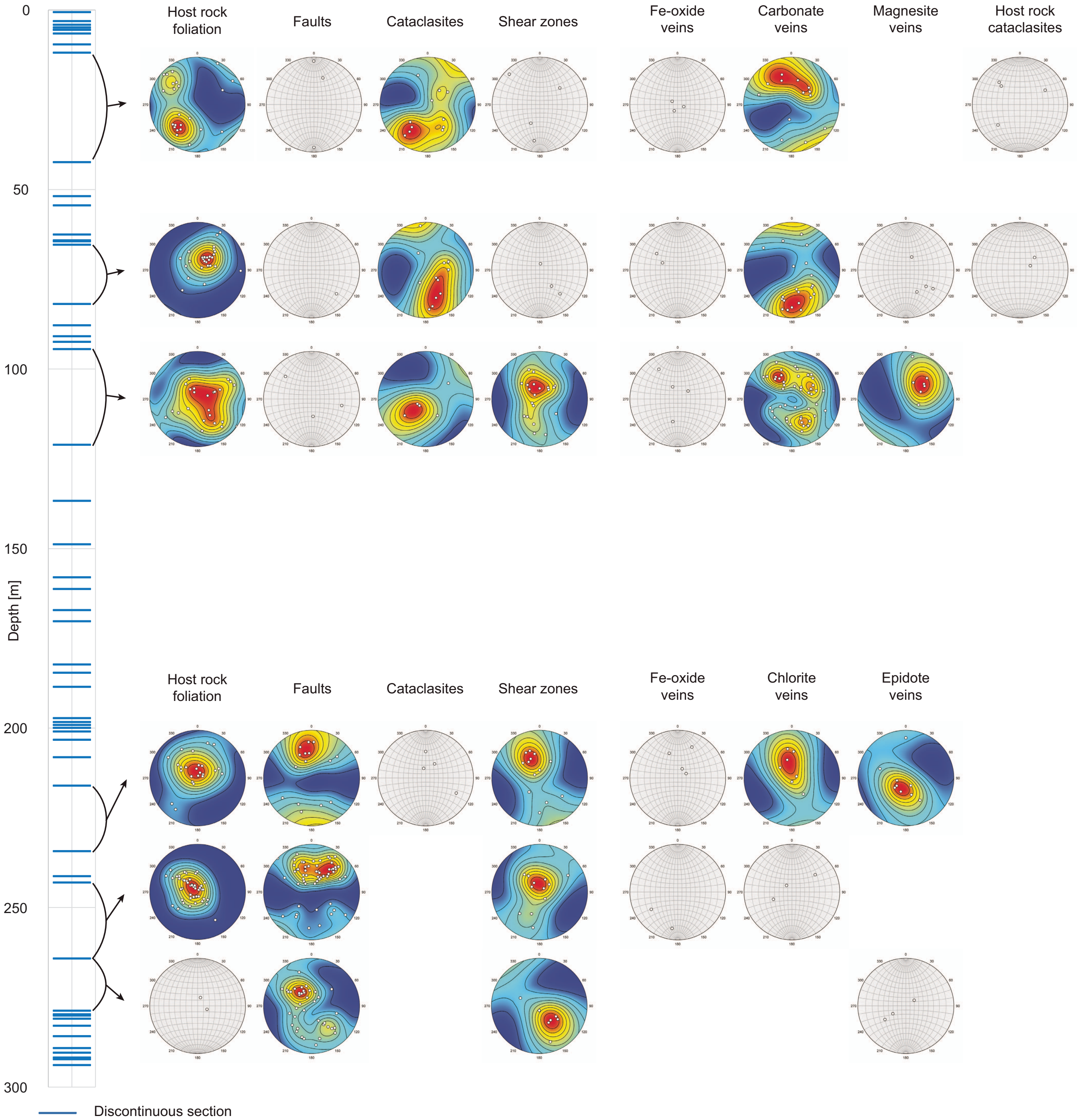

Figure F56. Dip plots for host rock and localized structures downhole. Green = serpentinites, gray = basal thrust.

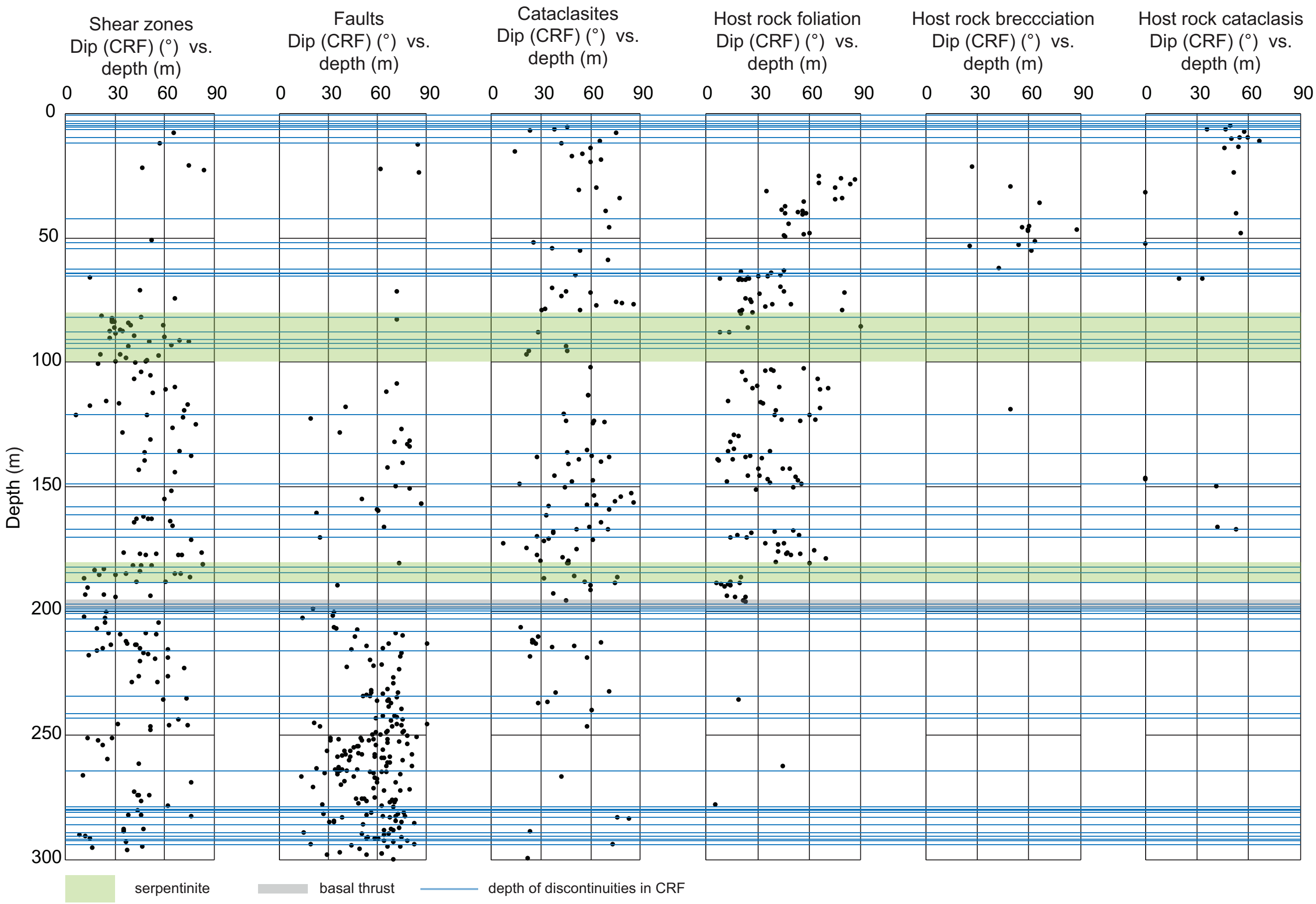

Figure F57. A–E. Dip histograms for foliation above and below the basal thrust (5° bins for 0°–90°).

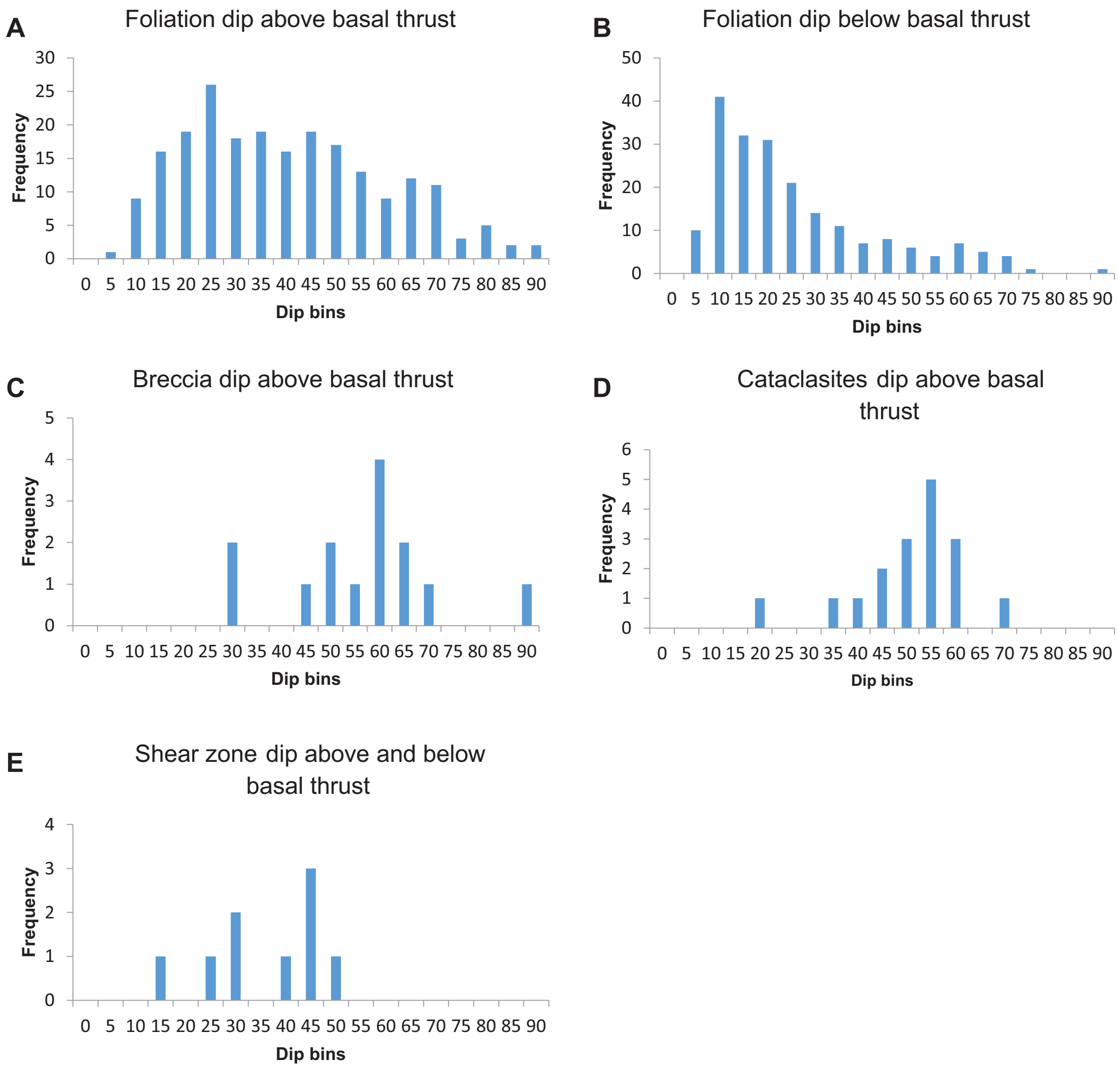

Figure F58. Foliation in host rock structure. **A.** Foliation defined by Fe oxyhydroxide veins in listvenite. **B.** Foliation and fold in listvenite characterized by Fe oxyhydroxide vein. **C.** Foliation in serpentinite. **D.** Foliation characterized by fuchsite and serpentine. **E.** Foliation characterized by elongated fuchsite. **F.** Foliation of metasediment in the metamorphic sole.

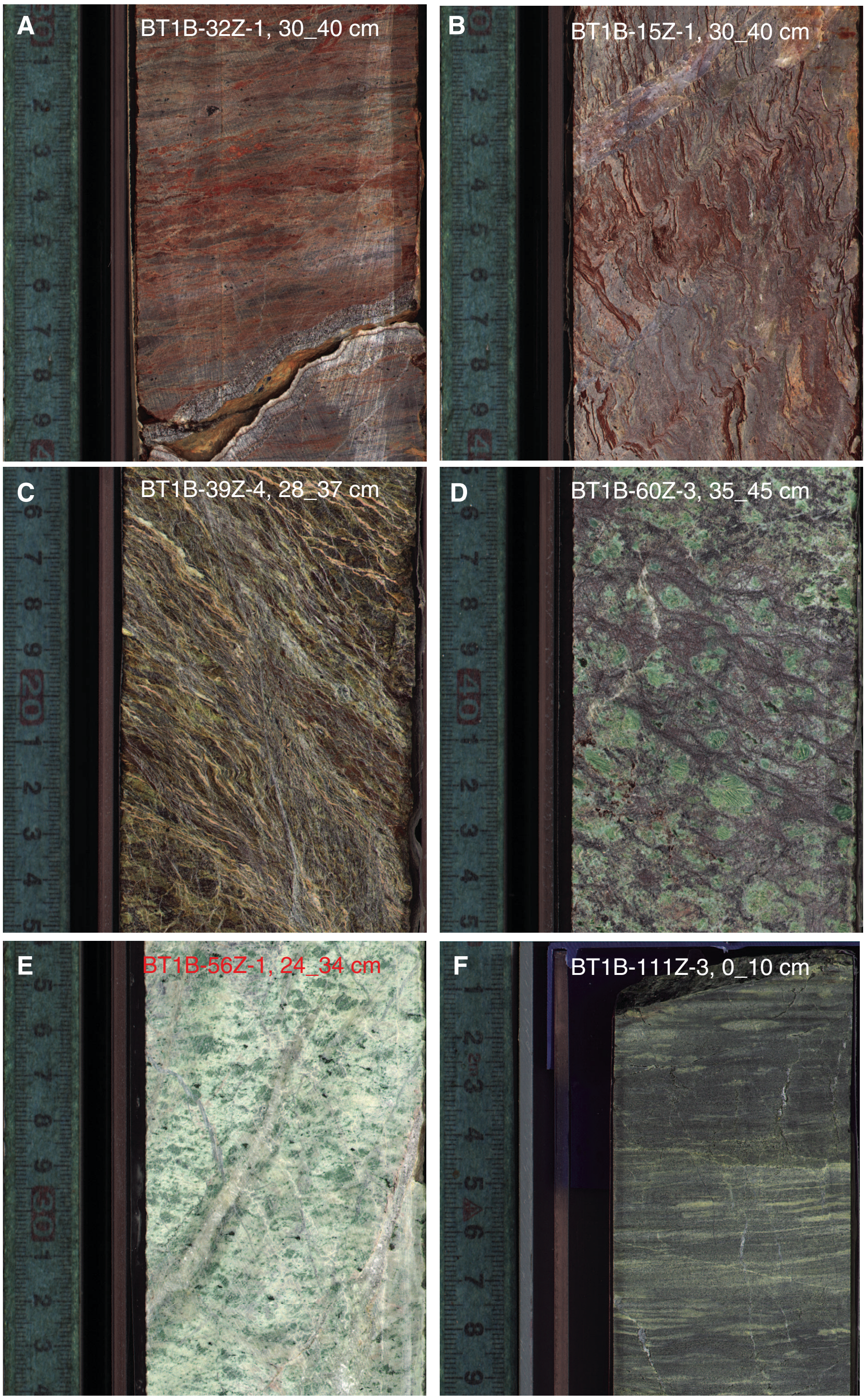

Figure F59. Representative foliation in the metamorphic sole (XPL). **A.** Schistosity developed by segregation of carbonate + albite and epidote-rich intervals in metabasic rocks. Foliation defined by SPO of deformed phases (97Z-2, 28–30 cm; TS267). **B.** Cleavage developed by segregation of quartz and mica-rich layers in metasediments (82Z-1, 65–69 cm; TS265). **C.** Microfolding in blue-green amphibole (88Z-2, 63–66 cm; TS262). **D.** Isoclinal folding contained within the foliation defined by alternating oxide-rich and albite + epidote ± quartz. Crosscut by later chlorite + albite vein (82Z-1, 65–69 cm; TS265).

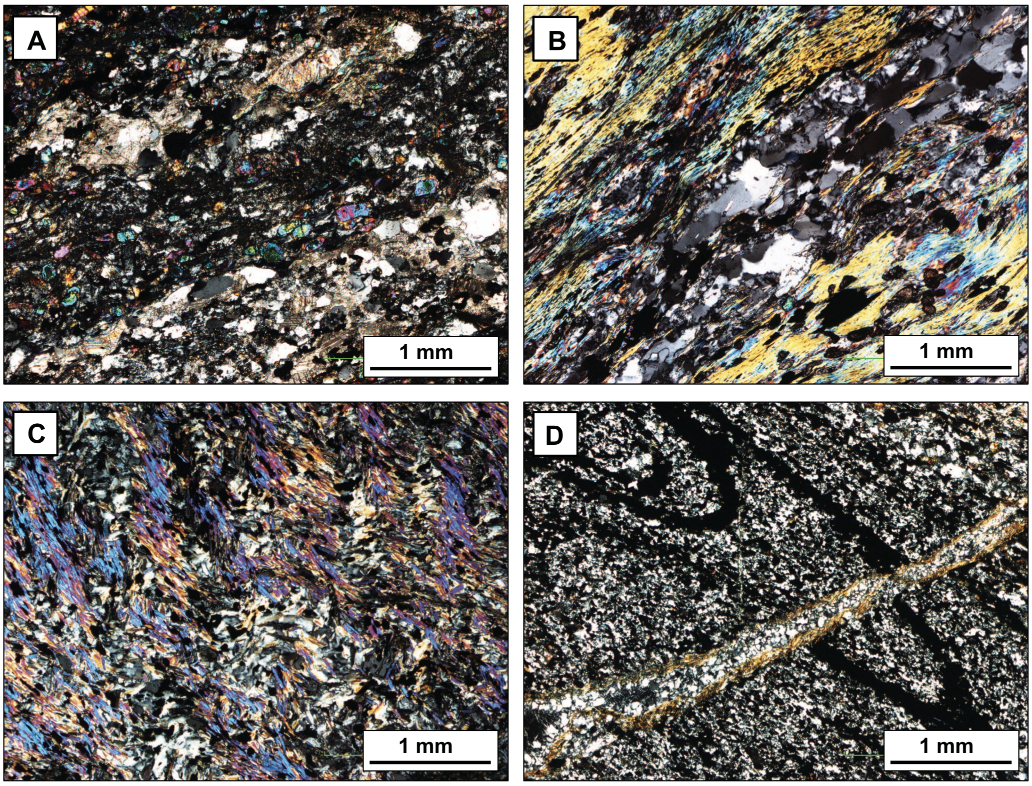

Figure F60. Intense shearing and folding of the foliation is evidenced by (**A**) a sheath fold, (**B**) folding of the original foliation/veins, and most commonly, (**C**) folding of just the host rock foliation.

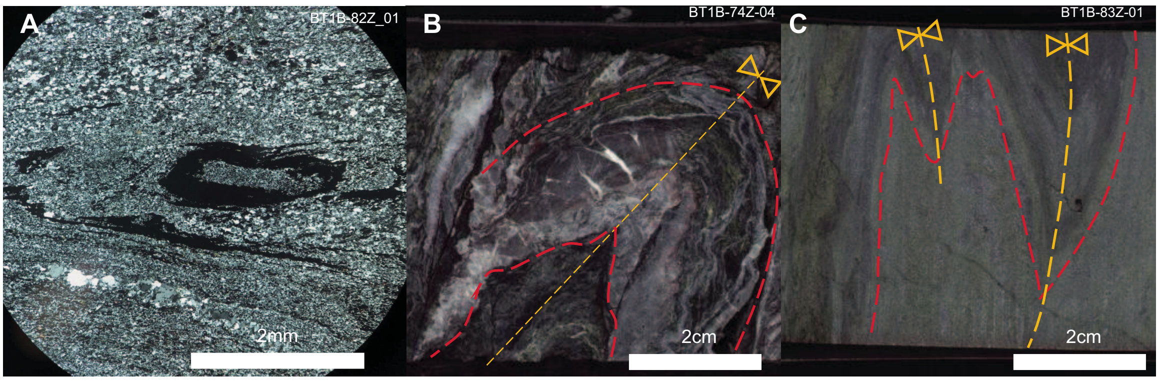

Figure F61. Fragmented host rock disrupted by veins. **A, B**. Host rock fragmented by vein in listvenite. **C**. Host rock fragmented by vein in serpentinite.

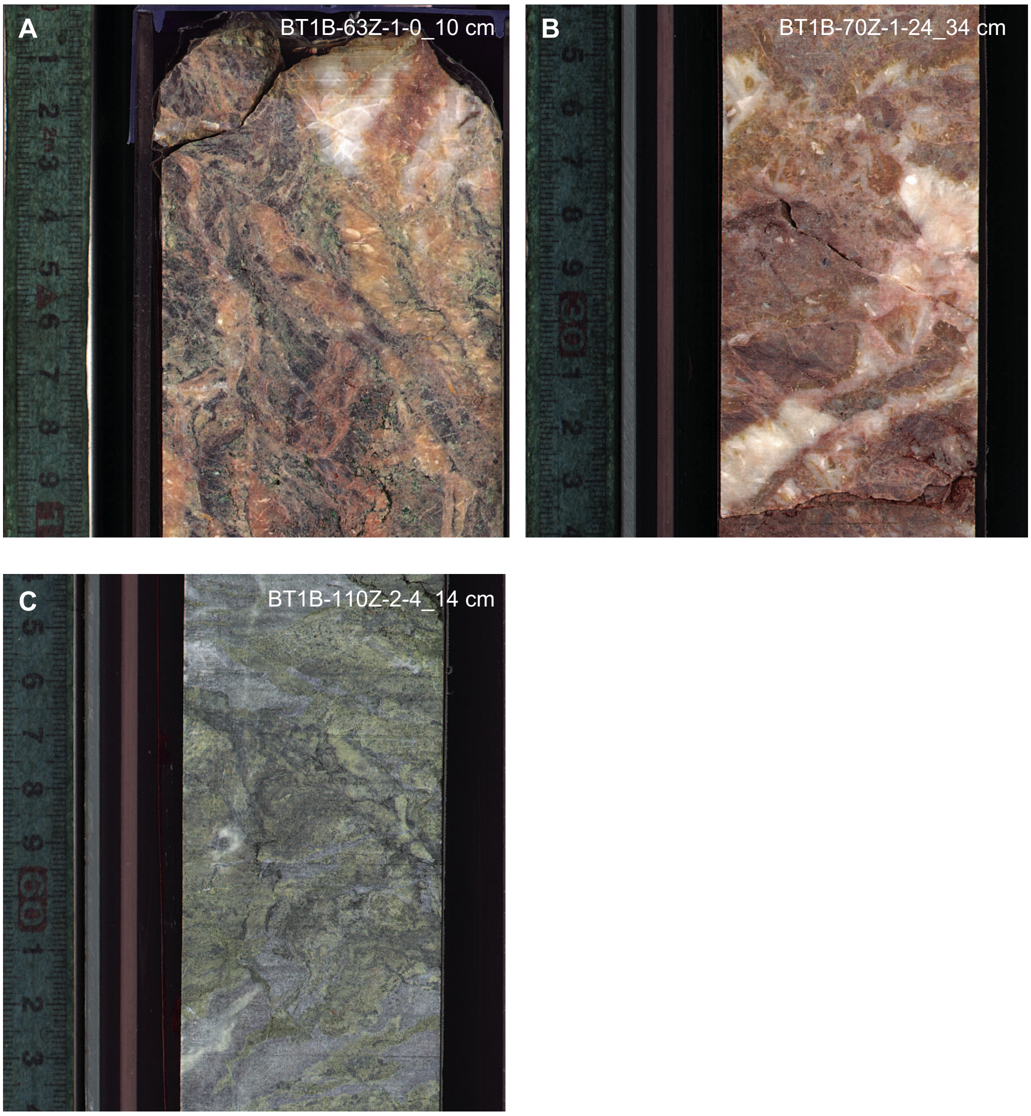

Figure F62. Frequency of localized brittle structures and different vein types per meter. Green = serpentinite layers, gray = basal thrust.

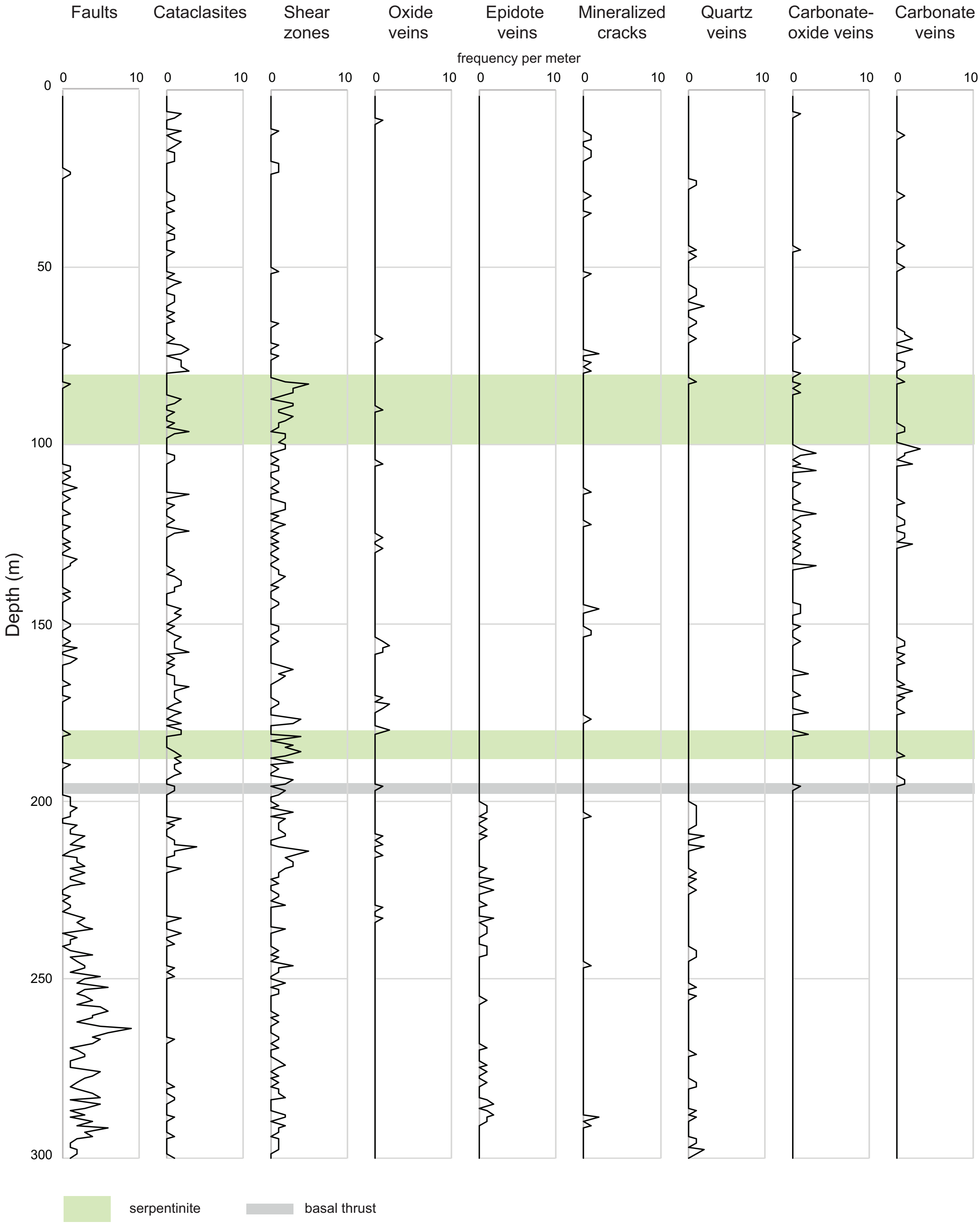

Figure F63. Dip histograms for localized brittle structures and different vein types in listvenites and serpentinites above the basal thrust.

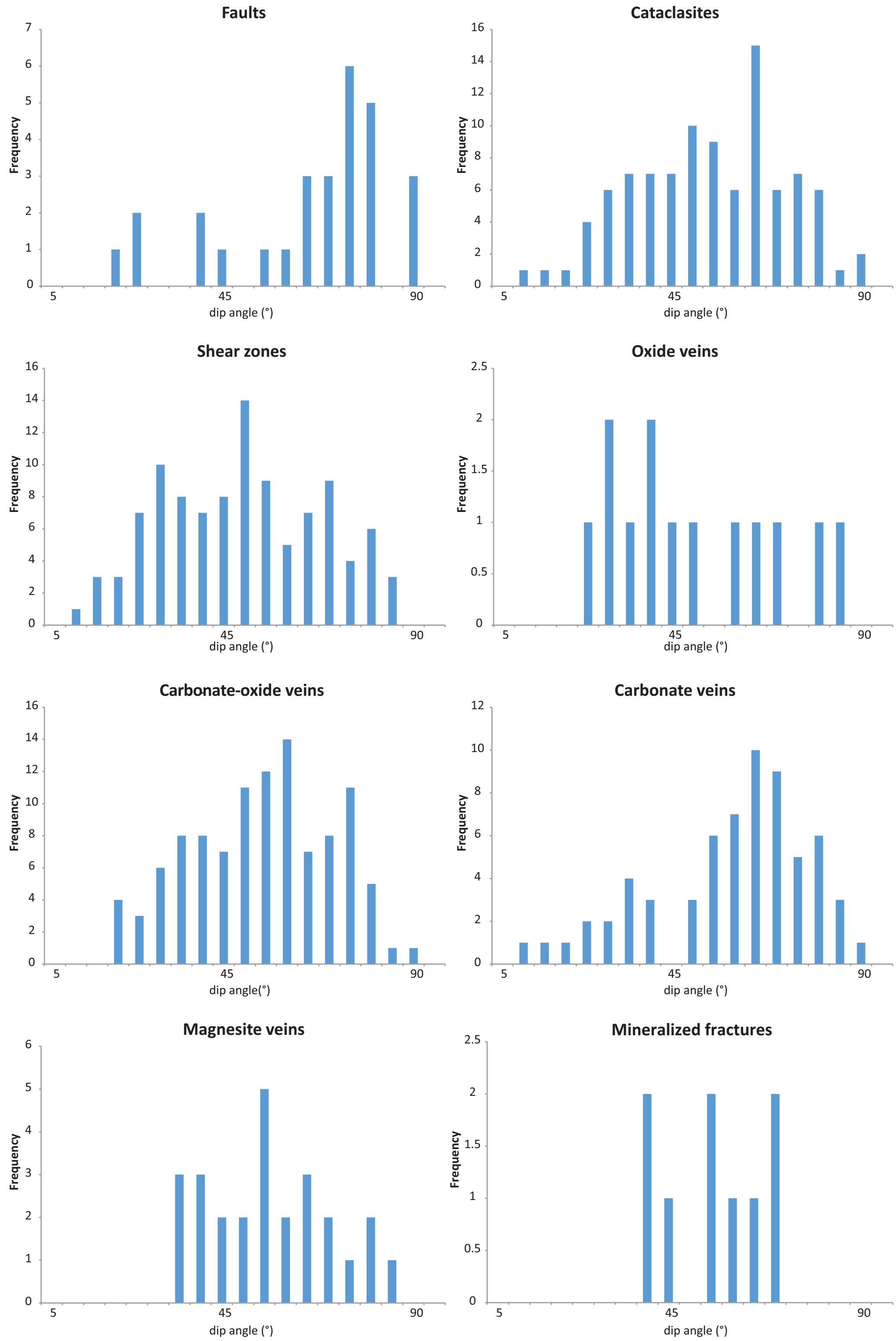

Figure F64. Dip histograms for localized brittle structures and different vein types in metamorphic sole below the basal thrust.

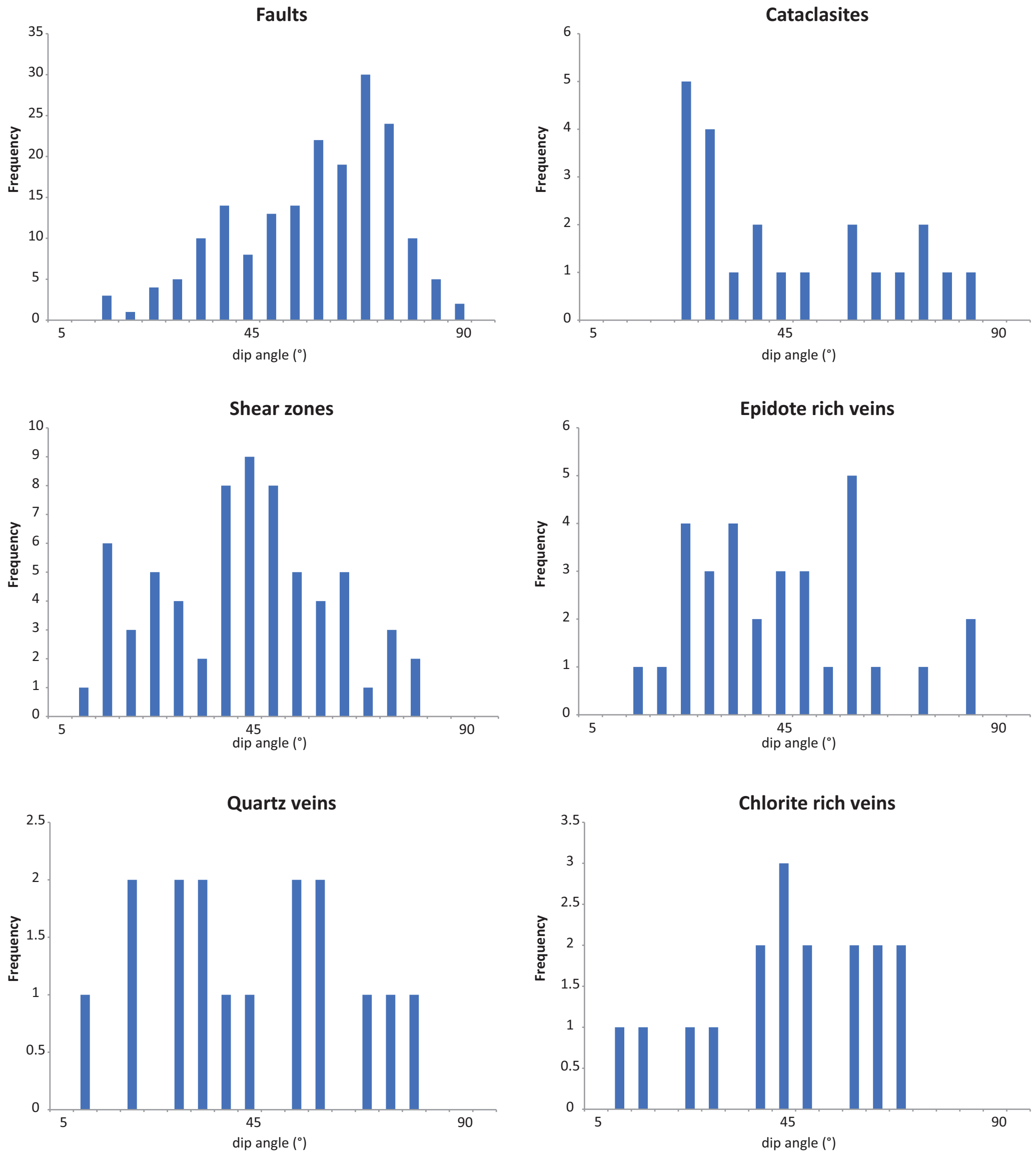

Figure F65. Dip plots for different vein types downhole. Green = serpentinites, gray = basal thrust.

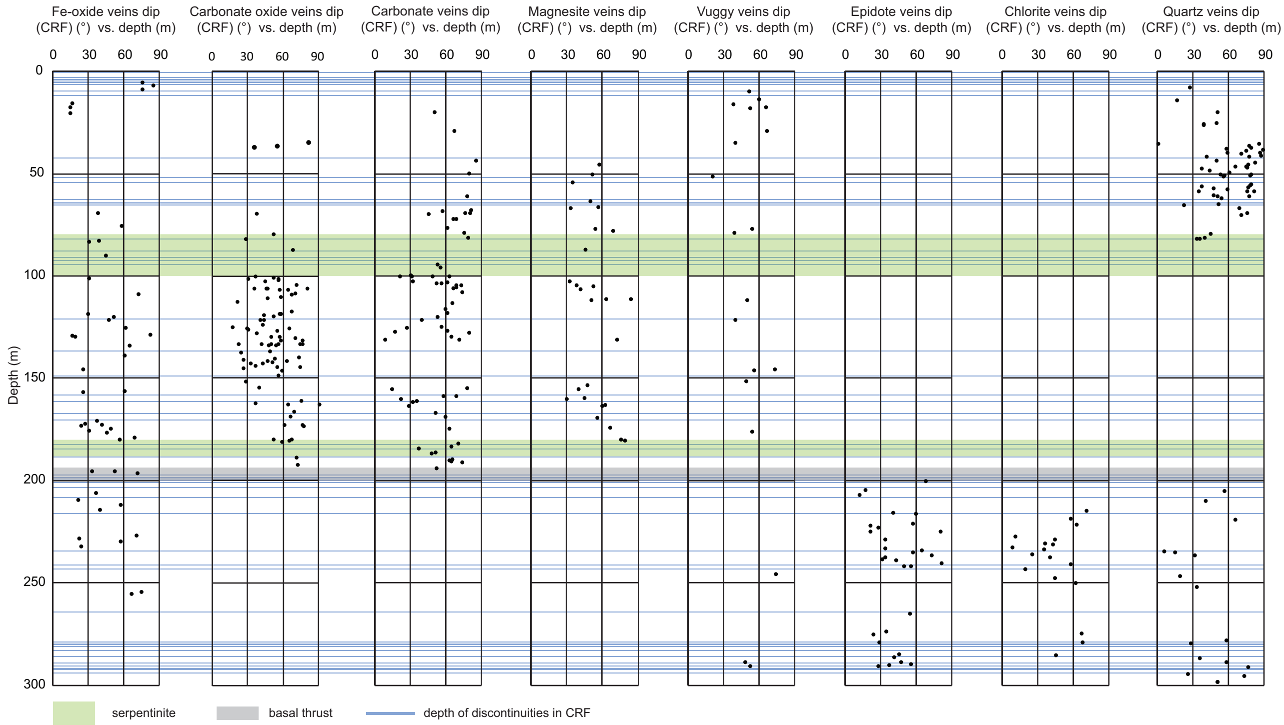

Figure F66. A. Veins in listvenite showing early Fe oxyhydroxide veins that define a foliation, crosscut by carbonate ± silica veins, crosscut by late magnesite veins (24Z-3, 30–47 cm). **B.** Veins in the metamorphic sole (86Z-1, 24–35 cm). Variable degrees of transposition of early epidote-quartz veining and late crosscutting by chlorite veins. **C.** Veins in serpentinites. Mesh textures are defined by carbonate and Fe oxyhydroxide veins (43Z-5, 4–16 cm). Shearing of these features and/or addition of more carbonate + Fe oxyhydroxide + serpentinite veins creates the main foliation. Late crosscutting semibrittle cataclasites and brittle faulting are also shown.

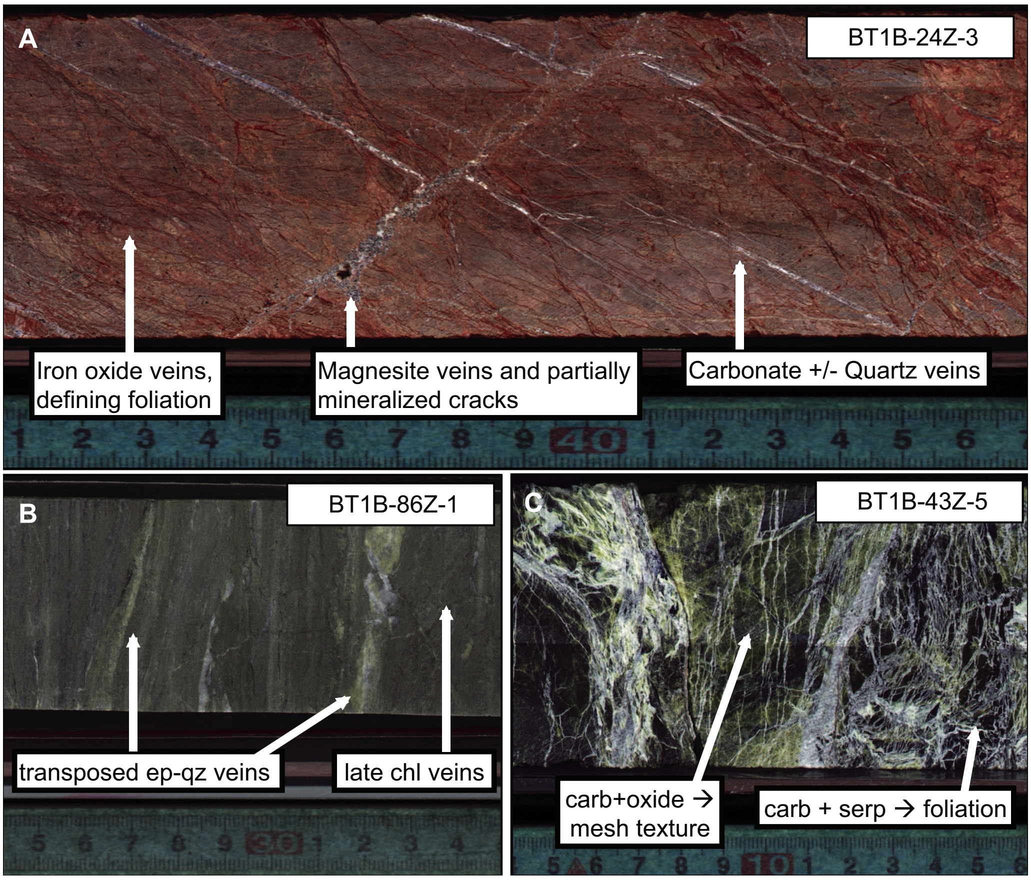

Figure F67. Carbonate vein with sharp contact to debris assemblage in originally open fracture. We infer that supersaturated fluid slowly mineralized the open space and cemented the debris in place and that the paleo-horizontal direction is still visible as the inclination of the contact. Single layer of quartz crystals on contact (32Z-2, 26–30.5 cm; TS234).

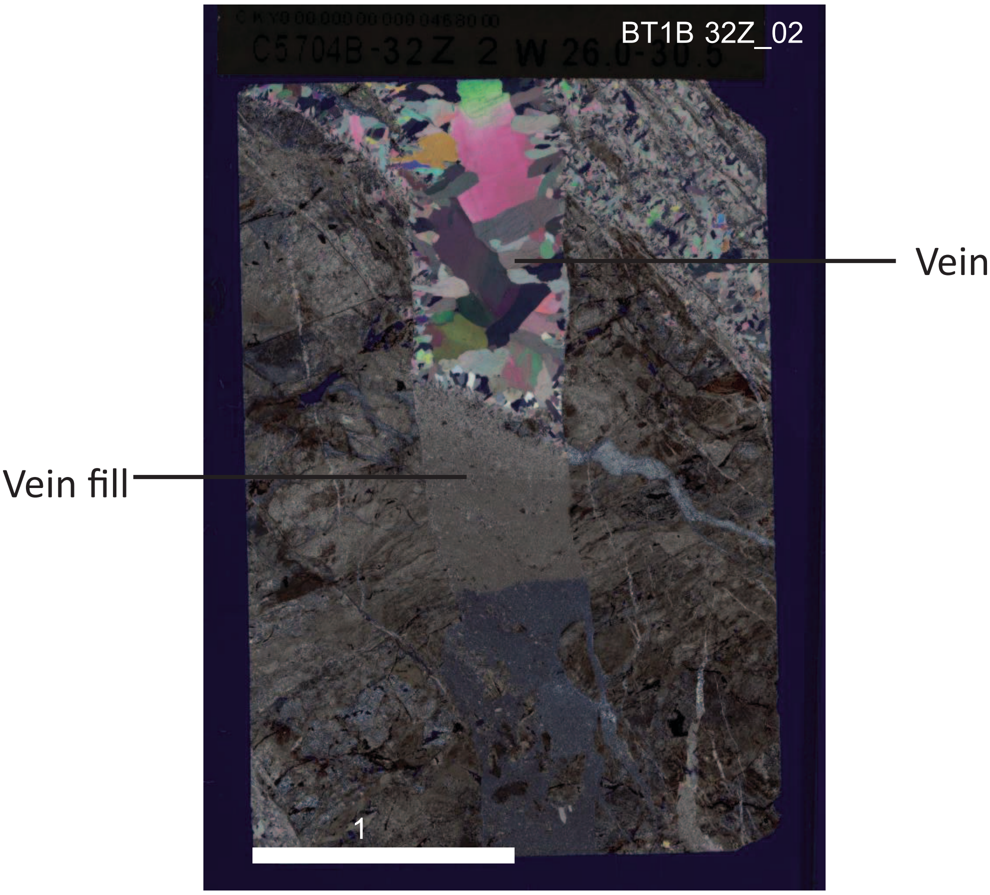

Figure F68. Fragmented carbonate veins deformed by faulting and shearing.

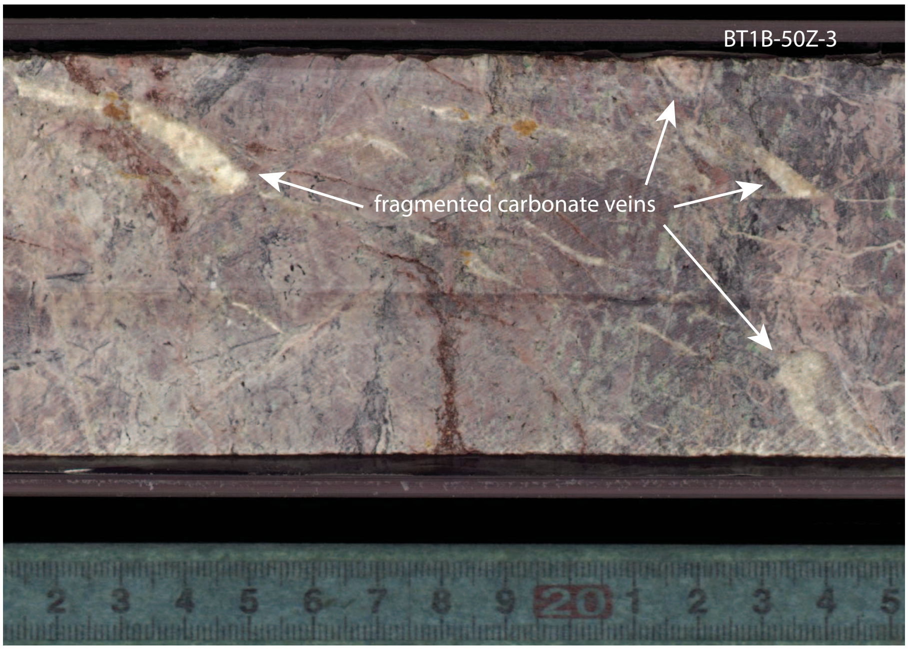

Figure F69. Representative cataclasites in host rock structure. **A.** Planar fault in listvenite cutting cataclastic breccia (see also Figure F54). **B.** Fault morphology in serpentinites is similar to those in the listvenites planar to splaying slip planes with cataclastic fault rocks. **C.** Faults in the metamorphic sole appear as abundant small-scale deformation features often splaying and with only few millimeters displacement. **D.** Close-up of fault shown in (A). Fault consists of a bright, completely planar carbonate vein along the faulted contact between two different types of breccia (17Z-2, 55–60 cm; TS217; XPL). **E.** Serpentinite cut by Fe oxyhydroxide veins and then faulted. Fault is mineralized with serpentine vein crosscut by late carbonate veins (74Z-1, 59–62 cm; TS258; XPL). **F.** Shear fault in metasediments. Assemblage of oxides and cataclastic grain size reduction along the fault (97Z-2, 28–30 cm; TS270).

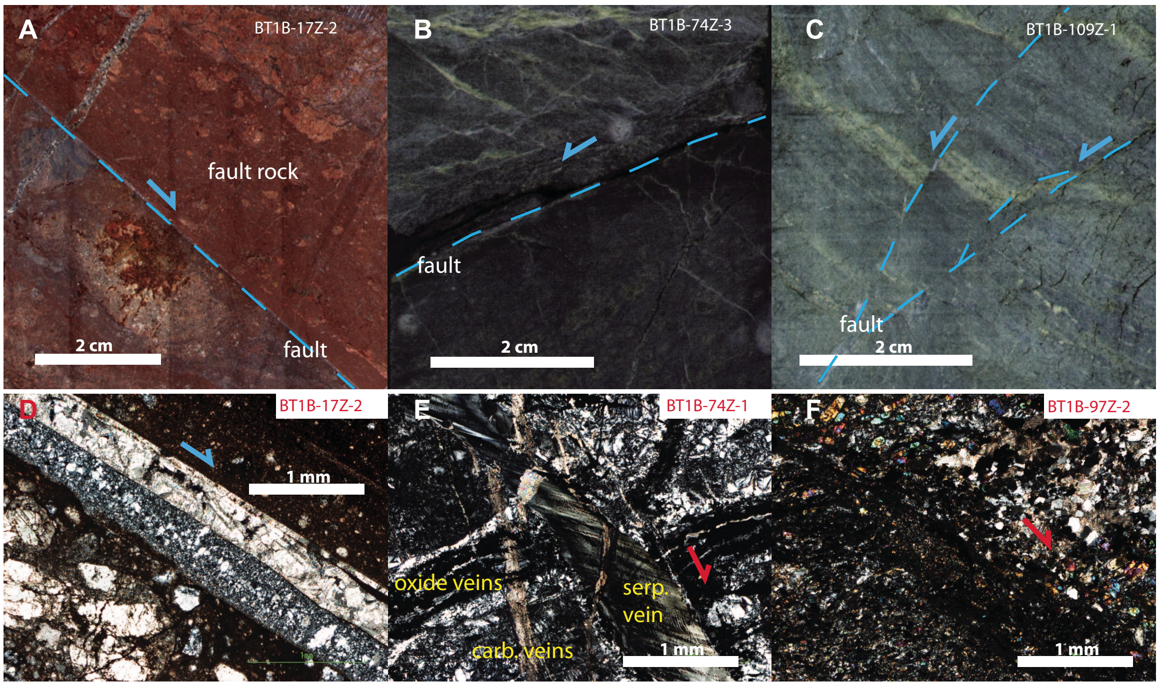

Figure F70. **A.** Centimeter-scale cataclasite in listvenite, fine-grained with some larger rounded clasts. **B.** Cataclasite in serpentinite associated with a high density of thin quartz veins. **C.** Thin cataclasite in the metamorphic sole outlined by red solid line. **D.** Microscale image of a cataclasite in listvenite. Cataclasite appears as darker band with fine grained oxide-rich matrix and larger rounded clasts (7Z-2, 76–79 cm; TS201; XPL). **E.** Cataclasite in metasediment is associated with high oxide contents and grain size reduction (97Z-2, 28–30 cm; TS270; XPL).

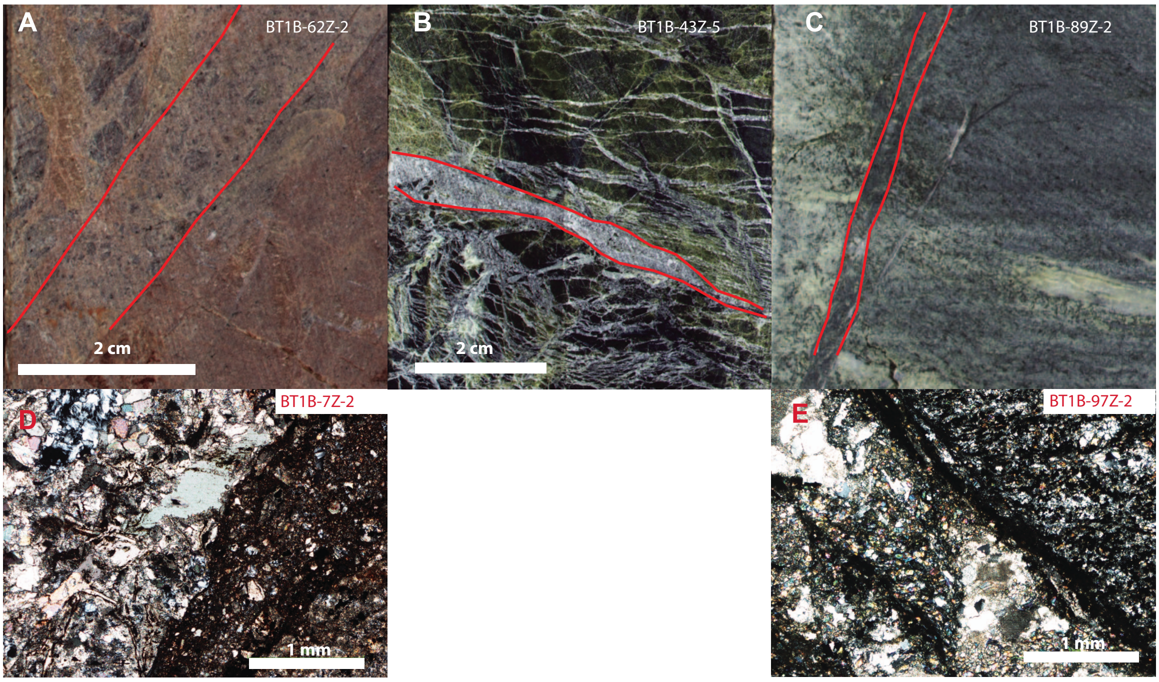

Figure F71. **A.** Shear zones in listvenite are abundant, commonly composed of thin zones of concentrated fine-grained red oxidized material derived from cataclastic grain size reduction of host rock material. **B.** Shear zones in serpentinite are defined by bundles of thinly spaced anastomosing quartz veins. **C.** Shear zones in the metamorphic sole often include a concentration of oxide minerals in thin foliated bands.

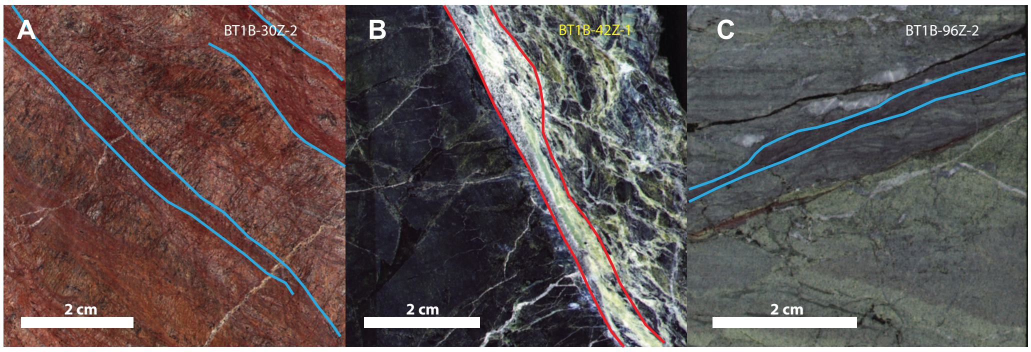

Figure F72. **A.** Folds in listvenite are rare; those few we observed show fold foliation or early Fe oxyhydroxide veins. **B.** Folded carbonate vein in the metamorphic sole cut by a fault. **C.** Folds in the metamorphic sole are mostly shear folds with fold axis planes roughly parallel to the lineation. **D.** Close-up of A. Fe oxyhydroxide veins are folded in fine-grained cataclastic matrix (15Z-1, 32–35.5 cm; TS216; XPL with gypsum plate). **E.** Close-up of C. Shear folds in metasediments defined by black oxide bands and crosscut by late quartz-chlorite vein (83Z-1, 37–40 cm; TS259; PPL).

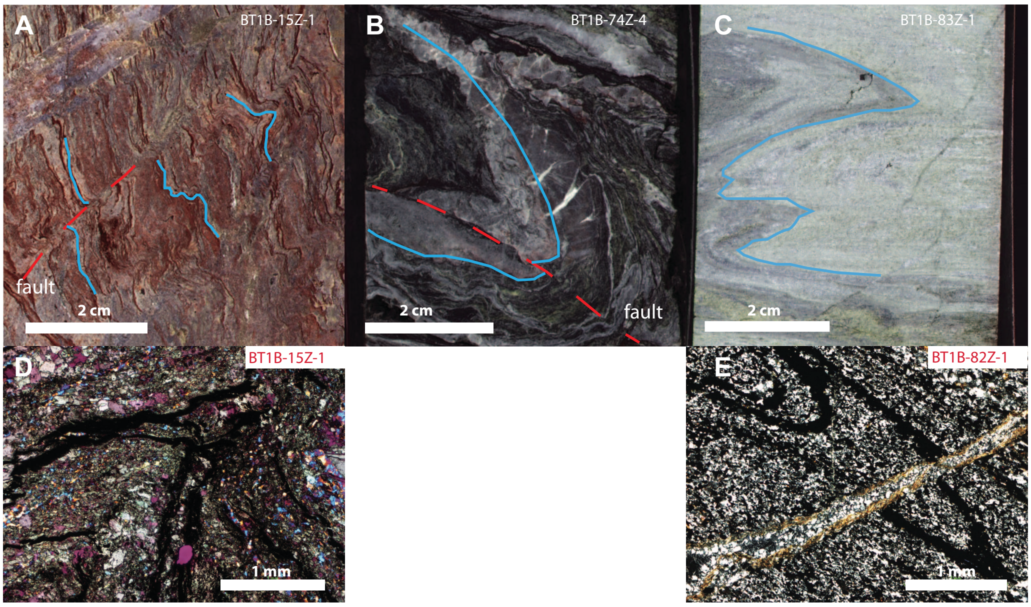

Figure F73. Multiple styles of folding in the metamorphic sole. **A.** Earliest stages of folding are ductile. Axial planes of isoclinal folds are parallel to foliation. Quartz shows subgrain formation, and micas are kinked (TS265; XPL). **B.** Late-stage folding is associated with brittle faults in the metabasic rocks (TS272; PPL).

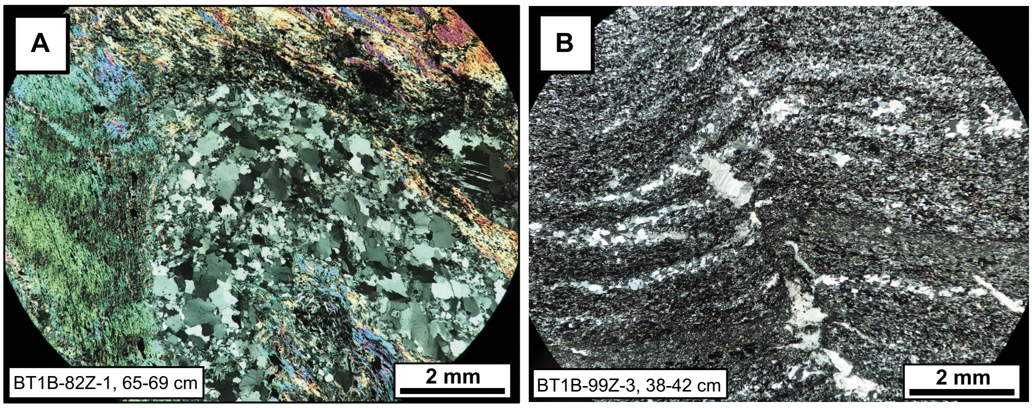

Figure F74. **A.** Vugs in veins in listvenite lined with euhedral carbonate crystals. **B.** Partially mineralized crack showing syntaxial crystal growth (31Z-4, 12–14.5 cm; TS232; PPL).

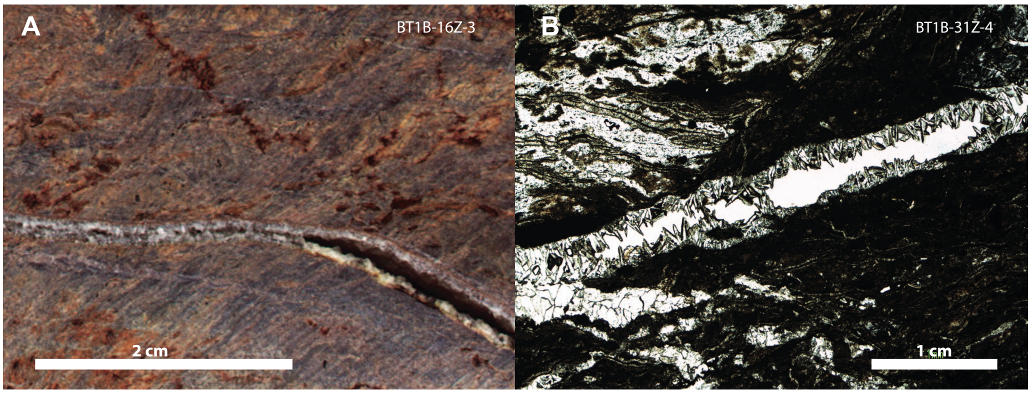

Figure F75. **A–C.** Relative age relationships including four generations of veining, cataclasites, shear zones, faults, and mineralized fractures in Hole BT1B.

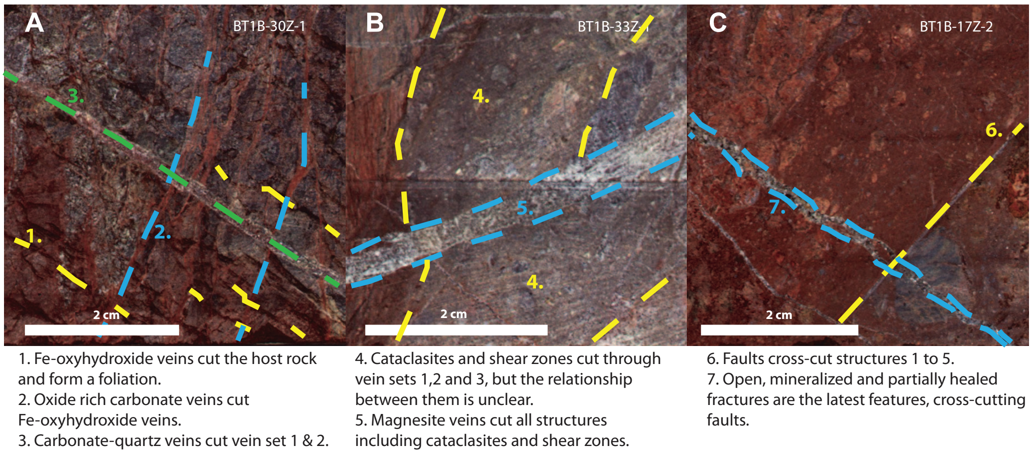

Figure F76. Histograms showing the occurrence of structural features and vein types in Hole BT1B as deformation generations D1, D2, and D3, where D1 is the oldest feature subsequently crosscut by D2 and D3.

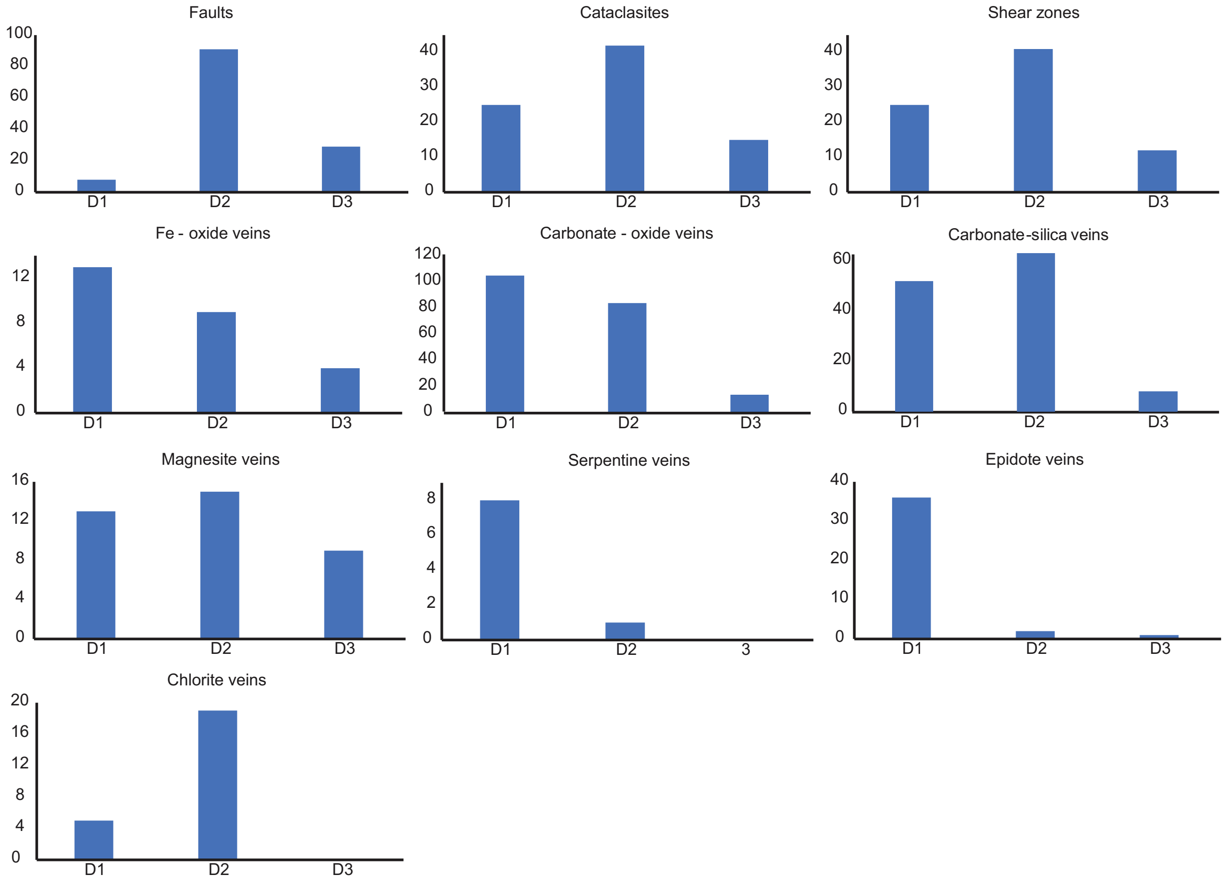

Figure F77. CO_2, H_2O, and inorganic carbon vs. LOI by lithology, Hole BT1B.

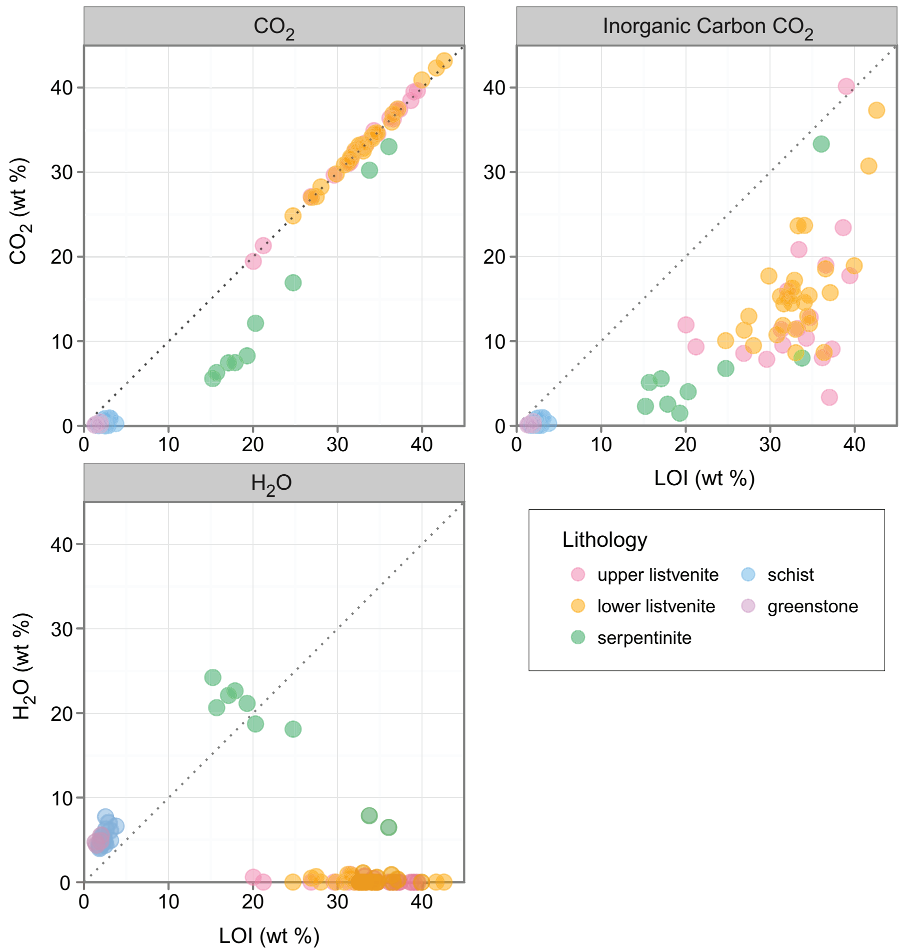

Figure F78. Calculated magnesite vs. relative abundance of magnesite determined by XRD, and calculated dolomite content vs. relative abundance of dolomite determined by XRD in Hole BT1B.

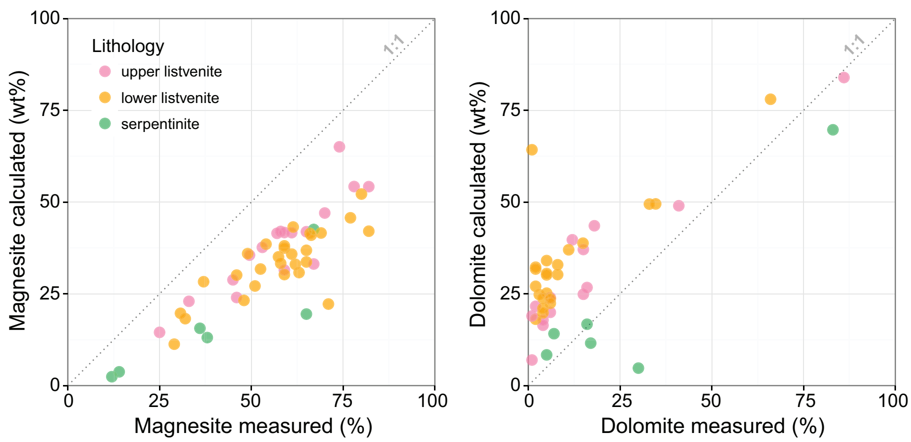

Figure F79. Downhole plots of lithology, LOI, Mg# (cationic Mg/[Mg + Fe]; calculated assuming all Fe as FeO), Al_2O_3, TiO_2, K_2O, and CaO in Hole BT1B. The average composition of Oman peridotites is shown for comparison (gray line; Godard et al., 2000; Hanghoj et al., 2010).

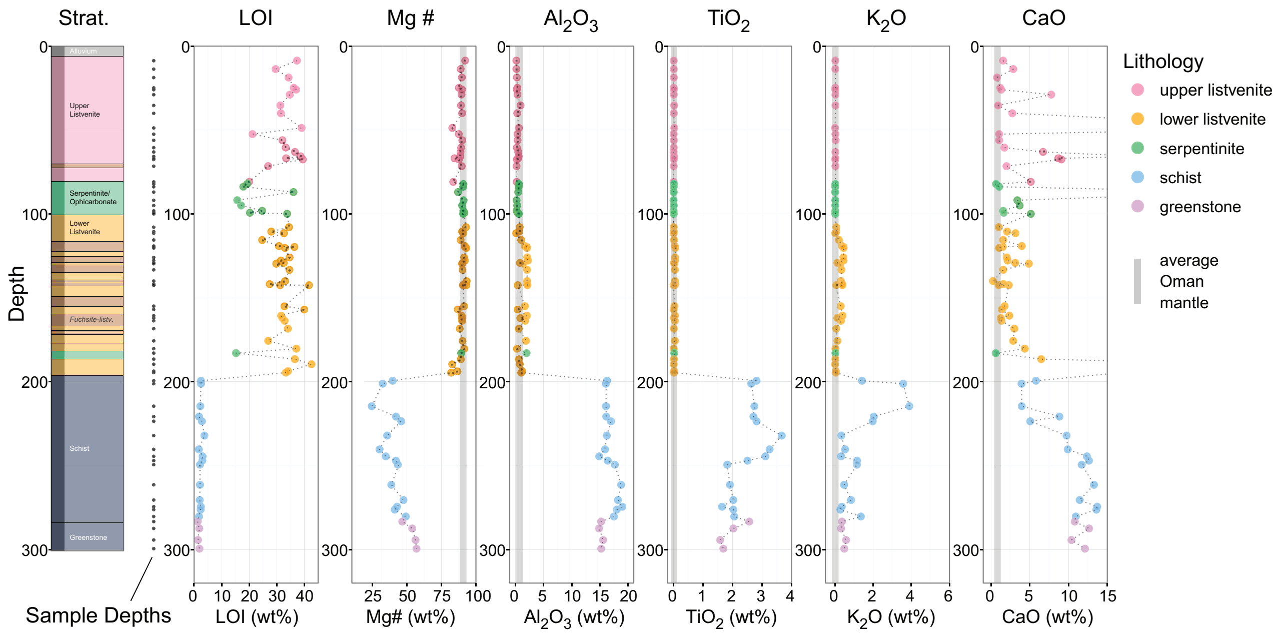

Figure F80. Downhole plots of lithology, Ni, Cr, Sc, Sr, and Y in Hole BT1B. The average composition of Oman peridotites is shown for comparison (gray line; Godard et al., 2000; Hanghoj et al., 2010).

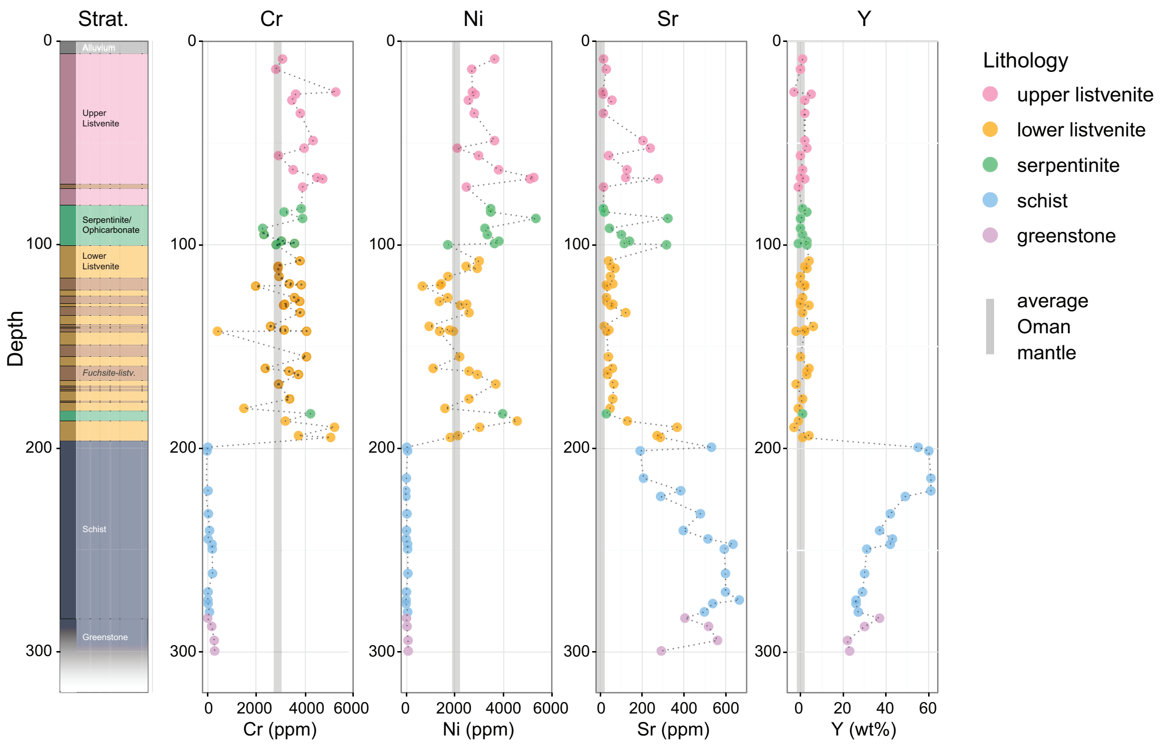

Figure F81. Molar MgO vs. molar SiO_2; molar MgO + CaO vs. molar SiO_2; and Mg# vs. molar SiO_2. The average composition of Oman peridotites is shown for comparison (blue dot; Godard et al., 2000; Hanghoj et al., 2010).

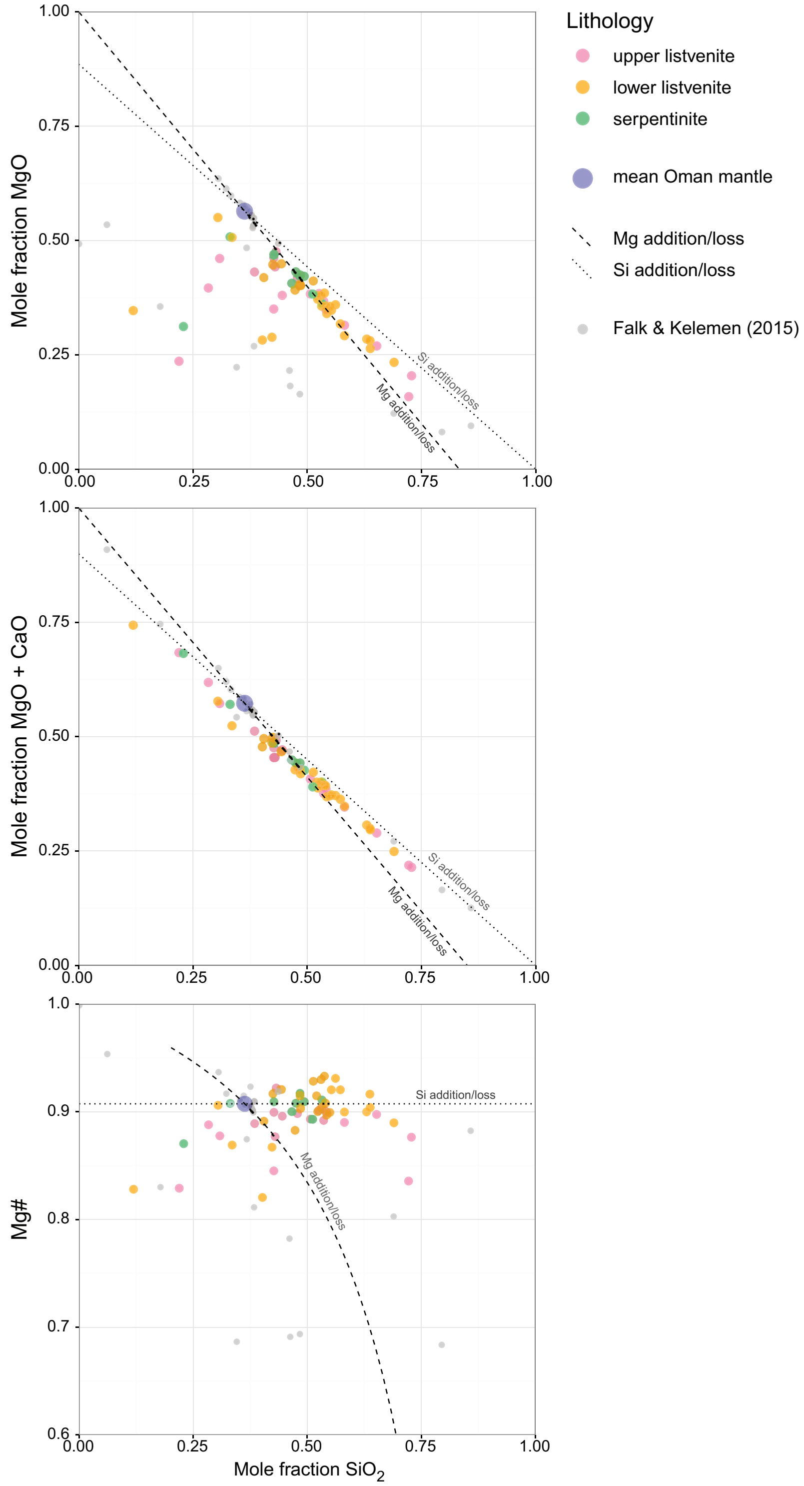

Figure F82. Downhole plots of lithology, Mg# (cationic Mg/[Mg + Fe]; calculated assuming all Fe as FeO), Al_2O_3, TiO_2, and K_2O in Hole BT1B. The average composition of Oman peridotites is shown for comparison (gray line; Godard et al., 2000; Hanghoj et al., 2010).

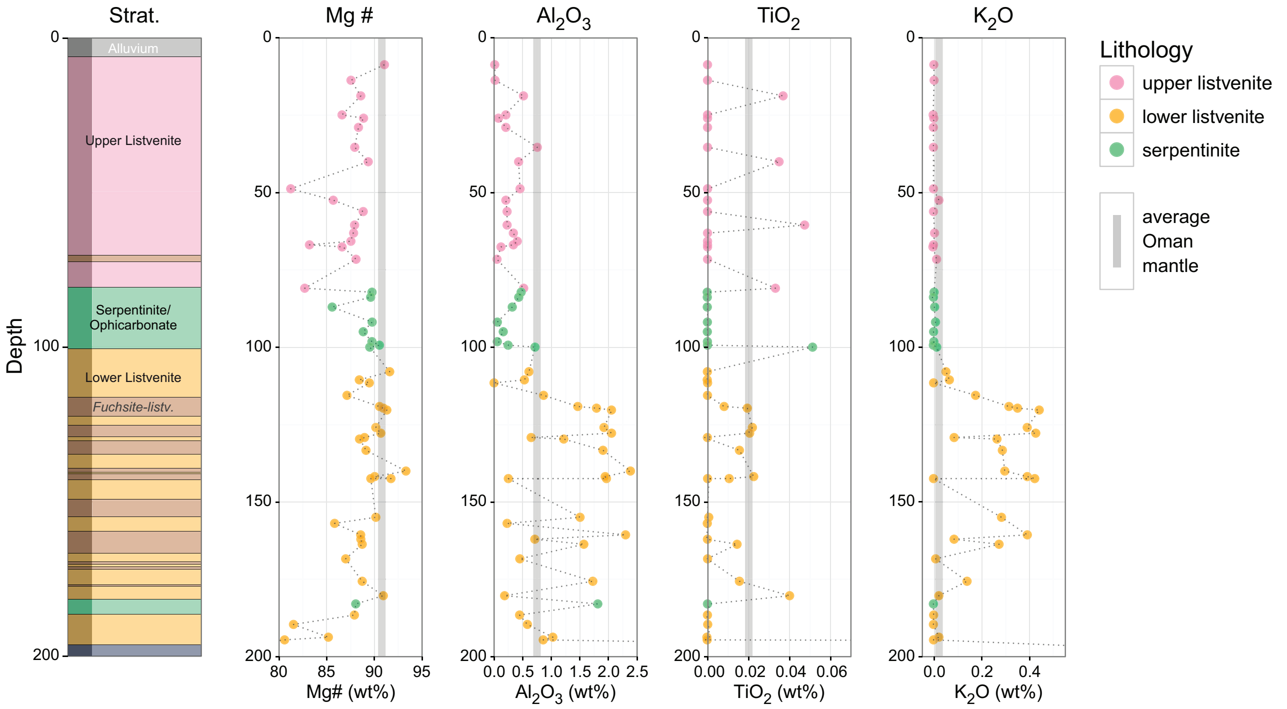

Figure F83. Downhole plots of lithology, Ni, Cr, Sc, and Sr in Hole BT1B. The average composition of Oman peridotites is shown for comparison (gray line; Godard et al., 2000; Hanghoj et al., 2010).

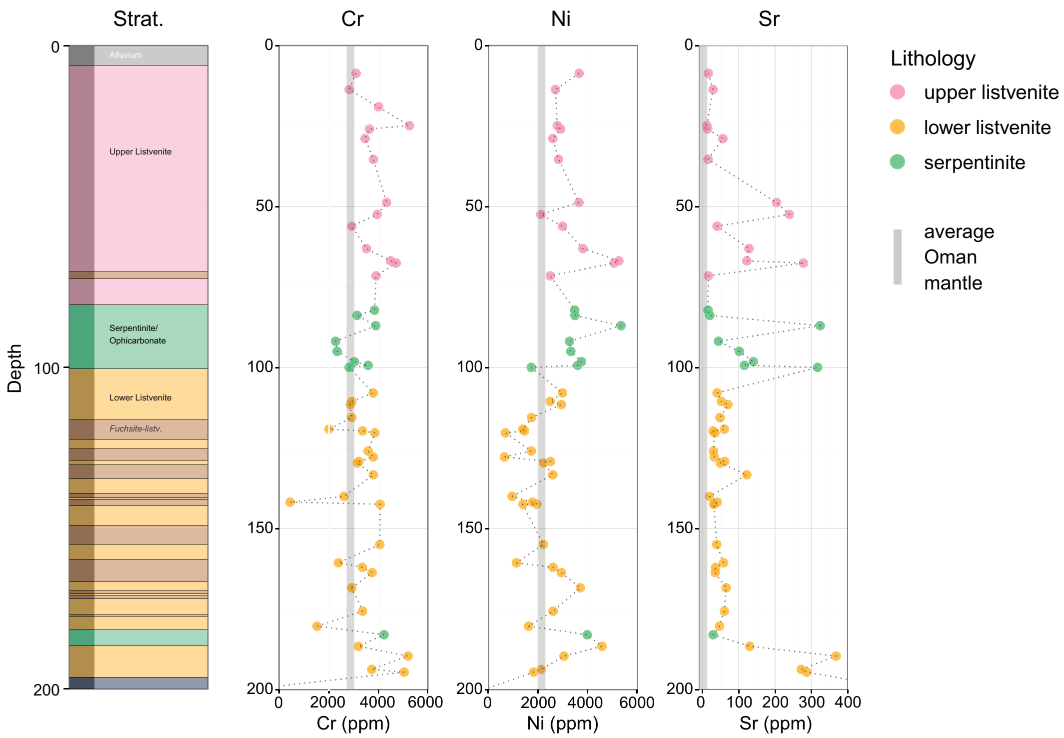

Figure F84. Trace element composition of samples recovered from Hole BT1B normalized to the average composition of Oman peridotites (Godard et al., 2000; Hanghoj et al., 2010).

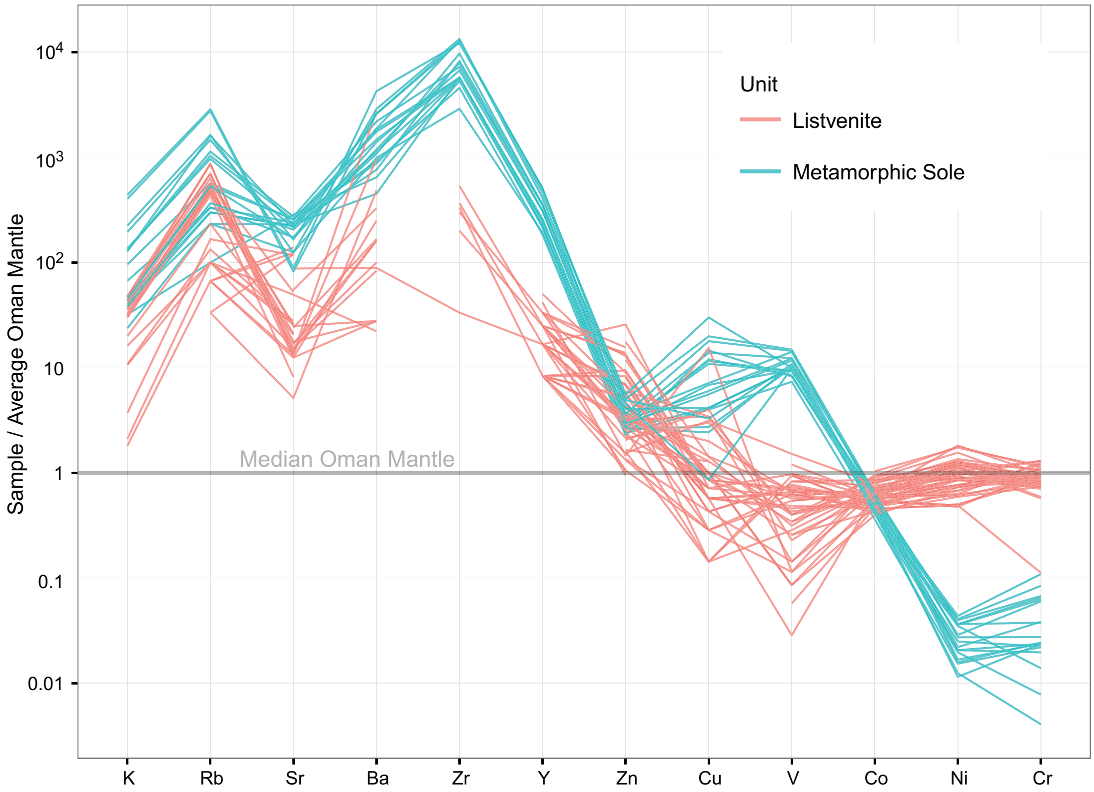

Figure F85. A. Downhole plots of discrete bulk magnetic susceptibility, NRM intensity, and Königsberger ratios. Light green horizontal bars = two thin serpentinite bands, black dashed line = depth of the basal thrust. **B**. Histograms of bulk susceptibility, NRM intensity, and *Q* values.

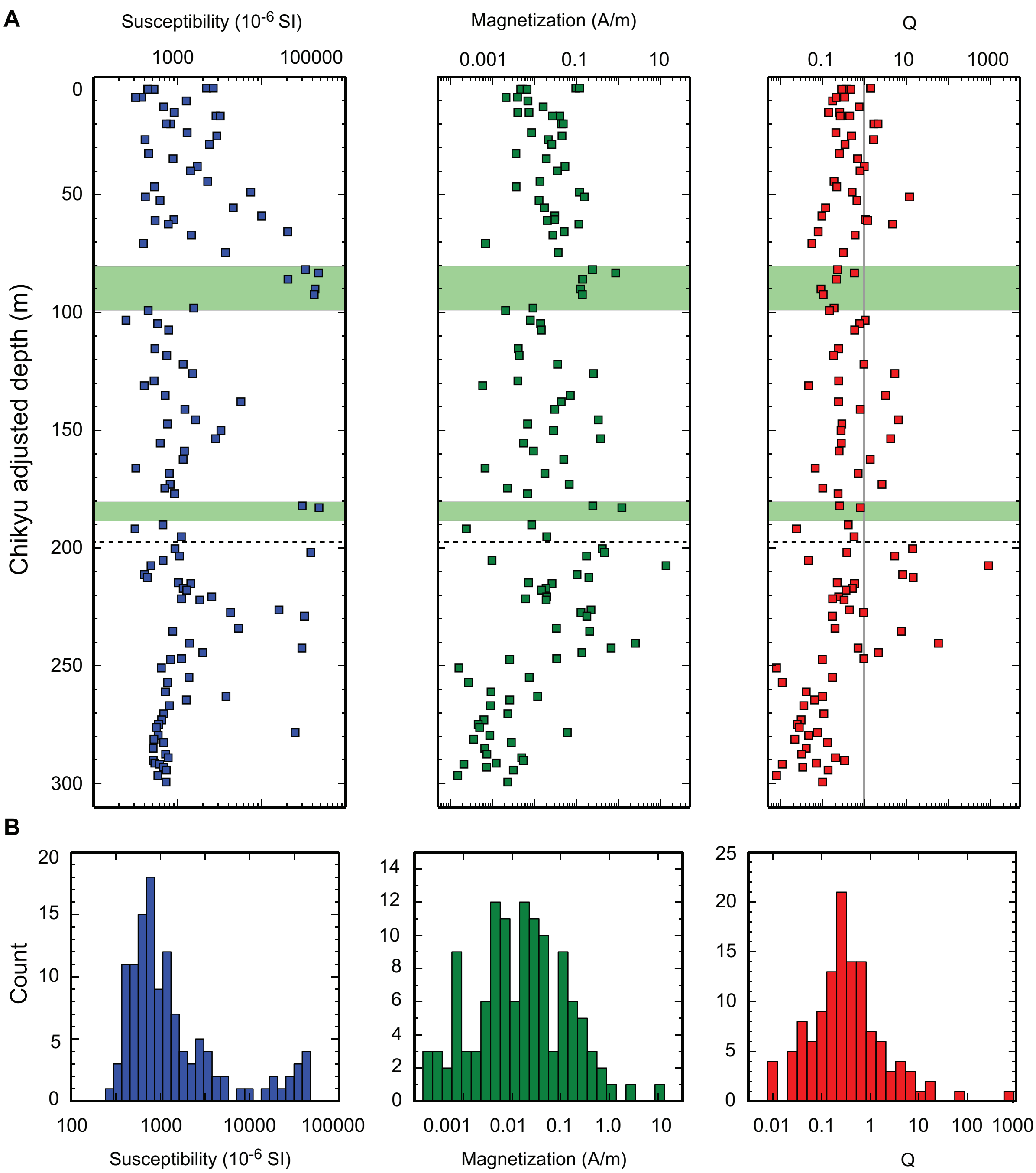

Figure F86. **A.** Representative orthogonal vector projections displaying behavior of magnetic remanence directions during progressive AF demagnetization of discrete samples. **B.** Curves of magnetic intensity as a function of field strength. Black lines = NRM intensity, red lines = vector difference sum.

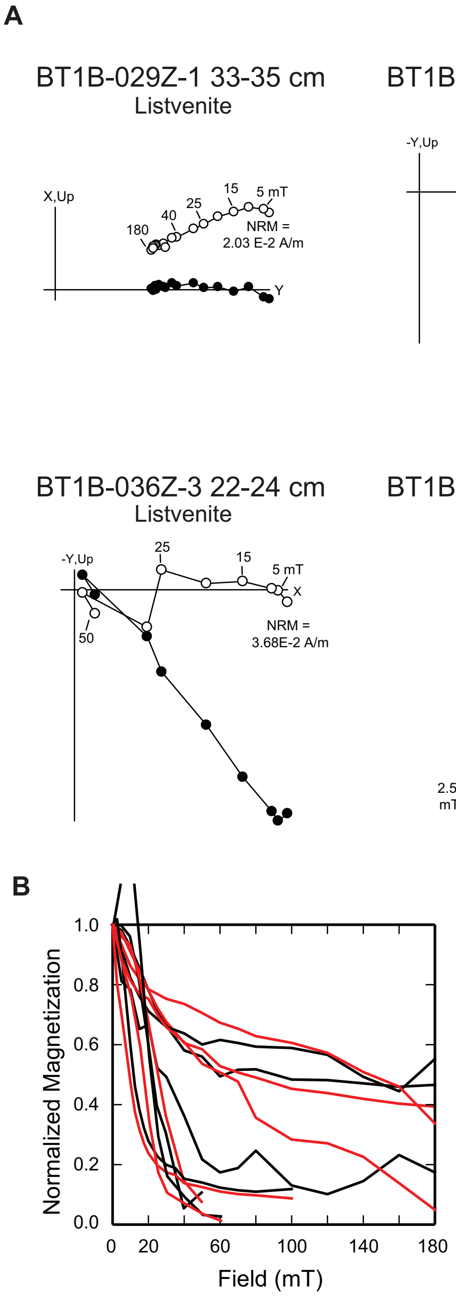

Figure F87. **A.** Orthogonal vector projections displaying behavior of magnetic remanence directions during progressive thermal demagnetization of discrete samples after AF demagnetization to 180 mT. **B.** Curves of intensity as a function of temperature. Black lines = NRM intensity, red lines = vector difference sum. **C.** Bulk susceptibility changes during progressive thermal demagnetization.

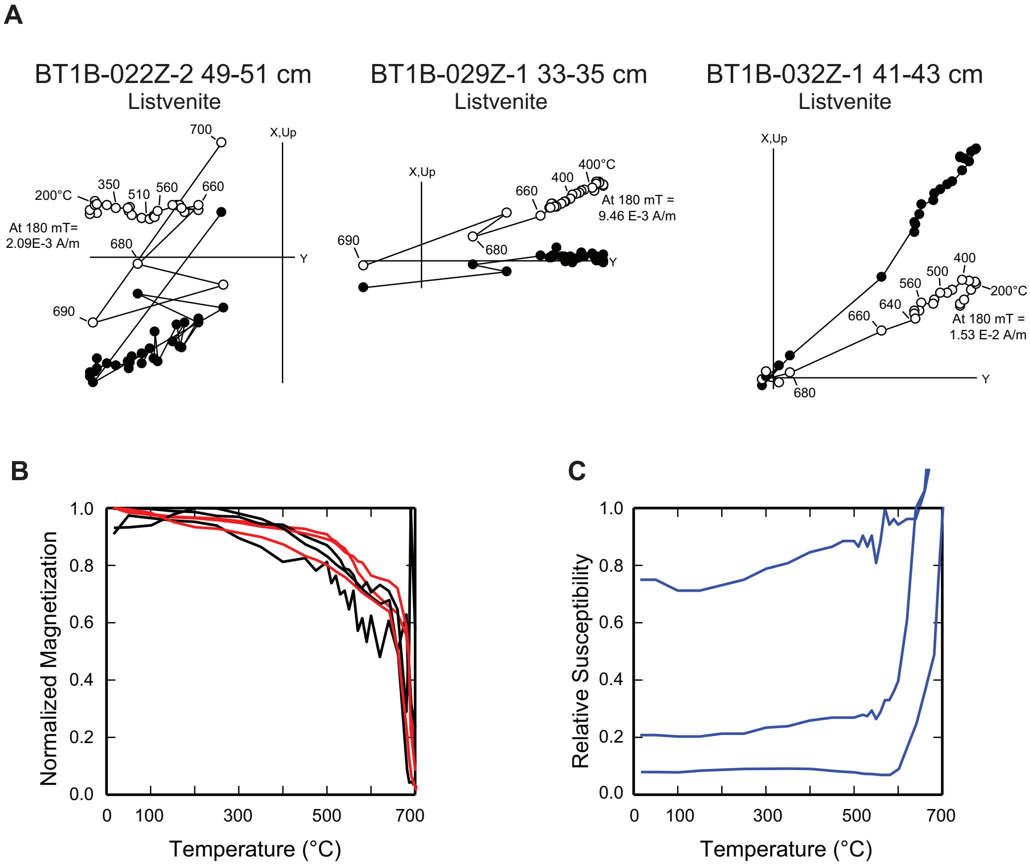

Figure F88. A. Representative orthogonal vector projections displaying behavior of magnetic remanence directions during progressive thermal demagnetization of discrete samples. **B.** Curves of intensity as a function of temperature. Black lines = NRM intensity, red lines = vector difference sum. **C.** Bulk susceptibility changes during progressive thermal demagnetization.

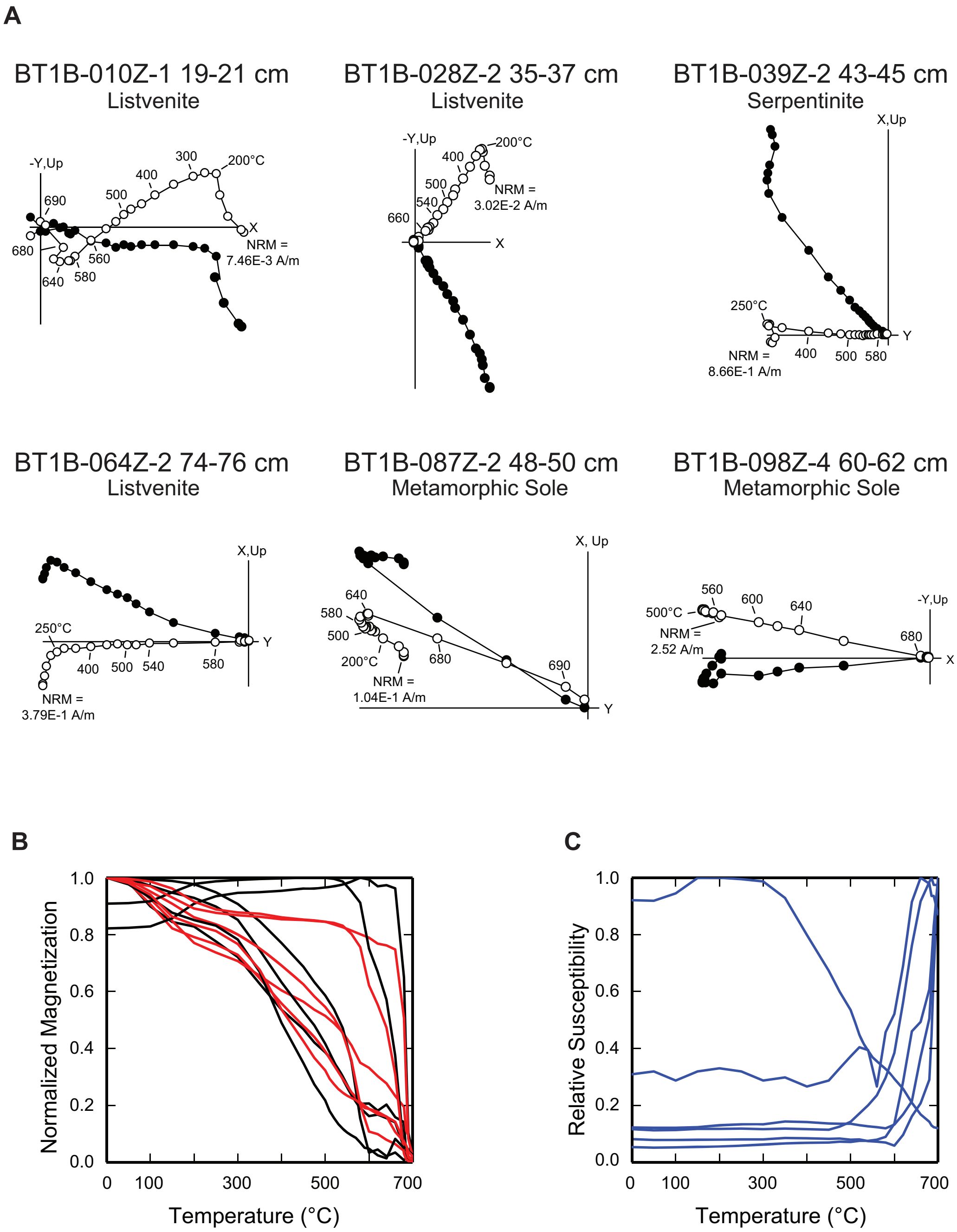

Figure F89. **A.** Orthogonal vector projections displaying additional varied behavior of magnetic remanence directions during progressive thermal demagnetization of discrete samples. Examples here show either rapid decrease in remanence at low to moderate temperatures, large scatter in directions during demagnetization, or a moderate to steep positive inclination component that persists up to 500°, 540°, or 580°C. **B.** Curves of intensity as a function of temperature. Black lines = NRM intensity, red lines = vector difference sum. **C.** Bulk susceptibility changes during progressive thermal demagnetization.

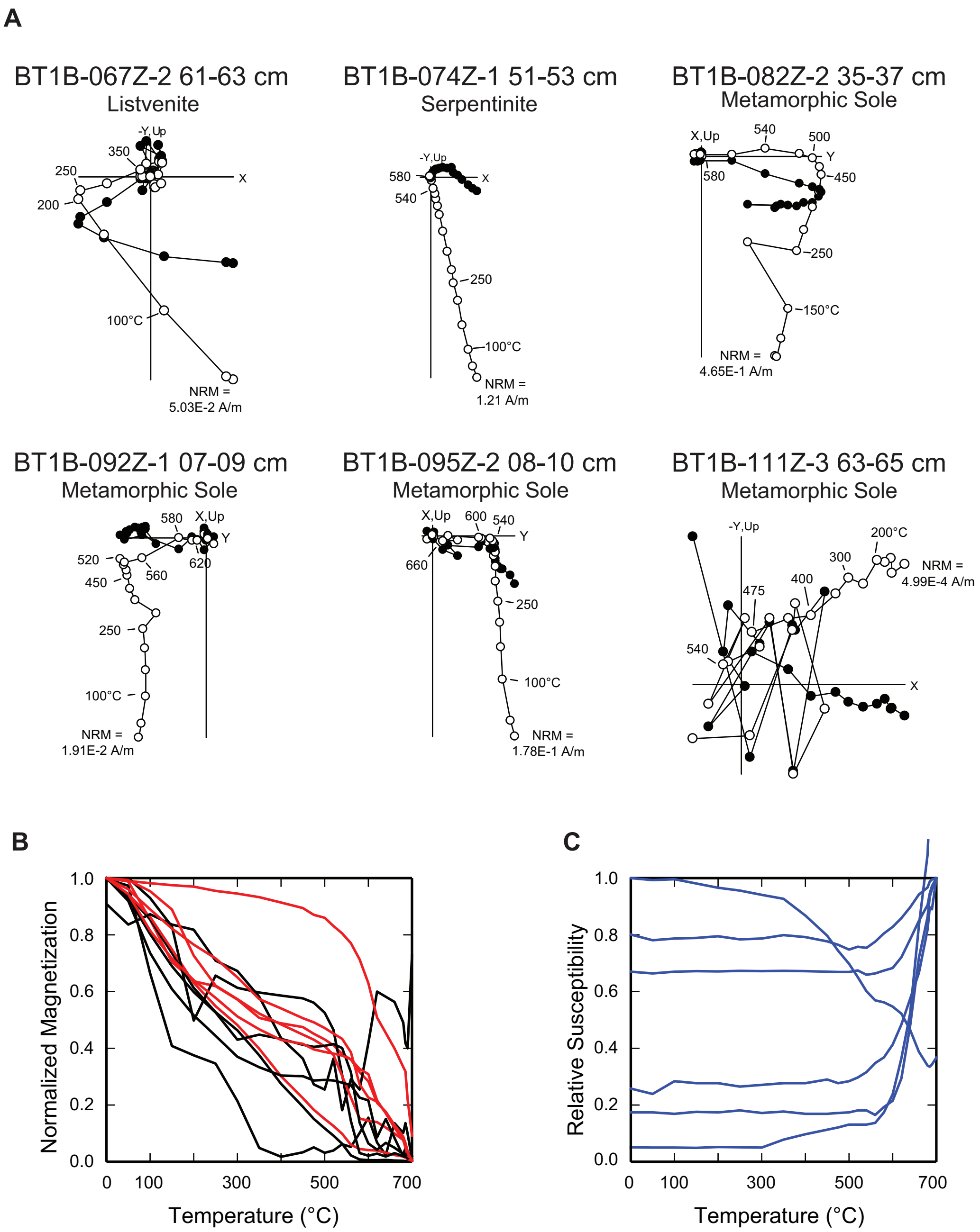

Figure F90. **A**. Stereoplot of characteristic remanence magnetization (ChRM) directions identified by principal component analysis of highest laboratory unblocking-temperature components. Open (solid) symbols represent upper (lower) hemisphere directions. **B**. Histogram of ChRM inclination values, in which the majority of the data have a shallow inclination. These diagrams must be interpreted with caution since the borehole is not vertical and rotation of core pieces around a non-vertical drilling direction would cause scatter in the inclination data.

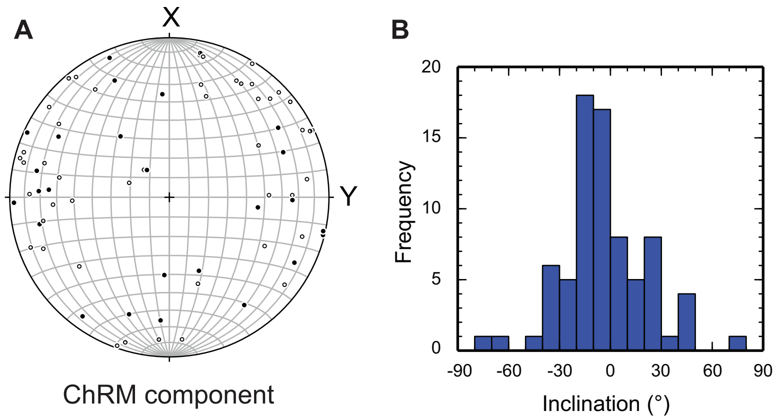

Figure F91. **A.** Downhole plots of magnetic anisotropy intensity, shape, K_{max} inclination and K_{min} inclination. Light green horizontal bars = thin bands of serpentinite, black dashed line = depth of the basal thrust. **B.** Degree of anisotropy (*P*′) as a function of bulk susceptibility. **C.** Shape parameter vs. degree of anisotropy of magnetic susceptibility. Note that a single discrete sample (99Z-3, 44–46 cm; 242.46 m) with the largest *P*′ value (2.49) is not shown on plots to allow trends in other samples to be visible.

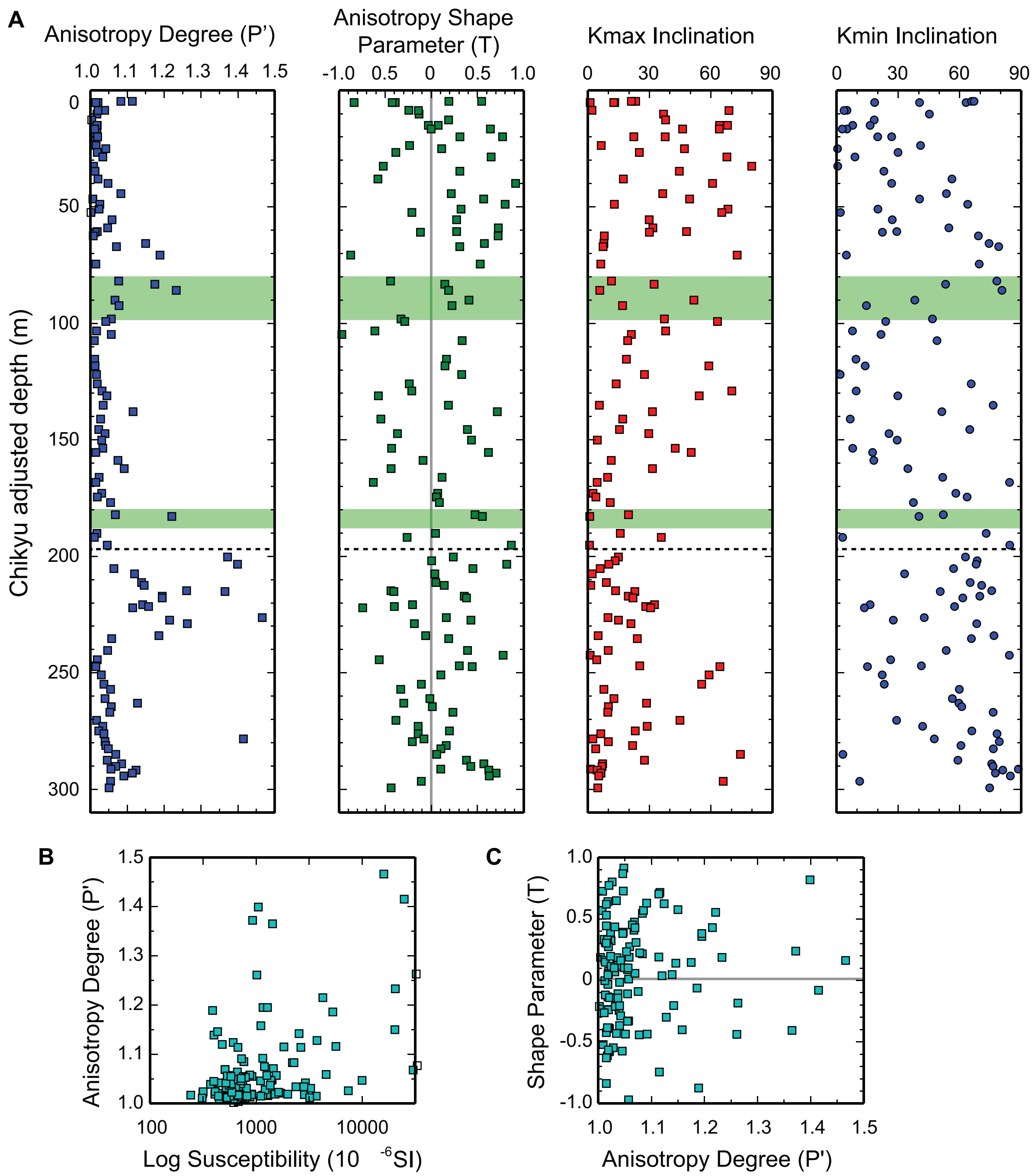

Figure F92. Representative susceptibility-temperature curves for samples from samples of listvenite, serpentinite, and the metamorphic sole. Red lines = susceptibility variation during heating of the sample, blue lines = susceptibility variation during cooling. A few listvenite samples were reheated a second time (shown by partially transparent curves).

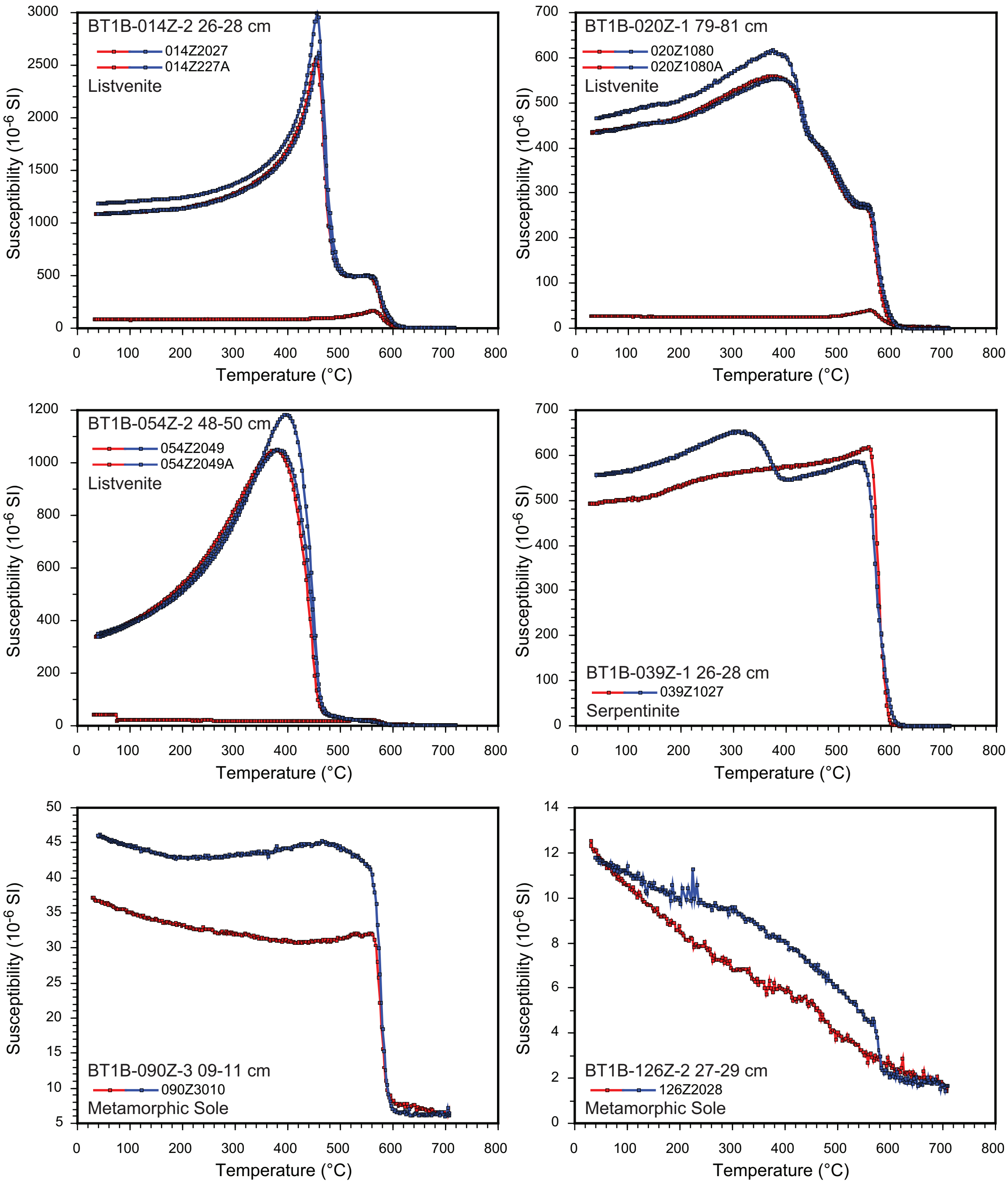

Figure F93. Downhole trend of CT number, GRA density, and color parameters (redness, greenness, blueness, and total RGB intensity) in Hole BT1B. Blue dots = slice averages (0.625 mm intervals), orange dots and line = mode and standard deviation of CT values per section.

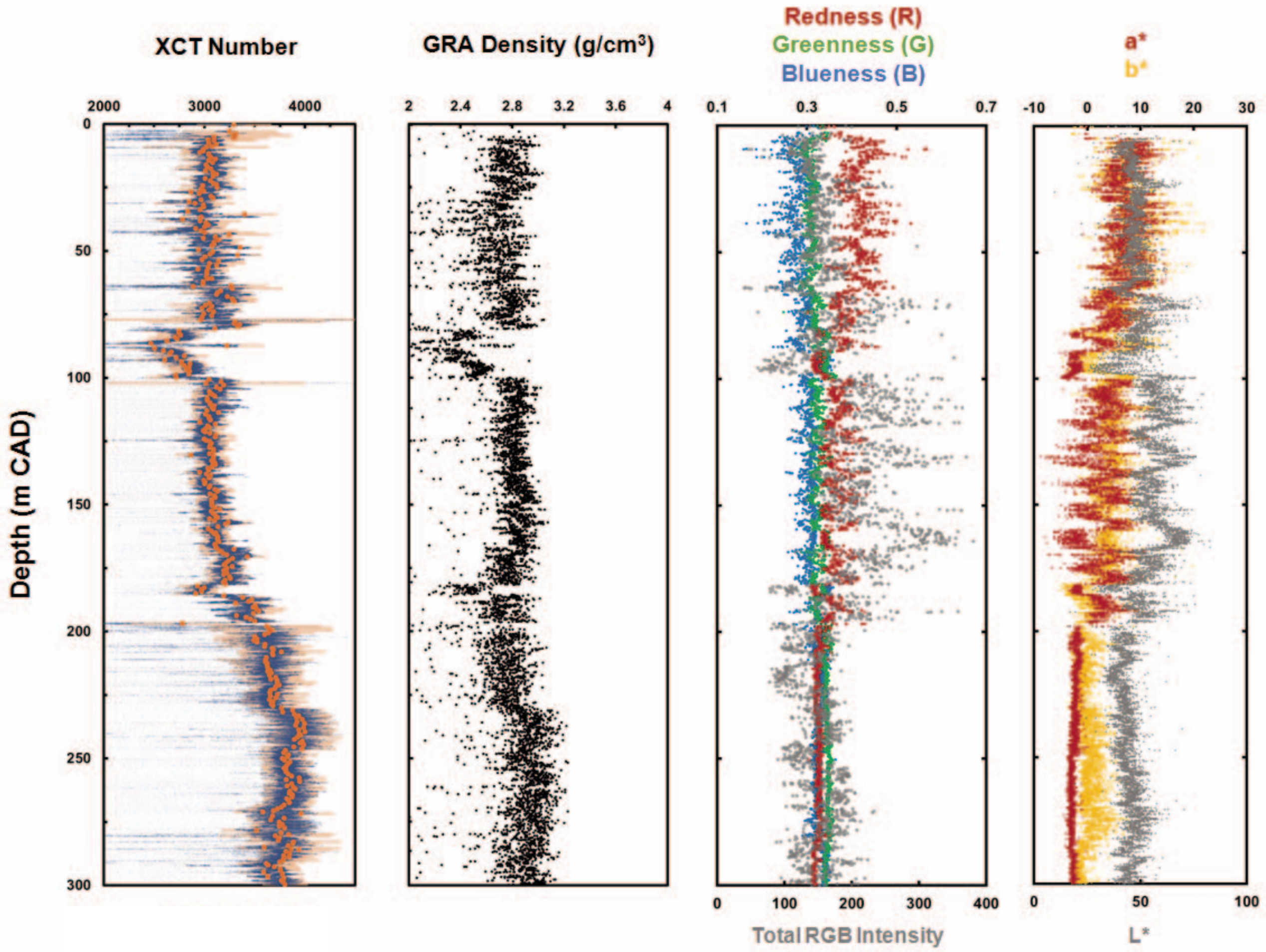

Figure F94. **A.** *XY* plot of CT number vs. GRA density with lithology in Hole BT1B. Dots = average CT and density values for 1 m intervals. In calculating the mean, all CT values < 2000 were omitted, as they represent intervals with empty space. **B.** Close-up of A focusing on listvenite units. Additional points from CT values scanned from quartz (qtz), magnesite (mgs), and dolomite (dol) specimens as well as the CT number acquired from a yellow magnesite (y. mgs) vein (see Figure **F95B** for more details). Dots with thick black outline = units < 30 m above the basal thrust.

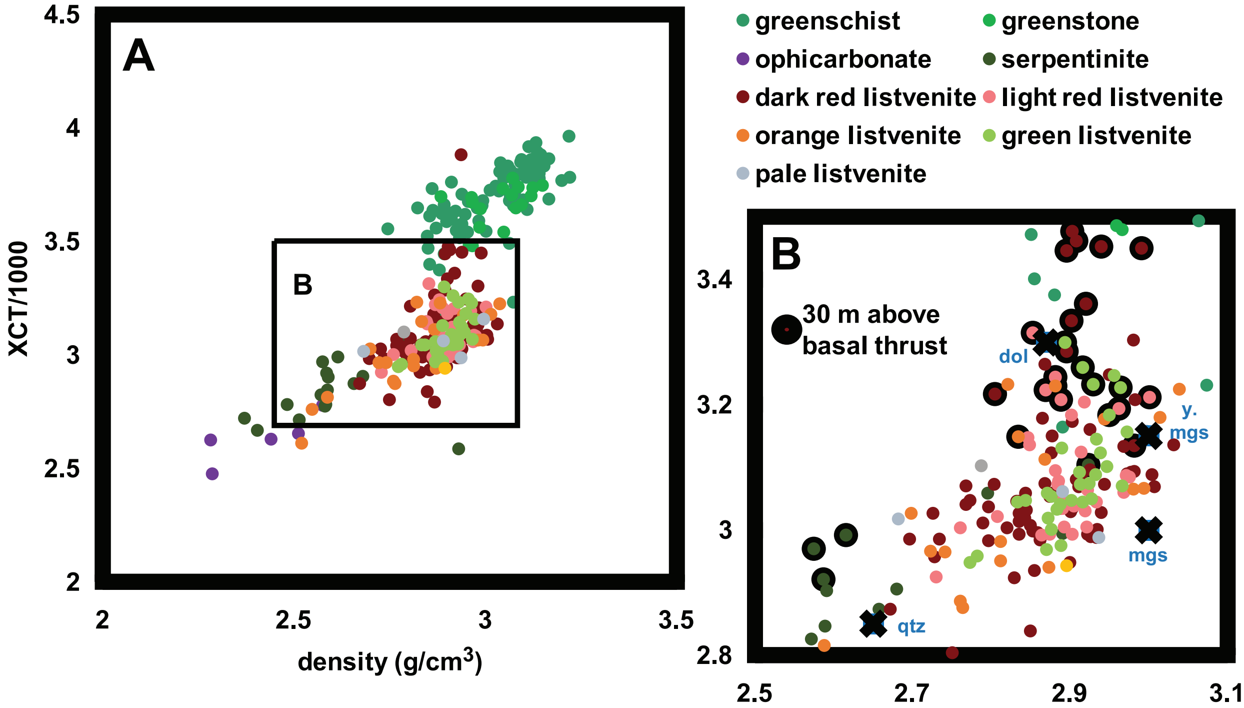

Figure F95. **A.** XCT scan of specimen samples of quartz (Morocco), magnesite (Brazil), dolomite, and calcite. The XY plot shows the CT number associated with these minerals. **B.** Yellow magnesite vein occurring in interval 50Z-1, 7–16 cm, with associated CT number determined from an area within the red box.

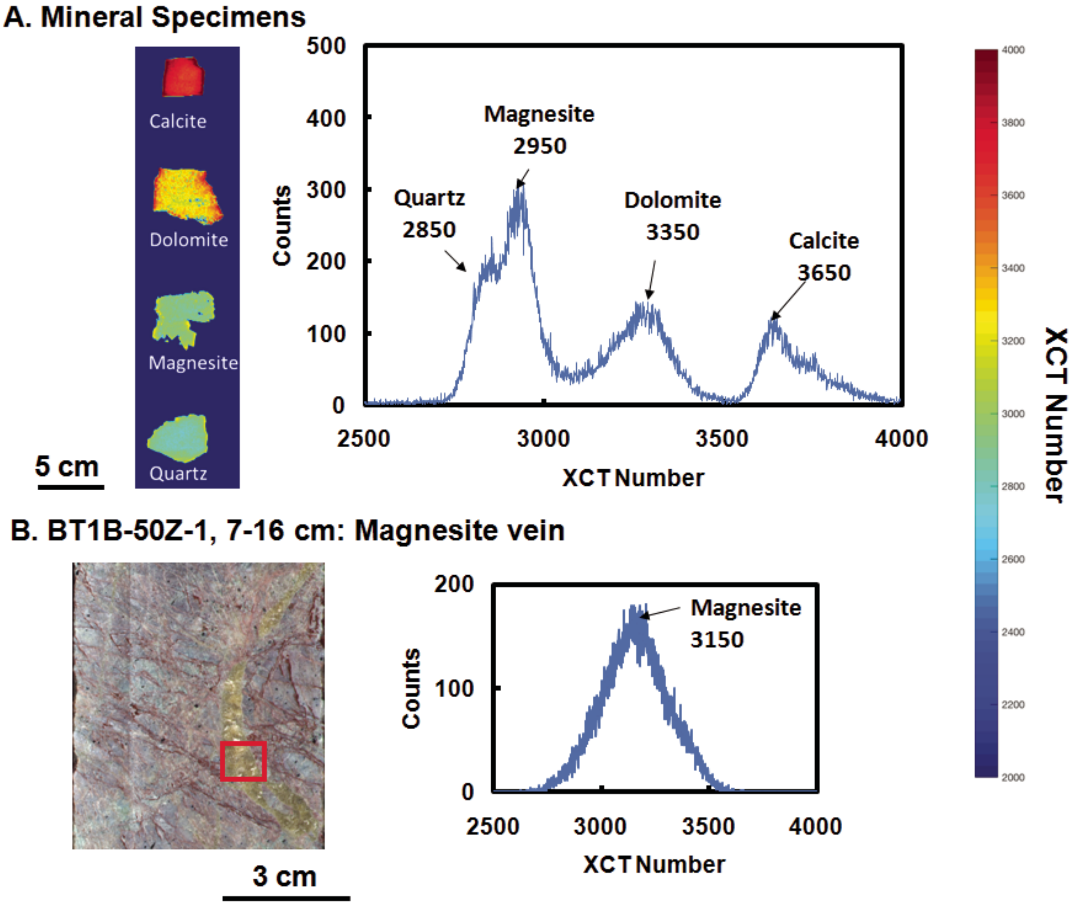

Figure F96. XCT, RGB, and L*a*b* trends.

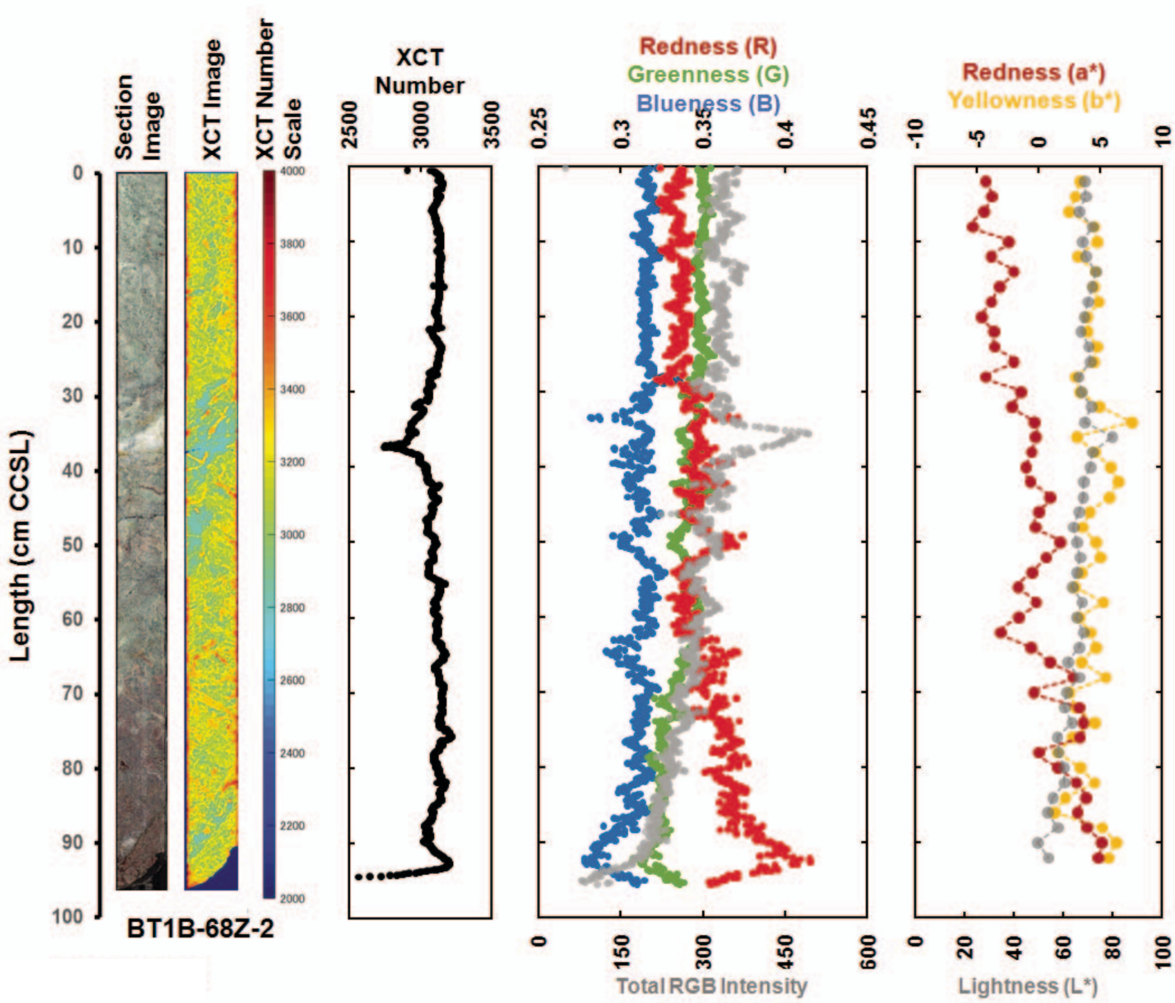

Figure F97. *XY* plot of color parameters (redness, greenness, total RGB intensity) of described lithologic units. Dots and lines = the average and standard deviation, respectively, for all 1 mm interval color data within a lithologic unit.

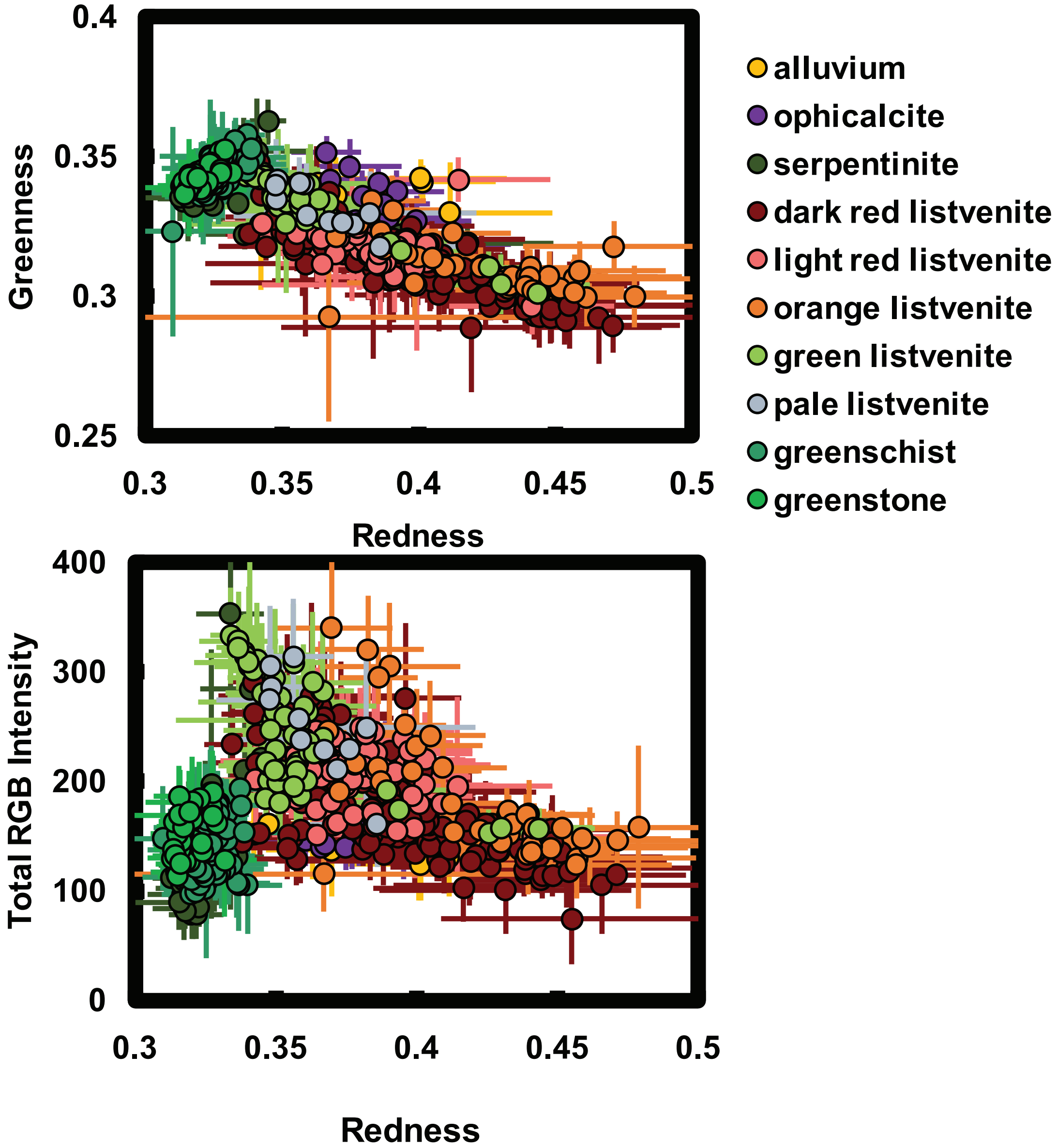

Figure F98. Downhole plots for (**A**) GRA density and MAD bulk density, (**B**) discrete *P*-wave velocity, (**C**) discrete porosity, and (**D**) magnetic susceptibility with logarithm scale, (**E**) filtered NGR, and (**F**) *P*-wave velocity measured by MSCL-W, with discrete sample measurements for comparison.

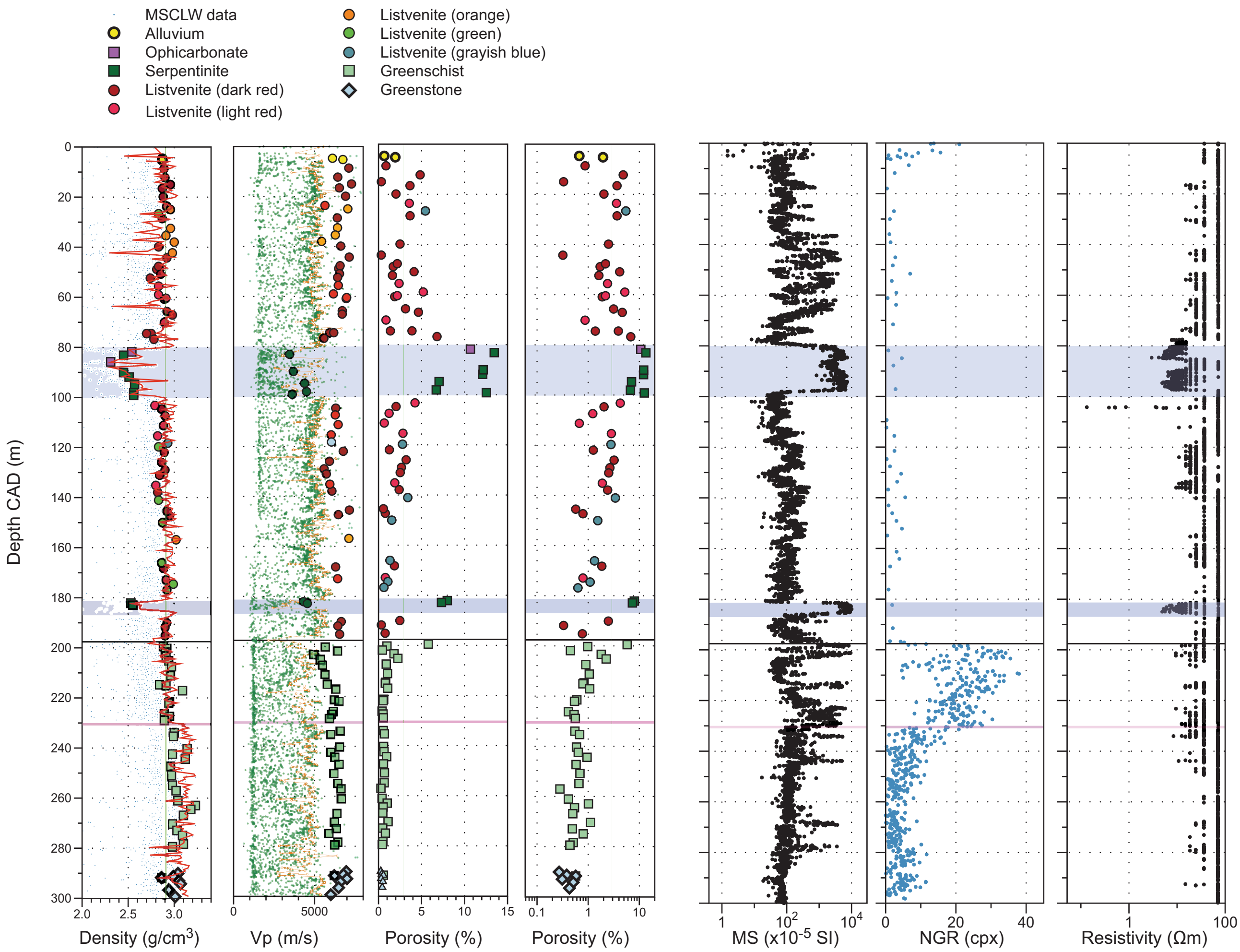

Figure F99. *P*-wave velocity vs. (**A**) bulk density and (**B**) porosity of different lithologies from Hole BT1B, plotted with data from Holes GT1A and GT2A and serpentinite cores from Hole 1274A, ODP Leg 209 (Kelemen et al., 2004).

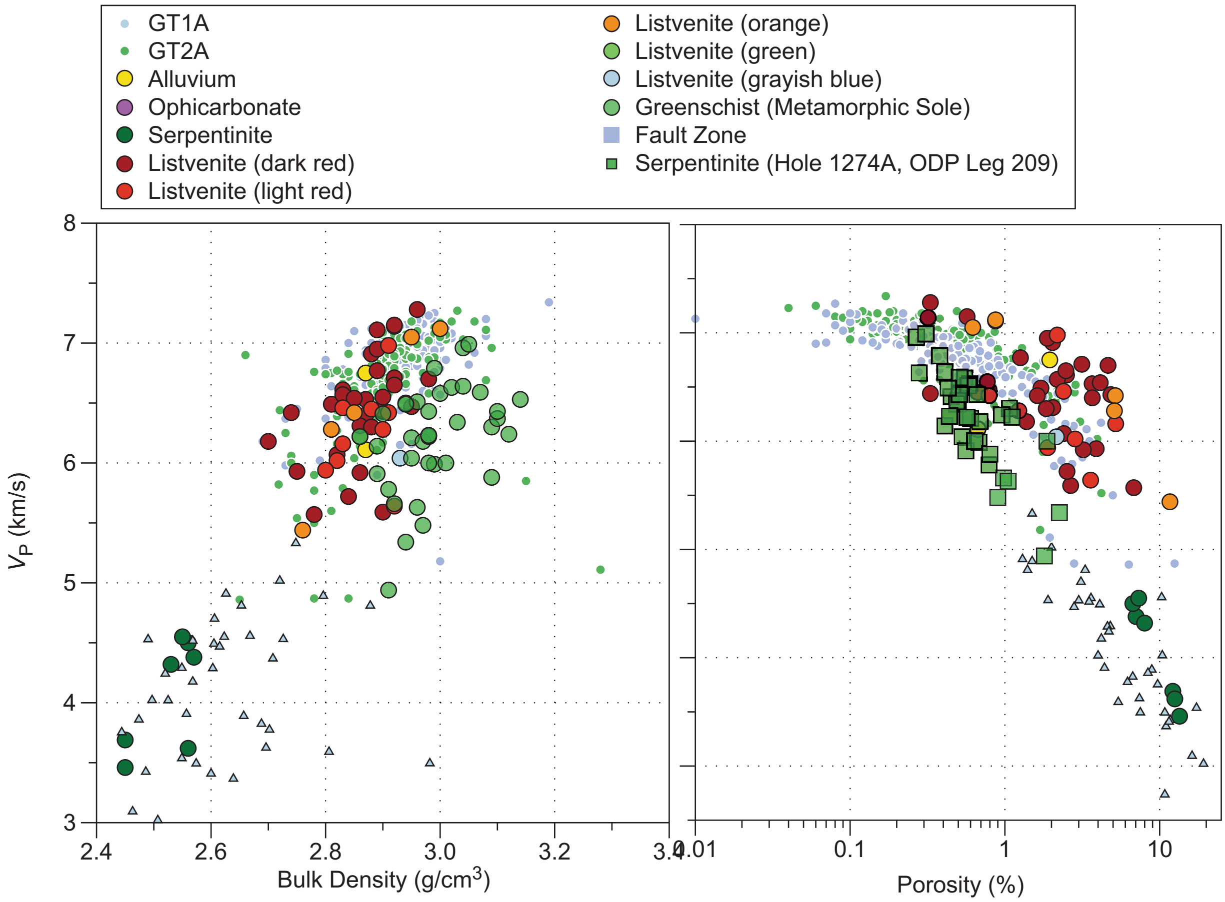

Figure F100. Linescan core image of a highly weathered interval of the core with high porosity and low density.

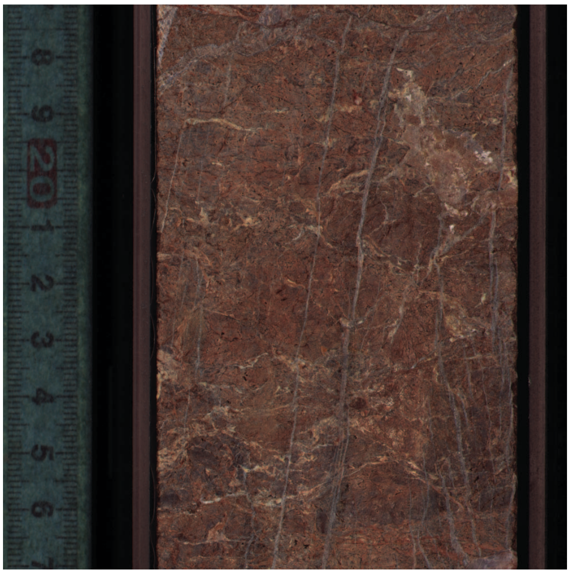

Depth CAD = 37.99 m

C5704B-19Z-3-1a-w-21-23 cm

Porosity = 11.65 %

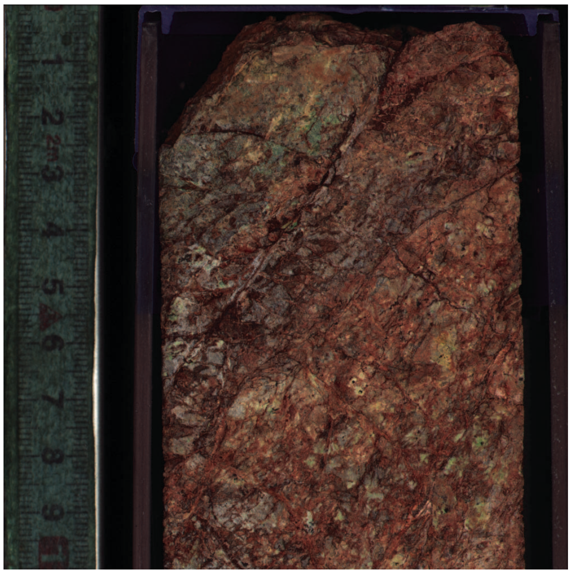

Depth CAD = 42.29 m

C5704B-21Z-1-1a-w-4-6 cm

Porosity = 21.28 %

Figure F101. Downhole distribution of thermal conductivity in Hole BT1B. The lithology of samples is that of the host igneous intervals.

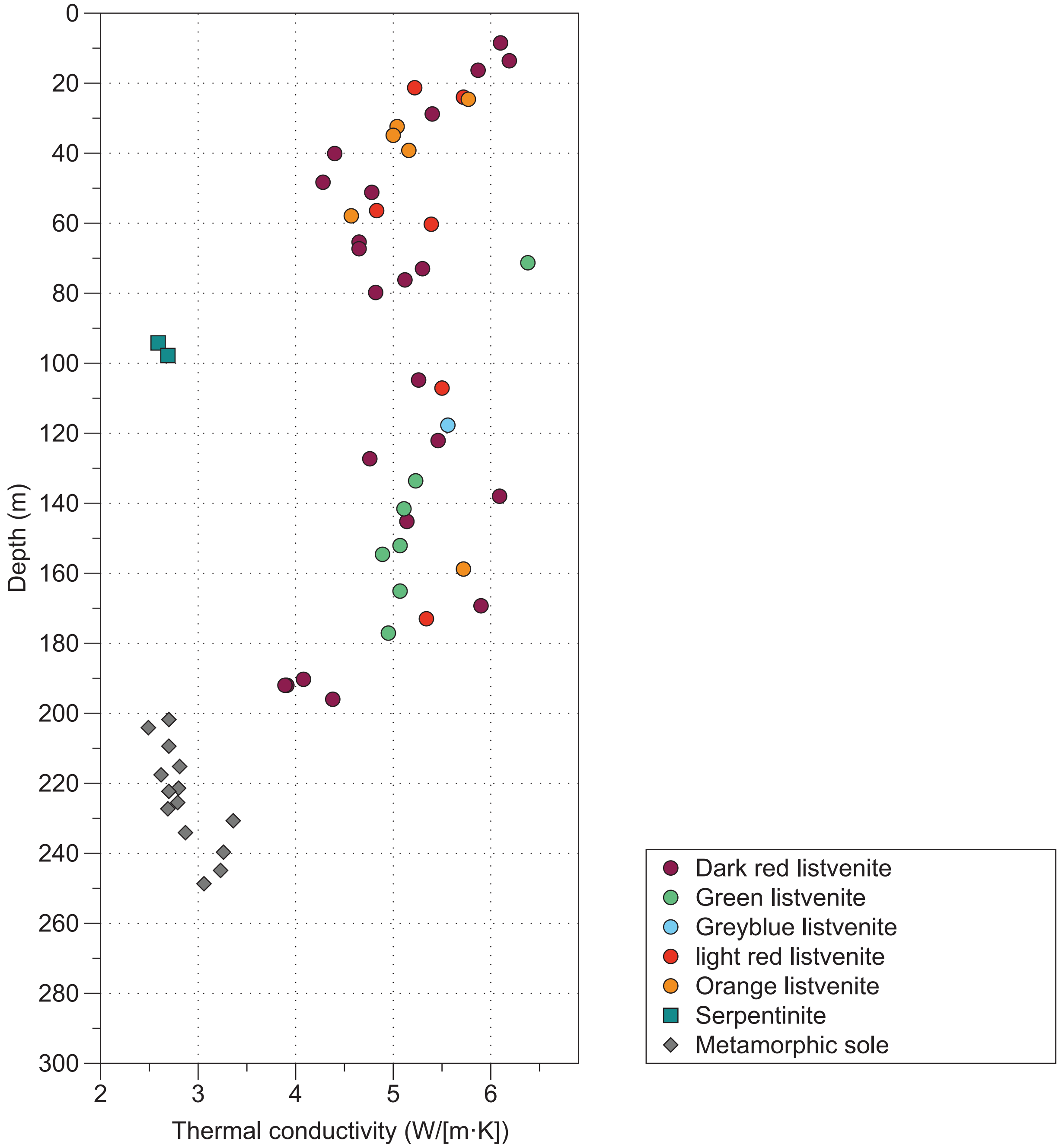

Figure F102. Histograms of thermal conductivity in Hole BT1B. Listvenite core samples are classified into 5 groups by the color of the host rock (see **Host rock** for detail of classification of listvenite cores).

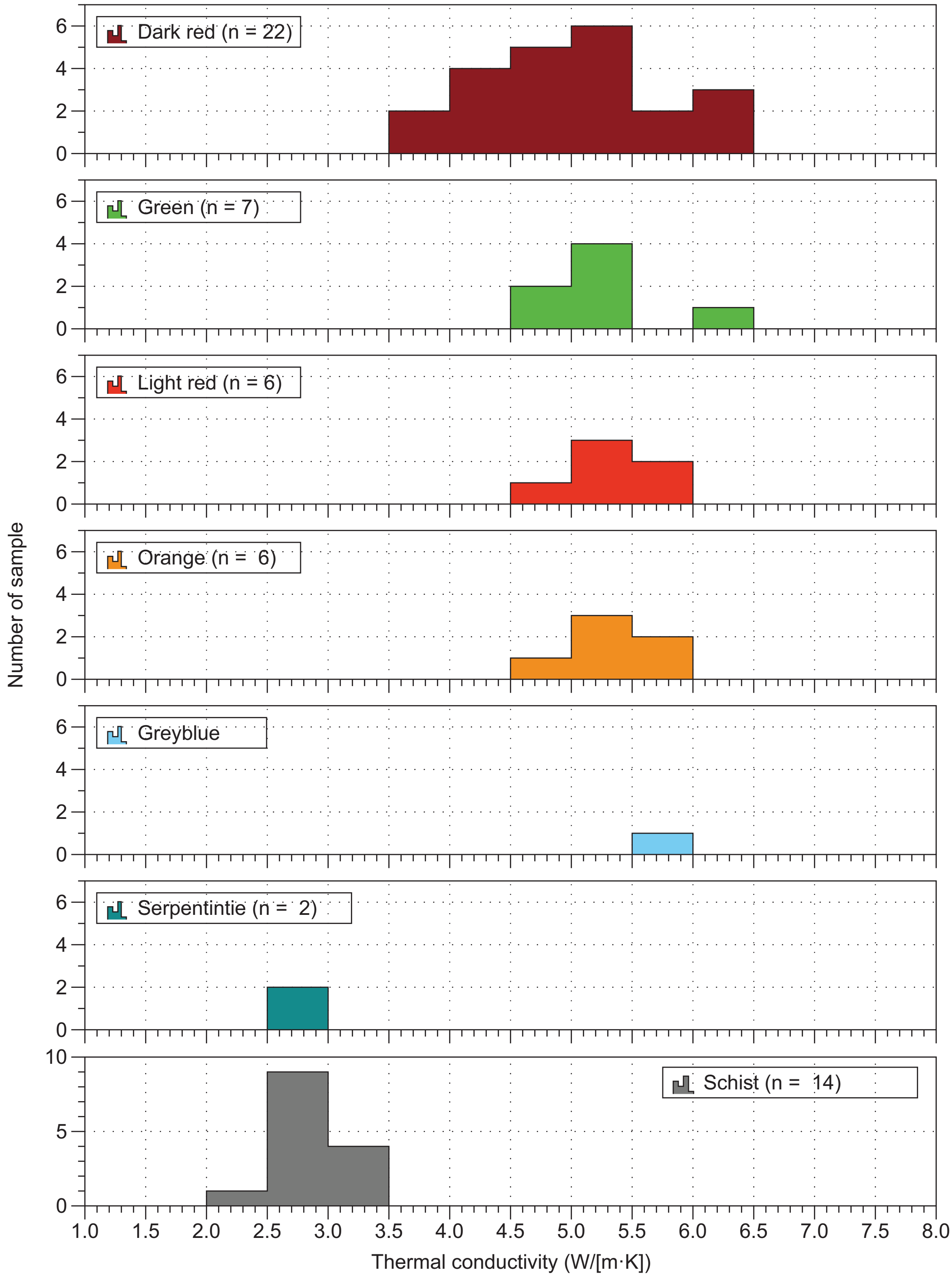

Tables

Table T1. Operations and coring summary, Hole BT1B. **This table is available in Microsoft Excel format.**

Table T2. Summary of units and their characteristics in Hole BT1B. **This table is available in Microsoft Excel format.**

Table T3. List of analyzed cores and areas measured by XRFCL. **This table is available in Microsoft Excel format.**

Table T4. Summary of mineralogy semiquantitative estimation from XRD measurements. **This table is available in Microsoft Excel format.**

Table T5. Summary of data extracted from the thin section description sheets for Hole BT1B. **This table is available in Microsoft Excel format.**

Table T6. Thin section summary for the serpentinite rock group. **This table is available in Microsoft Excel format.**

Table T7. Density of structural features by rock type, Hole BT1B. **This table is available in Microsoft Excel format.**

Table T8. Preliminary classification of veins in listvenites, Hole BT1B. **This table is available in Microsoft Excel format.**

Table T9. Preliminary classification of veins in serpentinites, Hole BT1B. **This table is available in Microsoft Excel format.**

Table T10. Preliminary classification of veins in footwall metamorphic rocks, Hole BT1B. **This table is available in Microsoft Excel format.**

Table T11. Host rock structural measurements, Hole BT1B. **This table is available in Microsoft Excel format.**

Table T12. Major, trace, and rare earth element concentrations, total volatiles, and CHNS in rock powders, Hole BT1B. **This table is available in Microsoft Excel format.**

Table T13. Natural remanent magnetization results, Hole BT1B. **This table is available in Microsoft Excel format.**

Table T14. Magnetic susceptibility values and anisotropy parameters, Hole BT1B. **This table is available in Microsoft Excel format.**

Table T15. Summary of discrete physical properties measurements, Hole BT1B. **This table is available in Microsoft Excel format.**

Table T16. Velocity, density, and porosity measurements. **This table is available in Microsoft Excel format.**

Table T17. Thermal conductivity measurements, Hole BT1B. **This table is available in Microsoft Excel format.**

Supplemental tables

Supplemental Table ST1. Vein log. **This table is available in Microsoft Excel format.**

Supplemental Table ST2. Vein XRD log. **This table is available in Microsoft Excel format.**

Supplemental Table ST3. Vein XRD summary. **This table is available in Adobe PDF format.**

Supplemental Table ST4. MSCL-W data. **This table is available in Microsoft Excel format.**

Supplemental Table ST5. MSCL-C data. **This table is available in Microsoft Excel format.**

Supplemental Table ST6. MSCL-I data. **This table is available in Microsoft Excel format.**